Titre: Title:	Design of Barricades Made of Waste Rocks for Backfilled Stopes
Auteur: Author:	Yulong Zhai
Date:	2021
Type:	Mémoire ou thèse / Dissertation or Thesis
Référence: Citation:	Zhai, Y. (2021). Design of Barricades Made of Waste Rocks for Backfilled Stopes [Thèse de doctorat, Polytechnique Montréal]. PolyPublie. https://publications.polymtl.ca/9991/

URL de PolyPublie: PolyPublie URL:	https://publications.polymtl.ca/9991/
Directeurs de recherche: Advisors:	Li Li
Programme: Program:	Génie minéral

POLYTECHNIQUE MONTRÉAL

affiliée à l'Université de Montréal

Design of barricades made of waste rocks for backfilled stopes

YULONG ZHAI

Département des génies civil, géologique et des mines

Thèse présentée en vue de l'obtention du diplôme de *philosophiae doctor*

Génie minéral

Décembre 2021

POLYTECHNIQUE MONTRÉAL

affiliée à l'Université de Montréal

Cette thèse intitulée :

Design of barricades made of waste rocks for backfilled stopes

présentée par **Yulong ZHAI**

en vue de l'obtention du diplôme de *Philosophiae Doctor*

a été dûment acceptée par le jury d'examen constitué de :

Richard SIMON, président
Li LI, membre et directeur de recherche
Samuel YNIESTA, membre
Biao LI, membre externe

DEDICATION

To my wife and son

To my parents

To my homeland

ACKNOWLEDGEMENTS

I feel very lucky that Prof. Li Li gave me an opportunity to continue the Ph.D. study. Prof. Li spends so much previous time helping with my project. He devotes his time to scientific research and spends much time on my project. He teaches me so many things like a very strict father. He shares precious knowledge and new ideas with me. I am deeply affected by his attitude to the research, for example, he focuses on all details and spends much time studying them. He understands and explains things from their basic and physical meaning. Many good articles are born of these details. The papers in this project cannot be perfect without his help and insistence. I will ever remember the chance Prof. Li Li gave and be grateful for this.

Lots of thanks to Prof. Richard Simon, Prof. Samuel Yniesta, and Prof. Biao Li for their valuable time to evaluate my thesis. Prof. Benoît Courcelles is gratefully acknowledged for his time to represent the Dean of Graduate Studies of Polytechnique Montreal.

Many thanks to Prof. Richard Simon, Dr. Feitao Zeng, and Dr. Jian Zheng for their precious time and evaluation of the pre-doctoral report during the Comprehensive Examination.

I would like to thank Prof. Robert P. Chapuis because he spends much time correcting the article and talking with me. I learned many things from his lecture. I also appreciate that my colleagues gave much help to me in life and academics such as Ali Reza Zafarani, Akram Deiminiat, Yuyu Zhang, Shengpeng Hao, Peiyong Qiu, Ruofan Wang, and Feitao Zeng. Dr. Feitao Zeng assisted me with a deeper understanding of the mechanics. For example, Feitao taught me how to understand the Mohr-Coulomb failure criterion by using the knowledge of friction we learned in high school. It is very helpful and I benefit a lot. Lots of thanks to Dr. Pengyu Yang who spent much time correcting the paper.

I want to acknowledge the financial support from the Natural Sciences and Engineering Research Council of Canada (NSERC 402318), Fonds de Recherche du Québec - Nature et Technologies (FRQNT 2015-MI-191676), the partners of the Research Institute on Mines and Environment

(RIME UQAT - Polytechnique; http://rime-irme.ca). Lots of thanks for the financial support from Mitacs and Young-Davidson mine. In the Young-Davidson mine, Dr. Yuhang Xu allowed me to have the internship and help me a lot in the mine. Mr. Travis Blake taught me much practical knowledge. Other colleges, such as Abdel. Belamri, Justin Faggioni, Patricia Stancheff, Robert Balliu, and Jai Pawan Chandh, also help me a lot. Lots of thanks to them.

Lastly, I have heartfelt gratitude for my wife Li Qin who accompanies me across the oceans from China to Canada. My parents always show selfless giving to me. My son Zhihaitang Zhai give me the happiness and courage to insist on my Ph.D. study. Lots of thanks to my family.

RÉSUMÉ

Les quantités massives de solides produits par les mines en formes de stériles et de résidus miniers sont déposées à la surface. Ces rejets miniers peuvent constituer la source d'aléas géotechniques et de problèmes environnementaux (drainage minier acide, drainage neutre contaminé). Pour minimiser les problèmes environnementaux et géotechniques, le remblayage des chantiers souterrains avec des rejets miniers est devenu une pratique populaire et largement adopté dans les mines modernes en souterrain. Une principale préoccupation correspondante est de savoir si les barricades ont une capacité suffisante pour retenir la boue de remblai fraîchement déversée dans les chantiers. La capacité (résistance) d'une barricade dépend de sa géométrie et du type de matériau. Au Canada, l'utilisation des roches stériles pour la construction des barricades est devenue populaire. Des solutions analytiques ont été proposées par Li et collaborateur pour dimensionner les barricades faites de roches stériles. Les solutions analytiques ont été calibrées ou validées par des résultats numériques obtenus avec des modèles bi- dimensionnels. De plus, aucune solution n'est disponible pour la conception de béton projeté appliqué sur les barricades en roches stériles. L'objectif de cette thèse est de développer des solutions analytiques pour la conception des barricades en roches stériles avec ou sans béton projeté.

Pour atteindre cet objectif, un outil numérique 3D est nécessaire. FLAC3D a été choisi pour sa disponibilité et son vaste application en géotechnique. Sa validité et son applicabilité ont été d'abord testées contre des solutions analytiques, développées pour estimer le débit d'eau à travers une digue en forme trapézoïdale. Ces travaux ont permis de montrer que seulement la solution analytique généralisée en 3D à partir de la théorie de Dupuit est capable de prédire correctement le débit d'eau. Plus de comparaisons montrent cependant que la solution généralisée en 3D de Dupuit ne permet de calculer correctement le débit d'eau lorsque la nappe d'eau en aval devient importante. Plus d'analyses ont permis de dévoiler que le modèle de Dupuit contient deux hypothèses non-représentatives, une sur la distance d'écoulement et l'autre sur l'aire transversale d'écoulement. La solution proposée basée sur la solution de Dupuit est modifiée en ajoutant deux coefficients

d'étalonnage, un pour la longueur du trajet d'écoulement et un autre pour la section transversale d'écoulement moyenne. Les deux coefficients sont calibrés par quelques résultats numériques avec FLAC3D pour un cas particulier. La solution analytique proposée et calibrée est ensuite validée par des résultats de modélisation numérique supplémentaires avec différents cas. Les solutions numériques et analytiques sont ensuite validées par des résultats expérimentaux obtenus par des essais d'infiltration effectués en laboratoire. La réalisation de ces travaux a finalement mené à la naissance d’une solution améliorée pour estimer le débit d’eau à travers une digue en remblai rocheux et à la validation du modèle numérique de FLAC3D. Le logiciel FLAC3D peut être utilisé pour analyser la stabilité des barricades construites de roches stériles avec ou sans béton projeté.

Une nouvelle solution analytique a été d'abord proposée pour estimer la cohésion de béton projeté requise avec une géométrie donnée ou pour estimer l'épaisseur du béton projeté requise avec un matériau de béton projeté donné. Les matériaux sont considérés comme élasto-plastiques obéissant au critère de Mohr-Coulomb. Un critère d'instabilité structurale, basé sur la première occurrence parmi les sauts de déplacement au sommet de la barricade ou la fusion des zones de plasticité, est introduit pour aider à juger d’une façon plus objective le début de l'instabilité d'une structure de barricade en roches stériles avec du béton projeté. La solution analytique proposée est d'abord calibrée par quelques résultats numériques. La capacité de prédiction de la solution analytique proposée a été vérifiée à l'aide des résultats numériques supplémentaires.

Lors de la réalisation des travaux précédents, on a constaté que le plan de glissement dans les modèles numériques est toujours incliné alors que les solutions analytiques proposées ont été établies en supposant un plan de glissement horizontal. En plus, la solution analytique de Yang et al. (2017) développée pour dimensionner des barricades construites en roches stériles a été seulement validée partiellement par des résultats numériques obtenus avec FLAC2D. Une mise à jour de la solution de Yang et al. (2017) est nécessaire en considérant un plan de glissement incliné, validée par des modélisations numériques tridimensionnelles. Le coefficient de pression des terres pour la stabilité globale et la stabilité locale est modifié en considérant sa définition donnée dans

le modèle de Yang et al. (2017). Ces modifications améliorent considérablement la solution car la solution proposée ne contient aucun coefficient de calibration empirique. La validité de la solution proposée est testée par des modélisations numériques avec FLAC3D. De nouveau, la première occurrence parmi les sauts de déplacement ou la fusion des zones de plasticité passant à travers la structure d'une barricade en roches stériles est utilisée comme le critère d'instabilité plus objectif pour estimer la longueur minimale requise d'une barricade en roches stériles. La solution proposée est ensuite validée contre des résultats expérimentaux disponibles dans la littérature.

ABSTRACT

Massive quantities of solid wastes produced by mines in the form of waste rocks and tailings are deposited on the ground surface. These mining wastes can be the source of geotechnical hazards and environmental problems (acid mine drainage, contaminated neutral drainage). To minimize environmental and geotechnical problems, stope backfilling with mine wastes has become popular and widely adopted by many modern underground mines. The main corresponding concern is whether the barricades have sufficient capacity to retain the freshly slurried backfill at the early age. The capacity (strength) of a barricade depends on its geometry and type of material. In Canada, using waste rocks to build barricades has become popular. Analytical solutions have been proposed by Li and coworkers to design waste rock barricades. Their solutions have been calibrated and validated by numerical results obtained by 2D models. In addition, there is no solution available to design shotcrete applied on waste rock barricades. The objective of this thesis is to develop analytical solutions for the design of waster rock barricades with or without shortcrete.

To reach this objective, a 3D numerical tool is necessary. FLAC3D was chosen for its availability and large application in geotechnical engineering. Its validity and applicability was first tested against analytical solutions developed to estimate the seepage through a trapezoidal dam. This work has shown that only the analytical solution generalized in 3D from the Dupuit theory is able to correctly predict the seepage rate. More comparisons show however that the generalized 3D Dupuit solution is not able to correctly calculate the seepage rate when the downstream water table becomes important. Further analysis revealed that the Dupuit model contains two non-representative assumptions, one on the flow distance and the other on the cross-section area. The proposed solution based on Dupuit's solution is modified by adding two calibration coefficients, one for the flow path length and another for the average area of cross section. Both coefficients are calibrated by some numerical results with FLAC3D for a particular case. The proposed and calibrated analytical solution is then validated by additional numerical modeling results with different cases. The numerical and analytical solutions are then validated by experimental results

obtained from laboratory infiltration tests. The realization of this work led to the birth of an improved solution for estimating the seepage rate through a rockfill dam and the validation of the numerical model of FLAC3D. The FLAC3D can thus be used to analyze the stability of waste rock barricades with or without shotcrete.

A new analytical solution was first proposed to estimate the required shotcrete cohesion with a given geometry or to estimate the required shotcrete thickness with a given shotcrete material. The materials are considered as elasto-plastic obeying the Mohr-Coulomb criterion. An instability criterion, based on the first occurrence among displacement jumps at the top of the barricade or the coalescence of plasticity zones, is introduced to help judge the onset of instability of waste rock barricades with shotcrete. The proposed analytical solution is first calibrated by some numerical results. The predictive capability of the proposed analytical solution was verified with additional numerical simulation results.

In the previous work, the sliding plane in the numerical models is always inclined while the proposed analytical solutions were developed by assuming a horizontal sliding plane. In addition, the analytical solution of Yang et al. (2017) developed to size waste rock barricades was only partially validated by numerical results obtained with FLAC2D. An update of the Yang et al. (2017) solution is required by considering an inclined sliding plane and validated by three-dimensional numerical modeling. The earth pressure coefficient for global stability and local stability is modified according to its definition given in Yang et al. (2017). These modifications significantly improve the solution because the proposed solution does not contain any empirical calibration coefficient. The validity of the proposed solution is tested by numerical models built with FLAC3D. Again, the first occurrence among the displacement jumps or coalescence of yield zones passing through the waste rock barricade is used as a more objective instability criterion to estimate the minimum required length of waste rock barricades. The proposed solution is then validated against experimental results available in the literature.

TABLE OF CONTENTS

LIST OF TABLES

LIST OF FIGURES

LIST OF SYMBOLS AND ABBREVIATIONS

Symbols

a	distance of the seepage surface along the downstream between the free surface and dike bottom (m)
a_0	vertical gap between the outcrop of the seepage face and the tail water surface (m)
B	width of the stope or the opening (m)
B_h	horizontal bending coefficient
B_v	vertical bending coefficient
c_b	interface cohesion between fill and lateral walls (kPa)
c_i	adhesion of shotcrete-rock interface (kPa)
c_s	cohesion of shotcrete (kPa)
C_G	calibration factor
C_L	calibration factor
C_M	calibration factor
Cw	solids concentrations (i.e., solid content by weight)
E_r	elastic modulus of rock mass (GPa or MPa)
E_s	elastic modulus of shotcrete (GPa or MPa)
E_{wr}	elastic modulus of waste rocks (GPa or MPa)
F_{ct}	tensile resistant force of concrete (kN)
F_{dow}	flexural reinforcement of concrete (kN)

F_{faile}	ultimate capacity of a slab or barricade (kN)
F_h	horizontal load acting on a barricade (kN)
F_{lex}	ultimate flexure load of a slab or barricade (kN)
F_p	resistant forces in the prestressed cable tendons (kN)
F_{pun}	ultimate punching load of a slab or barricade (kN)
F_{sw}	shear reinforcement of concrete (kN)
g	gravity (m/s^2)
h	elevation of water surface along the dike (m)
h_1	hydraulic head at the upstream of the dike (m)
h_2	hydraulic head at the downstream of the dike (m)
H	height of the backfilled stope (m)
H_d	height of the drift and the barricade (m)
H_s	height of the shotcrete (m)
k_h	saturated hydraulic conductivity (m/s)
k	permeability coefficient [m^2(Pa/s)]
K_0	at-rest earth pressure coefficient
K_a	active earth pressure coefficient
K_f	fluid bulk modulus (GPa or MPa)
K_p	passive pressure coefficient
l	horizontal distances measured along the free surface (m)

L	spacing of the plan projection of the upstream and downstream water surfaces (m)
L_{BB}	top length of the barricade (m)
L_{BT}	bottom length of the barricade (m)
L_c	spacing by considering an extra distance $0.3h_1/\tan\alpha_1$(m)
L_d	width of the drift and the barricade (m)
L_{SL}	top length of the shotcrete sprayed on the waste rock barricade (m)
L_{ST}	length of the shotcrete projected on the roof of the drift (m)
mp	plastic moment per unit length (kNm/m)
M_{cv}	vertical bending moment capacity per unit length (N·m)
M_{ch}	horizontal bending moment capacity per unit length (N·m)
N	normal forces along the sliding place in backfilled stope (kN)
p_f	fluid density (kg/m^3)
P	hydraulic pressure of backfill at the early age (kPa)
P_0	additional load from the location above backfill (kN)
P_{ar}	strength of an arched barricade (kPa)
P_b	designed pressure acting on a wall (kPa)
q	flow rate per linear meter (m^3/s)
Q	total seepage rate through a dike (m^3/s)
R	radius of an arched barricade (m)
s	inclined distances measured along the free surface (m)

t	barricade thickness (m)
T	shear forces along the sliding place in backfilled stope (kN)
v	Poisson's ratio of waste rocks
v_r	Poisson's ratio of rock mass
v_s	Poisson's ratio of shotcrete
w	water content
w_d	weight of the wedge (kN)
w_p	ultimate uniformly distributed pressure (kPa)
α_1	upstream slope angle of the waste rock barricade (°)
α_2	downstream slope angle of the waste rock barricade (°)
α_3	downstream slope angle of the shotcrete
γ_b	unit weight of backfill (kN/m^3)
γ_{wr}	unit weight of waste rocks (kN/m^3)
γ_r	unit weight of rock mass (kN/m^3)
γ_s	unit weight of shotcrete (kN/m^3)
ϕ'	internal friction angle of waste rocks (°)
ϕ_s'	internal friction angle of shotcrete (°)
δ	interface friction angle between waste rocks and rock walls (°)
δ_s	interface friction angle between shotcrete and rock walls (°)
σ_c	allowable compressive strength of a barricade (kPa)
σ_h	horizontal pressure acting on a barricade (kPa)

σ'_h	effective horizontal pressure acting on a barricade (kPa)
σ_{th}	total horizontal pressure acting on a barricade (kPa)
σ_t	allowable tensile strength of a barricade (kPa)
σ_u	ultimate compressive strength of a barricade (kPa)

Abbreviations

CPB	cemented paste backfill
CRF	cemented rock fill
FDM	finite difference method
FEM	finite element method
FLAC3D	Fast Lagrangian Analysis of Continua 3 Dimensions
FS	factor of safety
HF	hydraulic fill
MM	modified Mitchell
PWP	pore-water pressure
RPF	Rocky paste fill
UCS	unconfined compressive strength
VCL	vertical center line
WRB	waste rock barricade

LIST OF APPENDICES

CHAPTER 1 INTRODUCTION

1.1 Definition of the problem

The mining industry is a pillar of the economy in developed countries such as Canada and Australia. It is also of great importance in many developing countries like Brazil, Chile, and China. While producing a certain portion of valuable metals, hard rock mines also produce a large amount of mining wastes (tailings and waste rocks) and create many voids (underground stopes). The mining wastes deposited on the ground surface may cause environmental problems (e.g., acid mine drainage and neutral mine drainage) and geotechnical hazards.

Filling underground openings, known as stope backfilling, with backfill made of mining wastes helps reduce the amount of mine wastes disposed on the ground surface. The geotechnical and environmental risks associated with surface disposal of mine wastes can thus be reduced. In addition, stope backfilling helps improve ground stability, reduce ore dilution, increase ore recovery, and improve the efficiency of ventilation (Hassani and Archibald 1998; Potvin et al. 2005; Hambley 2011).

The successful application of backfills depends on the stability of a retaining structure, named barricades, constructed at the base of stope near the stope entrance in access drift to keep the slurried backfill in the stope (Grice 1998; Hassani and Archibald 1998; Potvin et al. 2005).

Over past decades, barricade failures have been reported. A barricade failure was usually accompanied by serious consequences such as flooding of drifts and working spaces, economic loss, personal injury, and even life loss (Soderberg and Busch 1985; Bloss and Chen 1998; Grice 1989, 1998, 2001; Helinski et al. 2006; Sivakugan et al. 2006; Revell and Sainsbury 2007*a*, 2007*b*; Yumlu and Guresci 2007; Hughes 2008). The design of barricades is thus a critical issue to ensure a safe and economic mining production.

In Canada, barricades made of waste rocks have been becoming a popular alternative to confine slurried backfill in stopes. The first solution to design waste rock barricades (WRB) was proposed by Li and coworkers (Li et al. 2009; Li and Aubertin 2011) based on the limit equilibrium analysis of a rectangular block model. An improved solution was later formulated by Yang et al. (2017a) by considering a more representative shape in the trapezoidal block. The proposed solution was developed by considering global and local internal stabilities. However, the proposed solution was calibrated and validated by 2D numerical modeling with FLAC-2D. Its validity in 3D conditions remains unknown. In addition, the proposed equation based on local stability analysis was developed by considering a horizontal sliding plane, while their 2D numerical results clearly showed that the sliding plane is inclined. A further update to the Yang et al. (2017a) solution is necessary

In practice, shotcrete is commonly sprayed on the upper part of the downstream slope of WRB. This is necessary when the access drift is not long enough to construct the desired WRB or when the top part of the barricade is problematic. However, there is no solution available to design the shotcrete (e.g., the strength of the material with a given geometry or the shotcrete thickness with a given material) applied on WRB.

1.2 Thesis objectives and methodology

The primary objective of this thesis is to provide solutions that can be used to design WRB with or without shotcrete for retaining slurried paste backfill by considering an iso-geostatic overburden pressure. The objective will be achieved through the realization of the following specific objectives (SOs):

SO 1: Test the validity and applicability of the numerical model of FLAC3D:

- Review of existing solutions developed to calculate the total seepage rate through a rockfill dike.

- Generalization of the 2D analytical solutions to 3D conditions for calculating the total seepage rate through a 3D rockfill dike.
- Calibration and validation of the proposed 3D solution by numerical simulations with FLAC3D.
- Laboratory total seepage tests through a rockfill dike.
- Validation of the calibrated proposed 3D solution and numerical model of FLAC3D by the laboratory test results.

SO 2: Develop a solution that can be used to design shotcreted WRB:

- Propose a 3D solution that can be used to design the shotcreted WRB by considering global and local stabilities.
- Calibrate and validate the proposed 3D solution against numerical results obtained with FLAC3D.

SO 3 Improve the Yang et al. (2017a) solution developed for the design of WRB:

- Review of the existing solutions developed for designing WRB.
- Numerical estimation of earth pressure coefficient based on its definition in Yang et al. (2017a) solution
- Development of a solution by considering the local internal stability with an inclined sliding plane.
- Development of an updated 3D solution that can be used to design WRB by considering global and local stabilities without a calibration coefficient.
- Validation of the proposed 3D solution against numerical results obtained with FLAC3D.

1.3 Contributions

The main contributions of this research project include the following three articles submitted to peer-reviewed journals:

Article 1:

Zhai YL, Li L & Chapuis RP. (2021). Analytical, numerical and experimental studies on steady-state seepage through 3D rockfill trapezoidal dikes. *Mine Water and the Environment*. Published on 28 August 2021, https://doi.org/10.1007/s10230-021-00798-8. This article is presented in Chapter 4.

Article 2:

Zhai YL, Yang PY & Li L. (2021). Analytical solutions for the design of shotcreted waste rock barricades to retain paste backfill. *Construction and Building Materials*. Published on 18 August 2021, https://doi.org/10.1016/j.conbuildmat.2021.124626. This article is presented in Chapter 5.

Article 3:

Zhai YL. (2021). An update of the 3D analytical solution for the design of barricades made of waste rocks. *International Journal of Rock Mechanics and Mining Sciences*. Submitted in October 2021. This article is presented in Chapter 6.

The realization of this project leads to the development of an improved solution that can be used to better estimate the seepage rate through a 3D rockfill dike. The validity and application of the FLAC3D numerical model were illustrated. An updated 3D solution was developed for the design of WRB. The analytical solutions developed for the design of WRB with shotcrete fill a gap identified for the design of shotcreted WRB.

1.4 Contents of the thesis

A general introduction of the thesis is presented in Chapter 1. Problem definition, thesis objectives and methodology, contributions, and thesis contents are presented.

Chapter 2 gives a literature review, which covers the following aspects:

- Underground mining methods with backfills.
- Three types of backfills are used to fill stopes in the underground mine.
- Pressures and stresses in backfilled stopes.
- Barricades design for backfilled stopes.

Chapter 3 presents the methodology of the research. The research method and the consistency of the three articles are presented.

Chapter 4 (Article 1) presents a 3D analytical solution for assessing the total seepage rate through the rockfill dikes resting on an impervious base under steady-state conditions. Existing 2D solutions developed for calculating the total seepage rate through 2D dikes under steady-state conditions are reviewed and generalized for 3D dikes. The validity of the generalized 3D solutions was tested by numerical modeling with FLAC3D. The results show that the generalized 3D Dupuit solution predicts well the variations of seepage as a function of the upstream hydraulic head, but fails to describe the variations of seepage as a function of the downstream hydraulic head. Further analysis on the explicit and implicit assumptions of the Dupuit model led to the proposition of two calibration factors: one for adjusting the flow path length, and another to calibrate the mean flow cross-section area. The two calibration coefficients were obtained by calibration against a few numerical results obtained with FLAC3D. The validity of the proposed and calibrated analytical solution was tested against additional numerical results. Both the numerical and analytical solutions were validated by laboratory test results. The water flow trends observed in laboratory tests are well captured by numerical modeling with FLAC3D.

Chapter 5 (Article 2) presents the development of a 3D solution for the design of shotcrete-reinforced WRB, including the required shotcrete thickness with a given material, the required shotcrete cohesion with a given dimension, and the required top length of the WRB with given shotcrete. Interface elements were used in the numerical models. The onset of failure (sliding) of shotcreted WRB modeled in FLAC3D has been evaluated using instability criterion based on the first occurrence of displacement jump or coalescence of currently yield zones.

Chapter 6 (Article 3) presents the development of an updated 3D solution to size the WRB by considering the global and local stabilities. The value of the earth pressure coefficient was estimated based on its definition given in the Yang et al. (2017a) model and numerical results obtained with FLAC3D. A new solution was developed by considering local stability with an inclined sliding plane. The structure instability of WRBs in FLAC3D is, for the first time, evaluated by considering the first occurrence among displacement jump or coalescence of currently yield zones passing through the WRB structure from the downstream to the upstream slope. The proposed analytical solution without any empirical coefficient was validated by numerical results obtained by FLAC3D and verified by an experimental result taken from the literature.

Chapter 7 gives a general discussion on the main results of the project. Some key points about the validation of numerical modeling are illustrated.

Chapter 8 presents the conclusions of this thesis and recommendations for further research.

Appendices are presented, mainly including filed testes in Young-Davidson Mine, sensitivity analyses of numerical modeling and instability criterion to evaluate the failure of the WRB in numerical simulations with FLAC3D.

CHAPTER 2 LITERATURE REVIEW

2.1 Mining methods with backfills

Ore can be extracted by surface mining methods or/and underground mining methods (Hamrin et al. 2001; SME 2011; Harraz 2016). Underground stopes are created during the mining operations. The main purpose of backfills is to control the stability of the stopes related to mining. In this section, these methods will be presented in relation to the application of backfill.

2.1.1 Naturally supported methods

In naturally supported methods, pillars are left in place to control the stability of extracted openings. Backfills can be used to recover the pillars left in place or adjacent stopes when the primary stopes are extracted. The application of backfill, in this case, belongs to the naturally supported methods.

2.1.1.1 Room-and-pillar mining method

Room and pillar methods are suitable for mechanization and are commonly used for sedimentary deposits such as shales, limestone, or sandstone containing copper, lead, and coal seams (Harraz 2016).

Pillars are kept in place in a planned mode staring at the farthest point from the stope access while the rooms are mined out (shown in Fig. 2.1). The roof is supported by natural pillars that are left standing in a systematic pattern. Pillars are planned to be mined out starting from a working area. The filling usually begins from the perimeter pillars towards the center of the filled area. The backfills can be used to alleviate wall convergence of these working panels and surface subsidence induced by the removal of the pillars (Lane et al. 2001; Tesarik et al. 2009; Harraz 2016). Barricades must be built between pillars around the perimeter to retain the specific fill such as hydraulic fill and cemented paste backfill.

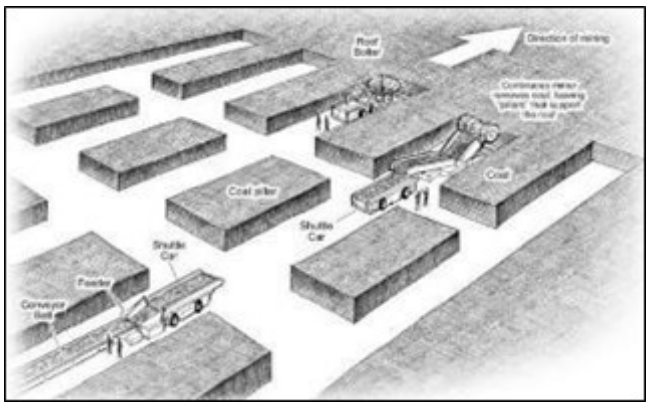

Figure 2.1 Schematic diagram of room-and-pillar mining method (taken from Harraz 2016, reprinted with permission of Dr. Hassan Z. Harraz)

2.1.1.2 Sublevel stoping

In sublevel stoping (shown in Fig. 2.2), stopes are commonly large. Holes are drilled underground in a perpendicular direction and a radial pattern around the drill access (Harraz 2016). The production for a mine using sublevel stoping is efficient and relatively safe because the mining is planned to retreat away from previously mined (Britton et al. 1992; Potvin et al. 2005).

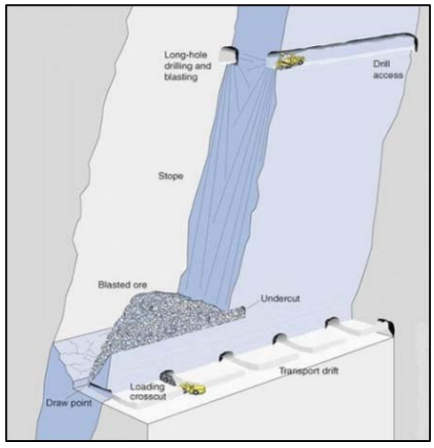

Figure 2.2 Illustration of sublevel and long-hole open stoping mining (taken from Harraz 2016, reprinted with permission of Dr. Hassan Z. Harraz)

Ore sections between stopes are reserved as pillars to support the hang walls. Based on the mining sequence, the stopes can be divided into primary and secondary stopes. The backfill with cement is needed for sublevel and long-hole open stoping when mining below (bottom exposure) or beside (side exposure) the cemented backfill. Barricades are necessary to retain the slurried backfill in the stopes.

2.1.2 Artificially supported methods

Under some circumstances, man-made structures are used to assist in meeting specific mining methods, such as cut-and-fill mining. The backfills can be used as man-made structures to increase the stability of the void.

2.1.2.1 Cut-and-fill mining

Cut-and-fill applies to high-grade ore bodies having steeply dipping orientation due to better selectivity (i.e., allowing selective mining for the ore) (Hamrin et al. 2001). Cut-and-fill mining extracts ore with a horizontal slice, advancing upward from the bottom (i.e., overhand) or starting from the base mining downward (i.e., underhand) (Harraz 2016).

Overhand cut-and-fill is used to the ore located underneath the working area (Harraz 2016). The backfill with or without cement can be used as a platform for the ore extraction advancing upward. The cemented fill in a top layer is often used to support heavy machinery. Underhand cut-and-fill is applied to the ore located beneath the working area (Harraz 2016). A high-strength sill mat at the stope based is needed for the underhand cut-and-fill. It is used to assist in recovering sill pillars or provide a safer workplace to continue the mining operations.

To retain the backfills related to cut-and-fill mining methods, barricades must be constructed in place to keep slurried backfill in the stopes.

2.1.2.2 Shrinkage stoping

Shrinkage stoping is a short-hole mining method (shown in Fig. 2.3), it is preferable for the steeply dipping orebodies ranging from 70° to 90° (Harraz 2016). Ore extraction is performed by using the gravity flow of orebodies dropping down to rail trucks through the chutes. The ore is removed from the bottom and advancing upwards with horizontal slices (Harraz 2016). During mining, a portion of the blasted ores (40 %) must be removed continuously to keep proper space between the back and the top of these ores and to provide a working platform for the next extraction (Hamrin et al. 2001). Depending on the rock conditions, the stope can be filled with backfills or kept void (Harraz 2016).

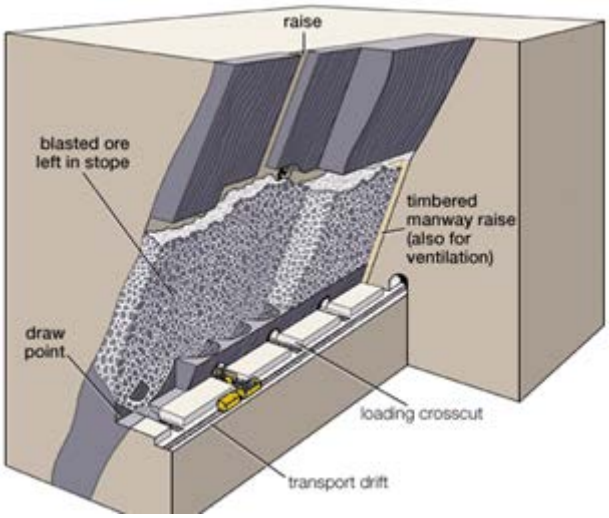

Figure 2.3 The layout of shrinkage stoping (taken from Hamrin et al. 2001, reprinted with permission of Society for Mining, Metallurgy and Exploration)

2.1.2.3 Vertical crater retreat

Vertical crater retreat is a mining method originally developed by INCO (a Canadian mining company) (Hamrin et al. 2001). Vertical long holes are drilled from drives developed in orebodies between two levels. Blasted ore creates the craters facing downward and the broken ore is

transported from the stope locating near draw-points at the lower level (shown in Fig. 2.4a) (Harraz 2016). Backfill can be used as a pillar (artificially supporting role) to recover the primary stope, while a fill barricade must be built at the base of the stope near the access drift to retain the slurried backfill (shown in Fig. 2.4b). Vertical crater retreat combined with the cemented backfill leads to high recovery of the ore reserves. To use this method, the barricade should be built in the access drift to retain the backfilled stopes.

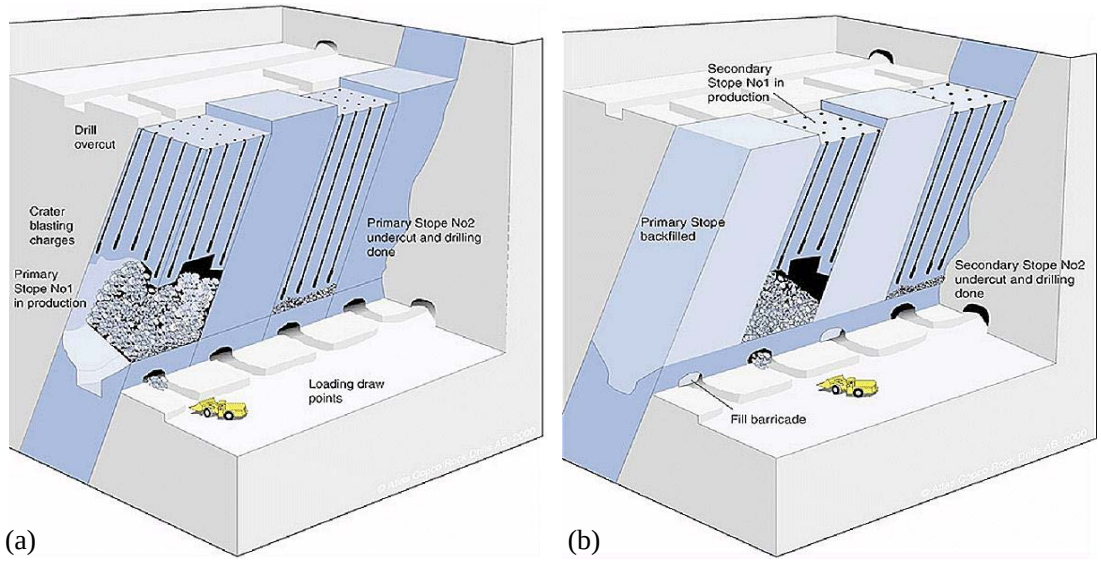

Figure 2.4 Layout of vertical crater retreat: (a) primary stopes, (b) secondary stopes recovery (taken from Harraz 2016, reprinted with permission of Dr. Hassan Z. Harraz)

2.2 Mining backfills

In underground mines, several types of backfill can be used to fill stopes. Here, one only presents the most used backfills, such as hydraulic fill, cemented paste backfill, and rockfill.

2.2.1 Hydraulic fill

In Potvin et al. (2005), backfill can be called hydraulic backfill when it contains at least 15% of

particles larger than 20 m. Hydraulic fill is transported with high-density slurry through pipelines to the underground voids after the tailings are dewatered. Hydraulic fill (HF) is defined as a low solid content (60% to 75%) slurry (Hassani and Archibald 1998; Potvin et al. 2005; Emad et al. 2015).

Rankine (2005) studied the hydraulic fills from 25 Australian mines. The specific gravity of the studied hydraulic fill ranges from 2.8 to 4.5. The porosity and void ratio of the settled backfill vary from 0.37 to 0.48 and from 0.58 to 0.93, respectively.

The particle size of hydraulic fill typically ranges from 1 to 1000 μm. Dewatering cyclone is commonly used to remove most of the finest particles in tailings to keep fines content below a certain level (at most 10% fines smaller than 10 microns) to obtain required permeability. HF is suggested to be prepared with solid content (by weight) no less than 70% (Grice 1998). The low solid content, in turn, contributes to the substantial amount of water that needs to be drained out from backfilled stopes through a permeable or non-permeable barricade with drainage pipes.

Grice (2001) reported that the hydraulic conductivity of uncemented HF in field conditions commonly varies from 10^{-6} m/s to 10^{-5} m/s. Rankine (2005) documented that the hydraulic conductivity of HF in Australian mines ranges from 2.78×10^{-6} to 8.33×10^{-6} m/s. Potvin et al. (2005) reported that the typical hydraulic conductivity of uncemented HF ranges from 10^{-7} to 10^{-5} m/s.

The friction angle ranges from 30° to 48° for cemented HF (CHF) from 35° to 37° for uncemented HF (Askew et al. 1978; Bloss 1992). The cohesion of the cemented CHF is determined by the binder type, binder content, and curing time. The cohesion of a CHF can range from 1.3 to 2.2 MPa when the cement content increases from 3 to 17% for 224 days' curing time (Askew et al. 1978).

2.2.2 Paste backfill

Since the use of paste backfill at the beginning of the 1970s, a backfill is called paste backfill when it is made of full tailings. Paste backfill contains at least 10% of particles smaller than 10 m and

does not bleed after its deposition (Potvin et al. 2005). Tailings are thickened to a certain solids concentration and transferred to disk filters in which the tailings are properly dewatered. The dewatered tailings are transported by the conveyor belt into a pug mixer where the cement is added. A certain amount of water is added to obtain the designed solid concentrations of the paste. The final paste fill enters a hopper before sending it to the underground.

The void ratio has a range from 1.1 to 1.4, unit weight from 18.4 to 20.1 kN/m^3, and saturation degree from 79% to 100% for the cemented paste backfill for 90 curing days (Le Roux et al. 2005). They also reported that in situ physical properties (e.g., saturation degree and void ratio) are higher or lower (about 10% or 20%) than the values obtained in laboratory tests. For the CPB samples with additives (slags) for curing days from 7 to 28 days, Yilmaz et al. (2015) conducted the laboratory tests and showed that water contents range from 13 to 24 %, saturation degree from 92.5 to 99.5%, and void ratio from 0.5 to 0.8 (estimated from the Fig. 8 in Yilmaz et al. 2015). The measured saturated hydraulic conductivity for cemented paste fill ranges from 2×10^{-8} to 5×10^{-9} m/s under different curing time and temperatures (Fall et al. 2009).

A direct way to obtain the mechanical properties is conducting UCS or triaxial tests. Fig. 2.5 shows the laboratory tests conducted by Ghirian and Fall (2014) for the CPB samples to obtain the shear strength (e.g., internal friction angle and cohesion). The cohesion can reach up to about 620 kPa and the internal friction is 55° for the sample (top of the column) with a curing time of 90 days. The nonlinear effects shown in the figure may be due to the stresses tested in the short or long term. At an early age, the samples are under undrained conditions and the total stress is tested. In the long term (150 days), the samples may be under fully dry conditions when excess pore water pressure dissipates and effective stress is obtained. In practice, the paste backfill would tend to dissipate through the waste rock barricades with high hydraulic conductivity.

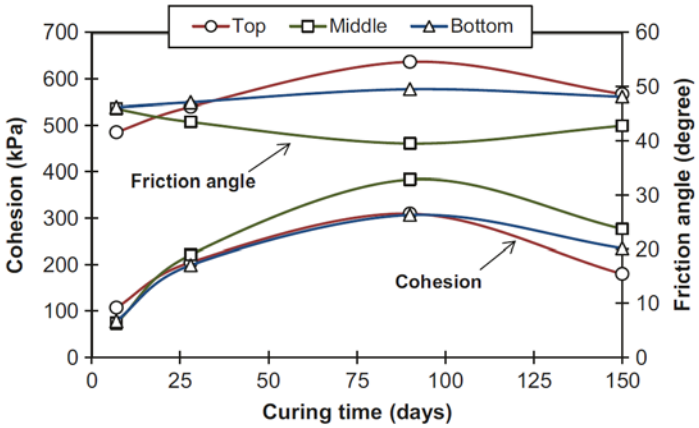

Figure 2.5 Shear strength as a function of curing days for the CPB samples (Ghirian and Fall 2014, reprinted with permission of ELSEVIER BV)

The cohesion is closely related to the binder type and content as well as curing days. For example, Rankine and Sivakugan (2007) conducted the experimental tests for CPB with 6% cement content for 1 to 9 months curing time under undrained and unconsolidated conditions and found that the cohesion varies from 158 to 384 kPa. Veenstra (2013) documented that the shear strength of CPB (3% binder content) had a cohesion of 40 kPa and an internal friction 41° at 28 days, and cohesion of 77 kPa and an internal friction 35° at 56 days.

The transportation of backfill (e.g., a high-density slurry) was performed by using pumping or gravity, or both from surface to underground with boreholes and/or pipelines. Typically, the density of the paste is adjusted to a certain range (i.e., 75 ~ 85% solid contents by weight) while ensuring it can be transported to the underground with controllable risk of blockages or pipeline breakages (Potvin et al. 2005).

The solid particles in paste backfill are non-settling and can be stopped and started without risk of causing system blockages for short periods (Potvin et al 2005). Based on the suggestion mentioned by Paterson and Cooke (1993), it is necessary to design the proper slurry parameters, such as solid contents by weight and fines content (e.g., particle size smaller than 20 μm) rather than solely

controlling the fluid properties of water and pipeline parameters.

2.2.3 Rock fill

Rock fill is typically made of development waste rocks produced during the development either by surface mining or underground operation. It can be uncemented or cemented

The internal friction angle typically ranges between 34 and 45° (Barton 2008; Azam 2009; McLemore et al. 2009; Aubertin 2013) depending on the material density and grain size distribution. The repose angle of rock fill varies between 35° and 55°, depending on its arrangement form and physical factors (Potvin et al. 2005). The angle of repose of rock fill can be increased by grading rock aggregate (enhance particle interlocking), and the density and strength are maximized during the progress (Potvin et al. 2005; Emad et al. 2015).

The optimum particle size distribution of rock fill used for rockfill in underground stopes is needed to be determined. For example, excessive fines within CRF can consume most of the binder; few fines and poorly graded aggregate in CRF will result in a higher void ratio (Bloss and Chen 1998). In longitudinal retreat methods, CRF as a delayed backfill is commonly used as a working floor (Emad et al. 2015).

The interface friction angle is two-third of the internal friction angle (CGS 2006; Pirapakaran 2008; Li et al. 2014), which is also suggested in geotechnical engineering textbooks (e.g., Bowles 1996; Das 2011). At larger scales, the determination of interface friction angle remains challenging because the interfaces between the barricade and rock walls can vary from regular and smooth to very irregular and rough. Yu and Counter (1983) performed laboratory and in situ tests for the cemented rock fill and reported the values of elastic modulus ranging from 2.0 to 3.8 GPa. By mixing finer materials and adding cement, the in situ UCS of cemented rock fill ranges from 1.3 MPa to 11 MPa (Annor 1999).

2.3 Pressures and stresses in backfilled stopes

The estimation of pressures exerted by backfilled stopes is of great importance for the design of the barricade. The pressures acting on barricades should be estimated to design the barricades. The estimation of the pressure acting on the barricades needs the knowledge of the stresses in the access drift and backfilled stopes.

2.3.1 Stresses in backfilled stopes

The stresses state of backfills placed in the stopes (a stiff confining structure) under fully dry or submerged conditions should be evaluated properly to design the barricade. To do so, numerical simulations can provide a preliminary study of the stresses state of backfilled stopes.

Many numerical simulations have been presented to assess the stress state within backfilled stopes (e.g., Askew et al. 1978; Aubertin et al. 2003; Li et al. 2003, 2009d;). Askew et al. (1978) performed numerical simulations with the finite element method to study the stress distribution of the cemented and uncemented backfilled stopes. Their results showed that the stresses transferred to rock walls are more prominent in the cemented fill (e.g., internal friction angle is 36° and cohesion is 70 kPa) when compared with the uncemented backfill (e.g., internal friction angle is = 30° and cohesion is = 0 kPa).

Aubertin et al. (2003) made the numerical simulations with finite element commercial code PHASE2 (RocScience 2002) to assess the stress state in narrow backfilled stopes under wall convergence. The rock mass, obeying the Hoek-Brown elastoplastic model (Hoek et al. 1995), is related to its convergence (ground reaction curves). The interface, obeying the Mohr-Coulomb failure criterion, is used between the backfill and the rock walls to allow the relative displacement between the two materials. With the effect of wall convergence, the vertical and horizontal stresses obtained by numerical simulation are much greater than the overburden stress expect for the stope base (about 40 ~ 45 m for vertical stress, 35 ~ 45 m for horizontal stress). It should be noted that

the horizontal stress is much bigger (almost 0.5 MPa) than the overburden due to wall convergence.

Li et al. (2003) performed numerical simulations with FLAC (Itasca 2002) to access the stress state in narrow backfilled stopes without considering wall convergence. The displacements caused by excavation are set to be zero before the placement of backfills. Fig. 2.6 presents the results of stresses calculated with analytical solutions and obtained with numerical simulations along the central line at different elevations. The results obtained with analytical solution and numerical simulation are close to the overburden when backfill depth is small (about 10 m). The results calculated by Marson theory commonly underestimate the stresses compared to the numerical simulation results due to the arching effect when the backfill depth increases.

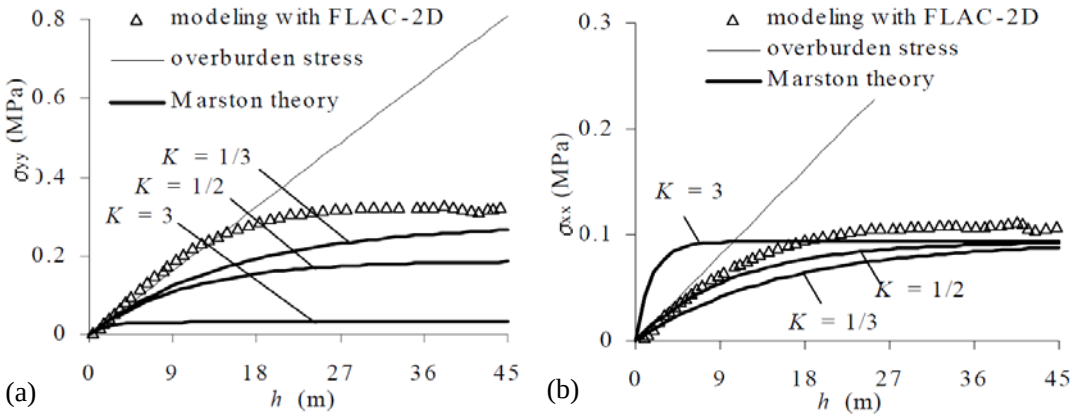

Figure 2.6 Comparison of stresses calculated with analytical solutions and obtained with numerical simulations along the central line at different elevations: (a) vertical stress; (b) horizontal stress (taken from Li et al. 2003, reprinted with permission of Taylor and Francis).

Li and Aubertin (2009c) performed numerical simulations (FLAC) to study the effect of different factors (e.g., inclination angle, Young's modulus, internal friction angle) on the stress distribution in inclined backfilled stopes. Based on the numerical analysis results, the inclination angle is relatively insensitive to the horizontal stress, while the vertical stress decreases significantly along the hanging wall and inclined central line when the inclination angle increased. Along the footwall,

the horizontal stress sees an increasing trend with an increase of inclination angle.

Jahanbakhshzadeh et al. (2017) proposed a 3D analytical solution calibrated by 3D numerical simulation results with FLAC3D to evaluate the vertical and horizontal stresses in the inclined. The results showed that the stresses tend to diminish with an increase of stope length. Fig. 2.7 presents the numerical simulation results for the vertical stress distributions at different elevations of the stope.

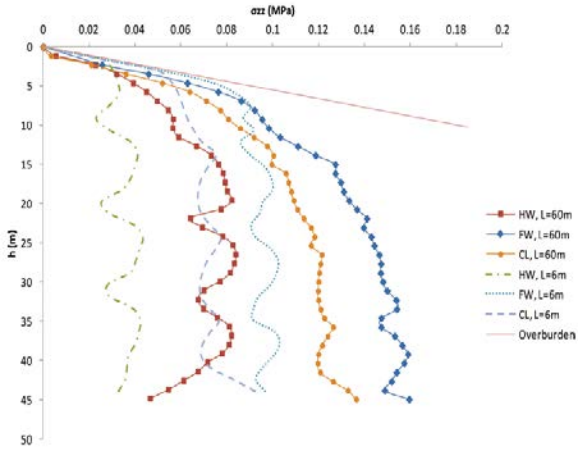

Figure 2.7 Comparison of vertical stress distributions for different stope length along the centerline (CL), footwall (FW), and hanging wall (HW) (Jahanbakhshzadeh et al. 2017, reprinted with permission of Canadian Science Publishing)

Fahey et al. (2009) conducted numerical simulations with PLAXIS (2008) to access the stress distributions within backfilled stope with a nonzero value of dilation angle (e.g., ψ = 10° or -5°). Interface elements with the same frictional properties of backfill were used along the backfill-rock boundary. As shown in Fig. 2.8, the angle of dilation significantly affects the stresses along the centerline of the backfilled stope. An increased dilatation angle from -5° to 10° (e.g., -5°, 0°, and10°) results in decreased vertical stress especially when backfill height reaches a certain depth (e.g., backfill height below top > 10 m), indicating an enhanced arching (e.g., Falaknaz et al. 2015).

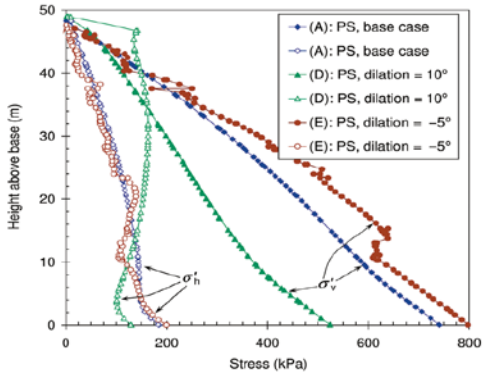

Figure 2.8 Stresses distribution along the centerline of backfilled stope for different dilation angles (taken from Fahey et al. 2009, reprinted with permission of National Research Council of Canada; Canadian Science Publishing)

Shahsavari and Grabinsky (2014) considered a boundary condition (newly deposited slurry) rather than a zero pore water pressure head at the top for cemented paste backfill to investigate the total pore pressure in the backfilled stopes. The results obtained by FLAC3D indicated that the slurry boundary on top tends to bring about excess pore pressure in the mid-height of the backfilled stopes. Fig. 2.9 shows the comparison of total pore pressure under two different boundary conditions.

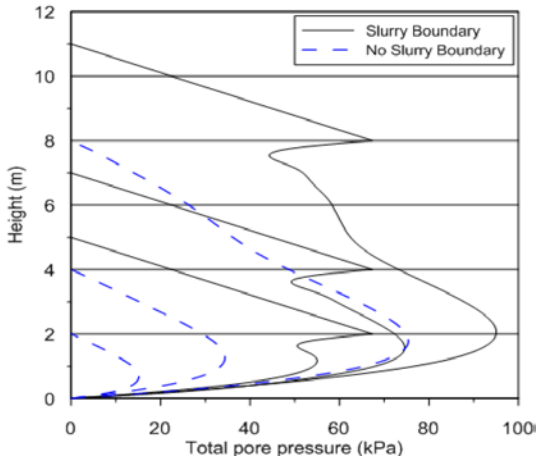

Figure 2.9 Comparison of total pore pressure with the elevation of height under slurry and no slurry boundary (taken from Shahsavari and Grabinsky 2014, reprinted with permission of Dr. Mohammad Shahsavari)

El Mkadmi et al. (2014) illustrated numerical simulation analyses with SIGMA/W for stope filling with three typical cases, such as (*i*) drained (dry) backfill that corresponds to rockfill or HF with sufficient drainage conditions, (*ii*) a rapid filling with drainage and consolidation, and (*iii*) sequential backfill with different filling rate, (*ii*) and (*iii*) correlate with paste fill. It was shown that drainage promotes the development of the horizontal effective stress between the backfill and rock wall, which in turn significantly reduces both stresses (horizontal and vertical) compared with the overburden pressure.

Yang et al. (2017a) studied the effect of the relationship between the internal friction angle ϕ' and Poisson's ratio v of the backfill on the stress distribution along the backfilled stopes. Their results revealed that near the centerline of the backfilled stopes, $K = K_{ps}$ ($K = \sigma'_h / \sigma'_v$, $K_{ps} = \sigma'_3 / \sigma'_1$) and this value is near to K_a (Rankine's earth pressure coefficient) when ϕ' or v is below the critical value based on Coulomb criterion. Near the rock walls, the K_{ps} is close to K_a, showing a yield state due to the arching effect.

Yang et al. (2017b) modeled a cemented paste backfill stope with a side exposure using FLAC3D, and an instability criterion based on objective standard (e.g., sudden increment of displacement, as shown in Fig. 2.10) is proposed to judge the required cohesion of backfill with a vertical exposure.

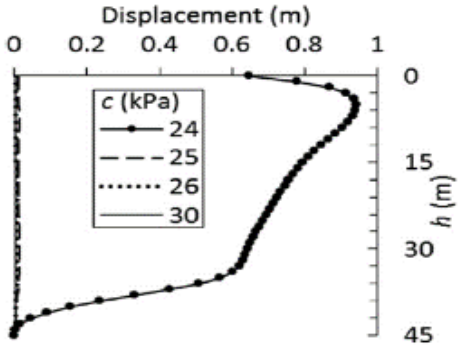

Figure 2.10 Instability standard for judging the required cohesion of backfill (taken from Yang et al. 2017b, reprinted with permission of American Society of Civil Engineers)

Zheng et al. (2020) proposed a solution for estimating the total and effective stresses in backfilled stopes by considering the drainage and consolidation of the slurried cohesionless backfill on an impervious base. The proposed solution provides a simple estimate of the total and effective stresses in backfilled stopes.

Zheng and Li (2020) conducted a series of experimental tests to study the vertical total stresses of paste backfill with different solid contents after finishing backfilling. Their results indicate that vertical total stresses show a decreasing trend with an increase of solid content by weight of backfill. The stresses of backfilled stopes are closely related to the solid content by weight of backfill.

2.3.2 Analytical, numerical and experimental results of pressures on barricades

2.3.2.1 Analytical solution for estimating the pressures on barricades

Mitchell et al. (1975) proposed a simple equation to evaluate the load on a barricade:

$$F_h = \frac{1}{2}\gamma_b H^2 L_d K_0 \tag{2.1}$$

where F_h (kN) is the horizontal load acting on the barricade, γ_b (kN/m^3) is the unit weight of the backfill, H (m) is the total fill height in the stope, and L_d (m) is the drift width. K_0 is the at-rest earth pressure coefficient. The load is independent of the height of the barricade is a limitation of the solution.

The Mitchell et al. solution overestimates the horizontal stress exerted on the barricade. Smith and Mitchell (1983) recorded an empirical solution by considering a distance l (m) from the stope brow to the barricade surface near to stope.

$$\sigma_h = 0.4\gamma_b H(1-0.6\frac{l}{L_d}) \tag{2.2}$$

where σ_h (kPa) is the horizontal pressure acting on a barricade.

The Mitchell et al. solution and Smith and Mitchell solution assume that the horizontal stress has a positive relationship with backfill height H, the impact of the barricade height is ignored.

Mitchell et al. (1982) and Mitchell (1983) proposed a more common approach to evaluate the horizontal stress acting on a barricade based on the limit equilibrium of a 3D wedge of backfill, as shown in Fig. 2.11. In this figure, L_s (m) is the stope length; H_d (m) is the height of drift; W_d (m) is the width of drift; w (kN) is the wedge weight; P_0 (kN) is the additional load from the above backfill; N (kN) and T (kN) are the normal and shear forces along the sliding plane; c_b (kPa) is the interface cohesion between the fill and lateral walls; c (kPa) is the cohesion of backfill; φ (°) is the internal friction angle of the backfill. F_h (kN) is the force provided by a smooth barricade to maintain the equilibrium of the wedge; α (= 45° +φ/2) is the inclination angle of the sliding plane.

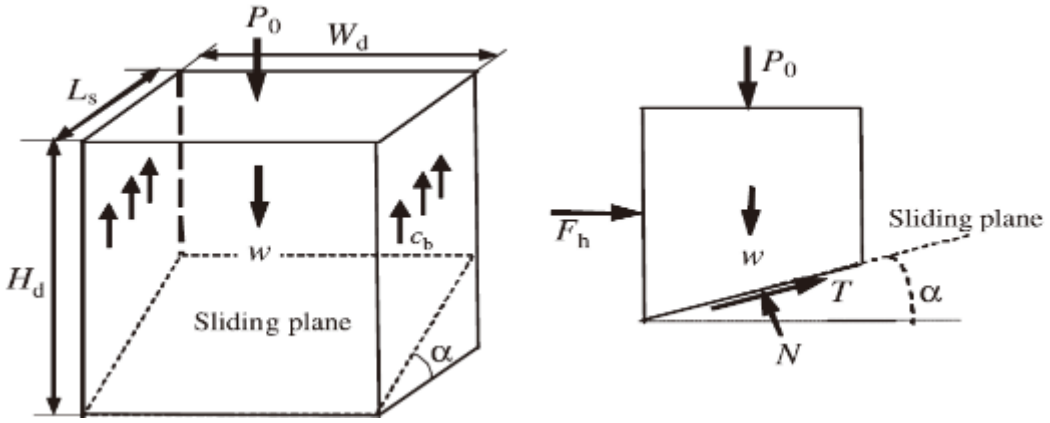

Figure 2.11 Wedge model of Mitchell et al. (1982) (taken from Li and Aubertin 2009a, reprinted with permission of Copyright Canadian Science Publishing)

The horizontal load exerted on the barricade is given by:

$$F_h = \frac{[P_0 + L_s(H_d - L_s \tan\alpha / 2)(\gamma_b W_d - 2c_b)](\sin\alpha - \cos\alpha \tan\phi) - cW_d L_s / \cos\alpha}{\sin\alpha \tan\phi + \cos\alpha} \quad (2.3)$$

The analytical solutions mentioned above fail to consider the frictional stress transfer between the backfill and walls of the stope and drift. Li and Aubertin (2009a) proposed a 3D analytical solution under fully drained conditions by considering the frictional stress transfer based on the limit equilibrium. The horizontal stress σ_h (kPa) in the drift axis direction at elevation h (m) is given by:

$$\sigma_h = \left[\frac{h}{H_d}\sigma_{hT0} + \left(1-\frac{h}{H_d}\right)\sigma_{hB0}\right]\left[\exp[-l\frac{2\tan\delta}{K_{dl}}\left(\frac{1}{H_d}+\frac{K_{dt}}{W_d}\right)\right], \text{ for } H \geq H_d \tag{2.4}$$

$$\sigma_h = \sigma_{hB0}\left(1-\frac{h}{H_d}\right)\exp\left[-l\frac{2\tan\delta}{K_{dl}}\left(\frac{1}{H}+\frac{K_{dt}}{W_d}\right)\right], \text{ for } H < H_d \tag{2.5}$$

where h (m) is the elevation in the drift; δ (°) is the interface friction angle between backfill and walls; σ_{hT0} (kPa) and σ_{hB0} (kPa) are the horizontal normal stresses at the top and base of the drift at the draw-points, which are calculated using the solution by Li et al. (2005). The earth pressure coefficient K_{dl} or K_{dt} is the ratio of the horizontal stress in the longitudinal or transverse direction to the vertical stress, respectively.

In Fig. 2.12, the layer element of thickness dl is subjected to horizontal compressive forces F (kN) and F + dF (kN), shear forces S_1 (kN) to S_5 (kN), and compressive forces C_1 (kN), C_2 (kN) acting on both sides, and C_3 (kN).

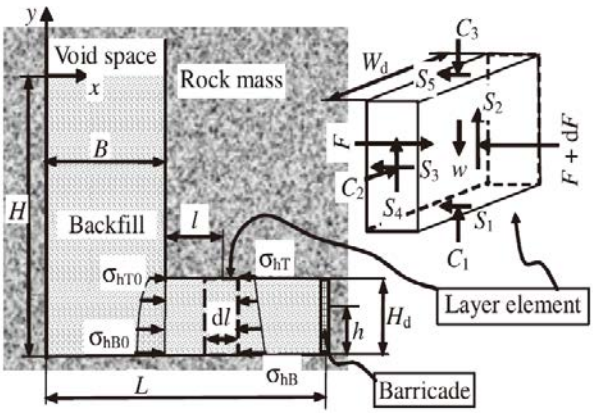

Figure 2.12 Model of a vertical backfilled stope with a barricade under a fully drained condition (Li and Aubertin 2009a, reprinted with permission of Canadian Science Publishing)

This analytical solution assumes that the horizontal stress is uniformly distributed from the top to the base of the drift. Li and Aubertin (2009a) validated their solution by using numerical modeling and physical model test, which showed a good agreement between them. The pressures on the barricade decreased significantly when the barricade is placed farther away from the stope. The solution proposed by Li and Aubertin (2009a) is used to estimate the horizontal pressure under fully drained conditions. The backfills under fully drained (dry) conditions (without pore water pressure) may be accumulated near the draw-points in access drift. There is no need to build a barricade to retain the dry materials when the retaining structure is far from the draw-points. Normally, a muck berm (i.e., a rock pile about 2.5 m high when drift height is about 5 m, Brown et al. 2019) is needed to be built near the draw-points to prevent the rolling of fallen rocks from the stops.

Li and Aubertin (2009b) further complemented Li and Aubertin (2009a) solution to formulate the pressure generated by the submerged fill on the barricade. Fig. 2.13 shows a model of a vertical backfilled stope with a barricade. The effective horizontal stress σ'_h (kPa) in the drift axis direction at elevation h (m) is given by:

$$\sigma'_h = \left[\frac{h}{H_d}\sigma'_{hT0} + \left(1-\frac{h}{H_d}\right)\sigma'_{hB0}\right]\left[\exp[-l\frac{2\tan\delta_{sat}}{K_{dl}}\left(\frac{1}{H_d}+\frac{K_{dt}}{W_d}\right)\right], \text{ for } H \geq H_d \tag{2.6}$$

$$\sigma'_h = \sigma'_{hB0}\left(1-\frac{h}{H_d}\right)\exp\left[-l\frac{2\tan\delta_{sat}}{K_{dl}}\left(\frac{1}{H_d}+\frac{K_{dt}}{W_d}\right)\right], \text{ for } H < H_d \tag{2.7}$$

where δ_{sat} (°) is the interface friction angle between saturated backfill and walls; σ'_{hT0} (kPa) and σ'_{hB0} (kPa) are the effective horizontal stresses at the top and base of the barricade drift at the draw-points, respectively

The total horizontal stress σ_{th} (kPa) can be expressed by:

$$\sigma_{th} = \sigma'_h + \gamma_w\left(H_w - h\right) \tag{2.8}$$

where γ_w (kN/m^3) is the unit weight of water; H_w (m) is the height of water in the stope.

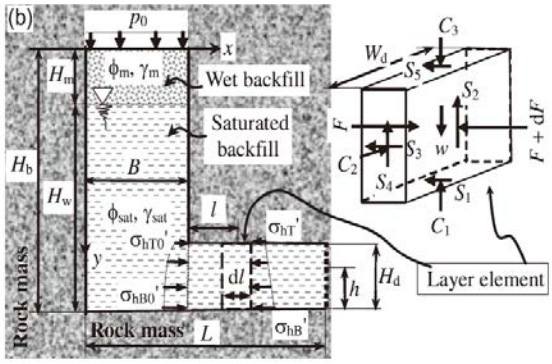

Figure 2.13 Schematic representation of a vertical backfilled stope with a barricade in the submerged conditions (Li and Aubertin 2009b, reprinted with permission of Canadian Science Publishing)

By validating the proposed solution with numerical simulations and laboratory tests, Li and Aubertin (2009b) concluded that the total stress is mainly dependent on PWP, the effective stress in barricade drift is less than those under drained conditions. The solution proposed by Li and Aubertin (2009b) is commonly used to calculate the pressure exerted by the backfilled stope on a barricade.

Zheng et al. (2018) proposed a solution based on Gibson approach for estimating the PWP of slurried paste backfill for the pervious base. They found that filling rate and backfill height can significantly affect the pressures in backfilled stopes for barricade design.

Zheng et al. (2019) proposed a solution to calculate the total and effective stresses in backfilled stopes on a pervious base for barricade design. When the filling rate is low and hydraulic conductivity of backfills is high, the arching effect is suggested to be considered because of dissipation of PWP.

2.3.2.2 Numerical results of pressures on barricades

Beer (1986) compared the results of numerical simulation with a full-scale pressure test of a barricade built with concrete bricks at Mount Isa. The back analysis is conducted to determine unknown material properties. It was found that the pins enhance the shear resistance of the barricade rather than altering the bending deformation, and the pressure on the center of the barricade is reduced because of the arching effect (Beet 1986)

Li and Aubertin (2009a) proposed a 3D analytical solution to estimate the load (horizontal pressure) exerted on the barricade based on limit equilibrium under the fully drained condition. The stress transferred from the backfilled stope to the access drift was considered. The transfer between vertical stress and horizontal stress along the backfilled stope was considered as active reaction coefficient (K_a) and an earth pressure coefficient (K_{dl} = 2) was used along the access drift. It was assumed that the stope and drift are first excavated and all convergence due to elastic strain in the rock mass is completed before filling. Fig. 2.14 shows numerical modeling of backfilled stope with a closer view near the drift.

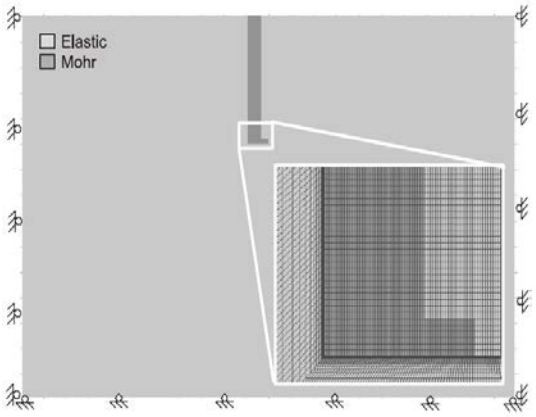

Figure 2.14 Numerical model of a backfilled stope with an access drift (taken from Li and Aubertin 2009a, reprinted with permission of Canadian Science Publishing)

Fig. 2.15 shows the comparison between the proposed solution and numerical simulation results

with different K_{dl}. In general, the analytical solution (K_{dl} = 2) agrees with numerical simulation results. The pressure exerted by the backfill can be significantly influenced by the position of the barricade.

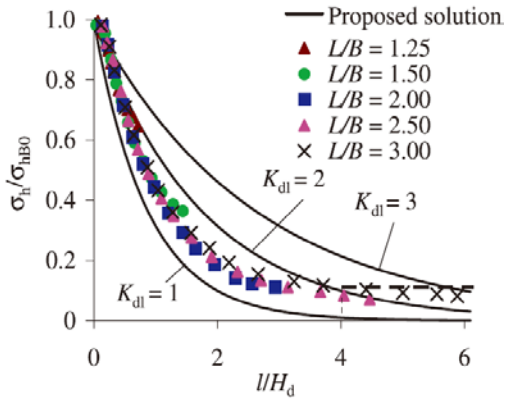

Figure 2.15 Comparison between the proposed solution and numerical results (taken from Li and Aubertin 2009a, reprinted with permission of Canadian Science Publishing)

Li and Aubertin (2009b) proposed a 3D analytical solution to estimate the load generated by submerged backfill on barricades at the early age. The effect of PWP is considered at the early age of the backfilled stopes. Fig. 2.16 shows a good agreement between the proposed solutions and numerical simulation results for total and effective horizontal stresses.

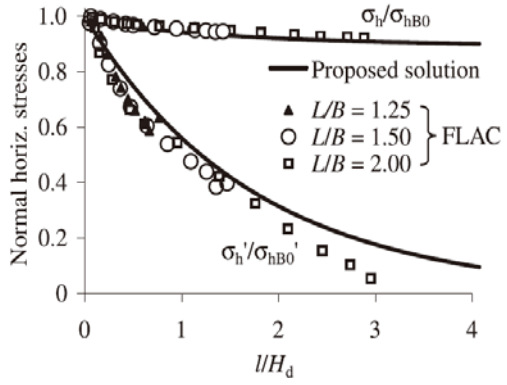

Figure 2.16 Comparison between the analytical solution and numerical simulations (Li and Aubertin 2009b, reprinted with permission of Canadian Science Publishing)

Doherty (2015) conducted numerical simulations, using a coupled multi-physics finite element model to illustrate the importance of elevation of the water table. The drainage pore fluid boundary conditions are used instead of fixing zero PWPs as the boundary condition, which means that the water only flows from the inside of the backfill to the outside of the barricade when pressure is positive. The simulation results show the significant dependence of PWP on soil-water retention properties. Fig. 2.17 shows the boundary conditions for the 2D backfilled stope model.

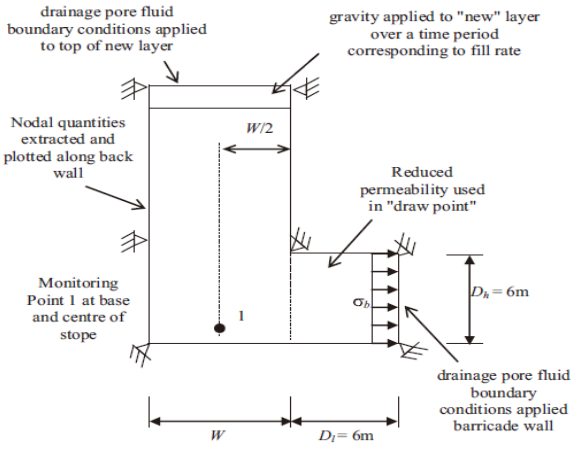

Figure 2.17 Boundary conditions for 2D backfilled stope model (taken from Doherty 2015, reprinted with permission of PERGAMON)

The accurate evaluation of the earth pressure coefficient within backfills is closely related to barricade design. Yang et al. (2017c) performed numerical simulations with FLAC and proposed that a critical value about Poisson's ratio and internal friction angle to estimate the earth pressure coefficient, based on the combination of generalized Hooke's law and Mohr-Coulomb failure criterion. Yang et al. (2017c) pointed out that the earth pressure coefficient K along the vertical central line within the backfill stope is close to Rankine's active earth pressure coefficient K_a when Poisson's ratio v or the internal friction angle ϕ' is below or equal to a critical value. In other cases, K is close to the at-rest earth pressure coefficient $(K_0)_v$ [$= v / (1-v)$].

Jaouhar et al. (2019) studied the stress distributions near the access drift with numerical simulation

SIGMA/W (2012), aiming to research the effect of stope dimension, barricade location, filling rate and drainage holes on the pressures exerted on the barricade. A number of drainage holes (i.e., n_d) can help significantly reduce the pore water pressure rather than the total stresses. The numerical results show that the addition of drainage holes can increase the long-term stability of a barricade with the drainage system, but it has little effect on the short-term stability (Jaouhar et al. 2019).

2.3.2.3 Stability analysis of barricades

Beer (1986) documented that a barricade constructed from concrete brick with pins was built in the access drift to retain hydraulic fill at Mount Isa. The results obtained with numerical modeling were used to compare with the behavior observed in the field. The stability analysis obtained with numerical simulations shows the bending failure of a barricade. The arching effect is observed in the backfills when the backfilled stope height increased to 3 m high above the barricade, which significantly affects the horizontal pressure applied on the barricade.

Bloss and Chen (1998) performed in-situ and laboratory tests to study the effect of drainage on the barricade for hydraulic fill at Mount Isa mines. The erosion connecting with the ponding water above the backfill leads to a hydrostatic pressure exerted on a barricade, increasing the potential for barricade failures. The barricade stability is suggested to be ensured by monitoring the pressures exerted by the backfilled stope and/or draining the ponding water.

Revell and Sainsbury (2007b) studied two main barricade geometries by using FLAC3D, which includes 5 × 5 m flat square and 5 × 5 m flat horseshoe. The arched barricade with a radius of curvature of 6.5 m was also studied for the horseshoe geometry, as shown in Fig. 2.18 taken from “Advancing Paste Fill Bulkhead Design Using Numerical Modeling” by Revell, M. B. and Sainsbury, D.P., MINEFILL2007, reprinted with permission of the Canadian Institute of Mining, Metallurgy and Petroleum.

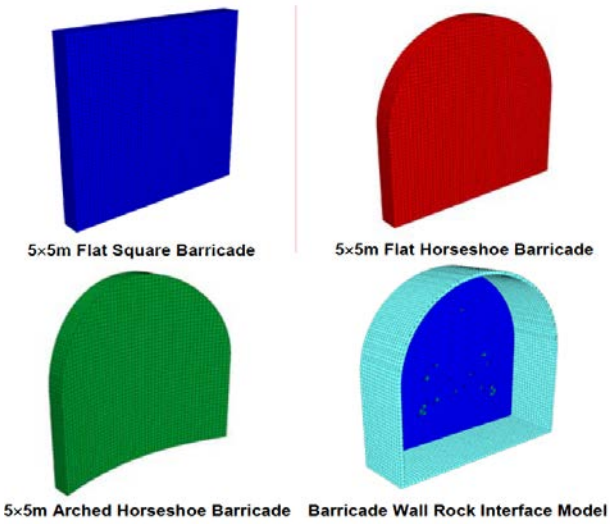

Figure 2.18 Barricade shapes investigated throughout the study (taken from Revell and Sainsbury 2007b, reprinted with permission of the Canadian Institute of Mining, Metallurgy and Petroleum)

Revell and Sainsbury (2007b) used the Mohr-Coulomb elastoplastic model with strain-softening to study the stability of a barricade because shotcrete as a brittle material tends to collapse much sooner after yielding occurs. It is assumed that cohesion and tensile strength would decrease from the maximum value to zero at a critical plastic strain value. The critical plastic strain can be obtained from the laboratory tests for a specific project such as the case shown in Fig. 2.19 taken from “Advancing Paste Fill Bulkhead Design Using Numerical Modeling ” by Revell, M. B. and Sainsbury, D.P., MINEFILL2007, reprinted with permission of the Canadian Institute of Mining, Metallurgy and Petroleum.

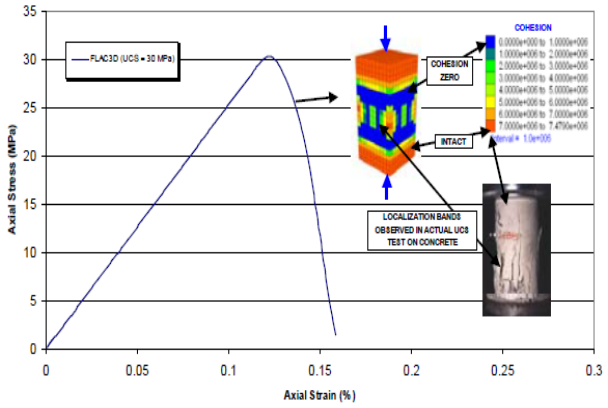

Figure 2.19 Stress-strain curve obtained from UCS test and simulated with FLAC3D (taken from Revell and Sainsbury 2007b, reprinted with permission of the Canadian Institute of Mining, Metallurgy and Petroleum)

Revell and Sainsbury (2007b) concluded that the ultimate failure pressure of the arched barricades can be increased compared to the flat barricades. The numerical modeling is not suggested to be used alone to design the barricade. All the necessary tests and back-analyses should be conducted to obtain the material properties for a specific condition.

Yang et al. (2017) applied the FLAC to validate the analytical solution in 2D conditions. Fig. 2.20 shows a schematic view of a typical backfilled stope with a trapezoidal waste rock barricade.

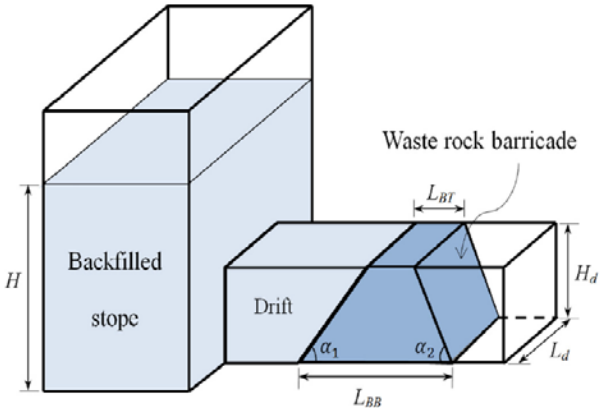

Figure 2.20 Schematic view of a typical backfilled stope with a trapezoidal barricade (Yang et al. 2017, reprinted with permission of American Society of Civil Engineers)

Failure states (e.g., tension and shear failure) are usually used to judge the stability of the structure in numerical simulations. When the interface between floor rock and barricade is relatively smooth and the interface friction angle is relatively small, the barricade acting as a stiff block may slip without showing obvious shear failure zones. Yang et al. (2017) proposed an instability criterion (i.e., abrupt displacement jump as a function of WRB top length) to judge the stability of the barricade, as shown in Fig. 2.21. The X displacement at the top center of the barricade top keeps stable when top length L_{BT} decreases from 3 to 1.6 m. The X displacement shows an abrupt increase when L_{BT} changes from 1.6 m to 1.5 m, indicating an unstable state of the barricade structure. The abrupt jump of displacement is used to subjectively estimate the stability of a structure.

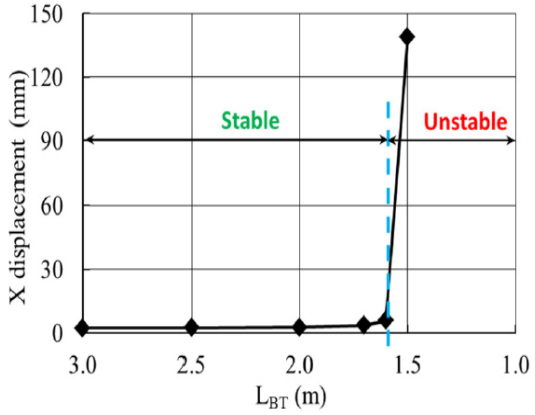

Figure 2.21 Displacement in the *x*-direction (i.e., X displacement) at the top center of the barricade (Yang et al. 2017, reprinted with permission of American Society of Civil Engineers)

2.3.2.4 Experimental results of pressures on barricades

In situ measurements and laboratory tests can be used as the benchmark to validate the numerical modeling or analytical solutions for the physical and mechanical parameters. Some precious full-scale experimental results (e.g., Garrett and Campbell 1958; Checkan 1985; Grice 1989) provide useful information to assist in deciding the ultimate capacity of the barricade.

Garrett and Campbell (1958) described an in-situ test on a bulkhead in the parallel access drift to determine its capacity. The test was conducted by gradually increasing pressures in about three months. Initially, heavy leakage along with the rock-concrete interface, particularly at hanging, was noticed. By using cementation at the contact between the rock and concrete, the leakage was reduced. An old diamond drill hole began to leak when pressure increased up to 20.68 MPa. Leakage was measured at about 582.4 L/h at 29.65 MPa and the leakage stopped when pressure was decreased to 13.79 MPa. Finally, the pressure (46.88 MPa) could not be raised further when leakages occurred in the footwall and Hanging of the main drive. Based on the field tests, it is too conservative to design the plug based on the shear strength under improper stress conditions

because no structural failure occurred at high pressure (e.g., 46.88 MPa). The leakage is usually dominant in the design of the plug that needs a greater length to resist high pressure (Garrett and Campbell 1958).

Checkan (1985) recorded an experiment for concrete barricades. By gradually increasing the hydrostatic pressure, the test procedure simulates the actual stress condition exerted on the barricade (e.g., build-up hydrostatic pressure reaches up to a maximum level). The results showed that the signs of failure occur when the pressure reached 275.8 kPa, the maximum pressure the barricade can withstand is 344.7 kPa. It should be noted that the design of the actual pressure should be kept below the maximum pressure due to the time factor.

Thompson et al. (2012) conducted in-situ measurements for the pressures acting on the barricade at Cayeli mine. Fig. 2.22 shows the pressures (e.g., total earth pressure and pore water pressure) measured on a barricade at different elevations. TEPCs (total earth pressure cells) 1 and 2 increased constantly to a peak value (about 42 kPa for TEP1 and 30 kPa for TEP 2) at 0.6 days. TEP 3 gives a different trend from the first two, showing a more significant increase in total earth pressure. Its peak value gives about 45 kPa at 2.75 days. The pore water pressures of the three sensors give the same trend, the peak value with 19 kPa can be observed from the figure.

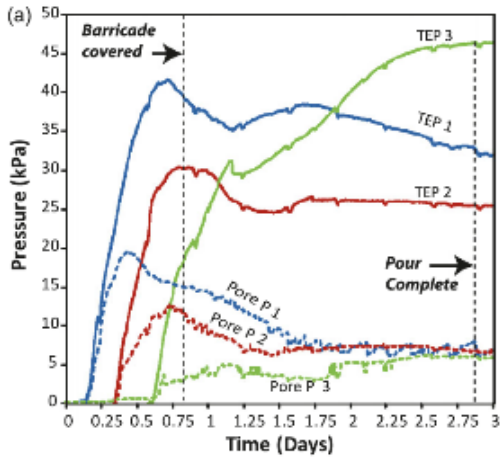

Figure 2.22 Total earth pressure (TEP) at different locations (e.g., TEP 1 at 1.4 m height, TEP 2 at 2.8 m, and TEP 3 at 4.2 m above the bottom) and pore water pressure (PWP) measured on the barricade (Thompson et al. 2012, reprinted with permission of Canadian Science Publishing)

Li et al. (2014) performed a project to research the continuous filling by using pressure sensors (total earth pressure and pore water pressure) to monitor the loading on the barricade. The peak value of pressures is observed shortly after the placement of the cemented paste backfill for different walls (No. 3 and No. 8). The temperature decreases when the pressure acting on the barricade is monitored and then increases over time because of cement hydration.

Doherty et al. (2015) investigated the pressure exerted by cemented paste backfill on a barricade. Fig. 2.23 shows the horizontal stress (σ_h) and pore water pressure (u) as a function of fill time on a barricade. The peak value of the pressures reached 120 kPa at the start of the resting period. This peak value of horizontal stress and pore water pressure are monitored almost simultaneously, indicating the critical period for the barricade design occurred at the early age of the backfilling.

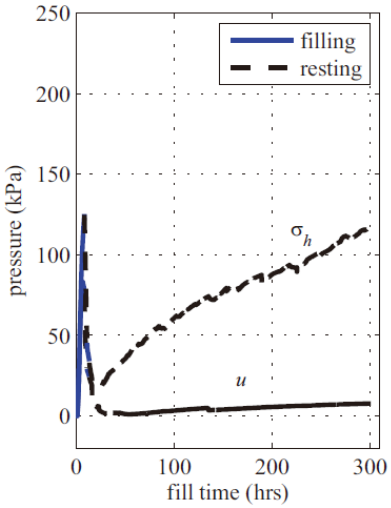

Figure 2.23 Horizontal stress (σ_h) and pore water pressure (u) as a function of fill time on the barricade (Doherty et al. 2015, reprinted with permission of Canadian Science Publishing)

Widisinghe (2014) conducted laboratory tests to study the lateral loading on the barricade for dry hydraulic fill with square drive and circular drive, respectively. The results show that the barricade stress increases with the circular and square drift width and presents a linear decrease with an increase of offset distance. It is suggested that the maximum vertical stress within the backfilled stope or the vertical stress at the center of the backfilled stope are considered to calculate the pressure on the barricade.

2.3.2.5 Experimental results of the capacity of barricades

A field test for a concrete barricade was carried out to determine its capacity exerted by excessive hydrostatic pressure (Garrett and Campbell 1958). Garrett and Campbell (1958) tested the capacity of the concrete barricade by gradually increasing the hydrostatic pressure while sealing the leaks with grouting. A maximum pressure value of 46.88 MPa was obtained based on an experimental plug with a thickness of 2.4 m when the pressure could not be raised further.

Checkan (1985) recorded a laboratory test for the concrete barricades with a thickness of about

0.41 m. It showed the signs of failure occurred when the pressure reached 275.8 kPa, the maximum pressure the barricade can withstand was 344.7 kPa. It should be noted that the design of the actual pressure should be kept below the maximum pressure.

Grice (1989) tested three barricades to obtain the capacity subjected to the pressures from the backfilled stopes. The first test was stopped at 460 kPa when the maximum water delivery rate equals leakage rate. For the second test, a pressure with 220 kPa was obtained before observing cracks. The third test reached 750 kPa and destroyed the barricade by greatly increasing the water delivery rate. A back analysis from videotape for the third test showed that the initial failure occurred as shearing around the perimeter, and the tensile cracks through the bricks and mortar were then observed.

The stope and the drift were constructed by Nujaim et al. (2018, 2020a, 2020b) with plexiglass. The backfill was made of clay having a unit weight of γ_b = 13.5 kN/m^3 (Nujaim et al. 2018, 2020a, 2020b). The WRB are characterized as L_{BT} = 0.072 m, L_{BB} = 0.25 m, H_d = 0.09 m, L_d = 0.09 m, and $\alpha_1 = \alpha_2 = 45°$. The slope angles of the WRB are calculated as $\alpha_1 = \alpha_2 = 45°$ based on the geometry of the WRB even though their trapezoidal mold appears to show an angle of 48° to 52° (Nujaim et al. 2018, 2020a, 2020b).

It should be mentioned that the failure tests (three cases) performed by Nujaim et al. (2020b) showed the pressure reached 120 kPa using the sensors placed in front of the barricade. This value shows an obvious difference with a pressure (4.63 kPa) recorded by Nujaim et al. (2018). To reply to this difference, one considers the details of the construction of the WRB recorded by Nujaim et al. (2018). The external manual piston was used to apply vertical pressure to increase the pressure on the WRB. A rapidly applied loading condition (manual piston) results in a sudden increase in pore water pressure. Several shims (pieces of plastic) at the base of the access gallery were used to increase the barricade-wall friction and to avoid sliding. While the reinforced structure (i.e. WRB with shims) plays a role in increasing the internal friction angle of the WRB. In addition, a trapezoidal mold was used to shape a WRB, which also reinforces the whole structure. The

pressures leading to a collapse of the WRB with shims (12.3 kPa) or without shims (4.63 kPa) indicate the difference (Nujaim et al. 2018). The WRB tests were conducted by using different grain sizes. The grain size can affect the porosity, density, and compressive strength of the WRB (Nujaim et al. 2018, 2020a, 2020b). For one group test, the barricade sliding pressures vary from 13 to 50 kPa with different grain sizes (see Fig. 6 in Nujaim et al. 2020a).

2.4 Barricades

Barricade is a term used to classify porous retaining structures under low loading conditions. Bulkhead would include the non-draining structures exerted by high pressures (Grice 1998). In this project, the two terms (i.e., barricade and bulkhead) are used interchangeably. Before the placement of the backfill in a stope, one of the major issues is to construct barricades.

2.4.1 Types of barricades

A variety of barricades have been developed to retain different types of backfill (e.g., hydraulic fill, rockfill, cemented paste backfill). In general, the commonly used materials of barricades can be divided into bricks, timber, concrete, shotcrete, fibrecrete, and waste rock. Normally, a barricade with drainage fittings is necessary to discharge the excess transport water in backfilled stopes (Checkan 1985; Potvin et al. 2005).

Table 2.1 gives a list of the barricades with different materials, dimensions, and drainage system to keep backfills (Potvin et al. 2005). The barricade made of different materials with various dimensions is given in the table, indicating the barricades design for different cases.

Table 2.1 The geometric parameters used in the barricades (Potvin et al. 2005)

Barricade materials	Dimension (height × width × thickness)	Drainage system
Concrete masonry wall	4 m × 4 m × 1 m	Yes
Porous concrete wall	4 m × 4 m × 0.46 m	No
Arched porous concrete wall	5.5 m × 6.5 m × 0.5 m	No
Reinforced fibrecrete wall	5.5 m × 6.5 m × 0.5 m	Yes

2.4.1.1 Permeable bricks barricade

The flat or arched wall constructed from permeable bricks with the convex side towards to stopes is constructed near the access drift to retain the backfills. Fig. 2.24 shows a barricade built with porous concrete bricks, allowing the excess transport water inside the backfilled stopes to drainage freely through the permeable bricks. Sivakugan et al. (2006) carried out a laboratory test and showed that the permeability of the bricks was approximately two to three orders of magnitude greater than those of the hydraulic fill.

Figure 2.24 Side view of the construction of a curved barricade (Sivakugan et al. 2006, reprinted with permission of Kluwer Academic Publishers)

The dimension of the bricks and their mass, as well as porosity, are shown in Table 2.2. Two types of brick dimensions are given in the table. In the current practice, bricks of type B are commonly used to build barricades. In the past, larger brick (type A) was used in the field (Duffield et al.

2003).

Table 2.2 The values of dimensions, mass, and porosity of the porous bricks (Sivakugan et al. 2006)

Brick type	Dimensions (mm)			Mass (g)	Porosity (%)
	Length	Width	height		
A	452	213	114	20444	22
B	394	189	91	13946	20

Kuganathan (2001) measured the uniaxial compressive strength (UCS) and showed that the UCS of porous bricks used in Mount Isa Mine ranges from 5 to 10 MPa. The bricks are normally soaked with water in the field condition. These results are useful to understand the UCS under pseudo dry conditions (specimens contain a little water), but not appropriate for evaluating the UCS of permeable bricks soaked with water. Duffield et al. (2003) conducted UCS tests for dry and saturated bricks. The compressive strengths of dry concrete blocks range from 9.5 to 26.3 MPa and the UCS values of saturated blocks range from 9.5 to 14.7 MPa. Berndt et al. (2007) conducted experimental tests by soaking the bricks under water for either 7 days or 90 days. The results show that the average strength and average modulus of bricks are 7 MPa and 1.7 GPa, respectively. Compared to the fully dry tested bricks, the strength of wetting tested bricks shows a decreased strength (e.g., about 25 %). Moreover, the average permeability of the porous bricks is larger than that of hydraulic fill (several orders of magnitude) (Sivakugan et al. 2006). The barricade built with permeable bricks can effectively prevent the build-up of hydraulic pressure on barricades.

The barricade capacity built with such porous bricks (UCS varies from 5 MPa to 26.3 MPa) can range from 71.6 kPa to 377 kPa (Kuganathan 2001; Duffield et al. 2003). These test results are useful to estimate the capacity of a barricade built from porous bricks, but the large difference (e.g., 305.4 = (377 – 71.6) kPa) of a barricade capacity remains uncertain for the design.

To build the barricades with permeable bricks is time-consuming because the construction requires better precision and experienced operators (Sivakugan et al. 2006).

2.4.1.2 Concrete barricade

A field test for a concrete barricade was carried out to determine its capacity exerted by excessive hydrostatic pressure (Garrett and Campbell 1958). Garrett and Campbell (1958) tested the capacity of the concrete barricade by gradually increasing the hydrostatic pressure while sealing the leaks with grouting. A maximum pressure value of 46.88 MPa was obtained based on an experimental plug with a thickness of 2.4 m when the pressure could not be raised further.

Checkan (1985) recorded a laboratory test for the concrete barricades with a thickness of about 0.41 m. It showed the signs of failure occurred when the pressure reached 275.8 kPa, the maximum pressure the barricade can withstand was 344.7 kPa. It should be noted that the design of the actual pressure should be kept below the maximum pressure.

Since the unwanted inflows of water from water-bearing strata or poorly sealed shafts, water levels in stopes can rise rapidly and pose a threat to adjacent active mines. A concrete barricade with high capacity is designed to build and prevent possible excessive pressure (Checkan 1985).

These experimental results provide useful information to assist in designing a barricade to prevent excessive pressures. The construction of a jumbo barricade is relatively expensive and time-consuming. The massive concrete barricade also delays the operation schedule between mining and backfilling due to the complicated construction procedure.

2.4.1.3 Aerated Cement barricade

The aerated cement material is used to build a barricade to retain 8 m height of fresh backfill (total pressure 137 kPa) and 35 m of hardened fill (total pressure 397 kPa) after comparing with other construction materials (Ras et al. 2007). The strength of the material can be varied by adjusting water content and foam density. To strengthen shear strength, solid steel rebar rods are adopted instead of steel cable. At first, the concrete frame around the surrounding rock walls needs to be cast to keep steel members fitted, and steel members should be tailored so that each position and

pinning hole is drilled in precise positions. The steel beams and struts supporting a grid and geotextile are anchored to the rock walls. In addition, steel beams and struts supporting a grid and geo-fabric need to be anchored to the rock walls (Ras et al. 2007).

At TARGET gold mine, a barricade of 4 m × 5 m × 2 m (height × width × thickness) was built in the access drift. The steel frame was filled with aerated cement material at a relative density of about 0.74. This requires the ratio of water to cement of 0.63 and the corresponding design strength is 2 MPa after a minimum of 48 hours. The density of the cement foam was maintained by limiting filling height to 2 m/d. The aerated cement material was injected into the wall-barricade interfaces under pressure to ensure complete contact (Ras et al. 2007).

Ras et al. (2007) generalized that the additional grid of reinforcing rods must be installed halfway between the two outer grids once the width or height of the drift is beyond 5 m or there is no guarantee for the surrounding rock wall quality.

To construct the aerated cement barricade commonly needs more time to prepare the materials and recipe to obtain the designed capacity.

2.4.1.4 Arched concrete barricade

The concrete block bonded with mortar is weak in shear and tension which can be reinforced by the arched design. Normally, a pad is poured at the construction site of a barricade. Hitches, recession, and prolonged sections are sometimes made along with the rock-barricade interface. The holes within the block are horizontally oriented towards stope to promote drainage (Smith and Mitchell 1982).

Hassani and Afrouz (2001) pointed that the arch design has a higher shear resistance than the flat design. In addition, a double row of bricks walls is suggested when the drift width exceeds 4.3 m. Concrete blocks pasted with mortar are constructed near draw-points to form the arch and wrapped with filters to screen out fines that may block up the holes. The double row of blocks is commonly

needed for a normal drift width (more than 4 m). In addition, these concrete blocks should be mortared in place with the holes horizontally oriented to the stopes to offer a drain path (Smith and Mitchell 1982; Hassani and Afrouz 2001).

Compared with a flat geometry, the capacity of the arched structure of the barricade has quite higher compressive strength based on the numerical simulation results (Revell and Sainsbury 2007b). The wall thickness on the top and bottom should be much thicker than the middle part because more shear resistance is needed for the arched wall. Recessing the ends of the barricade into lateral rock wall a certain distance is an alternative way to increase shear resistance. The arched structure transmits a lateral thrust to the surrounding rock. It should also be noted that surrounding rock stiffness and intactness can significantly influence the capacity of the barricade, particularly for the arched one.

Sinopoli (1998) suggested that arched barricades exerted by compressive stress should satisfy the following specifications: indentation at least should be more than 0.15 times of drift width; indentation at the mid-span should be 0.75 times of indentation at the quarter. The strength correction factors should be used if indentation is smaller than 0.15 times the drift width. The typical drift width is 5 m, so indentation should be a minimum of 0.75 m. Cheung (2012) concluded that arched barricades are significantly stronger than flat ones based on parametric analysis and numerical simulations. The variation range of CPB barricade strength can reach as much as 30% due to the stiffness of the surrounding rock wall.

To meet the requirements of the arched concrete barricade, more costs and time are needed because the recipe needs to be determined by tests.

2.4.1.5 Timber barricade

Timber barricades are relatively easy and rapid to construct. The wood material is easily available in most North American mining areas (Jessome 1977; Hassani and Afrouz, 2001). The types of wood used to build barricades consist of hardwood (maple, oak, or aspen) and softwood (fire, pine,

or spruce).

Timber has a higher ratio of deflection to load than concrete or waste rocks. However, timber has poor deterioration resistance under moisture circumstances, and it is combustible under high-temperature areas. Preservative treatment can expand the service life of timber barricades. The wood can be processed by decreasing the water content within timer (e.g., about 19%), and soaking in a mixture of creosote or chromate copper arsenate. With these mixtures, the wood can be preserved for approximately 20 to 50 years depending on field circumstances (Hassani and Afrouz, 2001).

Smith and Mitchell (1982) proposed a wooden barricade design wrapped with burlap and synthetic filter fabric and backed with bearing timbers which are fixed into the surrounding rock along the drift. A span between all timbers is needed for drainage. Quick-setting cement is commonly used to seal the perimeter of the barricade for better rock-timber interface contact and waterproof.

The metal sections should be designed based on drift dimension, the barricade width decided the number of braces, for example, the span between two braces is 1.5 m, 3 braces are enough for the barricade width of 5 m. In addition, the rock quality for placing the bearing plate of braces should be stiff enough. Barricades constructed by timber are inexpensive but not easy to quantify its performance, it highly depends on both timber quality and anchoring strength (Soderberg and Busch 1985). Smith and Mitchell (1982) mentioned that the factor of safety of 5 is required during a backfill pour in Canada. The operating pressures on a barricade must be calculated previously based on the allowable stresses in the timbers.

A central bracing design for the timber barricade retains seepage water pressures during pouring operations is commonly used, and the central support system is removable and can be used elsewhere after fining the task (Smith and Mitchell 1982). Taking apart and reusing timber can result in damage to the wooden structure, temporary metal braces thus can be designed for easy removal and reinstallation when central support is necessary. Smith and Mitchell (1982) pointed

that metal sections could be light enough for handing and would span up to 1.5 m of barricade width, for example, two braces for L_d = 3 m and three braces for L_d = 4.5 m. The horizontal beam could be a channel section (0.08 m × 0.2 m) and the braces can be pipe sections.

2.4.1.6 South African plug

During the late 1950s and early 1960s, plug research was conducted by South Africa to solve inundation problems. A laboratory test was carried out for the concrete plug under hydrostatic pressure over 41 MPa (Garrett and Campbell 1958). Three possible design methods for the plug are used, such as plate design (the plug with all sides recessed into the rock wall), a tapered plug design, and a grouting design between the irregular rock surface and plug. The parallel plug design is chosen by considering construction time.

Water leakage deteriorates the plug materials and eventually jeopardizes the integral structure of a plug. Water leaks along with the plug-rock interface through the cracks, or through the plug itself. During the curing period of a plug, cracking and shrinkage owing to the high heat of hydration are the important factors to weaken the strength of a plug, and shrinkage can influence the stability of anchorage. The choice of the admixture should be cautious because the properties of pozzolans and Portland cement varies.

2.4.1.7 Waste rock barricade

Waste rock barricades (WRB) refer to the barricades made of waste rocks, which are built at the base near the access drift (Li and Ouellet 2009; Yang et al. 2017). The construction materials (waste rocks) are easily available at the least cost from blasted ores. WRB can be easily removed and reused as rockfill or construction materials for other WRB when the placed cemented backfill behaves strong enough. The use of waste rocks produced during underground development avoids the transportation and hoisting of these materials from underground to surface, resulting in considerable energy and economic benefits.

Fig. 2.25 shows the trapezoidal barricade with shotcrete sprayed over the upper face on the downstream slope in the field. The upstream slope angle of the barricade is naturally developed due to the self-weight of waste rock (typically close to 37° ± 3°), the downstream slope angle can be manually created by a pushing machine (Aubertin 2013). In practice, shotcrete is usually applied on the downstream slope face at the top part of the barricade (about one-third of the barricade height). Li and Aubertin (2011) proposed an analytical solution based on the limit equilibrium for determining the required size of rectangular barricades made of waste rock. Yang et al. (2017) further proposed an improved analytical solution for designing a trapezoidal WRB by considering the global stability of the barricade block and the local internal stability of the top part of the barricades. However, there is no solution for sizing the shotcreted WRB based on the literature reviews.

Figure 2.25 Waste rock barricade sprayed with shotcrete (Personal collection of Prof. Li Li)

Fig. 2.26 shows a schematic diagram for a shotcreted WRB at access drift. In the figure, H (m) is the backfill height. H_d (m) and L_d (m) are the drift height and width, respectively; these correspond to the barricade height and width. L_{BT} (m) is the top length of WRB, and L_{BB} (m) is the bottom length. L_{SL} (m) is the top thickness of the shotcrete. H_s (m) is the height of shotcrete. α_1 (°) is the upstream slope angle of WRB. α_2 (°) is the downstream slope angle of WRB. α_3 (°) is the

downstream slope angle of shotcrete. The thickness of the shotcrete projected on the roof of the drift is noted as L_{ST} (m). In this project, an analytical solution will be developed for sizing the required minimum top length with a given shotcrete material and the required strength with a given dimension of shotcrete applied on waste rock barricades.

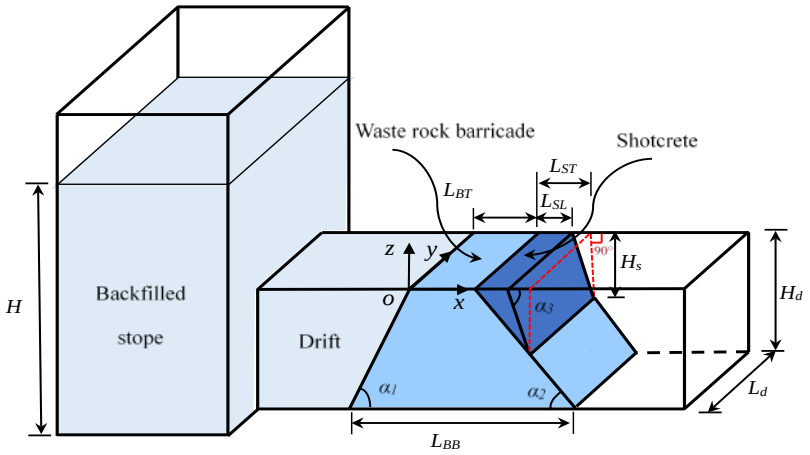

Figure 2.26 A backfilled stope with an access drift and a trapezoidal WRB sprayed with shotcrete (adapted from Li and Aubertin 2011, reprinted with permission of Canadian Science Publishing)

2.4.2 Solutions for the design of barricades

Analytical solutions (closed-form expressions) are used to solve a specific problem by hand or with Microsoft Excel®. Analytical solutions are a very popular and useful tool for a practitioner as they allow making quick calculations and parameter sensitivity analysis. In the following, analytical solutions used to estimate the pressures exerted by backfills and to design the geometry of the barricades will be presented.

With a given pressure exerted by the backfilled stopes, some existing analytical solutions can be used to design the geometry of a barricade. The barricades are constructed with timbers, permeable bricks, concrete blocks, shotcrete, foamcrete, aerated cement, and so on. Some equations for

designing the barricades are based on the empirical formula from relevant institute standards and the flexural failure mechanism (ACI 318-95; Djahanguiri and Abel 1997; Duffield et al. 2003).

2.4.2.1 Yield line theory

Yield line theory is an analysis for the ultimate load and is performed based on the bending moment of the structural elements at their collapse state (Jones 1967; Johansen 1972). The ultimate load is based on boundary conditions and the principle of virtual work (Kennedy and Goodchild 2004, Revell and Sainsbury 2007b).

Beer (1986) used the equation based on yield line analysis when all edges are simply supported, which assumes the barricades fail when tension cracks developing along the diagonal lines and the interface between barricade and rock. The following analytical solution is given to calculate the maximum load on the barricade.

$$w_p = \frac{24 m_p}{L_d^{\,2}} \tag{2.9}$$

with

$$m_p = \frac{L_B^{\,2}}{8}\sigma_c \tag{2.10}$$

where w_p (kPa) is the ultimate uniformly distributed pressure; m_p (kN·m/m) is the plastic moment (ultimate moment capacity) per unit length.

Timoshenko and Yong (1972) suggested an equation about the ultimate moment capacity per unit length related to the tensile strength:

$$m_p = \frac{L_B^{\,2}}{4}\sigma_t \tag{2.11}$$

Djahanguiri and Abel (1997) recorded the solution to calculate the maximum load on the barricade,

it can be calculated as follows:

$$w_p = \frac{8m_p}{L_d^{\ 2}} \tag{2.12}$$

The equations used to calculate the ultimate uniformly distributed pressure w_p and the required barricade thickness L_B under different supported conditions are summarized in Table 2.3 (Revel and Sainsbury 2007b).

Table 2.3 The relations between the w_p and m_p for different slab boundary conditions (Revel and Sainsbury 2007b)

Case	Equations	
All edges simply supported	$w_p = \frac{24m_p}{L_d^{\ 2}}$	$L_B = L_d\sqrt{\frac{w_p}{3\sigma_c}}$
All edges are fully fixed	$w_p = \frac{48m_p}{L_d^{\ 2}}$	$L_B = L_d\sqrt{\frac{w_p}{6\sigma_c}}$
Top and bottom edges fully clamped; left and right sides simply supported	$w_p = \frac{35.44m_p}{L_d^{\ 2}}$	$L_B = L_d\sqrt{\frac{8w_p}{35.44\sigma_c}}$
Lower edge simply supported; others are fully fixed	$w_p = \frac{41.36m_p}{L_d^{\ 2}}$	$L_B = L_d\sqrt{\frac{8w_p}{41.36\sigma_c}}$
Lower edge fixed, other three simply supported	$w_p = \frac{29.9m_p}{L_d^{\ 2}}$	$L_B = L_d\sqrt{\frac{8w_p}{29.9\sigma_c}}$

Duffield et al. (2003) considered reinforced and unreinforced concrete slabs (square or rectangular barricades) as fully restrained at all sides with compressive membrane action. The following solutions were given to calculate the maximum load on the barricade and the corresponding required barricade thickness:

$$w_p = \frac{20.4\sigma_c \beta_r L_B^2 \left[\frac{L_d}{H_d}\left(0.188 - 0.141\beta_r\right) + \left(0.479 - 0.245\beta_r\right) \right]}{H_d\left(3L_d - H_d\right)} \tag{2.13}$$

$$L_B = \sqrt{\frac{H_d w_p \left(3L_d - H_d\right)}{20.4\sigma_c \beta_r \left[\frac{L_d}{H_d}\left(0.188 - 0.141\beta_r\right) + \left(0.479 - 0.245\beta_r\right) \right]}} \tag{2.14}$$

where β_r is the ratio of the depth of the equivalent rectangular stress block to the neutral axis depth, as defined in ACI 318-95 (β_r = 0.85 for $\sigma_c \leq$ 30 MPa).

2.4.2.2 Beam deflection and flexural strength

Smith and Mitchell (1982) used the solutions documented by Timoshenko and MacCullough (1949) to calculate the timber deflection. The pressure acting on the barricade can be calculated by measuring the displacement of the timber, it can be expressed as:

$$D_t = \frac{5L_{fs}^4 w_u}{384 E_d I_y} \tag{2.15}$$

with

$$w_u = 0.14P \tag{2.16}$$

$$I_y = \frac{b_t \times h_t^3}{12} \tag{2.17}$$

where D_t (m) is mid-height timber deflection. L_{fs} (m) is the distance of free span; I_y (m^3) represents the second moment of the area for the y-axis; E_d (kPa) is average deflection modulus; w_u (kN/m) is load acting on the timber barricade per unit length. b_t (m) is timber width; h_t (m) is timber length.

Checkan (1985) considered the barricade as fixed on at least three sides (lateral and floor) under hydrostatic pressure and assumed that the flexural stress dominates the failure. The solution for estimating the flexural stress can be given by:

$$\sigma_t = \frac{\beta_t P H_d^2}{L_B^2} \tag{2.18}$$

where β_t is a correction factor depending on the ratio of width to height.

The concrete barricade is more easily cracked in compression, whereas the steel one is easy to crack in tension (Spiegel and Limbrunner 2003).

When a certain cross-section within a flat barricade (concrete or steel) is exposed to its ultimate flexural strength, the corresponding stresses and strains can be examined (Spiegel and Limbrunner 2003). The flat barricade is assumed to be a simply supported rectangular beam (restrained from the lateral wall). The beam has a width b (m), an effective depth d (m), and a reinforced steel area A_S (m^2). More details are shown by Spiegel and Limbrunner (2003). The flexural strength can be expressed by:

$$\sigma_t = \frac{\beta_1 \sigma_c b d}{A_s} \tag{2.19}$$

where β_1 is a constant as a function of the concrete strength σ_c defined in ACI Code (Table 22.2.2.4.3). The value of β_1 is shown in Table 2.4.

Table 2.4 Values of σ_c for equivalent rectangular concrete stress distribution (ACI, Table 22.2.2.4.3)

σ_c (MPa)	β_1
$17.24 \le \sigma_c \le 27.58$	0.85
$27.58 < \sigma_c < 55.16$	$0.85 - \frac{0.05(\sigma_c - 4000)}{1000}$
$\sigma_c \ge 55.16$	0.65

2.4.2.3 Punching failure

Menetrey (2002) considered a transition between punching and flexural failure by stress-strain

curves of slabs with different punching cone inclinations. The equation to calculate the punching load can be given by:

$$F_{fail} = F_{pun} + \left(F_{flex} - F_{pun}\right)\left\{\sin\left[\left(\alpha_{pb} - \alpha_{pp}\right)\frac{\pi}{\pi - 2\alpha_{pp}}\right]\right\}^{1/2} \tag{2.20}$$

where α_{pb} (°) is the crack angle when the material is exposed to punching with bending. α_{pp} (°) is the inclination of the punching crack when the material is subject to pure punching failure. F_{faile} (kN) is the ultimate capacity a slab (barricade) can withstand. F_{pun} (kN) is the ultimate punching load. F_{lex} (kN) is the ultimate flexure load.

Furthermore, pure punching failure is assumed to exist in a slab, the ultimate capacity of a slab for the punching crack inclination α_{pp} = 30° can be expressed as:

$$F_{fail} = F_{pun} + \left(F_{flex} - F_{pun}\right)\left\{\sin\left[\left(\frac{3}{2}\alpha_{pb} - 45^{\circ}\right)\right]\right\}^{1/2} \quad \text{with } 30° \le \alpha_{pb} \le 90° \tag{2.21}$$

The ultimate punching load for a general slab (flat barricade) can be given by (Menetrey 2002):

$$F_{pun} = F_{ct} + F_{dow} + F_{sw} + F_{p} \tag{2.22}$$

where, as shown in Fig. 2.27, F_{ct} (kN) is the tensile resistant force of concrete; F_{dow} (kN) is the flexural reinforcement of concrete; F_{sw} (kN) is the shear reinforcement of concrete, and F_p (kN) is the resistant forces in the pre-stressed cable tendons.

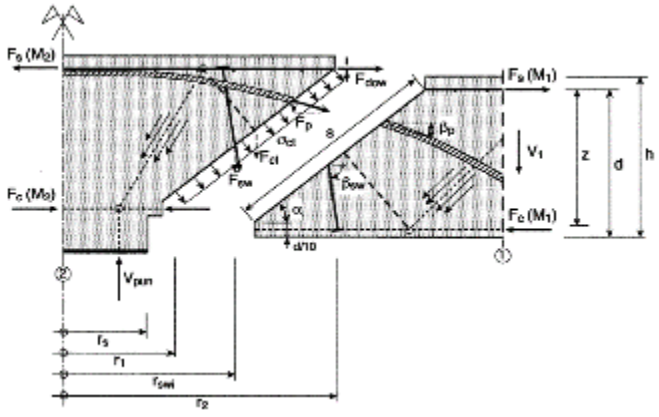

Figure 2.27 Schematic diagram of the punching shear capacity (Menetrey 2002, reprinted with permission of PERGAMON)

The solutions to estimate the tensile resistant force in concrete can be expressed as (Menetrey 2002):

$$F_{ct} = \pi\left(r_1 + r_2\right)s\sigma_v = \pi\left(r_1 + r_2\right)sf_t^{2/3}\xi\eta u \tag{2.23}$$

where the positive correlation between concrete tensile force (F_{ct}, kN) and concrete tensile strength ($f_t^{2/3}$, kPa) is considered, η, u, and ξ are the material parameters, s (m) is the inclined length.

It is assumed that the punching crack is a truncated cone in shape comprised between the radii r_1 (m) and r_2 (m), as shown in Fig. 2.28. The radii can be expressed by (Menetrey 2002):

$$r_1 = r_s + \frac{1}{10}\frac{d_c}{\tan\alpha} \tag{2.24}$$

$$r_2 = r_s + \frac{d_c}{\tan\alpha} \tag{2.25}$$

where r_s (m) is the radius of the column; d_c (m) is the effective thickness of the truncated cone of concrete.

The inclined length s (m) can be given by (Menetrey 2002):

$$s = \sqrt{\left(r_2 - r_1\right)^2 + \left(0.9d_c\right)^2} \tag{2.26}$$

The effect of the proportion factor ρ (%) on the tensile stresses was determined by the numerical simulations and can be expressed by (Menetrey 2002):

$$\xi = \begin{cases} -0.1\rho^2 + 0.46\rho + 0.35, & 0 < \rho < 2\% \\ 0.87, & \rho \geq 2\% \end{cases} \tag{2.27}$$

Based on the size-effect law (Menetrey et al. 1997), the parameter u can be expressed as

$$u = 1.6\left(1 + d_c / d_a\right)^{-1/2}, \quad d > 3d_a \tag{2.28}$$

where d_a (m) is the maximum aggregate size.

Another parameter η is proposed by (Menetrey 2002):

$$\eta = \begin{cases} 0.1\left(r_s / h\right)^2 - 0.5\left(r_s / h\right) + 1.25, & 0 < r_s / h < 2.5, \\ 0.625, & r_s / h \geq 2.5 \end{cases} \tag{2.29}$$

The equations to calculate the flexural reinforcement's resistant force can be given by (Menetrey 2002):

$$F_{dow} = \frac{1}{2}\sum^{bars} \varnothing_s^2 \sin\alpha \sqrt{f_c f_{ta}\left[1 - \left(\sigma_{ta} / f_{ta}\right)^2\right]} \tag{2.30}$$

Where $\varnothing_s$ (m) is the diameter of the steel reinforcements (bars); f_c (kPa) is the specified compressive strength of the concrete slab; f_{ta} (kPa) is the axial tensile strength of the steel reinforcements.

The axial tensile stress (σ_{ta}) in the reinforcing bars can be expressed by (Menetrey 2002):

$$\sigma_{ta} = \frac{F_{pun} / \tan\alpha_{pb}}{\sum^{bars} A_r} \tag{2.31}$$

A_r (m^2) is the area of reinforced bars.

Ramos et al. (2011) recorded punching resistance of a slab by considering both in-plane and out-of-plane forces due to prestress, it can be given by:

$$F_{pun} = 0.18k\left(100\rho_f f_c\right)^{1/3} A_{sl} d_c \tag{2.32}$$

with

$$k = 1 + \sqrt{0.2 / d_c} \tag{2.33}$$

where ρ_f (= $\rho_x\rho_y$) is the bonded flexural reinforcement ratio, and ρ_x and ρ_y are the ratios of side dimension; A_{sl} (=$4l_c$ + $4\pi d$, m) is the length of loaded area for side length (l_c); (f_c)$^{1/3}$ (kPa) is the cube root of specified compressive strength of the concrete slab.

Hoang (2011) assumed that punching failure occurs as sliding in four inclined crack planes, and used a model based on the crack sliding model to predict the punching load by considering punching shear strength, it can be given by:

$$F_{pun} = 8\frac{\tau_c t_s \left(b_i + x_h\right)}{x_h / t_s} \tag{2.34}$$

$$\tau_c = 0.059\lambda_0 f_c \tag{2.35}$$

$$\lambda_0 = \frac{0.88}{\sqrt{f_c}}\left(1 + \frac{1}{\sqrt{t_s}}\right)\left(1 + 26\rho_r\right) \le 1.0 \tag{2.36}$$

where τ_c (MPa) is the shear strength of the test specimens; t_s (m) is the depth of the slab; b_i (m) is the interval distance of the reinforcement bars; x_h (m, = cot$\alpha_{pb}d_c$) is the horizontal projection of the crack planes; λ_0 is a material parameter; ρ_r is the reinforcement ratio.

Documented in ACI 318-95 (1995), the punching shear strength should be the smallest of:

$$F_{pun} = \left(2 + \frac{4}{\beta_c}\right)\lambda\sqrt{f_c} b_0 d \tag{2.37}$$

$$F_{pun} = \left(2 + \frac{a_s d}{b_{0.5}} \right) \lambda \sqrt{f_c} b_0 d \tag{2.38}$$

$$F_{pun} = 4\lambda \sqrt{f_c} b_0 d \tag{2.39}$$

where λ is the modification factor reflecting the reduced mechanical properties of lightweight concrete, $\lambda = 1$ for normal concrete; $(f_c)^{1/2}$ (kPa) is the square root of specified compressive strength of the concrete slab; b_0 (m) is the perimeter of critical section for slabs and footings; d (m) is a distance from extreme compression fiber to centroid of longitudinal tension reinforcement. β_c is the ratio of long side over the short side of the column; α_s is 40, 30, and 20 for interior, edge, and corner columns, respectively.

2.4.2.4 Waste rock barricades design

In Canada and Australia, barricades made of waste rocks in underground mines have become more and more popular to confine slurried backfill in stopes. Compared to traditional barricades, waste rock barricades (WRBs) are faster, easier, and more economical to build. The construction material (waste rocks) can be available at the least cost. Waste rock barricades can be easily removed and reused as rockfill or construction materials for new WRB when the held cemented backfill becomes strong enough. The considerable energy and economic benefits can be achieved by avoiding the transportation and hoisting of these materials from underground to the surface.

Fig. 2.28 shows the model of Li and co-workers (Li et al. 2009; Li and Aubertin 2011) for the stability analysis of a rectangular WRB located in an access drift. On the figure, H (m) is the backfill height; L_d (m) and H_d (m) are the barricades (drift) width and height, respectively; L_B (m) is the barricade length.

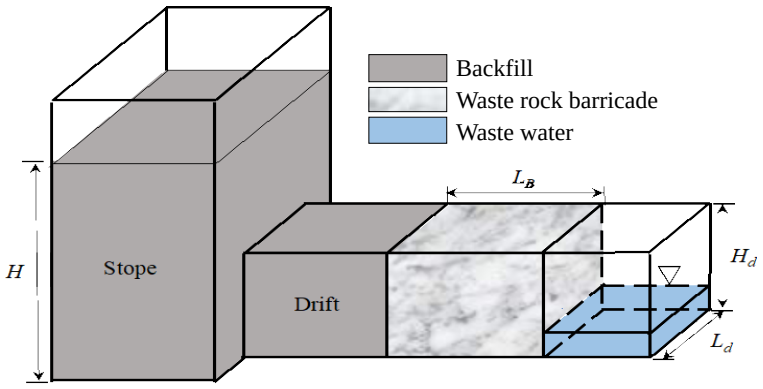

Figure 2.28 Schematic view of a backfilled stope with a rectangular WRB (adapted from Li and Aubertin 2011, reprinted with permission of Canadian Science Publishing)

$$L_B = \frac{P}{\gamma_{wr} H_d (L_d + K_{wr} H_d) \tan \delta_{wr}} \tag{2.40}$$

where P (kN) is the load acting on the stope-side wall of the rectangular WRB; γ_{wr} (kN/m^3) is the unit weight of waste rocks; δ_{wr} (°) is the interface friction angle between the drift walls (two lateral walls and floor) and the WRB; K_{wr} is the earth pressure coefficient of waste rocks that is defined as the ratio between the horizontal stress perpendicular to the axis of the drift and the vertical stress.

Yang et al. (2014) proposed an improved analytical solution compared with the existing solution, which considers a more realistic trapezoidal WRB and reduces the required volume of waste rocks up to about 50%. Engineers would usually estimate the apex length (L_{BT}) and base length (L_{BB}) of WRB in the field.

$$L_{BT} = L_B - \frac{H_d}{2}\left(\frac{1}{\tan \alpha_1} + \frac{1}{\tan \alpha_2}\right) \tag{2.41}$$

$$L_{BB} = L_B + \frac{H_d}{2}\left(\frac{1}{\tan \alpha_1} + \frac{1}{\tan \alpha_2}\right) \tag{2.42}$$

where α_1 (°) is the upstream slope angle of WRB near the stope side; α_2 (°) is the downstream slope

angle of WRB close to the drift side. It should be noted here that Eq. (2.41) and (2.42) may propose an excessively conservative design of WRB.

It should be noted that the solution of Li and Aubertin (2011) [Eq. (2.40)] is similar to a solution given by Checkan (1985). However, the two solutions are different from each other. The former was developed for the design of WRB by considering the stresses in the WRB equaling to those based on the overburden solution and the shear strength along the interface between the waste rocks and the roof of the drift was neglected. The latter was proposed for the design of a concrete barricade. The allowable shear stresses were assumed to be identical along the roof, floor, and two side walls of the drift. They were attributed to some specific values based on a few tests. For general cases, the allowable shear stresses remain unknown. This limitation explains its few applications in the practice. The model of Checkan (1985) is not suitable for the design of WRB because the assumption on the allowable shear stresses is unrealistic for WRB.

In practice, WRBs are trapezoidal and not rectangular due to the repose angle of waste rocks. An improvement on the solution of Li and Aubertin (2011) was then proposed by Yang et al. (2014). Fig. 2.29 shows the model of a trapezoidal WRB. In the figure, L_{BT} (m) and L_{BB} (m) are the top and bottom length of the trapezoidal WRB, respectively; α_1 (°) is the upstream slope angle, which is close to the repose angle of the waste rocks; α_2 (°) is the downstream slope angle of the WRB, which can be increased with a mechanical compactor (Yang et al. 2017).

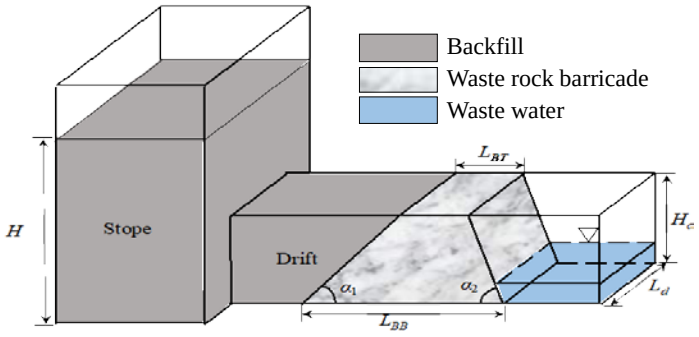

Figure 2.29 Schematic presentation of a backfilled stope with a trapezoidal WRB (adapted from Yang et al. 2014, reprinted with permission of Canadian Science Publishing)

By considering the equilibrium of the trapezoidal WRB in the drift axis direction, Yang et al. (2014) proposed the following equation to determine the required top length of the WRB for retaining paste backfill:

$$L_{BT} = \frac{\gamma_b\left(H-\frac{H_d}{2}\right)\left(\frac{FS}{\tan\delta_{wr}}-\frac{1}{\tan\alpha_1}\right)-\gamma_{wr}H_d\left(\frac{1}{2}+K\frac{H_d}{3L_d}\right)\left(\frac{1}{\tan\alpha_1}+\frac{1}{\tan\alpha_2}\right)}{\gamma_{wr}\left(1+K\frac{H_d}{L_d}\right)} \tag{2.43}$$

Bases on Eq. (2.43), the required top length of WRB can be significantly smaller than that based on the solution of Li and Aubertin (2011). This significant difference does not only come from the different considerations of WRB shape, but also from the fact that the vertical component of the total load *P* has the effect to increase the stability of the WRB. However, it was later found that the application of Eq. (2.43) can lead to a very small and even negative value in the required minimum top length L_{BT} of WRB when the interface friction angle between the waste rocks and rock walls is large. When the top length of WRB is very small, the sliding of the top part of the WRB can take place due to the large pressure of the paste backfill in the stope.

By considering the possible sliding and equilibrium of the top part of the trapezoidal WRB along a horizontal sliding plane, the following equation was proposed by Yang et al. (2017) to calculate the required top length of the WRB for retaining paste backfill in stope:

$$L_{BT} = \frac{\gamma_b}{\gamma_{wr}}\left(H-H_d\right)\left(\frac{C_M \times FS}{\tan\phi'_{wr}}-\frac{1}{\tan\alpha_1}\right) \tag{2.44}$$

where ϕ'_{wr} (°) is the internal friction angle of waste rock; C_M is the calibration factor, which was determined as equal to 1.5 based on numerical results obtained by numerical modeling with FLAC.

The proposed solution of Yang et al. (2017) is then composed of the following equations:

$$L_{BT}=\frac{\gamma_b\left(H-\frac{H_d}{2}\right)\left(\frac{FS}{\tan\delta_{wr}}-\frac{1}{\tan\alpha_1}\right)-\gamma_{wr}H_d\left(\frac{1}{2}+K\frac{H_d}{3L_d}\right)\left(\frac{1}{\tan\alpha_1}+\frac{1}{\tan\alpha_2}\right)}{\gamma_{wr}\left(1+K\frac{H_d}{L_d}\right)},\ \text{for } \delta_{wr}\le\delta_c \quad (2.45a)$$

$$L_{BT}=\frac{\gamma_b}{\gamma_{wr}}\left(H-H_d\right)\left(\frac{C_M\times FS}{\tan\phi'_{wr}}-\frac{1}{\tan\alpha_1}\right),\ \text{for } \delta_{wr}>\delta_c \quad (2.46b)$$

where δ_c (°) is the critical interface friction angle between the drift walls and the WRB, determined as follows:

$$\delta_c=\tan^{-1}\frac{FS\left(2H-H_d\right)\tan\alpha_1}{H_d+2\left(H-H_d\right)\left[\frac{C_M\times FS\times\tan\alpha_1}{\tan\phi'_{wr}}\left(1+K_{wr}\frac{H_d}{L_d}\right)-K_{wr}\frac{H_d}{L_d}\right]+\frac{\gamma_{wr}}{\gamma_b}H_d\left(1+K_{wr}\frac{2H_d}{3L_d}\right)\left(1+\frac{\tan\alpha_1}{\tan\alpha_2}\right)} \quad (2.47c)$$

Recently, Belem et al (2020) proposed an empirical solution to determine the top length of WRBs as follows:

$$L_{BT}=FS\left(2+\frac{H}{\left(80L_d+30\right)\left(L_d\right)^{-1.46}}\right) \quad (2.48)$$

It can be noted that the solution only involves the backfill height H in the stope and WRB width L_d. The height of barricade (or drift) H_d, the unit weight of the backfill γ_b, and the physical (γ_{wr}) and mechanical (ϕ'_{wr} and δ_{wr}) property parameters of waste rocks are absent in the solution. Therefore, the equation is a specific solution. Its validity is only limited to the tested cases, in which the specific numbers were obtained by adjustment. It cannot be used as a general solution.

2.4.3 Failure cases of barricades

There are some reasons (e.g., pipe erosion and maloperations) that may lead to the failure of the barricades. It is necessary to have a comprehensive understanding of the demand and capacity of the barricade.

2.4.3.1 Pipe erosion

Pipe erosion is the primary failure reason for the barricades built with previous brick (e.g., Bloss and Chen 1998). The flow of the water inside the backfilled stopes is driven by the pressure difference while solid particles are washed away. The pipe-shaped channel connecting the barricade and ponded water is progressively developed, resulting in a sudden rise in pressure on the retaining structure (Grice 1998; Potvin et al. 2005).

The laboratory tests conducted by Bloss and Chen (1998) showed that the increase of hydraulic pressure is observed when the barricades are sealed. A water-tight barricade is subjected to much higher hydraulic pressure than one that is constructed to drain freely. When hydrostatic pressure surpasses the capacity of the retaining structure, the failure of the barricade occurs that usually causes large quantities of water and fill (uncemented or unconsolidated) to rush into the access drift (Grice 1989).

Pressurization does not occur until a clear pipe connects with ponding water. Point loading eventually damages the barricade with the development of pipe erosion (Grice 1989).

Bloss and Chen (1998) and Grice (1998) suggested that several operational practices should be implemented to minimize the risk of barricade failure due to pipe erosion for HF, including:

- Limit fine particles of tailings (e.g., no more than 10% fines smaller than 10 microns);
- Solid content by weight should be controlled no less than 70%;
- Control the filling rate;
- Regular leakage examination of barricades;
- Control the ponding water height or remove the ponding water during the backfilling.

2.4.3.2 Maloperation during the backfilling

The backfilling for blind stopes with no access drift is challenging because it is relatively small

compared to open stopes and may be overfilled during the tight filling stage. In addition, the lack of air breather holes or the blocking during the final stage of tight fill may cause serious outcomes. Based on the field report (Yumlu and Guresci 2007), in stope S880S07, the increased pipeline pressure was recorded during the tight fill stage. The stope was backfilled through a 102 mm inclined hole without a separate air breather hole.

Another field report documented by Yumlu and Guresci (2007), a waste rock barricades failure occurred at the final stage of tight filling. The paste fill returns from the breather hole with the increased pipeline pressure and indicates the failure took place during the tight fill stage.

The waste rock barricade with a 7 m top length is constructed and the shotcrete is applied to enhance its capacity (Yumlu and Guresci 2007). The maloperation during the stage of tight fill may cause hydraulic pressure from the ground surface to the access drift in the underground, which puts extreme pressure on the barricade and ultimately damages the retaining structure.

Soderberg and Busch (1985) reported a case of barricade failure due to rockburst and build-up hydrostatic pressure. Rock burst happened during the backfilling. The build-up of PWP at an early age put the retaining structure in jeopardy because of the absence of a drainage system. The barricade constructed from wood with drains (wood box drains with burlap filters) was corrupted when these drains collapsed. The hydrostatic pressure builds up rapidly and destroys the barricade.

The groundwater from water-bearing strata abandoned mine areas, and poorly seal shafts may be the main sources of water inflow (Djahanguiri and Abel 1997). It increases the hydraulic pressure acting on the barricades when leakage flows into stope and mixes with slurried backfill. Revell and Sainsbury (2007b) recorded that the groundwater (0.25 L/s) flows into the stope, causing additional pressure against the barricade. After the barricade collapsed, uncemented powdery zones and splash marks on the walls and ventilation bag showed that higher hydraulic pressure significantly damages the barricade. Fig. 2.30 (taken from “Advancing Paste Fill Bulkhead Design Using Numerical Modeling” by Revell, M. B. and Sainsbury, D.P., MINEFILL2007, reprinted with

permission of the Canadian Institute of Mining, Metallurgy and Petroleum) shows the barricade failure due to high hydraulic pressure.

Figure 2.30 barricade failure under high hydraulic pressure (taken from Revell and Sainsbury 2007b, reprinted with permission of the Canadian Institute of Mining, Metallurgy and Petroleum)

Helinski and Grice (2007) concluded that inappropriate water management in HF is the main reason for barricade failure. Improper drainage measures can lead to build-up hydraulic pressure and increased pressures acting on the barricade in the stope side (Kuganathan 2002; Li and Aubertin 2009).

2.5 Summary

In this chapter, a literature view is given in relation with barricades. Underground mining methods by which backfills is necessary or can be used have been presented. The necessary of barricade construction was introduced. The three commonly used backfills in underground mine were presented. The mechanical and hydraulic properties vary as a function of backfills types. The pressures exerted by the backfills on the barricades depend on the types of backfills. A paste backfill of low solids content may have a fluid-like behavior and the pressure can be represented by the iso-geostatic overburden pressure. A dry rockfill may accumulate near the access brow and the

pressures acting on barricades may be small.

The estimation of pressure acting on the barricade can be done by analytical, numerical, and experimental methods. Much more work is still necessary to obtain a reliable estimation of backfill pressure exerted on barricades for the design of barricades.

The literature review also showed that the failure of barricades can be due to several factors, such as (references):

- inaccurate estimation of demand and capacity.
- maloperation during tight fill and blockage of air breather holes.
- fast filling rate and continuous filling.
- deficient curing time for shotcrete material.
- improper cement contents in backfills.
- inadequate management and monitoring system for backfills.
- low slurry density (solid contents by weight less than 70%) in hydraulic fill may cause pipe erosion.
- irrational particle size distribution curves.

With respect to the design of WRB, the first solution for sizing WRB was proposed by Li and his coworkers in 2009 and 2011 (Li et al. 2009; Li and Aubertin 2011). The shape of the waste rock barricade should be trapezoid because of the repose angle of the waste rocks. In 2014, Yang and his coworkers proposed a solution to design the trapezoidal waste rock barricade (Yang et al. 2014). A further improvement was given by considering the global and local stability in 2017 (Yang et al. 2017). These solutions solve the case without reinforcements applied on the waste rock barricades. However, the problem arises when there is a limited drift space. It means that the required length of the waste rock barricade based on calculation is longer than the drift space. In addition, the lab tests show ingression of paste backfill at the top of a WRB. It confirms the need for shotcrete at

the upper portion, about one-third of the barricade height. Applying shotcrete can prevent the leakage of backfill through the top. Therefore, it is necessary for the design of WRB with shotcrete. Besides, there are some limitations in Yang et al. (2017) solution. For example:

- the calibration and validation of the analytical solution were made against FLAC2D. In practice, WRB usually has the same order of dimension in the three mutually perpendicular directions. So, it is a 3D problem.
- the local solution is proposed by considering a horizontal sliding plane while their numerical modeling clearly showed the inclined sliding plane

More work is thus necessary to improve the design of WRB for retaining slurried backfill in mine stopes

CHAPTER 3 METHODOLOGY

The main objective of the thesis is to provide solutions that can be used for the design of waste rock barricades (WRB) for retaining slurred paste backfill in underground mine stopes. The literature review given in Chapter 2 allows us to identify two gaps and one aspect to be improved in this field:

- Gap 1: one sees a large number of publications on the stress estimation in backfilled stopes with dry backfill. One sees also a number of publications on the stress and pressure evaluation in backfilled stopes with water consideration. There is however no solution available to estimate the stresses and pressures around WRB.
- Gap 2: shotcrete on the upper part over the downstream slope of WRB is a quite often practice either for providing reinforcement or for preventing any problem associated with the top part of WRB. There is however no solution available to design the shotcrete.
- Aspect to be improved: Yang et al. (2017) solution was calibrated and validated by 2D numerical modeling. Its validity in 3D conditions remains unknown. Their local stability analysis was proposed by considering a horizontal sliding plane while the numerical modeling clearly showed an inclined plane.

In order to fill the gaps and improve the Yang et al. (2017) solution, one needs a numerical tool that can be used to correctly simulate the hydrogeotechnical behavior of slurried backfill interacting with waste rocks. FLAC3D was chosen for its availability and its large application examples in geotechnical engineering. Its validity and applicability in modeling the hydrogeotechnical behavior of slurried backfill interacting with waste rocks need to be tested.

To do so, a simple way is to study the water flow passing through a WRB. Laboratory tests of water flow passing through a WRB were realized with a narrow box made of glass. The water flow pattern through the WRB can then be easily observed during the test processes. The qualitative validation of the numerical model with FLAC3D was achieved by the good agreement between the observed

water flow pattern through the WRB and the numerical results of FLAC3D. The quantitative validation of the numerical model with FLAC3D against existing analytical solutions and laboratory tests led however to the following discoveries:

1) The 3D generalized solution of the Dupuit model is the most appropriate for estimating the total seepage rate through a 3D rockfill trapezoidal dike.
2) The Dupuit model contains some explicit and implicit assumptions which become inappropriate when the downstream hydraulic head is very different from the upstream hydraulic head. A new analytical solution was this proposed by adding two calibration coefficients: the first one for flow path length and the second one for the mean cross-section area of flow.
3) The two calibrations coefficients were obtained by fitting the numerical results to the proposed solution for a specific case. The values of these calibration coefficients along with the proposed equations are called the proposed calibrated solution for estimating the total water seepage rate through a 3D rockfill dyke.
4) The proposed calibrated solution was further validated by additional numerical modeling results.
5) The proposed calibrated solution and the numerical model of FLAC3D were further validated by the good agreements between the results obtained with FLAC3D, those calculated with the proposed calibrated solution, and experimental results obtained by seepage tests performed in the laboratory.
6) The numerical model of FLAC3D can be used to simulate the hydromechanical behavior of WRB.
7) This work led to the production of Article 1, published in Mine Water and the Environment.
8) Gap 1 was only partly filled. More work is still necessary by considering the hydromechanical

behavior of slurried backfill in interaction with WRB.

To fill Gap 2, an analytical solution was proposed based on limit equilibrium analysis to design the shotcrete sprayed on the upper part on the downstream slope of WRB, including the determination of the minimum required thickness with a given shotcrete material or the estimation of the minimum required cohesion with a given dimension of shotcrete. The proposed solution was first calibrated against a few numerical modeling results obtained with FLAC3D. The proposed calibrated solution was further validated by additional numerical modeling results obtained by FLAC3D. This work led to the production of Article 2 published in Construction and Building Materials. Nevertheless, more work is still necessary to develop a solution by considering the inclined slip plane without calibration coefficients. Experimental work is needed to test the validation of the proposed solution.

Finally, to improve the Yang et al. (2017) solution developed to size 3D WRB, a new solution was developed by considering an inclined sliding plane across the top part of a WRB. The numerical results obtained with FLAC3D were still used to validate the proposed solution. The subjectivity in evaluating the failure of a WRB structure in numerical modeling was reduced by observing the first occurrence among a jump of monitored displacement and the coalescence of plasticity zones passing through the simulated WRB. The value of the earth pressure coefficient used in the proposed solution was reevaluated by considering its definition given in Yang et al. (2017) model. The updated 3D analytical solution was validated by numerical results obtained with FLAC3D and some laboratory test results available in the literature. The realization of this work lead to the production of Article 3, submitted in International Journal of Rock Mechanics and Mining Sciences.

CHAPTER 4 ARTICLE 1: ANALYTICAL, NUMERICAL AND EXPERIMENTAL STUDIES ON STEADY-STATE SEEPAGE THROUGH 3D ROCKFILL TRAPEZOIDAL DIKES

Yulong Zhai, Li Li, Robert P. Chapuis

This article has been published online in Mine Water and the Environment on 28 August 2021

Abstract: Seepage through dikes under steady-state conditions is a classical problem in geotechnics. Several analytical solutions exist for estimating seepage through 2D dikes. In practice, many dikes have a limited length in the third dimension. This is particularly true for water flow through a waste rock barricade to hold backfill slurry in underground stopes. Three-dimensional solutions are necessary to evaluate seepage through 3D trapezoidal dikes. In this study, existing 2D solutions developed for estimating seepage through 2D dikes under steady-state conditions are presented and generalized for 3D dikes. The validity of these 3D generalized solutions is tested by numerical modeling with FLAC3D. Results show that the 3D solution based on a generalization of the Dupuit solution predicts seepage variation as a function of upstream hydraulic head well, but fails to describe seepage variation as a function of downstream hydraulic head. Further analyses reveal that the Dupuit model involves assumptions by which the flow path can be underestimated and the mean flow cross-section from the bottom to the top surface of the downstream water tends to be overestimated. The 3D generalized Dupuit solution was therefore modified by adding two calibration coefficients, one for the flow path length and another for the mean flow cross-section. The two calibration coefficients were then obtained by calibration against a few 3D numerical results. The validity of the proposed and calibrated analytical solution was then tested against additional numerical results. Finally, both the numerical model and the proposed calibrated analytical solutions were validated by laboratory test results.

Keywords: Total seepage rate; Dupuit theory; 3D solution; FLAC3D; Seepage tests.

4.1 Introduction

Seepage through a homogeneous dike resting on an impervious base under steady-state flow conditions is a classic problem in soil mechanics (Chapuis 1990; Chapuis and Aubertin 2001; Harr 1962). For most cases, dikes are constructed with available in site materials. The knowledge of seepage rates is necessary for estimating the water level of a reservoir (for a given dike design) or to properly size the dike geometry for reaching a target water level (Aubertin et al. 2003; Chapuis and Aubertin 2001). Knowledge of the water level variation, which depends on the seepage, evaporation, precipitation, inundation, and even melting snow in some regions, can be necessary for the design of a spillway or for estimating the security of the dikes. Piping or internal erosion due to seepage is another aspect that can affect dike stability (Richards and Reddy 2007). For mining engineers, seepage rate must be estimated to design required water collecting infrastructures of tailings storage facilities or to design the pumping system of underground mine backfilled stopes.

With a given material (e.g., soil or rockfill), the total seepage rate through the dike can be calculated by considering the geometry of the retaining dike, the boundary conditions, and the hydraulic properties of the dike material. Fig. 4.1 schematically shows a seepage problem with a two-dimensional (2D) homogeneous dike resting on a horizontal impervious base (Harr 1962), where: H_d (m) is the dike height; L_{BT} (m) and L_{BB} (m) are the top and bottom dike widths, respectively; h_1 (m) is the hydraulic head at the upstream of the dike; h_2 (m) is the downstream (tail) hydraulic head; α_1 (°) is the upstream slope angle; α_2 (°) is the downstream slope angle; L (m) is the spacing of the plan projection of the upstream and downstream water surfaces; L_c (m) is the spacing after considering an extra distance 0.3 h_1 / tanα_1 based on L; a_0 (m) is the vertical gap between the outcrop of the seepage face and the tail water surface; a (m) is the downstream distance of the seepage surface between the free surface and dike bottom; h (m) is the elevation of water surface along the dike; and l (m) and s (m) are the horizontal and inclined distances measured along the free surface. The total discharge through a 2D trapezoidal dike on a horizontal substratum was first

studied by Dupuit (1863), who made the following assumptions for unconfined 2D steady-state seepage:

- The equipotential lines were assumed to be vertical and the seepage lines were assumed to be almost horizontal;
- The hydraulic gradient *dh*/*dl* was assumed to be constant at different elevations;
- The hydraulic gradient was assumed to be equal to the slope of the water table surface; and,
- The unsaturated seepage was neglected.

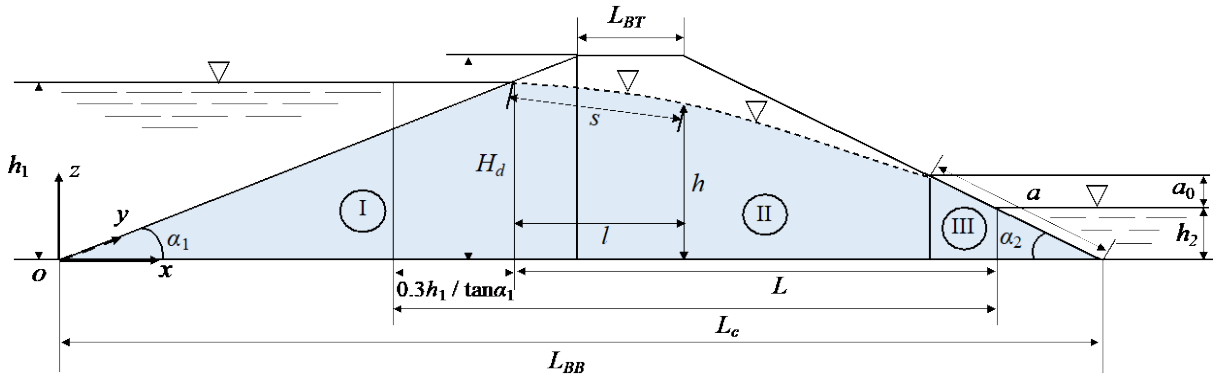

Figure 4.1 Schematic presentation of the cross-section of a 2D dike (adapted from Harr 1962).

With these assumptions, the 2D differential equations of unconfined aquifers become more easily solved 1D equations. Chapuis (2011) used a similar approach to simplify a complex problem of seepage in an unconfined aquifer on a sloping impervious substratum. Dupuit (1863) derived the following expression for the flow rate through a trapezoidal dike:

$$q = k_h \frac{h_1^2 - h_2^2}{2L} \quad \text{or} \quad \frac{q}{k_h} = \frac{h_1^2 - h_2^2}{2L} \tag{4.1}$$

with

$$L = L_{BB} - h_1 / \tan\alpha_1 - h_2 / \tan\alpha_2 \tag{4.2}$$

where q ($m^3/(s \cdot m)$) is the flow rate per linear meter; k_h (m/s) is the saturated hydraulic conductivity. In practice, a seepage face (i.e. the boundary between a saturated flow field and the atmosphere) can appear on the downstream slope face above the water table on the downstream side, as shown in Fig. 4.1. Schaffernak (1917) and Iterson (1917) considered this when deriving a 2D solution to evaluate the flow rate for the case of $h_2 = 0$ (no tail water) as follows:

$$q = k_h a \sin\alpha_2 \tan\alpha_2 \quad \text{or} \quad q / k_h = a \sin\alpha_2 \tan\alpha_2 \tag{4.3}$$

with

$$a = \frac{L}{\cos\alpha_2} - \sqrt{\frac{L^2}{\cos^2\alpha_2} - \frac{h_1^2}{\sin^2\alpha_2}} \tag{4.4}$$

Fifteen years later, Casagrande (1932) considered inclined flow lines and the difference between *dh*/*ds* and *dh*/*dl* in the hydraulic gradient calculation. An alternative 2D solution was given as follows (Casagrande 1932):

$$q = k_h a_c \sin^2\alpha_2 \quad \text{or} \quad q / k_h = a_c \sin^2\alpha_2 \tag{4.5}$$

with

$$a_c = \sqrt{h_1^2 + L_c^2} - \sqrt{L_c^2 - h_1^2 / \tan^2\alpha_2} \tag{4.6}$$

and

$$L_c = L + 0.3h_1 / \tan\alpha_1 \tag{4.7}$$

where a_c is an alternative expression of a, used in Casagrande (1932). Pavlovsky (1931) proposed to estimate the flow rate through a 2D dike by segmenting the dike into three zones (Fig. 4.2) for which simple seepage solutions were available (Harr 1962). In Zone I, the streamlines are assumed to be horizontal and the flow rate is estimated by the following equation:

$$q_1 = k_h \left(h_1 - h\right) \tan\alpha_1 \times \ln\frac{H_d}{H_d - h} \quad \text{or} \quad \frac{q_1}{k_h} = \left(h_1 - h\right) \tan\alpha_1 \times \ln\frac{H_d}{H_d - h} \tag{4.8a}$$

where q_1 (m^3/s) is the flow rate per linear meter in Zone I.

For Zone II, the flow rate is obtained by using Eq. (4.1) and is expressed as follows:

$$q_2 = k_h \frac{h^2 - \left(a_0 + h_2\right)^2}{2\left[L_{BT} + \dfrac{H_d - \left(a_0 + h_2\right)}{\tan\alpha_2}\right]} \quad \text{or} \quad \frac{q_2}{k_h} = \frac{h^2 - \left(a_0 + h_2\right)^2}{2\left[L_{BT} + \dfrac{H_d - \left(a_0 + h_2\right)}{\tan\alpha_2}\right]} \tag{4.8b}$$

where q_2 ($m^3/(s\cdot m)$) is the flow rate per linear meter in Zone II. For Zone III, where the flow is assumed horizontal again, the flow rate can be expressed by:

$$q_3 = k_h a_0 \tan\alpha_2 \left(1 + \ln\frac{a_0 + h_2}{a_0}\right) \quad \text{or} \quad \frac{q_3}{k_h} = a_0 \tan\alpha_2 \left(1 + \ln\frac{a_0 + h_2}{a_0}\right) \tag{4.8c}$$

where q_3 ($m^3/(s\cdot m)$) is the flow rate per linear meter in Zone III. Because $q_1 = q_2 = q_3$, the unknowns a_0 and h can be resolved, and the flow rate obtained.

While these 2D solutions provide a simple and efficient way to evaluate the seepage through a very long dike, one has to consider that many dikes are limited in size in the third direction. The seepage calculation becomes a 3D problem when the third dimension is not large enough compared to the two dimensions of the cross-section, as shown in Fig. 4.1 (Harr 1962). For instance, Chen and Zhang (2006) investigated the performance of a 3D rockfill dam with a numerical simulation. Their results showed that the flow rate and hydraulic gradients obtained by 3D simulations were different from those obtained by 2D numerical simulations. A 3D solution is deemed necessary to analyze water flow through a 3D rockfill dam.

Another example is the use of waste rock to construct a structure to retain slurried materials in underground mine backfilled stopes. This retaining trapezoidal structure, called a waste rock barricade (WRB), has become more and more popular in Canada and Australia. Solutions were proposed to determine the sizes of WRBs (Li et al. 2009; Li and Aubertin 2011; Yang et al. 2014,

2017), but water seepage through the WRB was never considered. Obviously, the four previously mentioned 2D solutions cannot be directly applied to estimate seepage through a 3D trapezoidal WRB if the upstream hydraulic head h_1 value can exceed the height of the WRB for backfilled stopes.

Li (2013) extended a 2D solution to assess the flow rate and pore-water pressure distribution for confined and unconfined steady flow to the 3D problem of a rectangular WRB. The analytical solution was validated by numerical results obtained with FLAC3D (Itasca 2017). However, this approach cannot be used to predict the 3D flow rate through a trapezoidal WRB. Therefore, in this work, the four previously mentioned 2D solutions were generalized to 3D conditions to calculate the flow rate through a 3D trapezoidal dike. The validity of the generalized 3D solutions was then tested against numerical results obtained with FLAC3D. A new 3D solution based on a 3D generalization of the Dupuit equation was then proposed for estimating the flow rate through a trapezoidal dike resting on an impervious base under steady-state conditions. The proposed solution was further validated by numerical results obtained with FLAC3D and experimental results obtained by reduced-scale tests in the laboratory.

4.2 Generalization of 2D solutions to a 3D dike under steady-state conditions

Fig. 4.2 shows the steady-state seepage flow through a homogeneous dike having a limited dimension in the third direction (i.e. L_d in the same order as those of H_d and L_{BB}; where L_d is the length of the dike), resting on an impervious horizontal base (Harr 1962). The boundary conditions are defined as a static pore-pressure distribution up to h_1 level on the upstream face, and up to h_2 on the downstream face, zero pore pressure from h_2 level to top on the downstream face, and to no-flow conditions across the remaining boundaries. Both ends (abutments) are assumed to have no effect on the flow.

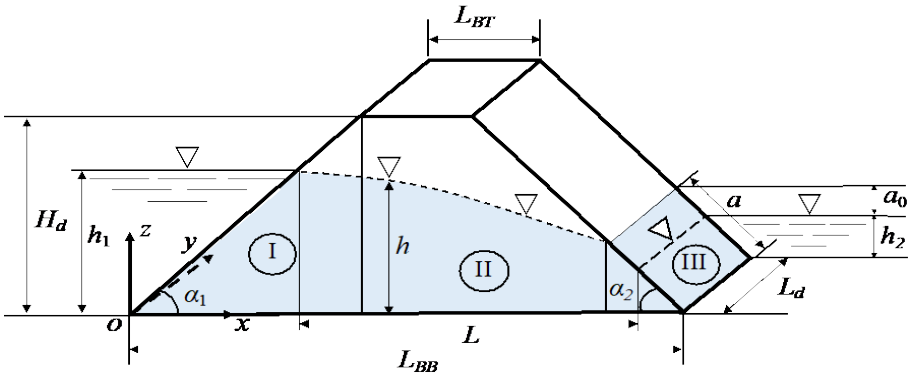

Figure 4.2 Schematic presentation of a 3D dike (adapted from Harr 1962).

A simple generalization of the 2D solution of Dupuit (1863) [Eq. (4.1)] to 3D condition is given as follows, after considering the third dimension L_d:

$$Q = k_h \frac{h_1^2 - h_2^2}{2L} \times L_d \quad \text{or} \quad \frac{Q}{k_h} = \frac{h_1^2 - h_2^2}{2L} \times L_d \tag{4.9}$$

where Q (m^3/s) is the flow rate through the dike. The generalization of the 2D solution of Schaffernak (1917) and Iterson (1917) [Eq. (4.3)] to 3D condition leads to the following equation:

$$Q = k_h a \sin\alpha_2 \tan\alpha_2 L_d \quad \text{or} \quad Q/k_h = a \sin\alpha_2 \tan\alpha_2 L_d \tag{4.10}$$

The 2D solution of Casagrande (1932) [Eq. (4.5)] can be generalized to the 3D condition as follows:

$$Q = k_h a_c \sin^2\alpha_2 L_d \quad \text{or} \quad Q/k_h = a_c \sin^2\alpha_2 L_d \tag{4.11}$$

The generalization of the 2D solutions of Pavlovsky (1931) [Eq. (4.8)] to the 3D condition results in the following expressions:

$$Q_1 = k_h (h_1 - h) \tan\alpha_1 \times \ln\frac{H_d}{H_d - h} \times L_d \quad \text{or} \quad \frac{Q_1}{k_h} = (h_1 - h) \tan\alpha_1 \times \ln\frac{H_d}{H_d - h} \times L_d \tag{4.12a}$$

$$Q_2 = k_h \frac{h^2 - (a_0 + h_2)^2}{2\left[L_{BT} + \frac{H_d - (a_0 + h_2)}{\tan\alpha_2}\right]} \times L_d \quad \text{or} \quad \frac{Q_2}{k_h} = \frac{h^2 - (a_0 + h_2)^2}{2\left[L_{BT} + \frac{H_d - (a_0 + h_2)}{\tan\alpha_2}\right]} \times L_d \tag{4.12b}$$

$$Q_3 = k_h a_0 \tan\alpha_2 \left(1 + \ln\frac{a_0 + h_2}{a_0}\right) \times L_d \quad \text{or} \quad \frac{Q_3}{k_h} = a_0 \tan\alpha_2 \left(1 + \ln\frac{a_0 + h_2}{a_0}\right) \times L_d \tag{4.12c}$$

where Q_1 (m^3/s), Q_2 (m^3/s), and Q_3 (m^3/s) are the seepage flow rate in Zones I, II, and III, respectively. The two unknowns a_0 and h can be resolved by considering $Q_1 = Q_2 = Q_3$. The flowrate can then be obtained. However, solving the two equations $Q_1 = Q_2 = Q_3$ is quite time-consuming.

To test the validity of the above generalized 3D solutions, Example 9.5a of Bowles (1984, pp. 295) was taken and reproduced by numerical modeling with FLAC3D. Table 4.1 presents the geometric parameters and material properties used in the numerical model of FLAC3D.

Table 4.1 Parameters of geometry and material property used in the numerical model of FLAC3D

Variables	Definition
L_{BT} (m)	Top length of a dike
L_{BB} (m)	Bottom length of a dike
H_d (m)	Height of a dike
L_d (m)	Width of a dike
α_1 (°)	Upstream slope angle
α_2 (°)	Downstream slope angle
k_h (m/s)	Saturated hydraulic conductivity
k [m^2(Pa/s)]	Isotropic permeability coefficient
K_f (kPa)	Fluid bulk modulus
ρ_f (kg/m^3)	Fluid density
g (m/s^2)	Gravity accelerator
L_z (m)	Maximum vertical zone size close to the water table (i.e., the mesh size in z direction of numerical model)

In FLAC3D, the isotropic permeability coefficient k [m^2(Pa/s)] is related to the saturated hydraulic conductivity k_h (m/s), fluid density ρ_f (kg/m^3) and gravity g (m/s^2) by the following equation (Itasca 2017):

$$k = \frac{k_h}{\rho_f g} \tag{4.13}$$

The fluid bulk modulus K_f (kPa) is defined as a function of fluid density ρ_f (kg/m^3), gravity g (m/s^2), and the maximum vertical zone size close to the water table L_z (m) to speed the calculation to a steady state (Itasca 2017):

$$K_f \geq 0.3\rho_f g L_z \tag{4.14}$$

Fig. 4.3 illustrates a numerical model of Example 9.5a of Bowles (1984, pp. 295), built with FLAC3D. The dike material is considered as homogenous and isotropic, characterized by a porosity n = 0.3 and a saturated hydraulic conductivity k_h = 6.67 × 10^{-6} m/s. The geometric parameters are L_{BT} = 10 m, L_{BB} = 100 m, H_d = 20 m, L_d = 1 m (unit thickness to simulate a 2D condition), α_1 = 21.8°, α_2 = 26.6°, h_1 = 18.5 m, and h_2 = 0 m. Applying Eqs. (4.13) and (4.14) with ρ_f = 1000 kg/m^3, g = 10 m/s^2, and L_z = 1 m leads to k = 6.67 × 10^{-10} m^2(Pa/s) and K_f = 3 kPa, respectively.

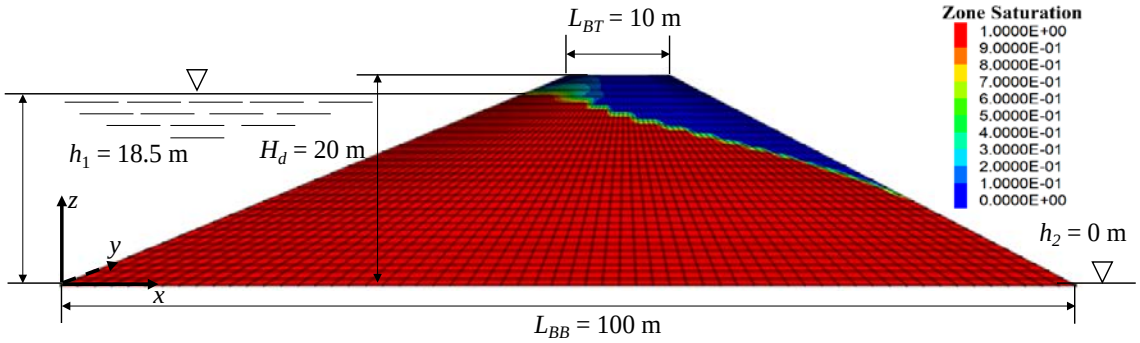

Figure 4.3 A numerical model of a homogeneous dike in Example 9.5a of Bowles (1984, pp. 295), built with FLAC3D.

The initial hydraulic boundary conditions of the numerical model were defined by imposing a hydrostatic water pressure linearly distributed from the base up to h_1 along the upstream slope of the dike to simulate the upstream water table and a hydrostatic water pressure linearly distributed from the base up to h_2 along the downstream slope of the dike to simulate the downstream water table. Zero pore pressure was imposed along the downstream slope face above the water table. Water flow passing through the bottom was prohibited along the base of the dike.

Sensitivity analyses show that using a convergence ratio of 10^{-3} and a meshing of 1.6 m × 1 m × 1 m (largest elements near the dike bottom) can ensure stable numerical results. In the *y* direction, a unit thickness is taken to simulate a 2D model (case of the example in Bowles 1984). Table 4.2 shows the total seepage rate estimated by applying a graphic solution given in Bowles (1984), the 3D generalized solutions, and that obtained by numerical modeling with FLAC3D. It can be seen that the numerical results obtained with FLAC3D correspond well to those obtained by the graphic solution of Bowles (1984) and the analytical solution Eq. (4.9) generalized from the 2D solution of Dupuit (1863). The 3D solution generalized from the 2D solution of Schaffernak (1917) and Iterson (1917) overestimate seepage while the 3D solution generalized from 2D solution of Casagrande (1932) and Pavlovsky (1931) underestimates the seepage rates compared to the numerical results with FLAC3D.

Table 4.2 Total seepage rate of Example 9.5a of Bowles (1984, pp. 295), calculated by analytical solutions and numerical simulations

References	q [$m^3/(s \cdot m)$]	Remarks
Bowles (1984)	2.13×10^{-5}	Graphic solution
Dupuit (1863)	2.12×10^{-5}	Eq. (4.9)
Schaffernak (1917) and Iterson (1917)	2.46×10^{-5}	Eq. (4.10)
Casagrande (1932)	1.75×10^{-5}	Eq. (4.11)
Pavlovsky (1931)	1.44×10^{-5}	Eq. (4.12)
Crespo (1994)	2.35×10^{-5}	Seep/W with coarse (2 m) mesh
Chapuis et al. (2001)	2.28×10^{-5}	Seep/W with fine (1 m) mesh
This study	2.15×10^{-5}	FLAC3D with optimal mesh

To further verify the validity of the 3D generalized analytical solutions, additional numerical simulations were performed by varying h_1 and h_2. Fig. 4.4 shows the variation of Q/k_h as a function of the upstream hydraulic head h_1 when $h_2 = 0$, obtained by numerical modeling with FLAC3D and calculated with the generalized 3D solutions. The results obtained with Eq. (4.9) agree well with the numerical results obtained by FLAC3D for h_1 varying from 0 to 20 m while the other three analytical solutions [Eqs. (4.10), (4.11), and (4.12)] also predict the numerical results quite well for h_1 less than 10 m. When h_1 exceeds 10 m, the numerical results of Q/k_h tend to be overestimated by the application of Eq. (4.10) and underestimated using Eqs. (4.11) and (4.12).

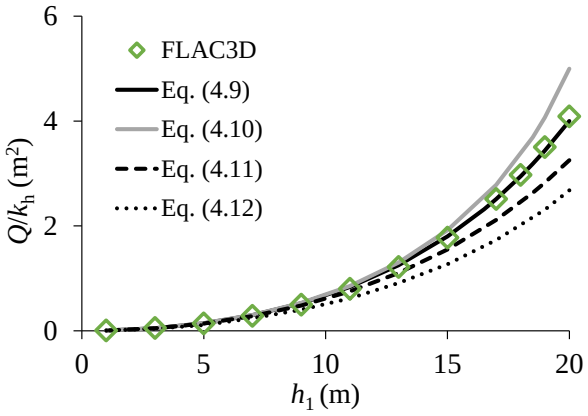

Figure 4.4 Variation of the ratio Q/k_h as a function of h_1 when $h_2 = 0$, obtained by numerical modeling with FLAC3D and predicted by applying the generalized analytical solutions [Eqs. (4.9) to (4.12)].

Having shown that Eq. (4.9) is the best performing solution among the predictive equations when $h_2 = 0$, its validity was further tested against numerical modeling results for the case of $h_2 > 0$. Fig. 4.5 shows the variation of Q/k_h as a function of the downstream hydraulic head h_2 for different values of the upstream hydraulic head h_1, obtained by numerical modeling with FLAC3D and calculated with the generalized 3D solution of Eq. (4.9). The results show that Eq. (4.9) tends to largely overestimate the flow rate, compared to the numerical results, especially when the upstream

hydraulic head h_1 is high. In addition, Eq. (4.9) predicts an increase of the Q/k_h ratio as the downstream hydraulic head h_2 increases from 0 to about 10 m before it reaches a peak value of ≈ 5 m^2 for the case of h_1 = 20 m. This trend does not correspond to what is observed in practice. An analysis of this unrealistic trend and modifications to Eq. (4.9) were thus necessary.

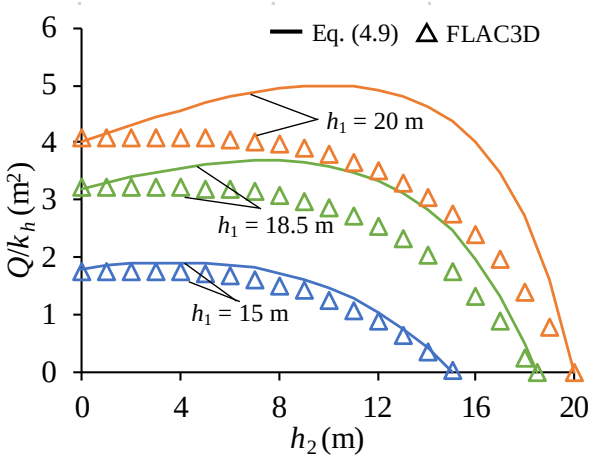

Figure 4.5 Variation of the ratio Q/k_h versus h_2, obtained by FLAC3D and calculated with Eq. (4.9).

4.3 Proposed solution for estimating total seepage rate through a dike

The previous section clearly showed that the 3D generalized solution of Dupuit model Eq. (4.9) can give the best prediction of the seepage rate among the four 3D generalized solutions (see Fig. 4-4). However, it fails to correctly predict the seepage rate with high upstream heads, as shown in Fig. 4.5, a situation that is common for waste rock barricades (WRB). Eq. (4.9) should then be modified to better estimate the total seepage with different upstream and downstream heads. Recalling that the Dupuit (1863) solution is a simple application of Darcy's law (Darcy 1856), Eq. (4.9) can be rewritten as follows for a 3D condition:

$$Q / k_h = Ai \tag{4.15}$$

where A (m^2) is the cross-section perpendicular to the flow line, which was expressed by Dupuit (1863) as follows:

$$A = L_d \left(h_1 + h_2 \right) / 2 \tag{4.16}$$

while i is the mean hydraulic gradient, given as follows by Dupuit (1863):

$$i = \left(h_1 - h_2 \right) / L \tag{4.17}$$

From the decomposition of Eq. (4.9), one can see that all the flow lines were assumed parallel to the horizontal base, as explicitly explained in the Dupuit (1863) model. The flow path lengths can then be calculated by Eq. (4.2), which assumes that the flow paths have the same length from the base to the top. This assumption can be realistic when the upstream hydraulic head h_1 is low or when the upstream (h_1) and downstream (h_2) hydraulic heads are close to each other or when the length is much larger than h_1 and h_2. This partly explains the good agreement between numerical and analytical results in Fig. 4.5 for any h_2 in the case of h_1 = 15 m or only for h_2 close to h_1 in the cases of h_1 larger than 15 m. When the h_1 value is much higher than the h_2 value, the seepage lines above the elevation of h_2 become inclined and curved. These flow lines significantly differ from those assumed to be nearly horizontal seepage lines in the 2D solution. An application of Eq. (4.2) would underestimate the flow path L used in Eq. (4.17), and then overestimate the hydraulic gradient and flowrate. This is why there is a poor agreement between numerical and analytical results (Fig. 4.5) for the cases of h_1 equal to or larger than 18 m when the values of h_2 are very different than those of h_1. In order to remedy this problem, Eq. (4.2) is modified as follows:

$$L = L_{BB} - h_1 / \tan \alpha_1 - C_L h_2 / \tan \alpha_2 \tag{4.18}$$

where C_L is a calibration coefficient, used to account for the real flow line lengths.

While the previous clarification can explain the overestimation of flowrate using the Dupuit (1863) model, it fails to explain the good agreement between the numerical and analytical solutions for any values of h_1 as long as the downstream hydraulic head is nil (i.e. h_2 = 0) or close to the value

of the upstream hydraulic head (i.e. $h_2 \approx h_1$). In addition, it fails to explain the increase of Q/k_h as h_2 increases from 0 to a critical height where the Q/k_h ratio reaches a peak value, because the numerical results of FLAC3D (Fig. 4.5) clearly indicate a monotonous decrease of the Q/k_h ratio as h_2 increases from 0 until to the value of h_2 in all cases (e.g., h_2 = 15, 18.5, or 20 m) with any values of h_1. More explanation is necessary.

Eq. (4.16) was used in the Dupuit (1863) model to calculate the mean cross-section area for seepage. It implicitly assumes a horizontal flow passing through a cuboid everywhere from the upstream to the downstream with a flow velocity uniformly distributed from the bottom to top surface of an equivalent seepage zone. When the downstream hydraulic head h_2 is equal or close to 0, the flow takes place everywhere from upstream to downstream and from the bottom to the top surface of the seepage zone. The good agreement between the numerical and analytical results tends to indicate that the assumptions of the Dupuit (1863) model for this condition are quite reasonable. When the value of the downstream hydraulic head h_2 is equal or quite close to the value of upstream hydraulic head h_1, the seepage zone would become rectangular from upstream to downstream of the dike. The assumptions of the Dupuit (1863) model are also quite close to reality. This explains why the application of Eq. (4.16) can yield good agreement between the numerical and analytical results (Fig. 4.5) for any values of h_1 as long as h_2 is close to h_1. When h_2 is very different from h_1 and intermediate between the two above extreme cases, is it still reasonable to assume that the arithmetic mean of Eq. (4.16) is still good to assess the mean cross-section area for all seepage everywhere?

$$A = L_d \left(h_1 + C_A h_2 \right) / 2 \tag{4.19}$$

where C_A is a calibration coefficient used to better represent the true mean cross-section area of flow due to the immobile water table at the downstream side of the dike. Introducing Eqs. (4.17)–(4.19) to Eq. (4.15) results in a modified and generalized 3D solution of Dupuit (1863):

$$Q = k_{\mathrm{h}} \frac{\left(h_1 + C_{\mathrm{A}} h_2\right)\left(h_1 - h_2\right)}{2\left(L_{\mathrm{BB}} - h_1 / \tan\alpha_1 - C_{\mathrm{L}} h_2 / \tan\alpha_2\right)} \times L_{\mathrm{d}} \tag{4.20}$$

with $1 \geq C_{\mathrm{L}} \geq 0$ and $1 \geq C_{\mathrm{A}} \geq 0$. Eq. (4.20) constitutes the proposed solution for estimating the flowrate through a 3D trapezoidal rockfill dike. It reduces to the original solution [Eq. (4.1)] of Dupuit (1863) for the case of 2D or the 3D solution [Eq. (4.9)] of Dupuit (1863) when $C_{\mathrm{A}} = 1$ and $C_{\mathrm{L}} = 1$. The validity of the proposed solution [Eq. (4.20)] was tested against numerical results.

Table 4.3 shows a program of numerical simulations performed with FLAC3D. Part of the numerical results of Case 0 is used for calibration to obtain the values of C_{L} and C_{A} while the remaining numerical result of Case 0 along with the numerical results of Cases 1 to 4 are used to test the validity of the calibrated solution [i.e. Eq. (4.20) with the calibrated C_{L} and C_{A}].

Table 4.3 Program of numerical simulations with FLAC3D for calibrating and validating the proposed solution Eq. (4.20); other parameters: $\rho_{\mathrm{f}} = 1000$ kg/m^3, $g = 10$ m/s^2, $n = 0.3$, $k = 6.67 \times 10^{-10}$ m^2(Pa/s), $K_{\mathrm{f}} = 3$ kPa, and $L_z = 1$ m

Case	Figure number	k_{h} (m/s)	L_{d} (m)	α_1 (°)	α_2 (°)	L_{BT} (m)	L_{BB} (m)	H_{d} (m)
0	6	6.67×10^{-6}	1	21.8	26.6	10	100	20
1	7*a*	Var	1	21.8	26.6	10	100	20
2	7*b*	6.67×10^{-6}	Var	21.8	26.6	10	100	20
3	7*c*	6.67×10^{-6}	1	Var	26.6	10	100	20
4	7*d*	6.67×10^{-6}	1	21.8	Var	10	100	20

Note: Var, variation.

Fig. 4.6 plots the ratio Q/k_{h} versus h_2 for different upstream hydraulic heads h_1, obtained by numerical modeling with FLAC3D (Case 0, Table 4.3). The results calculated with the proposed analytical solution [Eq. (4.20)] using $C_{\mathrm{L}} = 0.8$ and $C_{\mathrm{A}} = 0.6$ are plotted also in Fig. 4.6. The two calibration coefficients $C_{\mathrm{L}} = 0.8$ and $C_{\mathrm{A}} = 0.6$ were obtained by fitting the numerical results to the proposed solution for the case of $h_1 = 20$ m only. For the cases of h_1 equal to 15 and 18.5 m, the

agreements between the numerical results and those predicted by applying the proposed and calibrated analytical solution [Eq. (4.20) with C_L = 0.8 and C_A = 0.6] are still excellent. Eq. (4.20) along with C_L = 0.8 and C_A = 0.6 constitutes the proposed and calibrated analytical solution.

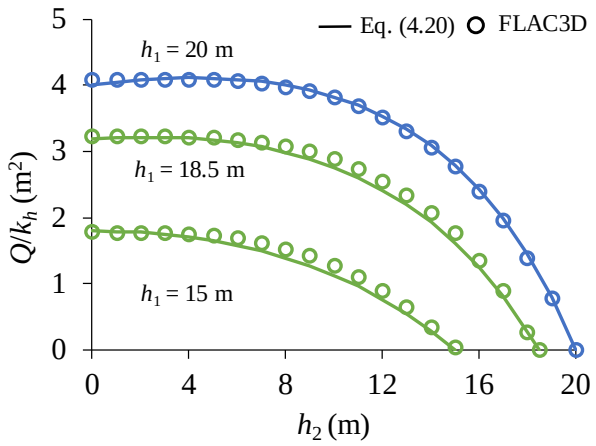

Figure 4.6 Variation of the ratio Q/k_h as a function of h_2 for different upstream hydraulic heads h_1, obtained by numerical modeling with FLAC3D (see more details given in Table 4.3, Case 0) and calculated with the proposed solution [Eq. (4.20) with C_L = 0.8 and C_A = 0.6]; the blue line is the results of calibration while the two green lines are the results of prediction.

To test the accuracy of the proposed calibrated analytical solution [Eq. (4.20) with C_L = 0.8 and C_A = 0.6], the numerical results of Cases 1 to 4 with FLAC3D were then compared with the results predicted by the proposed calibrated analytical solution. Fig. 4.7 show the variation of ratio Q/k_h as a function of tail hydraulic head h_2 for different values of hydraulic conductivity k_h (Fig. 4.7a), dike widths L_d (Fig. 4.7b), upstream slope angles α_1 (Fig. 4.7c) and downstream slope angles α_2 (Fig. 4.7d), obtained by numerical modeling with FLAC3D and predicted with the proposed calibrated analytical solution [Eq. (4.20) with C_L = 0.8 and C_A = 0.6]. The good agreement between the numerical results and the predictions with the proposed calibrated solution indicate that the latter [Eq. (4.20) with C_L = 0.8 and C_A = 0.6] can be used to describe and predict the seepage rate under different steady-state flow conditions through trapezoidal dikes.

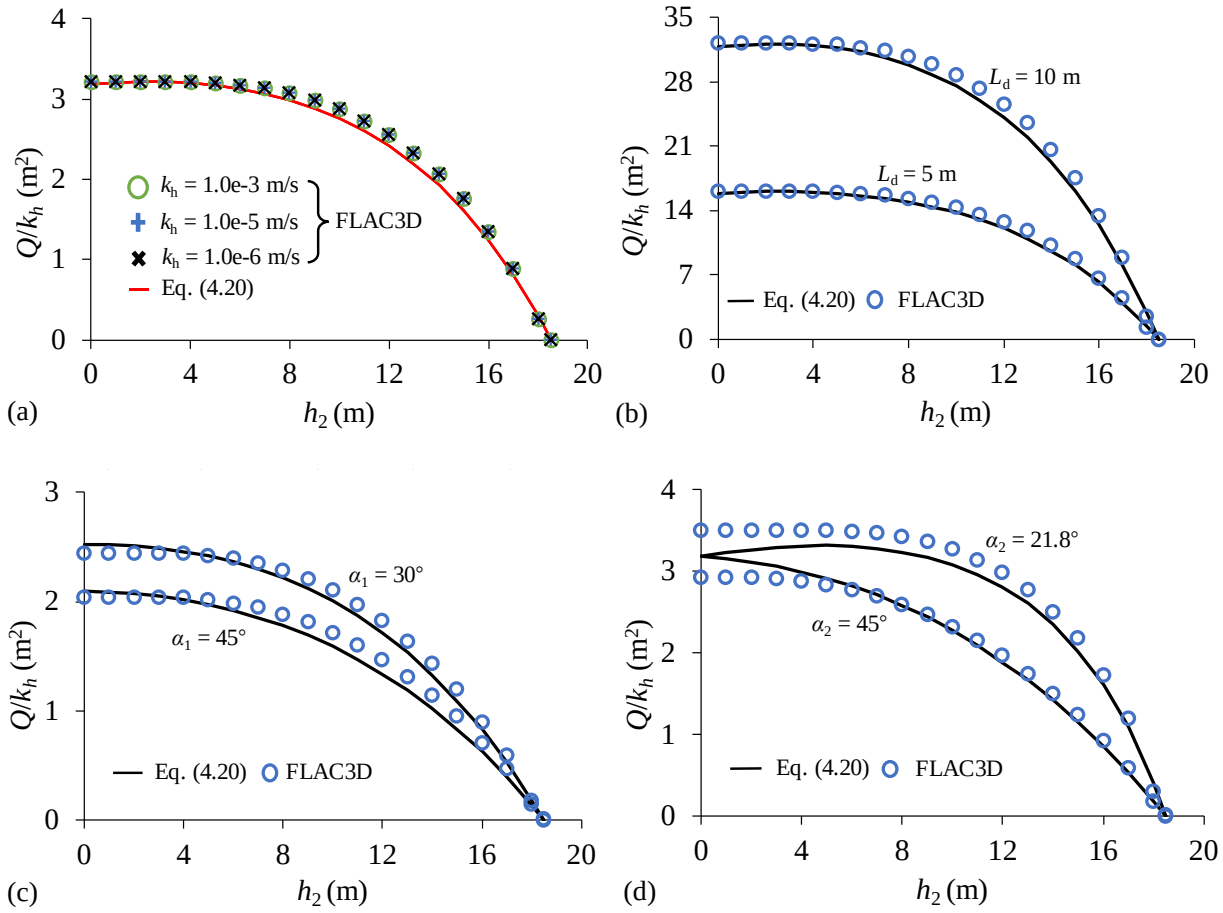

Figure 4.7 Variation of the ratio Q/k_h as a function of h_2, obtained by numerical modeling with FLAC3D and predicted by the proposed and calibrated analytical solutions [Eq. (4.20) with C_L = 0.8 and C_A = 0.6] for different parameters: (a) hydraulic conductivity k_h (Case 1 in Table 4.3); (b) dike width L_d (Case 2 in Table 4.3); (c) upstream slope angle α_1 (Case 3 in Table 4.3); (d) downstream slope angle α_2 (Case 4 in Table 4.3).

4.4 Validation of the numerical model and proposed solution by experimental results

In the previous section, an analytical solution was proposed and fitted to numerical modeling results with two calibration coefficients C_L = 0.8 and C_A = 0.6 (Fig. 4.6). The capacity of the

proposed calibrated analytical solution was further validated by additional numerical results (Fig. 4.7). To further verify the validity of the numerical model and the proposed calibrated analytical solution [Eq. (4.20) with C_L = 0.8 and C_A = 0.6] against physical reality, a reduced-scale test was performed in controlled laboratory conditions with a dike built with waste rock.

Fig. 4.8 shows a photo of the physical model, which was built in a glass box 0.6 m high, 0.053 m large, and 1.2 m long. The dike was constructed by naturally pouring waste rock at its central location to a height of 0.3 m. The resulting base length was 0.8 m while the angles of the upstream and downstream slopes were about 37° (i.e. α_1 = α_2 = 37°). Fig. 4.9 shows the particle size distribution of the waste rock. The particle sizes range from 0 to 9.51 mm, with 50% smaller than 4 mm.

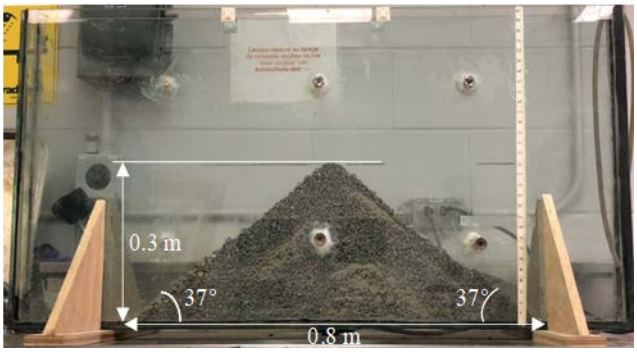

Figure 4.8 A physical model of a dike constructed by waste rocks.

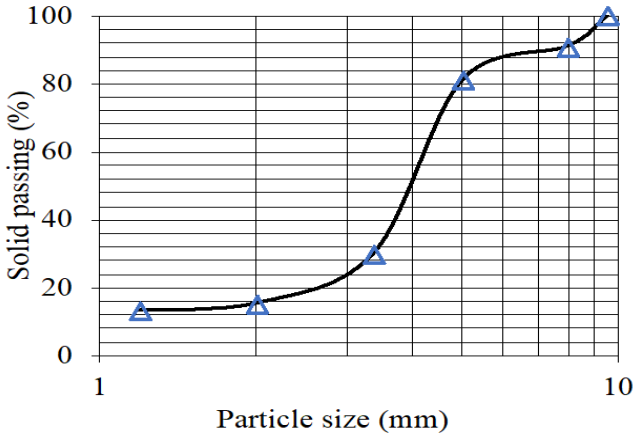

Figure 4.9 The particle size distribution of the waste rock used to build the dike.

After completion of the dike, the water seeped from right to left (Fig. 4.8), with reservoirs controlling the upstream and downstream constant hydraulic heads, h_1 and h_2. After reaching steady state, the value of the total flow rate was recorded. Experiments were done with h_2 values of 0.025, 0.03, 0.031, and 0.035 m, and h_1 values of 0.12, 0.18, 0.22, and 0.25 m, respectively. A stopwatch and a graduated cylinder were used to determine the flow rate. Each measured flow rate was obtained by averaging 10 test measurements.

Fig. 4.10 shows a numerical model of the laboratory test, built with FLAC3D after considering L_{BT} = 0 m, L_{BB} = 0.8 m, H_d = 0.3 m, L_d = 0.053 m, and $\alpha_1 = \alpha_2 = 37°$ (see Fig. 4.10). The application of the proposed calibrated analytical solution [Eq. (4.20) with C_L = 0.8 and C_A = 0.6] to the measured seepage rate of $Q = 1.61 \times 10^{-4}$ m^3/s leads to a hydraulic conductivity of $k_h = 4.39 \times 10^{-2}$ m/s. The dike material was assumed to have a porosity of n = 0.3.

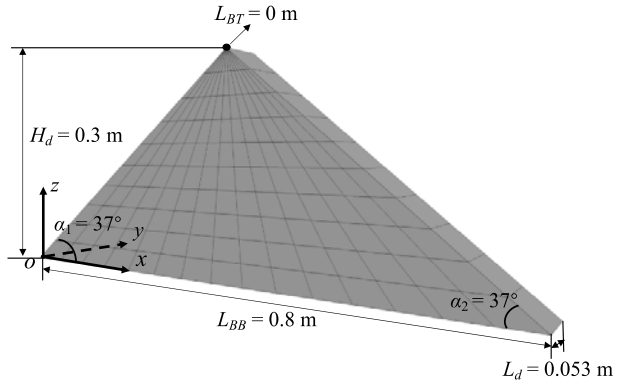

Figure 4.10 A numerical model of the dike flow test built with FLAC3D.

The hydraulic boundary conditions along the upstream and downstream slope faces were defined by a hydrostatic water pressure (linear distribution) up to h_1 and h_2, respectively, zero pore pressure along the downstream slope face above the water table, and no-flow conditions along the base of the dike. Sensitivity analyses of the mesh indicate that stable numerical results can be obtained

with the largest elements of 0.05 m × 0.05 m × 0.03 m at the bottom of the dike with a water bulk modulus K_f = 90 Pa (calculation made with ρ_f = 1000 kg/m^3, g = 10 m/s^2, and L_z = 0.03 m).

Fig. 4.11 illustrates the saturation zones in steady-state conditions as observed in the physical model tests when the upstream hydraulic head h_1 = 0.06 m (Fig. 4.11a), h_1 = 0.13 m (Fig. 4.11b), and h_1 = 0.25 m (Fig. 4.11c), respectively. The water flow trends obtained by numerical modeling with FLAC3D for the cases of h_1 = 0.06, 0.13, and 0.25 m are presented on the right side of Fig. 4.11. It appears that the seepage conditions obtained numerically with FLAC3D match those observed in the reduced-scale tests. In addition, it is interesting to note that even the unsaturated zone observed at the top of the dike is well captured by the numerical modeling with FLAC3D, as shown in Fig. 4.11c. These results indicate that FLAC3D can reproduce the experimental results, at least qualitatively.

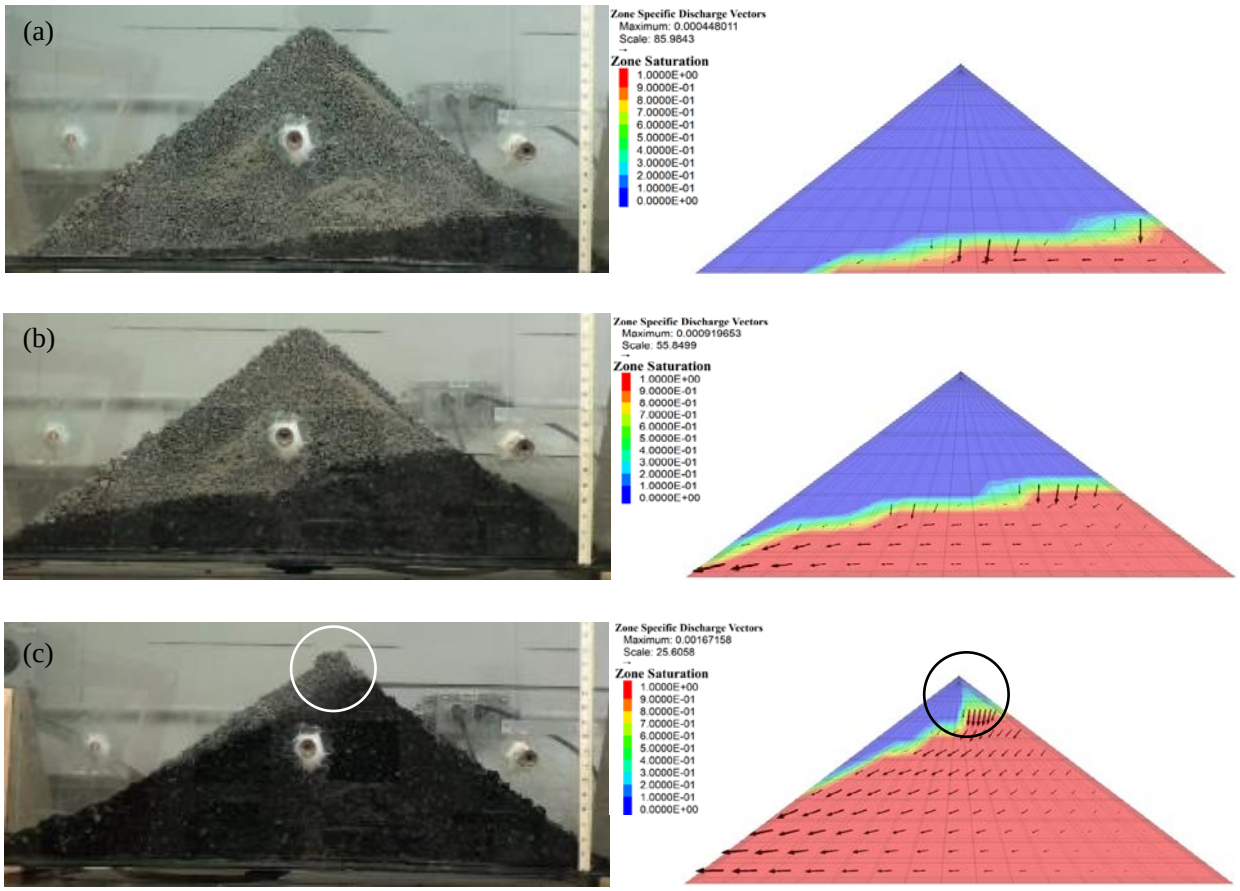

Figure 4.11 Variation of the water flow trends, obtained by the laboratory tests and numerical simulations with the different upstream hydraulic heads: (a) h_1 = 0.06 m; (b) h_1 = 0.13 m; (c) h_1 = 0.25 m. The iso-contours of FLAC3D are the degree of saturation. For example, the red color with 1.0E+00 indicates a degree of saturation of 100% while 5.0E-01 means a degree of saturation of 50%.

To further test the ability of the numerical model and the proposed calibrated analytical solution [Eq. (4.20) with C_L = 0.8 and C_A = 0.6], the total seepage rates through the trapezoidal dike at different upstream hydraulic heads h_1 (e.g., 0.12, 0.18, 0.22, and 0.25 m) were analyzed. Fig. 4.12 shows the variations of the ratio Q/k_h as a function of L_d $(h_1 - h_2)(h_1 + C_A h_2)/(2L_m)$ (where $L_m = L_{BB} - h_1/\tan\alpha_1 - C_L h_2/\tan\alpha_2$), obtained by the laboratory tests, numerical modeling with FLAC3D,

and application of the proposed calibrated analytical solution. All results (experimental, numerical, and analytical) agree, which confirms the capacities of the numerical and analytical solutions. The proposed calibrated analytical solution [Eq. (4.20) with C_L = 0.8 and C_A = 0.6] can thus be used to estimate the total seepage rate Q through a trapezoidal 3D dike resting on a horizontal impervious base under steady-state flow conditions, especially in the preliminary design stage of a project.

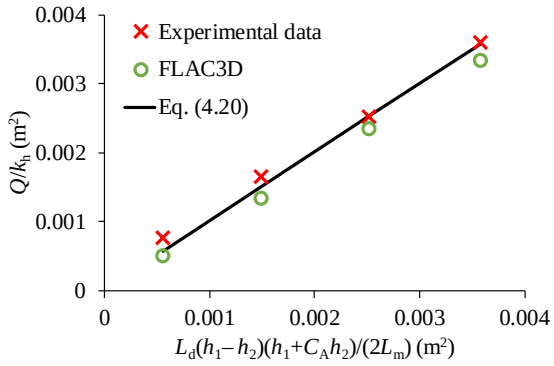

Figure 4.12 Variation of the ratio Q/k_h as a function of $L_d(h_1 - h_2)(h_1 + C_Ah_2)/(2L_m)$, obtained by the proposed calibrated solution [Eq. (4.20) with C_L = 0.8 and C_A = 0.6], numerical simulations, and laboratory tests.

4.5 Discussion

Analytical solutions are very popular and useful tools for a practitioner as they enable quick calculations and parameter sensitivity analysis. Most often, however, analytical solutions are only possible for very simple cases or simplified assumptions. Their application is thus useful in the preliminary design stage of a project. Numerical modeling is necessary for dikes with irregular shapes or those built with different materials (e.g., with a barrier core) or when the dike materials are heterogeneous or/and anisotropic.

In this study, a 3D generalized closed-form solution was proposed to estimate the total flow rate through a 3D trapezoidal dike or WRB under steady-state conditions. The proposed solution contains two calibration coefficients that were obtained as C_L = 0.8 and C_A = 0.6 by fitting

numerical results. The validity of the proposed calibrated analytical solution was confirmed by additional numerical and experimental results. The proposed calibrated analytical solution [Eq. (4.20) with C_L = 0.8 and C_A = 0.6] can thus be used to estimate the total seepage rate through a trapezoidal dike under steady-state flow conditions, at least for the preliminary design stage of a project. However, it should be noted that the validity and predictability of the proposed calibrated solution [Eq. (4.20) with C_L = 0.8 and C_A = 0.6] were tested only against a limited number of numerical and experimental results. More numerical and experimental results can be necessary to fully test the validity and predictability of the proposed calibrated solution. In addition, it should be kept in mind that the proposed analytical solution and the numerical models have a few limitations.

For instance, the dike material was considered as homogenous and isotropic in the analytical and numerical models of this study. In practice, the rockfill can be heterogeneous and/or anisotropic due to different sources of material, non-homogenous compactness or inappropriate construction. In this case, the application of the proposed solution with a unique value of hydraulic conductivity obtained by measurements on a small portion of well-controlled material may lead to significant error. Efforts are necessary to obtain more accurate and more representative hydraulic properties of field materials. After then, more work is necessary to take into account the heterogeneity and/or anisotropy in the analytical and numerical models.

In this study, the internal transition between saturated and unsaturated zones is considered in FLAC3D based on a simple law between fluid mobility and saturation (Itasca 2017), while hydraulic conductivity as a function of suction was not considered. The pores above the phreatic surface were assumed to be filled with air. The pore pressures above the phreatic surface were thus ignored. This assumption can only be roughly applicable for very large pore materials such as rockfill and waste rocks, which allows capillary moisture and seepage to be neglected. This has been partly verified by the flow pattern shown in Fig. 4.11 and the comparisons shown in Fig. 4.12. When the dikes were made of fine particle materials like sand, sandy silt, silt, and clayey silt, which

exhibit high suction under unsaturated state, Chapuis and Aubertin (2001) have shown through numerical modeling that neglecting unsaturated seepage can underestimate the flowrate by 10 to 20%. More work is needed to account for an unsaturated zone for materials ranging from coarse particles (present paper) to fine-particle dikes.

It is well-known that water flows faster in the middle of a channel than near the walls. The velocity of flow decreases from the center to the banks of the channel. Along the side walls, the flow velocity reduces to zero. It can thus be expected that the seepage rate is overestimated by numerical modeling and the proposed analytical solution. More work is needed to take this aspect into account in the future.

During the laboratory tests, fine particles moved away from the inside of the waste rock. This indicated internal erosion. Thus, the material porosity and hydraulic conductivity may have changed during the tests. More work is needed to analyze the changes in physical and hydraulic properties with the loss of fine particles during internal erosion.

To reduce the calculation time to reach a steady flow condition, the water bulk modulus K_f was defined as 3 kPa for the large dike case and as 90 Pa for the simulation of experimental test, based on Eq. (4.14). As a comparison, a larger value of K_f (e.g., 1000 kPa) was used to compute the total discharge rate and the same result was obtained with a longer calculation time (e.g., 11 sec with K_f = 90 Pa and ≈ 2 hr with K_f = 1 MPa).

4.6 Conclusion

In this article, existing 2D solutions for estimating the total seepage rate under steady-state conditions were presented and generalized to 3D trapezoidal dikes. A 3D solution based on Dupuit theory was proposed to estimate the seepage rate through a 3D trapezoidal dike or WRB as a function of the dike geometry and saturated hydraulic conductivity. The proposed solution was calibrated by a numerical modeling with FLAC3D. The proposed and calibrated analytical solution was then validated by additional numerical modeling results. Both the numerical and analytical

solutions were further validated by experimental results obtained by seepage tests performed in laboratory. The proposed and calibrated analytical solution can thus be used to estimate the total seepage rate through a 3D trapezoidal dike resting on a horizontal impervious base under steady-state conditions. The equation provides a rapid way for predicting the flow rate when used with due regard for its limitations. It is necessary to do all of the necessary tests to ensure the accuracy of this equation for a specific project.

Acknowledgments: The authors acknowledge the financial support from the Natural Sciences and Engineering Research Council of Canada (NSERC 402318), Fonds de Recherche du Québec - Nature et Technologies (FRQNT 2015-MI-191676), and the partners of the Research Institute on Mines and Environment (RIME UQAT - Polytechnique; http://rime-irme.ca). The anonymous reviewers are gratefully acknowledged for their critical questions and constructive comments, which helped the authors significantly improve the quality of the paper.

4.7 References

Aubertin M, Mbonimpa, M, Bussière B, Chapuis RP (2003) A model to predict the water retention curve from basic geotechnical properties. Can Geotech J 40(6): 1104-1122, https://doi.org/10.1139/t03-054

Bowles JE (1984) Physical and geotechnical properties of soils. 2nd edit, McGraw-Hill, NYC

Casagrande L (1932) Naeherungsmethoden zur Bestimmung von Art und Menge der Sickerung durch geschuettete Dämme (Approximate methods to determine the seepage through spillway dikes). Institute of Technology, Vienna [in German]

Chapuis RP (1990) Sand–bentonite liners: field control methods. Can Geotech J 27: 216–223, doi.org/10.1139/T10-035

Chapuis RP (2011) Steady state groundwater seepage in sloping unconfined aquifers. Bull Eng Geol Environ 70: 89-99, doi.org/10.1007/s10064-010-0282-2

Chapuis RP, Aubertin M (2001) A simplified method to estimate saturated and unsaturated seepage through dikes under steady-state conditions. Can Geotech J 38(6):1321–1328, https://doi.org/10.1139/t01-068

Chapuis RP, Chenaf D, Bussière B, Aubertin M, Crespo R (2001) A user's approach to assess numerical codes for saturated and unsaturated seepage conditions. Can Geotech J 38(5): 1113-1126, doi.org/10.1139/t01-055

Chen Q, Zhang LM (2006) Three-dimensional analysis of water infiltration into the Gouhou rockfill dam using saturated unsaturated seepage theory. Can Geotech J 43(5): 449-461, doi.org/10.1139/t06-011

Crespo R (1994) Modélisation des écoulements à travers les ouvrages de retenue et de confinement des résidus miniers par un logiciel d'éléments finis. MScA thesis, École Polytechnique de Montréal, Montréal

Darcy H (1856) Les fontaines publiques de la ville de Dijon. Dalmont, Paris

Dupuit J (1863) Études théoriques et pratiques sur le mouvement des eaux dans les canaux découverts et à travers les terrains perméables. 2nd edit, Dunod, Paris

Harr ME (1962) Groundwater and Seepage. McGraw-Hill, NYC

Itasca Consulting Group, Inc (2017) FLAC3D—Fast Lagrangian Analysis of Continua in Three-Dimensions, Ver. 6.0. Minneapolis

Iterson FKTV (1917) Eenige theoretische beschouwingen over kwel, De Ingenieur

Li L (2013) A simple solution to assess pore-water pressure in barricades made of waste rock. CIM J 4(1): 53–60

Li L, Aubertin M (2011) Limit equilibrium analysis for the design of backfilled stope barricades made of waste rock. Can Geotech J 48(11): 1713-1728, doi.org/10.1139/t11-063

Li L, Ouellet S, Aubertin M (2009) A method to evaluate the size of backfilled stope barricades made of waste rock. Proc, 62nd Canadian Geotechnical Conf and 10th Joint CGS/IAH-CNC Groundwater Specialty Conf, Canadian Geotechnical Soc, Richmond, BC, Canada, pp 497–503

Pavlovsky NN (1931) Seepage through earth dikes. Instit. Gidrotekhniki i Melioratsii, Leningrad

Richards, KS, Reddy, KR (2007) Critical appraisal of piping phenomena in earth dams. Bull Eng Geol Environ 66(4): 381-402, doi.org/10.1007/s10064-007-0095-0

Schaffernak F (1917) Über die Standicherheit durchlaessiger geschuetteter Dämme, Allge, Eauzeitung

Yang PY, Brochu-Baekelmans M, Li L, Aubertin M (2014) An improved solution for sizing barricades made of waste rock to retain cemented paste backfill. Proc, 67th Canadian Geotech Conf, Regina, Canada

Yang PY, Li L, Aubertin M, Brochu-Baekelmans M, Ouellet S (2017) Stability analyses of waste rock barricades designed to retain paste backfill. Int J Geomech 17(3): 04016079, doi.org/10.1061/(ASCE)GM.1943-5622.0000740

CHAPTER 5 ARTICLE 2: ANALYTICAL SOLUTIONS FOR THE DESIGN OF SHOTCRETED WASTE ROCK BARRICADES TO RETAIN SLURRIED PASTE BACKFILL

Yulong Zhai, Pengyu Yang, and Li Li

This article has been published online in Construction and Building Materials on 9 October 2021

Abstract: Over the past decades, filling underground mined-out openings (stopes) with slurried backfills has witnessed a significant growth in the mining industry. To do so, retaining structures frequently called barricades should be built in access drifts near draw points to keep the slurried filling materials in place. Barricades made of waste rock (often produced from underground development) are constructed in a more convenient and sustainable manner at lower cost, compared to traditional barricades made of high-strength man-made materials. In recent years, a few analytical solutions have been developed for sizing waste rock barricades (WRB) based on limit-equilibrium analysis. These solutions correspond to such cases when there are no reinforcements made to WRBs except for compaction. A full cover of the entire surface of downstream slope may result in poor drainage and built-up of high pore water pressures behind WRB. Shotcrete is thus usually sprayed over one third of the upper part. More commonly, when constructing a WRB, shotcrete is sprayed on the downstream slope over the upper part (about one third) of a barricade to promote its stability as a whole and to prevent local failures at the barricade top, especially for a WRB with limited top length. To take this aspect into account, new analytical solutions are proposed here to design the integrated backfill barricade built with waste rock and shotcrete. The proposed solutions can be used to estimate the dimensions of shotcreted WRB and strength of shotcrete. An instability criterion, based on the first occurrence among displacement jump of the barricade top or coalescence of currently yield zones, is introduced to help judge the onset of instability of a shotcreted WRB structure. The validity and predictivity of the proposed analytical

solutions were calibrated and verified using numerical simulations. Sample calculations are also conducted to illustrate the shotcreted WRB design (i.e., required cohesion and top length) by considering global and local stability. The proposed solutions correlate well with numerical simulations for representative stope height, barricade and shotcrete geometries and properties of waste rocks and shotcrete. The proposed solutions can thus be used to evaluate the required cohesion c_s and top length L_{SL} of shotcrete, based on the global and local stability analysis. The proposed solution can also be used to estimate the size of WRB when the parameters of shotcrete are known.

Keywords: Waste rock barricades; Shotcrete; Instability criterion; Analytical solutions; FLAC3D

5.1 Introduction

Backfilling underground mined-out openings (termed as stopes) with tailings or waste rock considerably reduces the amount of mine wastes on the ground surface. Various geotechnical and environmental risks associated with the surface disposal of mine wastes can thus be mitigated. Stope backfilling also helps improve ground stability, ore recovery and the efficiency of ventilation in underground operations (Aubertin et al. 2002; Hassani and Archibald 1998; Hambley 2005; Potvin et al. 2005; Xu and Cao 2019).

In recent decades, stope filling with slurried backfills, particularly cemented paste backfill (CPB), has become a common practice in many underground mines around the world. To retain the flowable filling materials in stopes, retaining structures, called barricades (or bulkheads), needs to be constructed in access drifts near drawpoints of mine stopes (Grice 1998; Hassani and Archibald 1998; Potvin et al. 2005; Revell and Sainsbury 2007; Yumlu and Guresci 2007). Over years, a number of reported barricade failures were seen to result in serious unfavorable situations such as flooding of drifts and working spaces, economic loss, personal injury and sometimes even life loss (Grice 1998, 1989, 2001; Soderberg and Busch 1985; Sivakugan et al. 2006a, 2006b; Bloss and Chen 1998; Helinski et al. 2006, 2011; Revell and Sainsbury 2007; Yumlu and Guresci 2007).

These documented barricade failures highlight the importance and challenges associated with barricade design, which in turn emphasize the need of reliable and economic design tools.

Barricades of high strength are traditionally built with man-made materials such as bricks, concrete blocks or shotcrete with or without reinforcements (Grabinsky 2010; Hughes et al. 2010; Lu et al. 2020; Nujaim et al. 2020; Sivakugan et al. 2006, 2008; Potvin 2005; Quezada et al. 2016; Yumlu and Guresci 2007; Zhao et al. 2020). In general, constructing such barricades are relatively expensive and time consuming. It is also quite difficult to dismantle such barricades prior to the recovery of adjacent stopes. In some underground mines, especially in Canada and Australia, a more and more popular practice is to construct barricades with waste rock. When compared to traditional barricades, waste rock barricades (WRB) are built in a more convenient and sustainable manner at lower cost. This is particularly true when waste rock is produced during underground operations, leading to more environment and economic benefits.

Basically, design methods for traditional barricades originate from the flexural failure mechanism of a concrete slab (Beer 1986; Duffield et al. 2003; Revell and Sainsbury 2007). However, such methods are not applicable to WRBs due to their more complex configurations and different failure modes. Over the last decade, a few attempts have been made to analyze the stability of a WRB and determine its dimensions based on limit-equilibrium analysis. Li and coworkers proposed analytical solutions for sizing a rectangular WRB by considering fully drained and submerged conditions (Li et al. 2009; Li and Aubertin 2011). On the basis of these works, Yang et al. (2014, 2017a) analyzed the global and local stability of a more realistic trapezoidal WRB. These solutions for sizing WRBs correspond to such situations when there are no reinforcements applied to WRBs except for mechanical compaction.

More commonly, when constructing a WRB, shotcrete is sprayed over the upper portion of a barricade from its downstream side to provide more resistances. This is particularly the case when long WRBs are not allowed due to limited drift space or production needs. Laboratory tests conducted by Nujaim et al. (Nujaim et al. 2018; 2020a; 2020b) indicated that ingression of paste

backfill at the top of a WRB can jeopardize its stability, confirming the need of shotcrete to support the upper portion (about one third of the barricade height). The applied shotcrete tends to reinforce the WRB and reduce the risks of local failure. Applying shotcrete on the upper portion of a WRB can also prevent the leakage of backfill through the gap between the roof and barricade top (Nujaim et al. 2020a). Apparently, high-strength shotcrete applied on a WRB tends to improve barricade stability. It can be expected that applying shotcrete would lead to significant stress transfer/redistribution within the integrated barricade body upon backfilling, thereby altering the mechanical responses and failure mechanisms of a WRB. Without considering these aspects, the existing solutions for sizing WRBs would lead to overly conservative barricade design which are impractical or even against the field conditions. Therefore, existing solutions for sizing WRBs are inappropriate for evaluating the integrated barricade system consisting of waste rock and shotcrete. It is thus deemed quite necessary to develop design approaches for shotcrete-reinforced waste rock barricades.

In the following, the theoretical development of the shotcreted WRB is first presented considering the global and local stability. Analytical solutions are then developed for estimating the minimum required dimension (top length) and the required strength (cohesion) of shotcrete applied on WRB. The proposed solutions are calibrated and validated by numerical simulations. Major assumptions and limitations are also discussed in this paper.

5.2 Stability analysis of a shotcreted WRB

Fig. 5.1 schematically shows that a trapezoidal shotcreted WRB is built in the access drift to retain slurried backfills poured into a mine stope. As illustrated in Fig. 5.1, the stope is filled to a height H. H_d and L_d are respectively the height and width of the drift as well as the barricade. L_{BT} represents the top length of a WRB while L_{BB} depicts its bottom length. α_1 and α_2 are respectively the upstream slope angle and downstream slope angle of a WRB; the former is close to the repose angle of waste rock and the latter could be increased by compaction. The repose angle of waste rock typically

varies from 34° to 40°, with a typical value of 37° (Aubertin 2013; Potvin et al. 2005). α_3 is the downstream slope angle of shotcrete. L_{SL} is the top length of the shotcrete while L_{ST} (m) is the length of the shotcrete projected on the roof of the drift. H_s is the height of shotcrete.

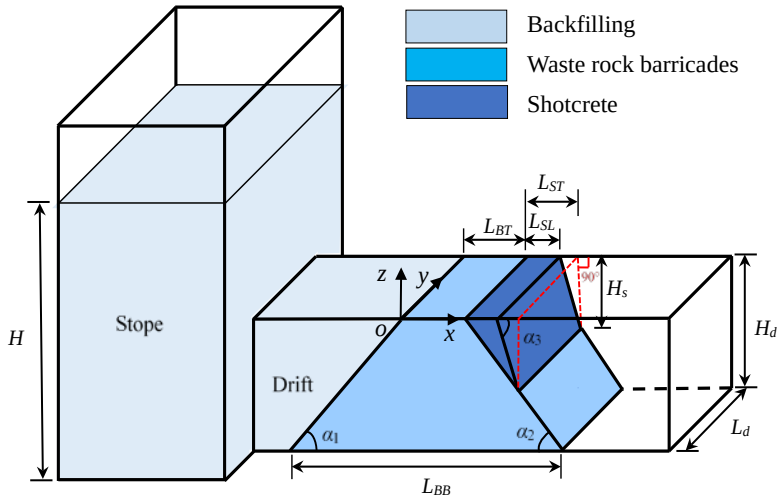

Figure 5.1 Schematic view of a backfilled mine stope with an access drift and a trapezoidal WRB reinforced by shotcrete (adapted from Li and Aubertin 2011).

Previous investigations have indicated that the failure mode of a WRB could translate from global sliding to top (local) sliding, depending on the nature of rock roughness and other field conditions (Yang et al. 2017a). In the following subsections, the global and local stability of a shotcreted WRB are theoretically analyzed based on limit-equilibrium and several simplifying assumptions.

5.2.1 Global stability of the shotcreted WRB

Fig. 5.2 illustrates various forces acting on the trapezoidal shotcreted WRB that can be decomposed into one quadrangular prism and three triangular prisms (upstream, downstream and shotcrete). On the figure, C_T and S_T are the normal compressive and shear forces at the top of the WRB, respectively. The normal compressive and shear forces mobilized along the bottom of the WRB are denoted by C_B and S_B. C_L and S_L are the normal compressive and shear forces exerted on the

interface between the barricade and the two lateral drift walls, respectively. C_{ST} and S_{ST} represent the normal compressive and shear forces along the top surface of the shotcrete, respectively. The normal compressive and shear forces along the shotcrete-wall interfaces are denoted by C_{LS} and S_{LS}. It is also seen from Fig. 5.2 that P is the force exerted on the barricade by slurried backfills. l represents the horizontal distance from the toe of the upstream slope or downstream slope to the calculation point for the WRB; d denote the vertical distances of calculating points measured from the top of the WRB.

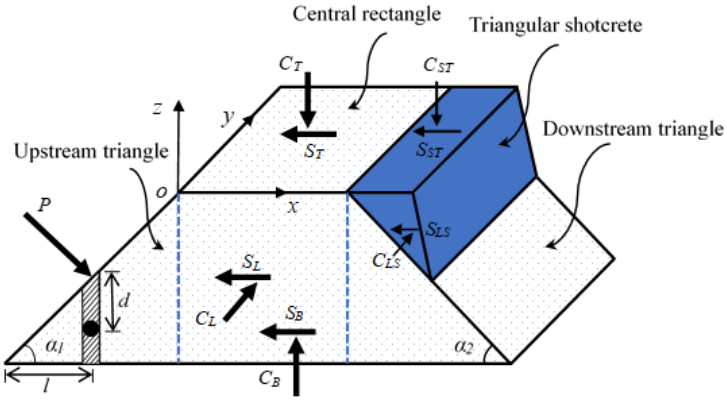

Figure 5.2 Schematic view of a shotcreted WRB with various acting forces for global stability analysis (modified from Yang et al. 2017a).

The following assumptions are considered in the stability analysis of a shotcreted WRB:

- The influence of pore water pressures (PWPs) in the WRB is ignored due to the fact that the permeability of waste rock is much larger (commonly several orders of magnitude) than that of the backfill.
- Vertical arching due to frictional stresses along the barricade-rock walls is neglected due to the limited height of the drifts, as postulated by Li and Aubertin (2011) and Yang et al. (2017a). The density of the shotcrete is neglected because of its self-adhesion to rock walls (e.g., the shotcrete

will keep in place without the support of a WRB). Hence, the vertical force C_B is expressed as

$$C_B = \gamma_{wr} H_d L_d \frac{L_{BT} + L_{BB}}{2} + P\cos\alpha_1 \tag{5.1}$$

where γ_{wr} is the unit weight of waste rock.

- The horizontal stresses σ_h acting on the two lateral walls are only dominated by the overburden pressures of waste rock and shotcrete (without considering the influence of the backfill pressures). It can then be given by

$$\sigma_h = K\gamma_{wr} d \tag{5.2}$$

where K is the earth pressure coefficient. The earth pressure coefficient K of waste rock is defined as the ratio of the horizontal stress perpendicular to the drift axis over the vertical stress.

As voids may be present above the barricade (i.e., C_T = 0), it is reasonable and conservative to ignore the shear strength between the top of the barricade and the drift roof. Only adhesion is considered along the shotcrete-roof interface. The shear force S_{ST} (with the first subscript S indicating shotcrete and the second subscript T standing for top part) acting on the top of the shotcrete can be expressed as

$$S_{ST} = c_i L_{SL} L_d \tag{5.3}$$

where c_i is the adhesion of shotcrete-rock interfaces.

The pushing force P acting on the upstream slope of the shotcreted WRB is calculated as

$$P = \bar{p}\frac{H_d L_d}{\sin\alpha_1} = \frac{1}{2}(p_t + p_b)\frac{H_d L_d}{\sin\alpha_1} \tag{5.4}$$

where $\bar{p} = (p_t + p_b)/2$ represents the averaged backfill pressure; p_t (= $\gamma_b(H - H_d)$) and p_b (= $\gamma_b H$) are the pressures at the top and base of the upstream slope of shotcreted WRB, respectively; γ_b is the unit weight of saturated backfill.

Considering the Mohr-Coulomb criterion, the shear resistance S_B (Fig. 5.2) at the bottom of the

barricade can be obtained by introducing Eqs. (5.1) and (5.4) in the following expression:

$$S_B = C_B \tan\delta = H_d L_d \left[\gamma_{wr} \frac{L_{BT} + L_{BB}}{2} + \frac{(p_t + p_b)}{2\tan\alpha_1} \right] \tan\delta \tag{5.5}$$

where δ is the interface friction angle between the WRB and rock walls.

The lateral compressive C_{LC} and shear S_{LC} forces (with the first subscript L indicating lateral walls and the second subscript C denoting central part) mobilized on two side walls of the central part of the barricade can be estimated as

$$S_{LC} = C_{LC} \tan\delta = \frac{K\gamma_{wr} H_d^2 L_{BT} \tan\delta}{2} \tag{5.6}$$

Likewise, lateral shear resistances acting between the three triangular prisms (S_{LS}, S_{LU} and S_{LD}) and lateral walls are given as follows (with subscripts U, D and S respectively standing for the upstream, downstream and shotcrete triangular prisms):

$$S_{LS} = \frac{H_s L_{SL} c_i}{2} \tag{5.7}$$

$$S_{LU} = C_{LU} \tan\delta = \frac{1}{2} K\gamma_{wr} \tan\delta \int_0^{\frac{H_d}{\tan\alpha_2}} (l\tan\alpha_1)^2 dl = \frac{K\gamma_{wr} H_d^3}{6\tan\alpha_1} \tan\delta \tag{5.8}$$

$$S_{LD} = C_{LD} \tan\delta = \frac{1}{2} K\gamma_{wr} \tan\delta \int_0^{\frac{H_d}{\tan\alpha_2}} (l\tan\alpha_2)^2 dl = \frac{K\gamma_{wr} H_d^3}{6\tan\alpha_2} \tan\delta \tag{5.9}$$

Experimental evidences have indicated that the adhesion c_i along shotcrete-rock interface is only a fraction of shotcrete cohesion c_s (Seymour et al. 2010):

$$c_i = r_i c_s \tag{5.10}$$

where r_i (= c_i/c_s; from 0 to 1) is the cohesion ratio of the shotcrete-rock interfaces; c_s is the cohesion of shotcrete.

Considering the limit equilibrium of the WRB in the drift-axis direction, the factor of safety (FS)

of a WRB against global sliding (S_T = 0 due to C_T = 0) can be given by

$$FS = \left(S_B + S_{ST} + 2S_L + 2S_{LS}\right) / \left(P \sin \alpha_1\right) \tag{5.11}$$

where

$$S_L = S_{LU} + S_{LC} + S_{LD} \tag{5.12}$$

Introducing Eqs. (5.3) – (5.10), (5.12) into Eq. (5.11) leads to the following equation to evaluate the global stability of a shotcreted WRB:

$$FS = \frac{2\gamma_{wr} L_{BT}\left(1 + K\frac{H_d}{L_d}\right)\tan\delta + \gamma_{wr} H_d\left(1 + K\frac{2H_d}{3L_d}\right)\left(\frac{1}{\tan\alpha_1} + \frac{1}{\tan\alpha_2}\right)\tan\delta + 2\frac{L_{SL} c_s r_i}{H_d}\left(1 + \frac{H_s}{L_d}\right) + \left(p_t + p_b\right)\frac{\tan\delta}{\tan\alpha_1}}{p_t + p_b} \tag{5.13}$$

As a special case when the shotcrete thickness L_{SL} = 0, Eq. (5.13) reduces to the global stability analysis solution of Yang et al. (2017a).

5.2.2 Internal local stability of the shotcreted WRB

When applying Eq. (5.13), the *FS* can sometimes become extremely small (or even negative) when the interface friction angle δ increases to a certain limit. Similar findings were reported by Yang et al. (2017a) for their global stability solution for sizing the top length L_{BT} of a WRB without shotcrete. Such solutions may result in unreasonable design that renders the barricade prone to local failures near the top. Therefore, the local stability of the top part of the shotcreted WRB needs to be investigated.

Fig. 5.3 schematically depicts the cross section (along the drift-axis direction) of the shotcreted WRB for analyzing its local stability. To simplify the theoretical development, the unstable upper part (with a height of *h*, m) of the shotcreted WRB is assumed to slide along a horizontal surface as treated by Yang et al. (2017a). The internal friction angles of waste rock ϕ' and shotcrete ϕ_s are viewed as interface friction angle of the potential sliding plane.

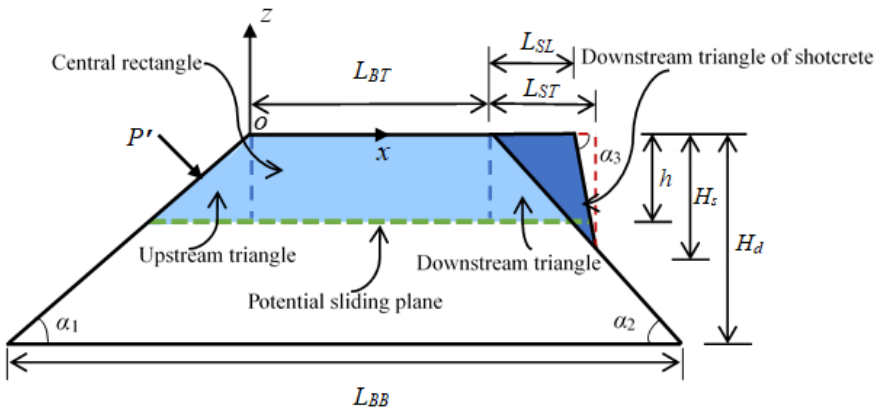

Figure 5.3 Schematic view of a shotcreted WRB for local stability analysis (modified from Yang et al. 2017a).

The pushing force P' (see Fig. 5.3) exerted by backfills on the upstream slope of the unstable upper section can be given by

$$P' = \left(p_t + \gamma_b \frac{h}{2} \right) \frac{hL_d}{\sin \alpha_1} \tag{5.14}$$

Depending on the position of sliding surface, two situations ($0 \le h < H_s$ and $h \ge H_s$) are introduced in the following.

When the potential sliding plane intercepts the shotcrete ($0 \le h < H_s$), the compression C'_B and shear S'_B forces at the base of the unstable upper section can be obtained by

$$S'_B = C'_B \tan \phi' = \left(\gamma_{wr} h L_d L_{BT} + \frac{\gamma_{wr} h^2 L_d}{2 \tan \alpha_1} + \frac{\gamma_{wr} h^2 L_d}{2 \tan \alpha_2} + P' \cos \alpha_1 \right) \tan \phi' \tag{5.15}$$

where ϕ' is the internal friction angle of waste rock.

In the central part of the upper portion, the shear (S'_{LC}) and compressive (C'_{LC}) forces exerted on the two lateral walls is calculated by

$$S'_{LC} = C'_{LC} \tan\delta = \frac{K\gamma_{wr} h^2 L_{BT} \tan\delta}{2} \tag{5.16}$$

The shear force S_{ST} acting on the top of the shotcrete can be expressed as

$$S'_{ST} = c_i L_{SL} L_d \tag{5.17}$$

The lateral shear resistances mobilized along two lateral walls for the three triangular prisms (S'_{LS}, S'_{LU} and S'_{LD}) are given by

$$S'_{LS} = \left(L_{SL} - \frac{h}{2\tan\alpha_2} + \frac{h}{2\tan\alpha_3} \right) h c_i = L_{SL} \left(1 - \frac{h}{2H_s} \right) h c_i \tag{5.18}$$

$$S'_{LU} = C'_{LU} \tan\delta = \frac{1}{2} K\gamma_{wr} \tan\delta \int_0^{\frac{h}{\tan\alpha_2}} h^2 dl = \frac{K\gamma_{wr} h^3}{6\tan\alpha_1} \tan\delta \tag{5.19}$$

$$S'_{LD} = C'_{LD} \tan\delta = \frac{1}{2} K\gamma_{wr} \tan\delta \int_0^{\frac{h}{\tan\alpha_2}} h^2 dl = \frac{K\gamma_{wr} h^3}{6\tan\alpha_2} \tan\delta \tag{5.20}$$

The limit equilibrium of the potentially unstable upper section of the shotcreted WRB along the drift-axis direction for the FS can be expressed as

$$FS = \left(S'_B + S'_{ST} + 2S'_L \right) / \left(P' \sin\alpha_1 \right) \tag{5.21}$$

$$S'_L = S'_{LU} + S'_{LC} + S'_{LD} \tag{5.22}$$

Introducing Eqs. (5.15) – (5.20), (5.22) into Eq. (5.21), the following equation is obtained to evaluate the local stability of the shotcreted WRB:

$$FS = \frac{\gamma_{wr} L_{BT} \left(\tan\phi' + \frac{Kh\tan\delta}{L_d} \right) + \gamma_{wr} h \left(\frac{1}{2}\tan\phi' + \frac{1}{3}\frac{Kh\tan\delta}{L_d} \right) \left(\frac{1}{\tan\alpha_1} + \frac{1}{\tan\alpha_2} \right) + L_{SL} c_s r_i \left(\frac{2}{L_d} + \frac{1}{h} - \frac{h}{H_s L_d} \right) + \left(p_t + \gamma_b \frac{h}{2} \right) \frac{\tan\phi'}{\tan\alpha_1}}{p_t + \gamma_b \frac{h}{2}} \tag{6.23}$$

When the potential sliding plane is below the shotcreted WRB ($h \geq H_s$), the lateral shear resistances mobilized along two shotcrete-rock lateral walls for the triangular section (S'_{LS}) can be calculated

by

$$S'_{LS} = \frac{H_s L_{SL} c_i}{2} \tag{5.24}$$

Introducing Eqs. (5.15) – (5.17), (5.19) – (5.20), (5.22), (5.24) into Eq. (5.21), the stability of shotcreted WRB can be estimated by the following equation:

$$FS = \frac{\gamma_{wr} L_{BT} \left(\tan\phi' + \frac{Kh\tan\delta}{L_d} \right) + \gamma_{wr} h \left(\frac{1}{2}\tan\phi' + \frac{1}{3}\frac{Kh\tan\delta}{L_d} \right) \left(\frac{1}{\tan\alpha_1} + \frac{1}{\tan\alpha_2} \right) + \frac{L_{SL} c_s r_i}{h} \left(1 + \frac{H_s}{L_d} \right) + \left(p_t + \gamma_b \frac{h}{2} \right) \frac{\tan\phi'}{\tan\alpha_1}}{p_t + \gamma_b \frac{h}{2}} \tag{5.25}$$

As a special case, when $h = H_d$, Eq. (5.25) becomes identical to the global stability solution Eq. (5.13) with $\phi' = \delta$.

Fig. 5.4 presents the variation of the required shotcrete thickness L_{SL} with typical geometric and mechanical parameters. L_{SL} is rearranged based on Eqs. (5.13) and (5.25). It can be observed that the value of L_{SL} reaches the maximum value for $h = H_s$. Thus, the critical horizontal sliding plane passes the bottom of the shotcrete.

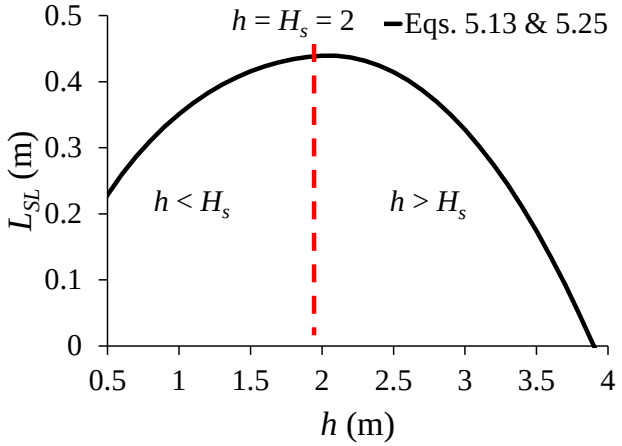

Figure 5.4 Variation of L_{SL} when the internal sliding plane passes from the top (h = 0.5) to the bottom (h is close to 4 m), calculations made with FS = 1.5, H = 12 m, H_s = 2 m, α_1 = 37°, α_2 = 50°, $H_d = L_d$ = 5 m, L_{BT} = 0.6 m, δ = 30°, ϕ' = 38°, $\gamma_{wr} = \gamma_b$ = 20 kN/m^3, $c_s = 2c_i$ = 200 kPa, and $K = K_a$.

Introducing $h = H_s$ to Eq. (5.23) or (5.25) leads to the following equation to evaluate the internal local stability of a shotcreted WRB:

$$FS = \frac{\gamma_{wr} L_{BT}\left(\tan\phi' + \frac{KH_s\tan\delta}{L_d}\right) + \gamma_{wr} H_s\left(\frac{1}{2}\tan\phi' + \frac{1}{3}\frac{KH_s\tan\delta}{L_d}\right)\left(\frac{1}{\tan\alpha_1} + \frac{1}{\tan\alpha_2}\right) + L_{SL} c_s r_i\left(\frac{1}{H_s} + \frac{1}{L_d}\right) + \left(p_t + \gamma_b\frac{H_s}{2}\right)\frac{\tan\phi'}{\tan\alpha_1}}{p_t + \gamma_b\frac{H_s}{2}} \quad (5.26)$$

5.3 Equations for evaluating the stability of shotcreted WRB

By summarizing the formulations presented in Sections 5.1 and 5.2, the stability of a shotcreted WRB can then be evaluated by the following equations:

$$FS = \frac{2\gamma_{wr} L_{BT}\left(1 + K\frac{H_d}{L_d}\right)\tan\delta + \gamma_{wr} H_d\left(1 + K\frac{2H_d}{3L_d}\right)\left(\frac{1}{\tan\alpha_1} + \frac{1}{\tan\alpha_2}\right)\tan\delta + \frac{2L_{SL} c_s r_i}{H_d}\left(1 + \frac{H_s}{L_d}\right) + \left(p_t + p_b\right)\frac{\tan\delta}{\tan\alpha_1}}{p_t + p_b}, \text{ for } \delta \le \delta_c \quad (5.27a)$$

$$FS = \frac{\gamma_{wr} L_{BT}\left(\tan\phi' + \frac{KH_s\tan\delta}{L_d}\right) + \gamma_{wr} H_s\left(\frac{\tan\phi'}{2} + \frac{KH_s\tan\delta}{3L_d}\right)\left(\frac{1}{\tan\alpha_1} + \frac{1}{\tan\alpha_2}\right) + L_{SL} c_s r_i\left(\frac{1}{H_s} + \frac{1}{L_d}\right) + \left(p_t + \gamma_b\frac{H_s}{2}\right)\frac{\tan\phi'}{\tan\alpha_1}}{p_t + \gamma_b\frac{H_s}{2}}, \text{ for } \delta > \delta_c \quad (5.27b)$$

where δ_c (°) is a critical value of interface friction angle, at which the stability control mechanism of the shotcreted WRB changes from block sliding to local top sliding. Its value is calculated as follows:

$$\delta_c = \tan^{-1}\frac{\left(p_t + p_b\right)\left[\gamma_{wr} L_{BT}\tan\phi' + \frac{1}{2}\gamma_{wr} H_s\tan\phi'\left(\frac{1}{\tan\alpha_1} + \frac{1}{\tan\alpha_2}\right) + \frac{L_{SL} c_s r_i}{H_s H_d L_d}\left(H_d L_d + H_s H_d - 2H_s L_d - 2H_s^2\right) + \left(p_t + \gamma_b\frac{H_s}{2}\right)\frac{\tan\phi'}{\tan\alpha_1}\right]}{\left(p_t + \gamma_b\frac{H_s}{2}\right)\left[\frac{\gamma_{wr} L_{BT}}{L_d}\left(2L_d + 2KH_d - KH_s\right) + \frac{\gamma_{wr}}{3L_d}\left(\frac{1}{\tan\alpha_1} + \frac{1}{\tan\alpha_2}\right)\left(3H_d L_d + 2KH_d^2 + KH_s^2\right) + \frac{\left(p_t + p_b\right)}{\tan\alpha_1}\right]} \quad (5.27c)$$

5.4 Numerical simulations

As the equations proposed above are obtained by limit equilibrium analysis based on several simplifying assumptions, their validity needs to be checked using other means. Due to the lack of experimental data, numerical modelling is performed with FLAC3D (Itasca 2013) to verify and

calibrate the equations proposed above.

Fig. 5.5(a) schematically shows a typical shotcreted WRB constructed to retain a slurried backfill, the corresponding numerical model (symmetric view) built with FLAC3D is illustrated in Fig. 5.5(b). The drift (barricade) height is 5 m. Both upstream α_1 and downstream α_2 slope angles are equal to 37°. The rock mass is simulated as an elastic material while the waste rock and shotcrete are modeled as an elastoplastic material obeying the Mohr-Coulomb criterion. The unit weight of rock mass is defined as γ_r = 26.5 kN/m^3. Young's modulus of rock mass is expressed as E_r = 30 GPa, and its Poisson's ratio v_r is 0.3. The waste rock is defined with a unit weight γ_{wr} = 19.6 kN/m^3, Young's modulus E_{wr} = 100 MPa and Poisson's ratio v = 0.3, respectively. The effective cohesion c' and internal friction angle ϕ' of the waste rock are 0 kPa and 38°, respectively. The internal friction angle of waste rocks typically ranges between 34 and 45°, with a typical value of 37° (Aubertin 2013; Azam et al. 2009; Barton 2008; Mclemoree et al. 2009). The shotcrete has a unit weight γ_s of 21.6 kN/m^3, a Young's modulus E_s of 10 GPa, a Poisson's ratio v_s of 0.3, a friction angle ϕ_s of 38°, and a cohesion (variable).

Fig. 5.5(b) illustrates a numerical model of the shotcreted WRB built with FLAC3D. To allow possible slide of barricade, interface elements, obeying Coulomb shear-strength criterion, are used in the numerical models between shotcrete and waste rock as well as their contact surfaces with surrounding rock walls (in total seven planes). Their normal (k_n) and shear (k_s) stiffness were calculated using the method suggested in the manual of FLAC3D (i.e. $k_n = k_s = 10 \times max\left(\frac{K+4G/3}{\Delta z_{min}}\right)$, with K and G the bulk and shear moduli of the waste rocks and Δz_{min} the smallest size of elements adjacent and normal to the interface) (Itasca 2013). The interface friction angles δ can vary from a relatively small value (smooth interface) to the internal friction angle of the barricade (rough interface). δ_s (°) is the interface friction angle between the shotcrete and rock walls. The top and bottom of the outer boundaries (rock mass) of the numerical model were fixed in all horizontal and vertical directions. The front and back outer boundaries (rock mass) were fixed in the y-direction. The two ends of the rock floor were fixed in the x-direction. There is a void

between the top of the waste rock barricade and the rock mass, while the top of the shotcrete is in contact with the rock mass. The linearly distributed (from top to bottom) pressure p perpendicularly applied on the upstream face of the barricade represents the pressure exerted by the backfill. A large number of sensitivity analyses were performed, and their results indicated that the optimal mesh size for the barricade is about 0.06 m × 0.25 m × 0.2 m (at the top of barricade) for the case with $\alpha_1 = \alpha_2 = 37°$, $H = 12$ m, $H_d = L_d = 5$ m, $L_{BT} = 0.6$ m, $\delta = \delta_s = 30°$, $\phi' = \phi_s = 38°$, $c_s = 2c_i$, $H_s = 2$ m, $L_{SL} = 0.4$ m. The observation point, marked by R [in Fig 5(b)], is chosen to monitor the displacement of the shotcreted WRB. The numerical simulations were performed using the option of small strain (default) of FLAC3D.

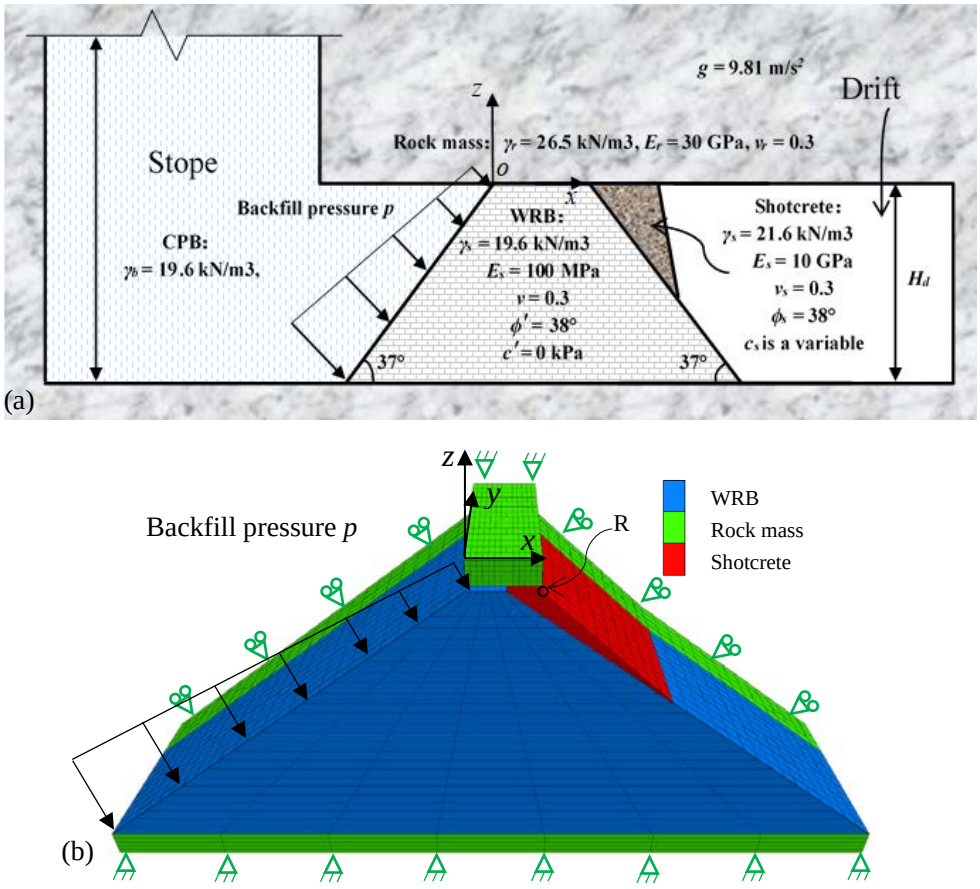

Figure 5.5 Model illustration of a shotcreted WRB: (a) physical model; (b) symmetric view (to the vertical plane passing the drift center) of numerical model.

In the absence of shotcrete, numerical analyses performed here with the given parameters have shown that large displacements can easily occur for undersized WRBs. The reinforcing effect of shotcreted WRB is numerically illustrated in Fig. 5.6, which shows the horizontal displacement contours of a WRB without (Fig. 5.6a) and with (Fig. 5.6b) shotcrete. As shown in Fig. 5.6a, the maximum *X*-displacement of the WRB surges significantly to 3 m after backfilling, indicating a local failure due to top sliding. The calculation was made with $\alpha_1 = \alpha_2 = 37°$, $H = 9$ m, $H_d = L_d = 5$ m, $L_{BT} = 0.6$ m, $\delta = 30°$, $\phi' = 38°$. By contrast, Fig. 5.6b illustrates that the top of the shotcreted WRB remains almost intact (i.e., about 0.008 m displacement in *x*-direction) attributed to the reinforcement provided by shotcrete. The calculation was made with $c_s = 2c_i = 300$ kPa, $H_s = 2$ m, $L_{SL} = 0.3$ m.

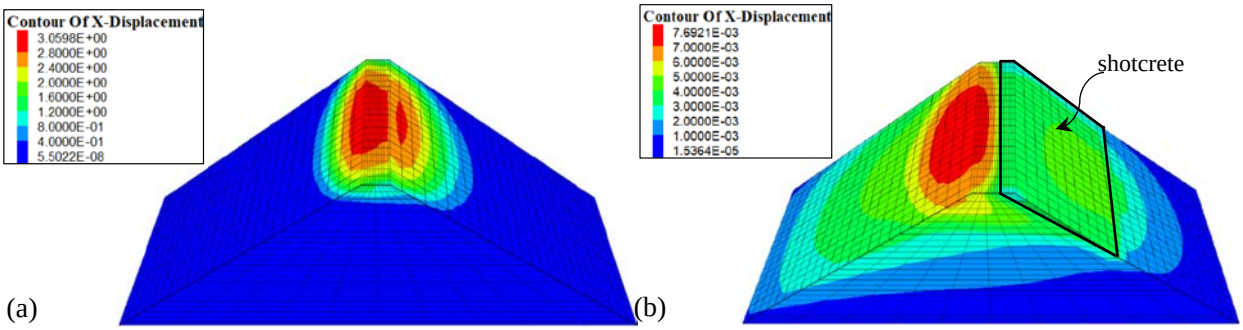

Figure 5.6 Contours of horizontal displacements (m) for a WRB: (a) without shotcrete; (b) with shotcrete.

Yang et al. (2017a) simulated the mechanical responses of WRBs using *FLAC*, and they evaluated the critical top length L_{BT} of a trapezoidal barricade for local and global stability. It was reported that the abrupt change in displacement with a slight variation in the size of the barricade is viewed as a major index for barricade instability. The WRBs with adequate top length L_{BT} can be used to retain the backfills deposited in the stope. Whereas, the shotcrete sprayed on the barricade gives rise to another crucial problem, namely that the shotcrete must have enough strength c_s to keep barricades stable for a given top length L_{SL}.

Yield state (shear or tension failure; or strength ratio) usually serves as a key index to help identify the failure state of simulated materials in numerical calculations. However, as will be shown below, these indexes may sometimes become unreliable (too subjective) for judging the stability of simulated structures. This is particularly the case for the global stability of a WRB when the interfaces are relatively smooth (Yang et al. 2017a). Such phenomenon is again confirmed here for shotcreted WRBs. Fig. 5.7 shows a combined view of *X*-displacement contour (the back half part) and yield states (the front half part) of a shotcreted WRB having an interface friction angle of $\delta = \delta_s = 16°$ when the shotcrete cohesion c_s is taken as 1.02 MPa (Fig. 5.7a) and 1.01 MPa (Fig. 5.7b), respectively (calculation made with $\alpha_1 = \alpha_2 = 37°$, $H = 12$ m, $H_d = L_d = 5$ m, $L_{BT} = 0.6$ m, $\delta = \delta_s = 16°$, $\phi' = \phi_s = 38°$, $c_s = 2c_i$, $H_s = 2$ m, $L_{SL} = 0.4$ m). When the shotcrete cohesion is 1.02 MPa (see Fig. 5.7a), the maximum *X*-displacement remains at 0.006 m and only a few sporadic zones of currently yield (indicated by shear-n) can be observed. As the c_s is slightly reduced from 1.02 MPa to 1.01 MPa, the maximum *X*-displacement dramatically jumps to about 1 m, indicating the transition from a marginal stable state to failure (Fig. 5.7b). However, Fig. 5.7b indicates that there is no clear indication of such failure based on yield state. The critical cohesion of the shotcreted WRB is 1.02 MPa for this case. One calls this case as a global stability analysis because the instability of the shotcreted WRB is caused by the sliding of the whole shotcreted WRB structure.

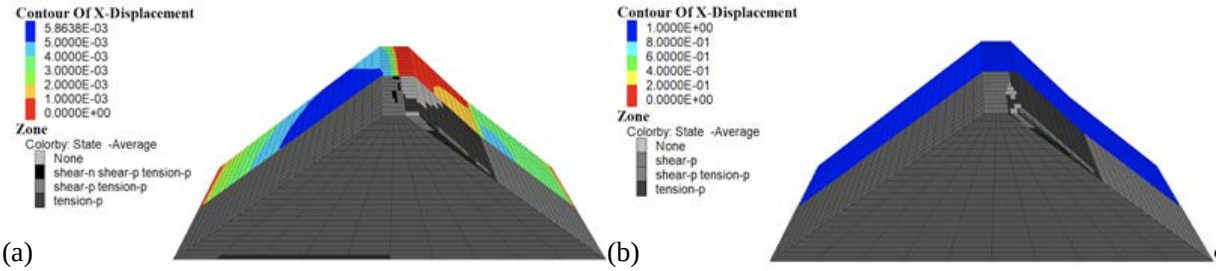

Figure 5.7 Contour of *X*-displacement (back half) and yield states (front half) of the WRB for $\delta = \delta_s = 16°$: (a) $c_s = 1.02$ MPa; (b) $c_s = 1.01$ MPa (shear-n indicates the occurrence of currently yield by shear; shear-p and tension-p indicate the occurrence of shear and tension in the past).

Fig. 5.8 shows the combined view of *X*-displacement contour (the back half part) and yield states (the front half part) of a shotcreted WRB having an interface friction angle of $\delta = \delta_s = 30°$ when the shotcrete cohesion c_s is taken as 0.15 MPa (Fig. 5.8a), 0.14 MPa (Fig. 5.8b) and 0.13 MPa (Fig. 5.8c), respectively (calculation made with $\alpha_1 = \alpha_2 = 37°$, $H = 12$ m, $H_d = L_d = 5$ m, $L_{BT} = 0.6$ m, $\delta = \delta_s = 16°$, $\phi' = \phi_s = 38°$, $c_s = 2c_i$, $H_s = 2$ m, $L_{SL} = 0.4$ m). It is seen from Fig. 5.8a that when the shotcrete cohesion c_s is 0.15 MPa, sporadic zones of currently yield can be observed. The maximum *X*-displacement of 0.042 m indicates that the shotcreted WRB structure is stable. When the shotcrete cohesion c_s is reduced to 0.14 MPa, the maximum *X*-displacement increases significantly to 0.13 m. Accordingly, the currently yield by shear zones coalesce and form a wedge sliding along an inclined plane near the top of the WRB. These results indicate that the shotcreted WRB becomes unstable even though the maximum *X*-displacement of 0.13 m cannot yet be qualified as a jump, compared to that of 0.042 m at $c_s = 0.15$ MPa. The critical cohesion of the shotcreted WRB is 0.15 MPa for this case. When the cohesion of the shotcreted WRB is further reduced to $c_s = 0.13$ MPa, the maximum *X*-displacement jumps to 1 m, further indicating the occurrence of instability of the WRB structure. The instability associated with the sliding of the top part of the WRB is called local instability.

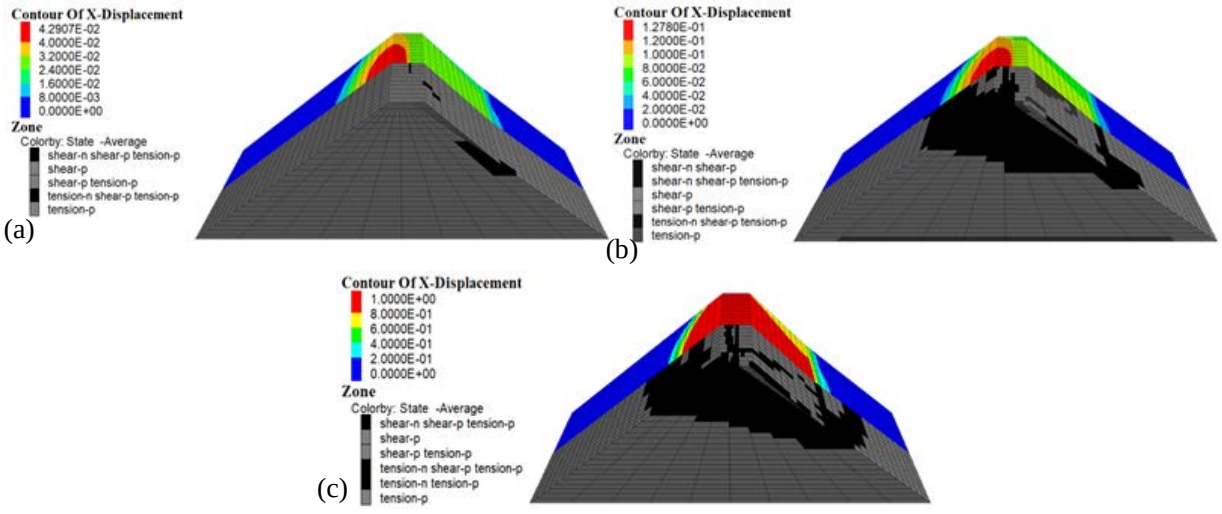

Figure 5.8 Contour of *X*-displacement (back half) and yield states (front half) of the WRB for $\delta = \delta_s = 30°$: (a) $c_s = 0.15$ MPa; (b) $c_s = 0.14$ MPa; (c) $c_s = 0.13$ MPa.

The results shown in Figure 5.8 also indicate that the structure of shotcreted WRB can fail by the coalescence of yield zones before the occurrence of displacement jump.

In summary, the onset of the structure instability of a shotcreted WRB in numerical models built with FLAC3D should be evaluated based on the displacement jump of the barricade top or the coalescence of currently yield zones passing through the shotcreted WRB, whichever comes first. In this study, the former generally applies to global instability while the latter to local instability of shotcreted WRB.

Table 5.1 summarizes the stability analysis results of the shotcreted WRB obtained from numerical simulations conducted with FLAC3D and analytical solution Eq. (5.27). The c_s ratio is defined as c_s obtained from Eq. (5.27) to the one obtained with FLAC3D. The L_{SL} ratio is defined as L_{SL} obtained from Eq. (5.27) to the one obtained with FLAC3D.

Table 5.1 Stability analysis results of the shotcreted WRB obtained by numerical simulations conducted with FLAC3D and analytical solution Eq. (5.27) (other parameters are: $\alpha_1 = \alpha_2 = 37°$, $p_t = 140$ kPa, $p_b = 240$ kPa, $\gamma_{wr} = \gamma_b = 20$ kN/m^3, $H_d = 5$ m, $L_d = 5$ m, $L_{BT} = 0.6$ m, $\phi' = 38°$, $H_s = 2$ m, $K = K_a$, $FS = 1$).

δ (°)	L_{SL} (m)	c_s (kPa)		c_s *ratio*	c_s (kPa)	L_{SL} (m)		L_{SL} *ratio*
		FLAC3D	Eq. (5.27)			FLAC3D	Eq. (5.27)	
15	0.4	1230	1379	1.12	500	1	1.1	1.1
16	0.4	1020	1238	1.21	500	0.86	0.99	1.15
17	0.4	680	1095	1.61	500	0.64	0.87	1.36
18	0.4	400	951	2.38	500	0.35	0.76	2.17
21	0.4	240	508	2.12	500	0.22	0.4	1.82
25	0.4	200	-110	-0.55	500	0.18	-0.38	-2.11
30	0.4	150	-495	-3.3	500	0.16	-0.4	-2.5
35	0.4	120	-514	-4.28	500	0.14	-0.41	-2.93
40	0.4	100	-535	-5.35	500	0.14	-0.43	-3.07

The c_s ratio and L_{SL} ratio are plotted in Fig. 5.9 to judge the stability of the shotcreted WRB. Fig. 5.9 shows the variation of FS (i.e., c_s ratio and L_{SL} ratio) as a function of the interface friction angle δ based on the results presented in Table 5.1.

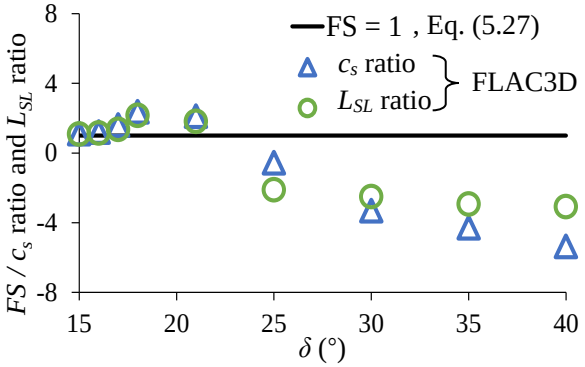

Figure 5.9 Variation of FS as a function of the interface friction angle δ calculated from the numerical simulations and analytical solution Eq. (5.27).

It can be seen from Fig. 5.9 that there is a poor agreement among the c_s ratio, L_{SL} ratio and FS. To

obtain the good agreement, three calibration factors (C_M, C_G, and C_L) are introduced to the proposed solutions for evaluating the stability of the shotcreted WRB.

$$FS = \frac{2\gamma_{wr}L_{BT}\left(1+K\frac{H_d}{L_d}\right)\tan\delta+\gamma_{wr}H_dC_G\left(1+K\frac{2H_d}{3L_d}\right)\left(\frac{1}{\tan\alpha_1}+\frac{1}{\tan\alpha_2}\right)\tan\delta+2\frac{L_{SL}c_sr_i}{H_d}\left(1+\frac{H_s}{L_d}\right)+(p_t+p_b)\frac{\tan\delta}{\tan\alpha_1}}{(p_t+p_b)C_M}, \text{ for } \delta > \delta_c \quad (5.28a)$$

$$FS = \frac{\gamma_{wr}L_{BT}\left(\tan\phi'+\frac{KH_s\tan\delta}{L_d}\right)+\gamma_{wr}H_s\left(\frac{1}{2}\tan\phi'+\frac{1}{3}\frac{KH_s\tan\delta}{L_d}\right)\left(\frac{1}{\tan\alpha_1}+\frac{1}{\tan\alpha_2}\right)+L_{SL}c_sr_i\left(\frac{1}{H_s}+\frac{1}{L_d}\right)+\left(p_t+\gamma_b\frac{H_s}{2}\right)\frac{\tan\phi'}{\tan\alpha_1}}{(p_t+\gamma_bH_s/2)C_L}, \text{ for } \delta \le \delta_c \quad (5.28b)$$

$$\delta_c = \tan^{-1}\frac{C_M(p_t+p_b)\left[\gamma_{wr}L_{BT}\tan\phi'+\frac{1}{2}\gamma_{wr}H_s\tan\phi'\left(\frac{1}{\tan\alpha_1}+\frac{1}{\tan\alpha_2}\right)+\frac{L_{SL}c_sr_i}{H_sH_dL_d}\left(H_dL_d+H_sH_d-2H_sL_d-2H_s^2\right)+\left(p_t+\gamma_b\frac{H_s}{2}\right)\frac{\tan\phi'}{\tan\alpha_1}\right]}{C_L\left(p_t+\gamma_b\frac{H_s}{2}\right)\left[\frac{\gamma_{wr}L_{BT}}{L_d}\left(2L_d+2KH_d-KH_s\right)+\frac{\gamma_{wr}}{3L_d}\left(\frac{1}{\tan\alpha_1}+\frac{1}{\tan\alpha_2}\right)\left(3H_dL_dC_G+2KH_d^2C_G+KH_s^2\right)+\frac{(p_t+p_b)}{\tan\alpha_1}\right]} \quad (5.28c)$$

Table 5.2 presents the stability analysis results of the shotcreted WRB obtained by numerical calculations done with FLAC3D and proposed analytical solution after calibrations [Eq. (5.28)].

Table 5.2 Stability analysis results of the shotcreted WRB obtained by numerical models performed with FLAC3D and proposed analytical solution [Eq. (5.28)] with calibration (i.e., C_M = 1.6, C_G = 3.9, C_L =1.56).

δ (°)	L_{SL} (m)	c_s (kPa)		c_s *ratio*	c_s (kPa)	L_{SL} (m)		L_{SL} *ratio*
		FLAC3D	Eq. (5.28)			FLAC3D	Eq. (5.28)	
15	0.4	1230	1282	1.04	500	1	1.03	1.03
16	0.4	1020	991	0.97	500	0.86	0.79	0.92
17	0.4	680	697	1.03	500	0.64	0.56	0.88
18	0.4	400	400	1.00	500	0.35	0.32	0.91
21	0.4	240	222	0.93	500	0.22	0.18	0.77
25	0.4	200	220	1.1	500	0.18	0.18	0.98
30	0.4	150	216	1.44	500	0.16	0.17	1.02
35	0.4	120	212	1.76	500	0.14	0.17	1.15
40	0.4	100	207	2.07	500	0.14	0.17	1.19

Fig. 5.10 shows the variation of *FS* as a function of the interface friction angle δ obtained from numerical simulations and analytical solutions after calibration. The calibrated solution [Eq. (5.28)]

represents c_s ratio and L_{SL} ratio quite well except for the case of large interface friction angle δ.

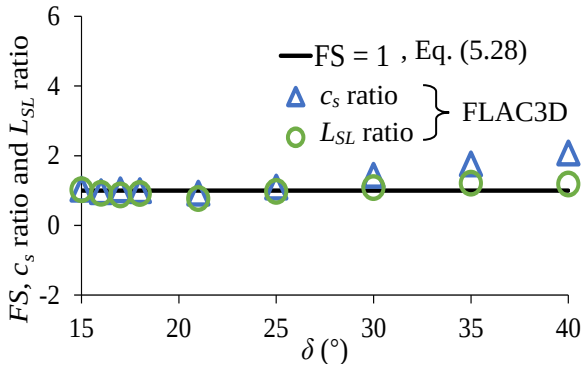

Figure 5.10 Variation of FS as a function of the interface friction angle δ obtained from the numerical simulations and the calibrated analytical solution [Eq. (5.28)] with calibration coefficients (i.e., C_M = 1.6, C_G = 3.9, C_L =1.56).

5.5 Proposed analytical solutions

Eq. (5.28) constitutes the initially developed formulations to evaluate the stability of the shotcreted WRB. Based on the previous developments, the design of the shotcrete (i.e., the required thickness L_{SL} for a given shotcrete material or the required cohesion c_s for a predefined dimension of shotcrete) applied on a WRB and the design of a WRB (i.e., the required top length L_{BT}) with a given shotcrete will be introduced in the following.

5.5.1 Solution for the design of shotcrete for a given WRB

For a given dimension of the shotcreted WRB, the calibrated analytical solutions for calculating the required cohesion c_s of shotcrete are proposed below by considering the global and local stability:

$$c_s = \frac{\frac{H_d L_d}{2}\left(p_t + p_b\right)\left(\frac{FS \times 1.6}{\tan\delta} - \frac{1}{\tan\alpha_1}\right) - \gamma_{wr} H_d L_{BT}\left(L_d + KH_d\right) - \gamma_{wr} H_d^{\,2}\left(\frac{1}{2}L_d + \frac{1}{3}KH_d\right)\left(\frac{1}{\tan\alpha_1} + \frac{1}{\tan\alpha_2}\right) \times 3.9}{r_i L_{SL}\left(L_d + H_s\right)/\tan\delta}, \text{ for } \delta \le \delta_c \quad (5.29a)$$

$$c_s = \frac{L_d\left(p_t+\gamma_b\frac{H_s}{2}\right)\left(FS\times 1.56-\frac{\tan\phi'}{\tan\alpha_1}\right)-\gamma_{wr}L_{BT}\left(L_d\tan\phi'+KH_s\tan\delta\right)-\gamma_{wr}H_s\left(\frac{1}{2}L_d\tan\phi'+\frac{1}{3}KH_s\tan\delta\right)\left(\frac{1}{\tan\alpha_1}+\frac{1}{\tan\alpha_2}\right)}{r_i L_{SL}\left(L_d/H_s+1\right)}, \text{ for } \delta > \delta_c \quad (5.29b)$$

Similarly, the calibrated analytical solutions for estimating the required top length of shotcrete L_{SL} for a given shotcrete material are proposed based on the global and local stability analysis of shotcreted WRB:

$$L_{SL} = \frac{\frac{H_d L_d}{2}\left(p_t+p_b\right)\left(\frac{FS\times 1.6}{\tan\delta}-\frac{1}{\tan\alpha_1}\right)-\gamma_{wr}H_d L_{BT}\left(L_d+KH_d\right)-\gamma_{wr}H_d{}^2\left(\frac{1}{2}L_d+\frac{1}{3}KH_d\right)\left(\frac{1}{\tan\alpha_1}+\frac{1}{\tan\alpha_2}\right)\times 3.9}{c_s r_i\left(L_d+H_s\right)/\tan\delta}, \text{ for } \delta \le \delta_c \quad (5.30a)$$

$$L_{SL} = \frac{L_d\left(p_t+\gamma_b\frac{H_s}{2}\right)\left(FS\times 1.56-\frac{\tan\phi'}{\tan\alpha_1}\right)-\gamma_{wr}L_{BT}\left(L_d\tan\phi'+KH_s\tan\delta\right)-\gamma_{wr}H_s\left(\frac{1}{2}L_d\tan\phi'+\frac{1}{3}KH_s\tan\delta\right)\left(\frac{1}{\tan\alpha_1}+\frac{1}{\tan\alpha_2}\right)}{c_s r_i\left(L_d/H_s+1\right)}, \text{ for } \delta > \delta_c \quad (5.30b)$$

Table 5.3 lists a program of numerical simulations performed with FLAC3D. The numerical results of Cases 1 to 4 will be used to test the predictive ability of the proposed solution after calibrations [i.e. Eq. (5.29) and Eq. (5.30)].

Table 5.3 Program of numerical simulations conducted with FLAC3D for validating the proposed solutions Eqs. (5.29) – (5.31) (other parameters are: $\alpha_1 = \alpha_2 = 37°$, $15° \le \delta \le 40°$, $L_{BT} = 0.6$ m, $H_s = 2$ m).

Case	Figure number	H (m)	L_d (m)	H_d (m)	ϕ' (°)
1	11*a*, 12*a*, 13*a*	Variable	5	5	38
2	11*b*, 12*b*	12	Variable	5	38
3	11*c*, 12*c*, 13*b*	12	5	Variable	38
4	11*d*, 12*d*	12	5	5	Variable

Fig. 5.11 illustrates the variation of the required c_s with a predefined dimension of shotcrete (L_{SL} = 0.4 m) as a function of interface friction angle δ, obtained from the proposed solutions Eq. (5.29) and numerical simulations. Fig. 5.11a shows the change of c_s calculated from the numerical simulations and Eq. (5.29) when the backfill height H varies from 10 to 14 m. The increased H

indicates the increased backfill pressures resulting from overburden pressures at the early age of filling (e.g., CPB), which leads to significant increase of the required shotcrete cohesion c_s for a given interface friction angle. Fig. 5.11b illustrates the variation of c_s obtained from numerical calculations and Eq. (5.29) as the barricade width L_d changes from 3 to 7 m. When the barricade becomes wider, the confining effect provided by the two lateral rock walls becomes weaker, resulting in an increased c_s for a given interface friction angle. Fig. 5.11c shows the change of c_s calculated by numerical simulations and the proposed analytical solution when the barricade (drift) height H_d increases from 3 to 7 m. The increased or decreased difference between CPB (in the stope) and barricade mainly accounts for an increase or reduction of loads acting on the upper portion of barricade, leading to an increased or decreased c_s. Fig. 5.11d illustrates the variation of c_s obtained by the numerical models and Eq. (5.29) as ϕ' increases from 34 to 40°. It can be clearly seen that c_s decreases significantly with an increase of ϕ'. This reduction is mainly due to a change in the Rankine's active earth pressure coefficient K_a associated with the ϕ'.

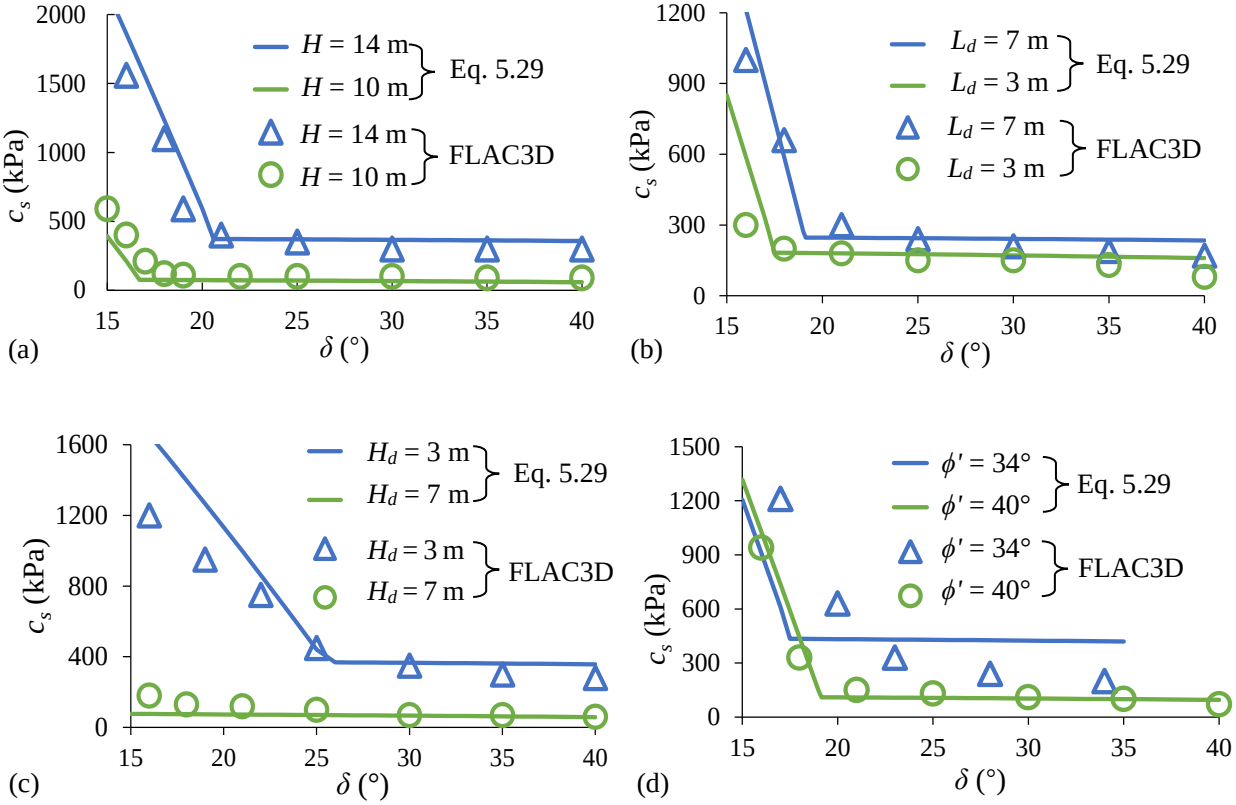

Figure 5.11 Variation of the required cohesion c_s as a function of interface friction angle δ, calculated from numerical simulations and the proposed 3D solution after calibrations [Eq. (5.29)] for different (a) slurried backfill heights H (Case 1 in Table 5.3), (b) barricade widths L_d (Case 2 in Table 5.3), (c) barricade heights H_d (Case 3 in Table 5.3), (d) internal friction angles ϕ' (Case 4 in Table 5.3).

Fig. 5.12 illustrates the variation of the required top length L_{SL} for a given shotcrete material (c_s = 500 kPa) with the interface friction angle δ, as obtained from the proposed solutions Eq. (5.30) and numerical simulation. Fig. 5.12a indicates that, as the backfill height H varies from 10 m to 14 m, the value of L_{SL} increases for a given interface friction angle. Fig. 5.12b shows the variation of L_{SL} calculated by simulations and Eq. (5.30) when the barricade width L_d changes from 3 to 7 m. Fig. 5.12c illustrates the change of L_{SL} obtained by numerical models and Eq. (5.30) as the barricade

height H_d varies from 3 to 7 m. Fig. 5.12d shows the variation of L_{SL} calculated from the numerical simulations and Eq. (5.30) when ϕ' increase from 34 to 40°. It is seen that for both global and local stability, the theoretical and numerical approaches correlate well with each other for representative stope height, barricade and shotcrete geometries and internal friction angles of waste rocks.

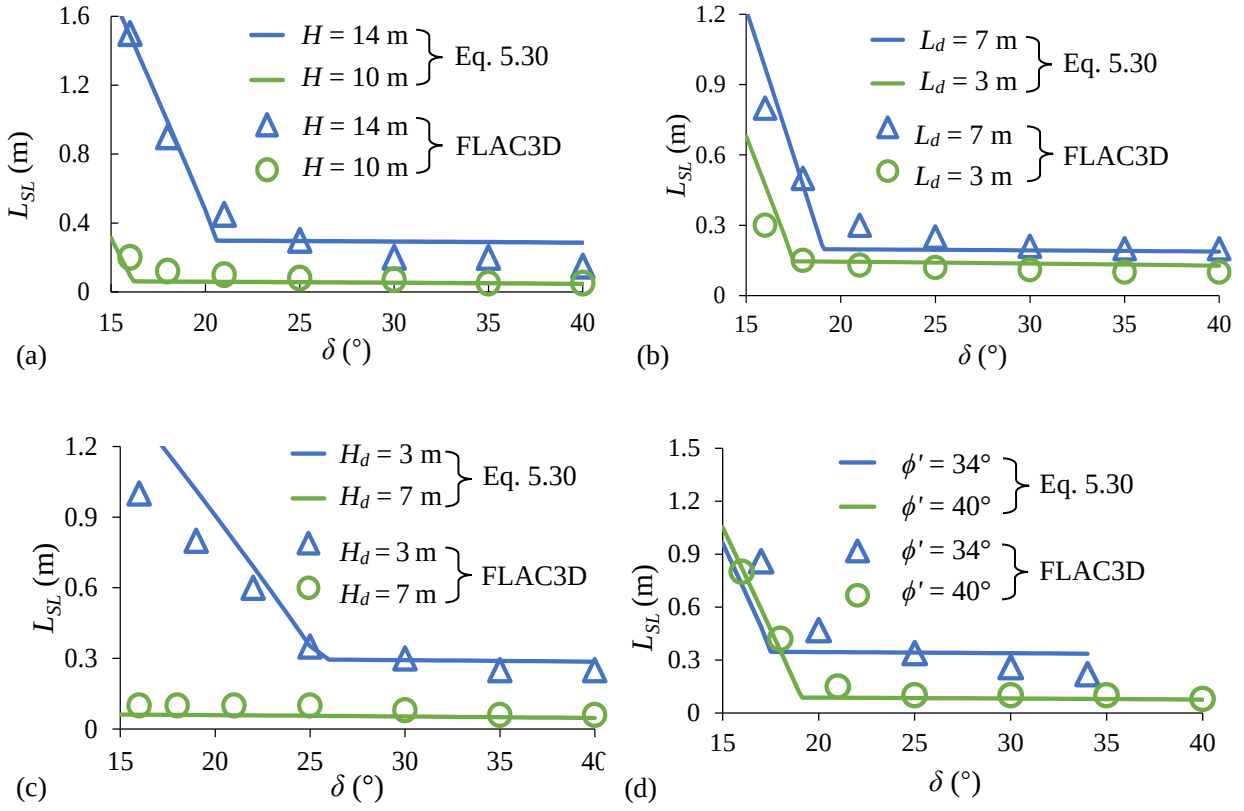

Figure 5.12 Variation of the required shotcrete top length L_{SL} with the interface friction angle δ, obtained from numerical simulations and the calibrated 3D solution [Eq. (5.30)] for different (a) slurried backfill heights H (Case 1 in Table 5.3), (b) barricade widths L_d (Case 2 in Table 5.3), (c) barricade heights H_d (Case 3 in Table 5.3), (d) internal friction angles ϕ' (Case 4 in Table 5.3).

5.5.2 Solution for the design of a WRB for a given shotcrete

The calibrated analytical solutions for calculating the required top length of WRB for a given

shotcrete are proposed below by considering the global and local stability:

$$L_{BT}=\frac{\frac{L_d}{2}\left(p_t+p_b\right)\left(\frac{FS\times 1.6}{\tan\delta}-\frac{1}{\tan\alpha_1}\right)-\gamma_{wr}H_d\left(\frac{1}{2}L_d+\frac{1}{3}KH_d\right)\left(\frac{1}{\tan\alpha_1}+\frac{1}{\tan\alpha_2}\right)\times 3.9-\frac{L_{SL}c_s r_i}{H_d\tan\delta}\left(L_d+H_s\right)}{\gamma_{wr}\left(L_d+KH_d\right)},\ \text{for } \delta\le\delta_c \qquad (5.31a)$$

$$L_{BT}=\frac{L_d\left(p_t+\gamma_b\frac{H_s}{2}\right)\left(FS\times 1.56-\frac{\tan\phi'}{\tan\alpha_1}\right)-\gamma_{wr}H_s\left(\frac{1}{2}L_d\tan\phi'+\frac{1}{3}KH_s\tan\delta\right)\left(\frac{1}{\tan\alpha_1}+\frac{1}{\tan\alpha_2}\right)-L_{SL}c_s r_i\left(1+\frac{L_d}{H_s}\right)}{\gamma_{wr}\left(L_d\tan\phi'+KH_s\tan\delta\right)},\ \text{for } \delta>\delta_c \qquad (5.31b)$$

Fig. 5.13 illustrates the change of the required top length of WRB L_{BT} for a given shotcrete (c_s = 200 kPa and L_{SL} = 0.4 m) as a function of the interface friction angle δ, obtained from Eq. (5.31) and numerical simulations. Fig. 5.13a shows the variation of L_{BT} calculated by numerical modeling and the proposed solution when the barricade height H varies from 10 to 14 m. Fig. 5.13b presents the change of L_{BT} obtained from the numerical simulations and the proposed solution as H_d increase from 3 to 7 m. It is seen from Fig. 5.13 that for global stability, the barricade top length given by the numerical simulations are slightly smaller than those predicted by the proposed analytical solutions, while these two different approaches lead to quite similar results for local stability.

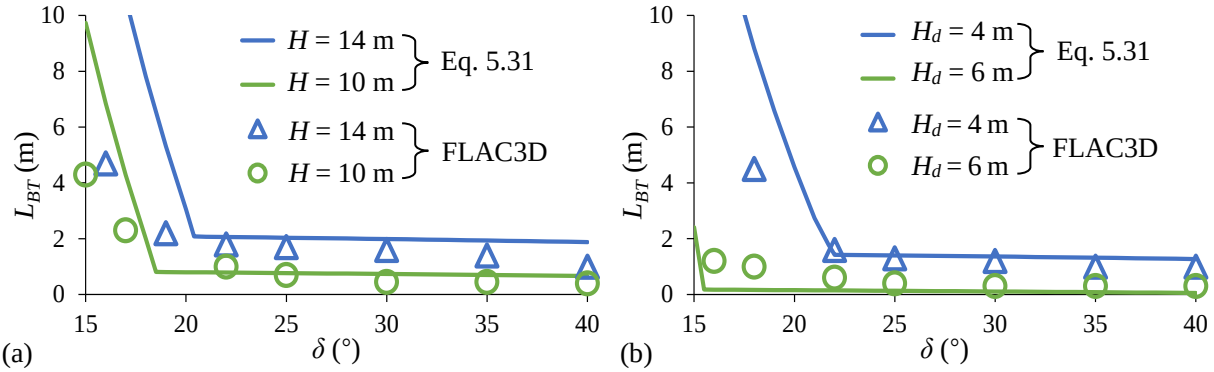

Figure 5.13 Variation of the required shotcrete top length L_{BT} with the interface friction angle δ, calculated by numerical simulations and calibrated 3D solution [Eq. (5.31)] for different (a) slurried backfill heights H (Case 1 in Table 5.3), (b) barricade heights H_d (Case 3 in Table 5.3).

In general, the proposed solutions [Eqs. (5.29), (5.30) and (5.31)] agree well with the numerical results obtained with FLAC3D for both global and local stability. As the surrounding rock walls are usually rough, it can be expected that the shotcrete design is mainly determined by the local stability. The proposed solutions can thus be used for calculating the shotcrete strength c_s or dimensions of shotcreted WRB (L_{SL} and L_{BT}).

5.6 Discussion

This study investigates the global and local stability of shotcreted WRB. The proposed analytical solutions have been first calibrated against numerical results obtained with FLAC3D for various cases (as shown above). Calibration factors (C_M, C_G, and C_L) were introduced into the proposed analytical solutions for good agreement with numerical results. The validity (predictivity) of calibrated solutions was then tested using additional numerical calculations. Overall, it has been seen that the proposed analytical solutions can be used for predicting the design size or strength of shotcrete applied on the WRB. However, it is noted that the calibrated analytical solutions [Eqs. (5.29), (5.30) and (5.31)] should be used carefully due to several simplifying assumptions and limitations.

It is noted that the hydro-geotechnical properties of WRB, including void ratio and hydraulic conductivity, could be gradually altered by the migration of fine backfill particles during stope filling; this is particularly true for the upstream portion of the barricade. Another associated challenge is the appropriate determination of backfill pressures acting on the upstream slope of the barricade, depending on the types of backfills, binder content and the filling operations. Additional work is required to further address these aspects in order to solve practical problem.

The influence of PWPs within the WRB is not taken into account. This hypothesis is supported by the significant contrast in permeability between the slurried backfills and waste rock. It should be noted that the permeability of waste rock could be significantly reduced when shotcrete is applied. Practically however, the shotcrete is only sprayed to the upper portion (weak point) of the WRB.

Hence, the drainage paths of decanted water are not blocked. It is then deemed reasonable to ignore the effect of water for shotcreted WRB. However, the effect of water could be amplified once the voids of waste rocks are filled with fines backfill particles.

In numerical simulations presented above, the tensile strength of shotcrete is assumed to be a nonzero value, e.g., T_s = unconfined compressive strength (UCS)/10. This is believed to be more rational and realistic than the default T_s = 0 (tension cut-off) in FLAC3D. Cohesion of shotcrete can vary from about 1 to 6 MPa within 10 days, and up to about 3.5 MPa in one day based on Mohr-Coulomb criterion (Hustrulid et al. 2001). Adhesion of shotcrete applied on rock walls in underground mines typically varies from 0.5 to 2 MPa depending on the curing time and testing methods (Saiang et al. 2005; Seymour et al. 2010). It is well known that the mixture proportion and some other factors, including spray location, finishing and curing time, can significantly affect the shotcrete (or concrete) strength. It should be mentioned that the tensile strength (T_s) of cemented materials (like shotcrete) is much smaller than its compressive strength due to brittleness (Spiegel and Limbrunner 2003). Therefore, a conservative but somewhat realistic value of shotcrete tensile strength (i.e., T_s = UCS/10) is used in numerical simulations (Mitchell and Wong 1982; Yang et al. 2017b).

It is well known that interfaces properties play a key role when interpreting the mechanical behaviors of integrated structures. The effect of all contact interfaces in shotcreted WRB are mimicked using interface elements provided by FLAC3D. Such treatment could not only facilitate displacement and stress transmission between different materials (Itasca 2013), but also reflect reality as adhesion does exist along surfaces in contact with shotcrete due to cementation. For simplicity, the same parameters are used for shotcrete-waste rock interfaces and shotcrete-rock wall interfaces.

The numerical simulation results show that the local stability mainly governs the shotcrete design when $\delta = \delta_s$ ranges from 15 to 40° [e.g., Fig. 5.11(c, H_d = 7 m)]. These results indicate that the critical interface friction angle δ_c dictated by analytical solutions may lead to a conservative result.

Once the WRB is reinforced with shotcrete, the shotcreted barricade with stable upper section (mainly dominated by local stability) can partly explain this.

It is noted that a horizontal sliding plane is assumed to facilitate the theoretical development, as is the case of Yang et al. (2017a). However, previous and current numerical results all indicate that the sliding plane is actually inclined (see Fig. 5.8b); this can partly account for the calibration factors introduced in the proposed (local) solutions.

The calibrated analytical solutions [Eqs. (5.29), (5.30) and (5.31)] are mainly illustrated to design a shotcreted WRB to retain CPB in this paper. With the proper estimation of the pressures at the top (p_t) and base (p_b) of the upstream slope of the shotcreted WRB, the calibrated analytical solutions could also be used for other types of mine backfill (e.g., hydraulic fill).

In 2009, the numerical simulation results of Li and Aubertin (Li and Aubertin 2009) have shown that dilation angle can significantly influence the stress distribution in backfilled stopes. Later, Helinski et al. (2011) conducted numerical models to simulate the behaviour of barricades and their results indicated that dilation angle tends to affect the stability of a WRB. However, the application of dilation angle in practical design is much more complicated, particularly for waste rocks. For cohesionless geomaterials, dilative behavior depends on the initial state of compaction and confining pressure. A loose sand may exhibit a mechanical behavior of dense sand (i.e., dilation) under very low confining pressure (Holtz et al. 1981). For this reason, a rockfill may not certainly have a zero dilation angle due only to its poor compaction. Experimental work is necessary to clarify this aspect.

It is recalled that a zero dilation angle was used for waste rocks in numerical calculations. This is in line with the basic assumptions associated with the elasto-plastic constitutive model, implying a zero volumetric plastic strain once the ultimate state is reached. Non-zero dilation angles are usually introduced in numerical simulations based on associated flow rule. However, it is noted that such treatment has received many criticisms because of the contradictory between an elasto-

plastic framework which assumes constant volumetric strains while an introduction of dilation angle leads to variable volumetric strains after yield. In practice, plastic volumetric changes (compressibility or dilatancy) can occur in granular materials before the ultimate strength is reached, depending on the initial void ratio and stress path. More work is thus needed to consider the dilation angle in both theoretical and numerical models.

Even if dilation angle can be incorporated into theoretical and numerical work, another challenge is the measurement of dilation angle and friction angle for rockfills or waste rocks due to the large size of particles. Recently, Deiminiat et al. (2020) have indicated that the minimum required ratio of 10 between specimen size and the maximum particle size of tested sample suggested by ASTM D3080 for direct shear tests is not large enough to eliminate the specimen size effect. Deiminiat et al. (2021) further showed that a minimum value of 60 between specimen size and the maximum particle of tested sample is needed. It would be quite challenging to have a direct shear test apparatus that can be used to measure the friction angle and dilation angle of rockfills and waste rocks with a specimen size of 60 times the maximum particle size.

It’s quite logic to think that using a limit equilibrium code (such as Slide3) should produce more consistent results with a closed-form solution that is also based on limit equilibrium analysis. In this study however, a WRB can fail as a bloc (i.e., controlled by global stability) or on top within the rockfill (i.e., controlled by internal local stability). The former cannot be handled by a limit equilibrium code, and FLAC3D is thus preferred.

Finally, it is worth mentioning that “slurried paste backfill” was used in this paper for a backfill that meets the criterion of paste backfill in particle size distribution, but not the criterion of paste backfill in solids content. According to Potvin et al. (2005), a backfill can be called paste backfill only when it contains at least 10% of particles smaller than 10 μm and it does not bleed of water after its deposition. As stated in Zheng and Li (2021) the criterion in particle size distribution can be satisfied with the full tailings of most modern hard rock mines while the criterion in term of water bleeding is not satisfied in most cases. According to Zheng and Li (2021), a backfill meeting

the second criterion is in an unsaturated state, which results in an apparent cohesion and make the transportation by pipes very difficult. This explains why more (than needed) water has to be added in paste backfill in practice to form a slurried paste backfill. Some prefer calling such backfill as “hydraulic backfill”. This is not appropriate either because a hydraulic backfill should contain at least 15% of particles larger than 20 μm [3]. In order to avoid any debate on the terminology, slurried paste backfill is used here. In addition, the iso-geostatic overburden pressure is mostly applicable to slurried paste backfill during or shortly after its deposition in stopes (Thompson et al. 2012).

5.7 Conclusions

Theoretical and numerical models are developed in this study to investigate the reinforcing effect of shotcrete sprayed on the barricade made of waste rocks. Analytical solutions are proposed for evaluating the required cohesion c_s and top length L_{SL} of shotcrete, based on the global and local stability analysis. The proposed solution can also be used to estimate the size of WRB when the parameters of shotcrete are known. The proposed solutions can provide handy tools for mining engineers at the preliminary design stage of projects. These analytical solutions have been calibrated and verified using numerical simulations conducted with FLAC3D. The effects of various influencing parameters are analyzed using analytical and numerical approaches. The results show that there is good agreement between the analytical solutions and numerical simulation.

Numerical simulations are performed with FLAC3D with complex and realistic interface elements obeying Coulomb sliding. The onset of failure (sliding) of shotcreted WRB modeled in FLAC3D can be judged objectively using instability criterion based on the first occurrence of displacement jump or coalescence of currently yield zones. The numerical simulation results indicate that the shotcrete applied on WRB can greatly improve its stability, especially at the top of the downstream side.

The newly proposed solutions correlate well with numerical simulations for representative stope

height (9 m ≤ H ≤ 18 m), barricade and shotcrete geometries (3 m ≤ H_d ≤ 7 m, 3 m ≤ L_d ≤ 7 m, 1 m ≤ H_s ≤ 3 m) and properties of waste rock and shotcrete (34° ≤ ϕ' ≤ 40°). Analytical solutions with simple but useful functions (calculations made with Microsoft Excel®) are preferable in engineering practice.

Acknowledgments: The authors acknowledge the financial support from the Natural Sciences and Engineering Research Council of Canada (NSERC 402318), Fonds de Recherche du Québec - Nature et Technologies (FRQNT 2015-MI-191676), and the partners of the Research Institute on Mines and Environment (RIME UQAT - Polytechnique; http://rime-irme.ca).

5.8 Appendix Sample Calculations

The application of the proposed analytical solutions [Eq. (5.29), Eq. (5.30), and Eq. (5.31)] are illustrated below for slurried backfill with typical geometric and material parameters:

p_t = 140 kPa, p_b = 240 kPa, L_d = 5m, H_d = 5 m, L_{BT} = 2 m, H_s = 2 m, α_1 = 37°, α_2 = 45°, γ_{wr} = γ_b = 20 kN/m^3, ϕ' = 37°

The factor of safety, calibration factors and earth pressure coefficient are given by:

FS = 1.5, C_M = 1.6, C_G = 3.9, C_L = 1.56, K = K_a = 0.2486

Case 1:

The designed top length of shotcrete L_{SL} is 0.5 m. When the interface is smooth (e.g., δ = δ_s = 20° < δ_c = 26°), the required cohesion of shotcrete can be expressed as [Eq. (5.29a)]

$$c_s = \frac{\frac{H_d L_d}{2}\left(p_t + p_b\right)\left(\frac{FS \times C_M}{\tan\delta} - \frac{1}{\tan\alpha_1}\right) - \gamma_{wr} H_d L_{BT}\left(L_d + KH_d\right) - \gamma_{wr} H_d^2\left(\frac{1}{2}L_d + \frac{1}{3}KH_d\right)\left(\frac{1}{\tan\alpha_1} + \frac{1}{\tan\alpha_2}\right)C_G}{r_i L_{SL}\left(L_d + H_s\right)/\tan\delta}$$

$$= \frac{\frac{5\text{m}\times 5\text{m}}{2}\left(140\text{kPa} + 240\text{kPa}\right)\left(\frac{1.5\times 1.6}{\tan 20^\circ} - \frac{1}{\tan 37^\circ}\right) - 20\text{KN/m}^3 \times 5\text{m} \times 2\text{m}\left(5\text{m} + 0.2486 \times 5\text{m}\right) - 20\text{KN/m}^3 \times 5^2\text{m}^2\left(\frac{1}{2}\times 5\text{m} + \frac{1}{3}\times 0.2486 \times 5\text{m}\right)\left(\frac{1}{\tan 37^\circ} + \frac{1}{\tan 45^\circ}\right) \times 3.9}{0.5 \times 0.5\text{m}\left(5\text{m} + 2\text{m}\right)/\tan 20^\circ}$$

$$= 2193 \text{ kPa}$$

When c_s = 2 MPa and r_i = 0.5, the required top length of shotcrete L_{SL} is given by [Eq. (5.30a)]

$$L_{SL} = \frac{\frac{H_d L_d}{2}\left(p_t + p_b\right)\left(\frac{FS \times C_M}{\tan\delta} - \frac{1}{\tan\alpha_1}\right) - \gamma_{wr} H_d L_{BT}\left(L_d + KH_d\right) - \gamma_{wr} H_d{}^2\left(\frac{1}{2}L_d + \frac{1}{3}KH_d\right)\left(\frac{1}{\tan\alpha_1} + \frac{1}{\tan\alpha_2}\right)C_G}{c_s r_i\left(L_d + H_s\right)/\tan\delta}$$

$$= \frac{\frac{5\text{m}\times 5\text{m}}{2}\left(140\text{kPa} + 240\text{kPa}\right)\left(\frac{1.5\times 1.6}{\tan 16^\circ} - \frac{1}{\tan 37^\circ}\right) - 20\text{KN/m}^3 \times 5\text{m} \times 2\text{m}\left(5\text{m} + 0.2486\times 5\text{m}\right) - 20\text{KN/m}^3 \times 5^2\text{m}^2\left(\frac{1}{2}\times 5\text{m} + \frac{1}{3}\times 0.2486\times 5\text{m}\right)\left(\frac{1}{\tan 37^\circ} + \frac{1}{\tan 45^\circ}\right)\times 3.9}{2000\text{kPa}\times 0.5\left(5\text{m} + 2\text{m}\right)/\tan 16^\circ}$$

$$= 0.55\text{ m}$$

Case 2:

When the interface is rough (e.g., $\delta = \delta_s = 30° > \delta_c = 26°$), the required cohesion of shotcrete with a designed top length ($L_{SL} = 0.3$ m) is given by [Eq. (5.29b)]

$$c_s = \frac{L_d\left(p_t + \gamma_b\frac{H_s}{2}\right)\left(FS\times C_L - \frac{\tan\phi'}{\tan\alpha_1}\right) - \gamma_{wr} L_{BT}\left(L_d\tan\phi' + KH_s\tan\delta\right) - \gamma_{wr} H_s\left(\frac{1}{2}L_d\tan\phi' + \frac{1}{3}KH_s\tan\delta\right)\left(\frac{1}{\tan\alpha_1} + \frac{1}{\tan\alpha_2}\right)}{r_i L_{SL}\left(L_d/H_s + 1\right)}$$

$$= \frac{5\text{m}\left(140\text{kPa} + 20\text{KN/m}^3\frac{2\text{m}}{2}\right)\left(1.5\times 1.56 - \frac{\tan 37^\circ}{\tan 37^\circ}\right) - 20\text{KN/m}^3\times 2\text{m}\left(5\text{m}\times\tan 37^\circ + 0.2486\times 2\text{m}\times\tan 30^\circ\right) - 20\text{KN/m}^3\times 2\text{m}\left(\frac{1}{2}\times 5\text{m}\times\tan 37^\circ + \frac{1}{3}\times 0.2486\times 2\text{m}\times\tan 30^\circ\right)\left(\frac{1}{\tan 37^\circ} + \frac{1}{\tan 45^\circ}\right)}{0.5\times 0.3\text{m}\left(5\text{m}/2\text{m} + 1\right)}$$

$$= 1382\text{kPa}$$

For $c_s = 2$ MPa and $r_i = 0.5$, the required top length of shotcrete can be expressed as [Eq. (5.30b)]

$$L_{SL} = \frac{L_d\left(p_t + \gamma_b\frac{H_s}{2}\right)\left(FS\times C_L - \frac{\tan\phi'}{\tan\alpha_1}\right) - \gamma_{wr} L_{BT}\left(L_d\tan\phi' + KH_s\tan\delta\right) - \gamma_{wr} H_s\left(\frac{1}{2}L_d\tan\phi' + \frac{1}{3}KH_s\tan\delta\right)\left(\frac{1}{\tan\alpha_1} + \frac{1}{\tan\alpha_2}\right)}{c_s r_i\left(\frac{L_d}{H_s} + 1\right)}$$

$$= \frac{5\text{m}\left(140\text{kPa} + 20\text{KN/m}^3\frac{2\text{m}}{2}\right)\left(1.5\times 1.56 - \frac{\tan 37^\circ}{\tan 37^\circ}\right) - 20\text{KN/m}^3\times 2\text{m}\left(5\text{m}\times\tan 37^\circ + 0.2486\times 2\text{m}\times\tan 30^\circ\right) - 20\text{KN/m}^3\times 2\text{m}\left(\frac{1}{2}\times 5\text{m}\times\tan 37^\circ + \frac{1}{3}\times 0.2486\times 2\text{m}\times\tan 30^\circ\right)\left(\frac{1}{\tan 37^\circ} + \frac{1}{\tan 45^\circ}\right)}{2000\text{kPa}\times 0.5\left(\frac{5\text{m}}{2\text{m}} + 1\right)}$$

$$= 0.21\text{ m}$$

Case 3:

With a given shotcrete (e.g., $c_s = 1000$ kPa and $L_{SL} = 0.4$ m), the required top length L_{BT} is given by [Eq. (5.31a)] when the interface is smooth (e.g., $\delta = \delta_s = 20° < \delta_c = 26°$)

$$L_{BT} = \frac{\frac{L_d}{2}\left(p_t + p_b\right)\left(\frac{FS\times C_M}{\tan\delta} - \frac{1}{\tan\alpha_1}\right) - \gamma_{wr} H_d\left(\frac{1}{2}L_d + \frac{1}{3}KH_d\right)\left(\frac{1}{\tan\alpha_1} + \frac{1}{\tan\alpha_2}\right)C_G - \frac{L_{SL} c_s r_i}{H_d\tan\delta}\left(L_d + H_s\right)}{\gamma_{wr}\left(L_d + KH_d\right)}$$

$$= \frac{\frac{5\text{m}}{2}\left(140\text{kPa} + 240\text{kPa}\right)\left(\frac{1.5\times 1.6}{\tan 20^\circ} - \frac{1}{\tan 37^\circ}\right) - 20\text{KN/m}^3\times 5\text{m}\left(\frac{1}{2}\times 5\text{m} + \frac{1}{3}\times 0.2486\times 5\text{m}\right)\left(\frac{1}{\tan 37^\circ} + \frac{1}{\tan 45^\circ}\right)\times 3.9 - \frac{0.4\text{m}\times 1000\text{kPa}\times 0.5}{5\text{m}\times\tan 20^\circ}\left(5\text{m} + 2\text{m}\right)}{20\text{KN/m}^3\left(5\text{m} + 0.2486\times 5\text{m}\right)}$$

$$= 12.73\text{m}$$

When the interface is rough (e.g., $\delta = \delta_s = 30° > \delta_c = 26°$), the required top length L_{BT} is given by

[Eq. (5.31b)]

$$L_{BT} = \frac{L_d\left(p_t + \gamma_b \frac{H_s}{2}\right)\left(FS \times C_L - \frac{\tan\phi'}{\tan\alpha_1}\right) - \gamma_{wr} H_s\left(\frac{1}{2}L_d \tan\phi' + \frac{1}{3}KH_s \tan\delta\right)\left(\frac{1}{\tan\alpha_1} + \frac{1}{\tan\alpha_2}\right) - L_{SL} c_s r_i\left(1 + \frac{L_d}{H_s}\right)}{\gamma_{wr}\left(L_d \tan\phi' + KH_s \tan\delta\right)}$$

$$= \frac{5\text{m}\left(140\text{kPa} + 20\text{KN/m}^3 \frac{2\text{m}}{2}\right)\left(1.5 \times 1.56 - \frac{\tan 37^\circ}{\tan 37^\circ}\right) - 20\text{KN/m}^3 \times 2\text{m}\left(\frac{1}{2} \times 5\text{m} \times \tan 37^\circ + \frac{1}{3} \times 0.2486 \times 2\text{m} \times \tan 30^\circ\right)\left(\frac{1}{\tan 37^\circ} + \frac{1}{\tan 45^\circ}\right) - 0.4\text{m} \times 1000\text{kPa} \times 0.5\left(1 + \frac{5\text{m}}{2\text{m}}\right)}{20\text{KN/m}^3\left(5\text{m} \times \tan 37^\circ + 0.2486 \times 2\text{m} \times \tan 30^\circ\right)}$$

$$= 2.31\text{m}$$

5.9 References

Aubertin, M., Bussière, B., and Bernier, L. (2002). Environnement et gestion des rejets miniers (CD-ROM), Presses Internationales Polytechnique, Montréal (in French).

Azam S, Wilson GW, Fredlund DG, Van Zyl D. (2009). Geotechnical characterization of mine waste rock. In Proceedings of the 17th International Conference on Soil Mechanics and Geotechnical Engineering. Alexandria, Egypt:3421-3425.

Barton NR. (2008). Shear strength of rockfill, interfaces and rock joints, and their points of contact in rock dump design. In Proceedings of the First International Seminar on the Management of Rock Dumps, Stockpiles and Heap Leach Pads. Australian Centre for Geomechanics:3-17.

Beer G. (1986). Design of brick bulkheads: numerical modelling. *CSIRO Institute of Energy and Earth Resources*, Division of Geomechanics, Long Pocket Laboratories, Project Report 1.

Bloss, M. L., and Chen, J. (1998). Drainage research at Mount Isa Mines Limited 1992–1997. *Proc*., 6*th Int*. *Symp*. *on Mining with Backfill*, M. Bloss, ed., AusIMM, Carlton, Victoria, Australia, 111–116.

Duffield, W.A., Gad, E., Bamford, W. (2003). Investigation into the structural behaviour of mine brick barricades. *Aust Inst Min Metall*, 2(2), 45-50.

Deiminiat A, Deiminiat A, Li L, Zeng F, Pabst, T, Chiasson P, Chapuis R. (2020) Determination of

the shear strength of rockfill from small-scale laboratory shear tests: a critical review. Adv Civ Eng.

Deiminiat A, Li L, Zeng F. Minimum specimen size to maximum particle size ratio required to eliminate specimen size effect in direct shear tests. J Rock Mech Geotech Eng (under review, submitted March 2021)

Grabinsky, M. W. (2010). In situ monitoring for ground truthing paste backfill designs. *Proc., Paste 2010*, Australian Centre for Geomechanics, Crawley, Australia, 85–98.

Grice AG. (1989). Fill research at Mount Isa mines limited. *Innovations in Mining Backfill Technology*, Hassani et al. (eds), 1989, A.A. Balkema, Rotterdam, 15-22.

Grice, T. (1998). Stability of hydraulic backfill barricades. *Proc., 6th Int. Symp. on Mining with Backfill*, M. Bloss, ed., AusIMM, Carlton, Victoria, Australia, 117–120.

Grice, T. (2001). Recent mine fill developments in Australia. *Proc., 7th Int. Symp. on Mining with Backfill*, Society for Mining, Metallurgy & Exploration, Englewood, CO, 351–357.

Hambley, D. F. (2011). Backfill mining. *SME mining engineering handbook* (*vol. 1*), Darling, P., ed., Vol. 1, Society for Mining, Metallurgy & Exploration, Englewood, CO, 1375–1384.

Hassani, F., and Archibald, J. (1998). *Mine backfill* (CD-ROM), Canadian Institute of Mining, Metallurgy and Petroleum, Montréal.

Helinski, M., Fourie, A., and Fahey, M. (2006). Mechanics of early age cemented paste backfill. *Proc., Symp. at the 9th Int. Seminar on Paste and Thickened Tailings*, R. Jewell, S. Lawson, and P. Newman, eds., Australian Centre for Geomechanics, Perth, Australia, 313–322.

Hughes, P.B., Pakalnis, R., Hitch, M., and Corey, G. (2010). Composite paste barricade performance at Goldcorp Inc. Red Lake Mine, Ontario, Canada. *Int. J. Min, Reclam., Environ.*, 24(2), 138–150.

Hustrulid, W.A., Bullock, R.L. and Bullock, R.C. (2001). Underground mining methods:

Engineering fundamentals and international case studies. SME.

Holtz R.D., Holtz R.D., Kovacs W.D., Sheahan T.C. An introduction to geotechnical engineering (Vol. 733). Englewood Cliffs: Prentice-Hall; 1981.

Itasca. (2013). *FLAC3D*: *Fast Lagrangian analysis of continua in 3 dimensions; user's guide, version 5.01,* Itasca Consulting Group, Minneapolis, MN.

Li, L., Ouellet, S., and Aubertin, M. (2009). A method to evaluate the size of backfilled stope barricades made of waste rock. *Proc., 62nd Canadian Geotechnical Conf. and 10th Joint CGS/IAH-CNC Groundwater Specialty Conf.,* Canadian Geotechnical Society, Richmond, BC, Canada, 497–503.

Li, L., and Aubertin, M. (2009a). A three-dimensional analysis of the total and effective stresses in submerged backfilled stopes. *Geotech. Geol. Eng.*, 27(4), 559–569.

Li, L., and Aubertin, M. (2009b). Horizontal pressure on barricades for backfilled stopes. Part I: Fully drained conditions. *Can. Geotech. J.*, 46(1), 37–46.

Li, L., and Aubertin, M. (2009c). Horizontal pressure on barricades for backfilled stopes. Part II: Submerged conditions. *Can. Geotech. J.*, 46(1), 47–56.

Li, L., and Aubertin, M. (2011). Limit equilibrium analysis for the design of backfilled stope barricades made of waste rock. *Can. Geotech. J.*, 48(11), 1713–1728.

Liu, G., Li, L., Yang, X. and Guo, L. (2018). Required strength estimation of a cemented backfill with the front wall exposed and back wall pressured. *International Journal of Mining and Mineral Engineering*, 9(1), 1-20.

Lu H, Qi C, Li C, Gan D, Du Y, Li S. (2020). A light barricade for tailings recycling as cemented paste backfill. J Clean Prod; 247:119388.

McLemore VT, Fakhimi A, van Zyl D, Ayakwah GF, Anim K, Boakye K, Ennin F, Felli P, Fredlund D, Gutierrez LA, Nunoo S. (2009). Literature review of other rock piles: characterization,

weathering, and stability. Questa Rock Pile Weathering Stability Project. New Mexico Bureau of Geology and Mineral Resources. New Mexico Tech, USA.

Mitchell, R. J., and Wong, B.C. (1982). Behaviour of cemented tailings sands. *Can. Geotech. J.*, 19(3), 289–295.

Nujaim, M., Auvray, C. and Belem, T. (2018). Geomechanical behaviour of a rock barricade and cemented paste backfill: Laboratory experiments on a reduced-scale model. In *Geomechanics and Geodynamics of Rock Masses, Volume 1: Proceedings of the 2018 European Rock Mechanics Symposium*. CRC Press.

Nujaim M, Belem T, Auvray C. (2020a). Small-scale model preliminary testing on the interaction between paste backfills and waste rock barricades. In Rock Mechanics for Natural Resources and Infrastructure Development, Volume 6: Proceedings in Earth and Geosciences. CRC Press.

Nujaim M, Belem T, Giraud A. (22020b). Experimental tests on a small-scale model of a mine stope to study the behavior of waste rock barricades during backfilling. Minerals 2020; 10(11):941.

Potvin, Y., Thomas, E., and Fourie, A. (2005). *Handbook on mine fill*, Australian Centre for Geomechanics, Perth, Australia.

Quezada JC, Vincens E, Mouterde R, Morel JC. (2016). 3D failure of a scale-down dry stone retaining wall: A DEM modelling. Eng Struct; 117:506-517.

Revell, M.B. and Sainsbury, D.P. (2007). Advancing paste fill barricade design using numerical modeling. 9*th International Symposium on Mining with Backfill*, Montréal, QC, Canada.

Saiang D, Malmgren L, Nordlund E. (2005). Laboratory tests on shotcrete-rock joints in direct shear, tension and compression. Rock mech rock eng., 38(4):275-297.

Seymour, B., Martin, L., Clark, C., Stepan, M., Jacksha, R., Pakalnis, R., Roworth, M. and Caceres, C. (2010). A practical method of measuring shotcrete adhesion strength. In *Proceedings, SME*

Annual Meeting and Exhibit, 1-9.

Soderberg, R.L., and Busch, R.A. (1985). *Bulkheads and drains for high sandfill stopes*, U.S. Dept. of the Interior, Bureau of Mines, Washington, DC.

Sivakugan, N., Rankine, R.M., Rankine, K. J., and Rankine, K. S. (2006a). Geotechnical considerations in mine backfilling in Australia. *J. Cleaner Prod*., 14(12–13), 1168–1175.

Sivakugan, N., Rankine, K. J., and Rankine, R. M. (2006b). Permeability of hydraulic fills and barricade bricks. *Geotech. Geol. Eng*., 24, 661–673.

Sivakugan, N. (2008). Geotechnical issues of mining with hydraulic backfills. *Elect. J. Geotech. Eng*., Special Volume: Bouquet 08.

Saiang, D., Malmgren, L. and Nordlund, E. (2005). Laboratory tests on shotcrete-rock joints in direct shear, tension and compression. *Rock mechanics and rock engineering*, 38(4), 275-297.

Spiegel, L. and Limbrunner, F.G. (2003). Reinforced concrete design, 5th Edition. Prentice Hall.

Thompson, B.D., Grabinsky, M. W., and Bawden, W. F. (2012). In-situ measurements of cemented paste backfill at the Cayeli Mine. *Can. Geotech. J*., 49(7), 755–772.

Xu W, Cao Y, Liu B. (2019). Strength efficiency evaluation of cemented tailings backfill with different stratified structures. Eng Struct;180(1):18-28.

Yumlu, M., and Guresci, M. (2007). Paste backfill bulkhead monitoring-A case study from Inmet's Cayeli mine. *Proc., 9th Int. Symp. in Mining with Backfill* (*CD-ROM*), Canadian Institute of Mining, Metallurgy and Petroleum, Montréal.

Yang P. Y., Brochu-Baekelmans, M., Li, L., and Aubertin, M. (2014). An improved solution for sizing barricades made of waste rock to retain cemented paste backfill. *Proc., 67th Canadian Geotechnical Conf*., Canadian Geotechnical Society, Richmond, BC, Canada.

Yang, P.Y., Li, L., Aubertin, M., Brochu-Baekelmans, M., and Ouellet, S. (2017a). Stability analyses of waste rock barricades designed to retain paste backfill. *Int. J. Geomech.* 17(3),

04016079.

Yang, P.Y., Li, L. and Aubertin, M. (2017b). A new solution to assess the required strength of mine backfill with a vertical exposure. *Int. J. Geomech.* 17(10), 04017084-1–04017084-13.

Zheng J, Zheng J, Li L. (2021). Experimental study of the “short-term” pressures of uncemented paste backfill with different solid contents for barricade design. J Cleaner Production. 275, 123068.

Zhao X, Fourie A, Veenstra R, Qi CC. (2020). Safety of barricades in cemented paste-backfilled stopes. Int J Min Met Mater 2020; 27(8):1054-1064.

CHAPTER 6 ARTICLE 3: AN UPDATE OF THE 3D ANALYTICAL SOLUTION FOR THE DESIGN OF BARRICADES MADE OF WASTE ROCKS

Yulong Zhai

This article was submitted to the International Journal of Rock Mechanics and Mining Sciences in October 2021

Abstract: Stope backfilling is increasingly used in underground mines. Barricades are necessary to retain slurried backfill poured in mine stopes. In Canada, waste rock barricades (WRB) have been becoming more and more popular to retain paste backfill in stopes. A few solutions have been developed to size the WRB. Among them, a solution developed by Yang and coworkers in 2017 is particularly relevant. However, this solution was calibrated and validated by 2D numerical modeling. Its validity in 3D conditions remains unknown. In addition, the local stability analysis was made by considering a horizontal sliding plane while their numerical modeling clearly showed an inclined plane. In this study, the validity of the Yang et al. solution is first evaluated against a few numerical results obtained with FLAC3D. The subjectivity in evaluating the instability onset of a structure in numerical modeling is further reduced by considering the first occurrence between displacement jump and coalescence of current yield zones passing through a WRB structure from the downstream to upstream slopes. The results show that both the global and local stability analysis equations of the Yang et al. solution need to be updated. For the global stability analysis, the value of the earth pressure coefficient needs to be modified while an inclined sliding plane needs to be considered for the local stability analysis. These considerations result in a considerable improvement because the updated solution does not contain any empirical calibration coefficient. Good agreements are obtained between the results obtained with numerical simulations and those predicted by the updated 3D analytical solution. The proposed solution is then further validated by

experimental result recently available in the literature. It can be used to design WRB to retain fluid-like paste backfill at the preliminary stage of a project.

Author keywords: Waste rock barricades; Instability criterion; Analytical solutions; FLAC3D.

6.1 Introduction

Filling underground mine stopes with tailings-based backfill is environment friendly because it helps reducing surface disposal of mine wastes. The use of cemented backfill allows improving ground stability condition, increasing ore recovery, minimizing ore dilution, alleviating ground subsidence, and improving ventilation efficiency (Grice 2001; Aubertin et al. 2002; Potvin et al. 2005; Hambley 2011).

Since the recent decades, cemented paste fill has become very popular in underground mines all over the world. Depending on the solid content (or water content), it may behave like a solid-like cake or fluid-like mud (Zheng and Li 2020). For most cases, it should contain enough water to ensure workability and facilitate transportation by pipes. When it is placed in a stope, a retaining structure, called a barricade, must be built at the base of the stope in the access drift near the drawing point to hold the slurried backfill in the stope.

Traditionally, barricades are constructed with concrete, shotcrete, fibercrete, timbers, or permeable bricks (Sivakugan et al. 2006; Berndt et al. 2007; Yumlu and Guresci 2007; Sivakugan 2008; Grabinsky 2010; Hughes et al. 2010; Lu et al. 2020). The construction of these types of the barricade is usually expensive and time-consuming. In Canada, barricades made of waste rocks have become more and more popular to confine slurried backfill in stopes. Compared to traditional barricades, the construction of waste rock barricades (WRB) is faster, easier and more economic. The construction material (waste rocks) can be available at the least cost. When the held cemented backfill becomes strong enough, the waste rocks used to build the barricades can easily be removed and reused as rockfill or construction material for other WRB. The use of waste rocks produced

during underground development avoids the transportation and hoisting of these materials from underground to surface, resulting in considerable energy and economic benefits.

Despite these numerous advantages, the design of WRB was mainly based on an approach of trial-and-error due to the unavailability of analytical solutions. A first solution for sizing WRB was proposed by Li and coworkers (Li et al. 2009; Li and Aubertin 2011) through the equilibrium analysis of a rectangular WRB. The solution tends to largely overestimate the required length of WRB due to the unrealistic consideration of WRB geometry. A modification had been made by Yang et al. (2014) after considering the equilibrium of a more realistic trapezoidal WRB. However, the application of the modified solution of Yang et al. (2014) may result in zero or negative value in the minimum required length of WRB as long as the interface friction angle between WRB and rock walls becomes high enough. A further improvement of the modified solution was given by considering the possible sliding of the top part of the trapezoidal WRB. A complete solution was then formulated by Yang et al. (2017a) after considering the equilibrium of the WRB block and the possible sliding within the WRB. The former was called global stability analysis while the latter was named local stability analysis (2017a). The solution of Yang et al. (2017a) thus contains two equations, one for global stability analysis and the other for local stability analysis of WRB. For both cases, Rankine's active earth pressure was used. In addition, the local stability analysis equation contains an empirical calibration coefficient. The calibration (for finding the value of the empirical calibration coefficient) and validation of the analytical solution were made against numerical modeling with FLAC2D. In practice, WRB usually has the same order of dimensions in the three mutually perpendicular directions and its stability analysis is typically a 3D problem. The solution proposed by Yang et al. (2017a) cannot be considered fully validated by numerical modeling. In addition, this solution for local stability is developed by considering a horizontal sliding plane while their numerical modeling clearly showed inclined sliding planes, which are recently further confirmed by laboratory WRB instability tests of Nujaim and coworkers (Nujaim et al. 2018, 2020a, 2020b). The validity of the Yang et al. (2017a) solution against 3D numerical

modeling is needed. The local stability analysis equation is also needed to be updated by considering a more realistic inclined sliding plane.

In this paper, the available analytical solutions used to size WRB are first reviewed. The validity of the Yang et al. (2017a) solution is then tested against numerical results obtained by numerical modeling with FLAC3D. The first update of this solution is then proposed by considering a more realistic earth pressure coefficient for the global and local stability analysis. The second update of the Yang et al. (2017a) solution is given by considering an inclined sliding plane for the local stability analysis. The updated 3D analytical solution is then validated against numerical results obtained by numerical modeling with FLAC3D without any calibration. The application of the proposed analytical solution and numerical modeling with FLAC3D is further illustrated in a laboratory test available in the literature.

6.2 Existing analytical solutions for the design of WRB

While a number of works have been published on the design of convention barricades (e.g., Wise and Strache 1914; Garcia and Cassidy 1937; Garrett and Campbell 1958; Mitchell et al. 1975; Smith and Mitchell 1982; Checkan 1985; Mitchell 1992; Hassani and Afrouz 2001; Kalsi 1994; Djahanguiri and Abel Jr 1997; Grice 1998; Kuganathan 2002; Harteis and Dolinar 2006; Sivakugan et al. 2006; Berndt et l. 2007; Nortjé et al. 2007; Revell and Sainsbury 2007a, 2007b; Sawyer and Watson 2007; Yumlu and Guresci 2007; Harteis et al. 2008; Hughes 2008; Sivakugan 2008; Grabinsky 2010; Hughes et al. 2010; Li et al. 2015; Lu et al. 2020), there are very few publications, if not any, on the design of barricades made of rockfill or waste rocks. To the authors' knowledge, Li and coworkers (Li et al. 2009; Li and Aubertin 2011) are the first who proposed an analytical solution for the design of WRB for underground mine backfilled stopes through a limit equilibrium analysis on a rectangular WRB. In practice, WRBs are trapezoidal and not rectangular due to the repose angle of waste rocks. An improvement on the solution of Li and Aubertin (2011) was then proposed by Yang et al. (2014).

Fig. 6.1 shows the Yang et al. (2014) model with a trapezoidal WRB. On the figure, H (m) is the backfill height; L_d (m) and H_d (m) are the barricades (drift) width and height, respectively; L_{BT} (m) and L_{BB} (m) are the top and bottom lengths of the trapezoidal WRB, respectively; α_1 (°) is the upstream slope angle, which is close to the repose angle of the waste rocks; α_2 (°) is the downstream slope angle of the WRB, which can be increased with a mechanical compactor.

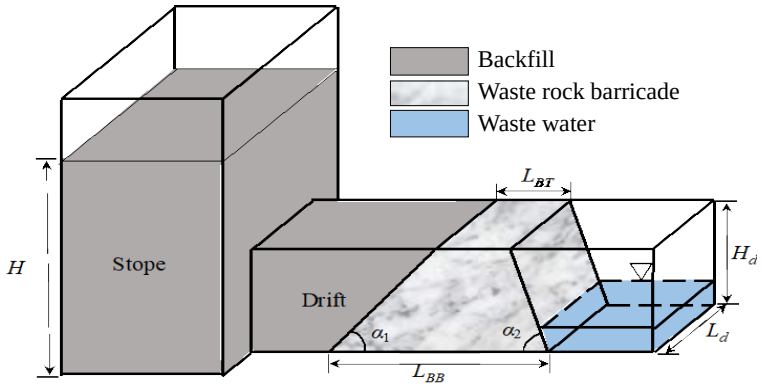

Figure 6.1 Schematic presentation of a backfilled stope with a trapezoidal WRB (adapted from Yang et al. 2014)

By considering the equilibrium of the trapezoidal WRB in the drift axis direction, Yang et al. (2014) proposed the following equation to determine the required top length of the WRB for retaining paste backfill:

$$L_{BT} = \frac{\gamma_b\left(H-\frac{H_d}{2}\right)\left(\frac{FS}{tan\,\delta_{wr}}-\frac{1}{tan\,\alpha_1}\right)-\gamma_{wr}H_d\left(\frac{1}{2}+K\frac{H_d}{3L_d}\right)\left(\frac{1}{tan\,\alpha_1}+\frac{1}{tan\,\alpha_2}\right)}{\gamma_{wr}\left(1+K\frac{H_d}{L_d}\right)} \quad (6.1)$$

where γ_b (kN/m^3) is the unit weight of slurried backfill; γ_{wr} (kN/m^3) is the unit weight of waste rocks; δ_{wr} (°) is the int erface friction angle between the drift walls (two lateral walls and floor) and the WRB; K is the earth pressure coefficient of waste rocks that is defined as the ratio between the horizontal stress perpendicular to the axis of the drift and the vertical stress, expressed as follows:

$$K = \frac{1-sin\,\phi_{wr}}{1+sin\,\phi_{wr}} \quad (6.2)$$

where ϕ_{wr} (°) is the internal friction angle of waste rock.

It should be noted that Eq. (6.1) implies that the total stress acting on the upstream slope of the WRB is close to the iso-geostatic pressure based on the overburden of the paste backfill. This is true during the pouring operation of a fluid-like paste backfill (Thompson et al. 2012; Jaouhar 2019; Zheng and Li 2020). When the paste backfill has a very high solid content, it may have a solid-like behavior. The pressure on barricades can be small, but the transportation by pipes becomes very difficult without powerful positive-displacement pumping (Zheng and Li 2020). In all cases, the consideration of an iso-geostatic overburden pressure results in a conservative design of WRB.

The application of Eq. (6.1) leads to a required top length of WRB significantly smaller than that calculated with the solution of Li and Aubertin (2011). This significant difference does not only come from the different considerations of WRB shape, but also from the fact that the vertical component of the total load perpendicularly acting on the upstream slope has the effect to increase the stability of the WRB. However, the application of Eq. (6.1) can also lead to a very small and even negative value in the minimum required top length L_{BT} of WRB when the interface friction angle between the waste rocks and rock walls is very large. Something should be wrong or incorrectly neglected. This consideration led to the internal local stability analysis on the WRB.

When the top length of WRB is very small, the top part of the WRB can be pushed away if the paste backfill pressure in the stope is large enough. By considering the possible sliding and equilibrium of the top part of the trapezoidal WRB along a horizontal sliding plane, the following equation was proposed by Yang et al. (2017a) to calculate the required top length of the WRB for retaining paste backfill in stopes:

$$L_{BT} = \frac{\gamma_b}{\gamma_{wr}}(H - H_d)\left(\frac{C_M \times FS}{tan\phi_{wr}} - \frac{1}{tan\,\alpha_1}\right) \tag{6.3}$$

where C_M is a calibration factor, which was determined as equal to 1.5 based on numerical results obtained by numerical modeling with FLAC2D.

The proposed solution of Yang et al. (2017a) is then composed of the following equations:

$$L_{BT} = \frac{\gamma_b\left(H-\frac{H_d}{2}\right)\left(\frac{FS}{tan\,\delta_{wr}}-\frac{1}{tan\,\alpha_1}\right)-\gamma_{wr}H_d\left(\frac{1}{2}+K\frac{H_d}{3L_d}\right)\left(\frac{1}{tan\,\alpha_1}+\frac{1}{tan\,\alpha_2}\right)}{\gamma_{wr}\left(1+K\frac{H_d}{L_d}\right)}, \text{ for } \delta_{wr} \le \delta_c \quad (6.4a)$$

$$L_{BT} = \frac{\gamma_b}{\gamma_{wr}}(H - H_d)\left(\frac{C_M \times FS}{tan\phi_{wr}} - \frac{1}{tan\,\alpha_1}\right), \text{ for } \delta_{wr} > \delta_c \quad (6.4b)$$

where δ_c (°) is a critical value of δ_{wr}, beyond which the local stability prevails. It is determined as follows:

$$\delta_c = tan^{-1}\frac{FS(2H-H_d)\,tan\,\alpha_1}{H_d+2(H-H_d)\left[\frac{C_M\times FS\times tan\,\alpha_1}{tan\phi_{wr}}\left(1+K_G\frac{H_d}{L_d}\right)-K_G\frac{H_d}{L_d}\right]+\frac{\gamma_{wr}}{\gamma_b}H_d\left(1+K_G\frac{2H_d}{3L_d}\right)\left(1+\frac{tan\,\alpha_1}{tan\,\alpha_2}\right)} \quad (6.4c)$$

Recently, Belem et al. (2020) proposed an empirical solution to determine the top length of WRB as follows:

$$L_{BT} = FS\left(2+\frac{H}{(80L_d+30)(L_d)^{-1.46}}\right) \quad (6.5)$$

This equation only involves the backfill height H (m) in the stope and WRB width L_d. The height of barricade (or drift) H_d (m), the unit weight of the backfill γ_b, and the physical (γ_{wr}) and mechanical (ϕ_{wr} and δ_{wr}) property parameters of waste rocks are absent in the equation. The equation is a specific solution with some specific numbers obtained through a process of calibration for and limited to the tested specific cases. It predicts a minimum (i.e with FS = 1) required top length of L_{BT} = 2 m, even the stope is empty without any backfill (i.e., H = 0). It cannot be used as a general solution for the design of WRB and will not be further discussed in this study.

6.3 Validity of the Yang et al. (2017a) solution against 3D numerical modeling

The solution of Yang et al. (2017a) developed for the design of WRB has only been calibrated and validated by numerical results obtained with FLAC-2D. Its validity in 3D conditions remains unknown.

The elastoplastic model with Mohr-Coulomb failure criterion used in FLAC3D has been largely used to analyze diverse problems in geotechnical engineering (Liu et al. 2016; Yang et al. 2017b).

Its validity against the analytical solution of Salençon (1969) has been shown in the manual of FLAC3D (Itasca 2013) and reproduced by the authors. Its validity against experimental results has been illustrated by Liu et al. (2016), who successfully reproduced the physical model tests of Mitchell et al. (1982) by numerical modeling with FLAC3D. Recently, Zhai et al. (2021) have validated once again the numerical model of FLAC3D against laboratory tests for the case of water seepage through a rockfill dike. FLAC3D can thus be considered as an efficient and effective tool for the analyses of diverse geotechnical problems as long as it is correctly used. Here, the validity of the Yang et al. (2017) solution in 3D conditions is tested by numerical modeling with FLAC3D.

Fig. 6.2a shows a WRB subjected to a linearly distributed pressure (p, kPa) associated with a fluid-like paste backfill placed shortly in the stope. Considering the iso-geostatic overburden pressure of a paste fill plug having a height of H = 12 m and a unit weight of γ_b = 19.6 kN/m^3 leads to a pressure of p = 137.2 kPa at the top of the WRB. The WRB is characterized as H_d = 5 m, L_d = 5 m, α_1 = 37° and α_2 = 37°. The waste rocks used to construct the barricade are considered to be homogeneous, isotropic, and elastoplastic, obeying the Mohr-Coulomb criterion. The physical and mechanical properties are: γ_{wr} = 19.6 kN/m^3 (unit weight), E_{wr} = 100 MPa (Young's modulus), ν_{wr} = 0.3 (Poisson's ratio), ϕ_{wr} = 38° (internal friction angle), and c_{wr} = 0 kPa (cohesion). The rock mass is linearly elastic and characterized as γ_r = 26.5 kN/m^3 (unit weight), E_r = 30 GPa (Young's modulus), and ν_r = 0.3 (Poisson's ratio).

Fig. 6.2b shows a numerical model of the WRB built with FLAC3D. Interface elements are introduced between the WRB and side rock walls as well as between the WRB and drift floor in rock. Their normal (k_n) and shear (k_s) stiffness were calculated by following the suggestion given in the manual of FLAC3D (Itasca 2013). The interface friction angle δ_{wr} between the WRB and rock walls as well as between the WRB and drift floor in rock can be taken as equal to the friction angle of the waste rocks if the rock surfaces are rough or to two-third of the friction angle of the waste rocks if the rock surfaces are flat. The bottom in the rock of the out boundary of the numerical model was fixed in all horizontal and vertical directions. The front and back out boundaries in rock

were fixed in the *Y*-direction. The two ends of the rock floor were fixed in the *X*-direction. After a series of sensitivity analyses of mesh size, an optimal mesh of 0.1 m × 0.25 m × 0.2 m (at the top of the barricade) was determined and used to analyze the stability of the WRB for the case of H = 9 m, L_d = 5 m, H_d = 5 m $\alpha_1 = \alpha_2 = 37°$, $\phi_{wr} = 38°$ and $\delta_{wr} = 30°$. Finer or coarser meshes can be used at the base of a case by case to obtain stable and reliable numerical results, depending on the value of L_{BT} and the corresponding sensitivity analysis of mesh. Sensitivity analysis of domain does not show any significant influence of this parameter on the numerical results. Subsequently, the front and back rock walls were taken as 1 m while the rock floor was taken as 0.5 m. The numerical simulations were performed by using the (default) option of the small strain of FLAC3D.

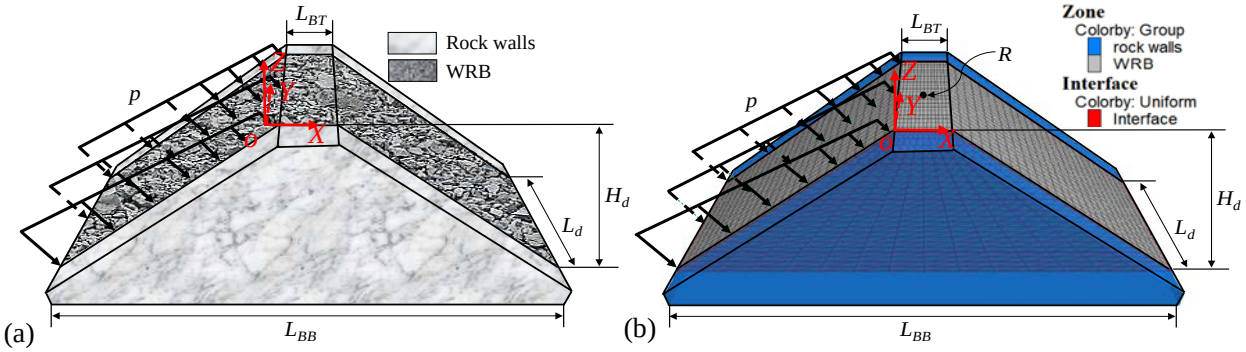

Figure 6.2 (a) A trapezoidal WRB submitted to a paste backfill pressure p along the upstream slope face [adapted from Yang et al. (2017a)]; (b) A numerical model of the trapezoidal WRB built with FLAC3D; *R* is a monitoring point

To evaluate if a WRB is stable or becomes unstable, a common way is to verify the yield state of the structure material by tension or shear (e.g., Beer 1986; Revell and Sainsbury 2007a, 2007b). Yang et al. (2017a) have shown that this manner of instability evaluation can be quite subjective. They further proposed to use a criterion of structure instability by observing the displacements at some critical points. The structure of WRB is considered as unstable as long as the displacements at the monitored points jump (i.e., increase substantially) with a slight decrease of the WRB length.

The criterion of structure instability based on displacement is particularly useful to reduce the subjectivity in evaluating the failure of a WRB structure due to global instability. For example, Fig. 6.3 shows a combined view of *X*-displacement (i.e., horizontal displacement in the *X* direction) contour (the back half part) and yield states (the front half part) of a WRB having an interface friction angle of δ_{wr} = 15° when the top length L_{BT} is taken as 5.4 m (Fig. 6.3a) and 5.3 m (Fig. 6.3b), respectively. In both cases, current yield zones are absent and the structures of WRB seem to be stable. However, the maximum *X*-displacement jumps from 4.83 mm when L_{BT} = 5.4 m to about 4 m when L_{BT} is slightly reduced to 5.3 m. The WRB structure remains stable at L_{BT} = 5.4 m and becomes unstable at L_{BT} = 5.3 m. The minimum required top length of the WRB is 5.4 m for this case. One recalls that this is a case of global stability analysis because the instability of the WRB is caused by the sliding of the whole WRB structure.

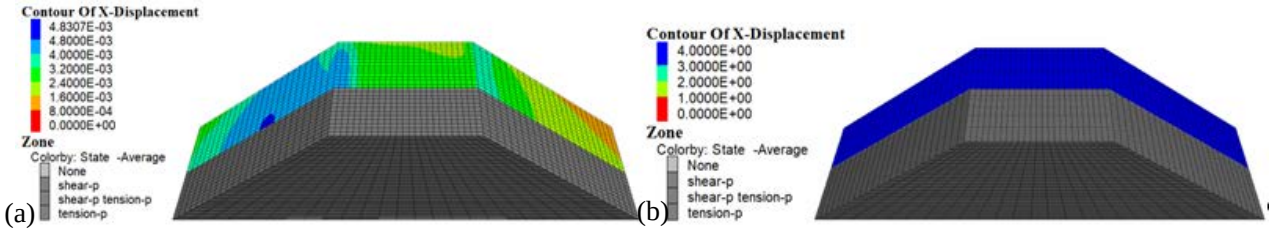

Figure 6.3 The contour of *X*-displacement (back half) and yield states (front half) of the WRB for δ_{wr} = 15°: (a) L_{BT} = 5.4 m; (b) L_{BT} = 5.3 m (shear-p and tension-p indicate the occurrence of shear and tension in the past, but not now)

While the criterion of structure instability based on displacements has been successfully used to evaluate the failure of WRB and side-exposed backfill (Yang et al. 2017b; Liu et al. 2018; Wang et al. 2021), a few studies showed that the use of this criterion can also involve a certain subjectivity (Pagé et al. 2019; Keita et al. 2021). This is further shown here for the local stability analysis of WRB with numerical modeling.

Fig. 6.4 shows the combined view of *X*-displacement contour (the back half part) and yield states (the front half part) of a WRB having an interface friction angle of δ_{wr} = 35° when the top length L_{BT} is taken as 2.2 m (Fig. 6.4a), 2.1 m (Fig. 6.4b) and 2 m (Fig. 6.4c), respectively. When the WRB top length is 2.2 m, sporadic zones of current yield (indicated by shear-n) can be observed. The small value of 0.0695 m in the maximum *X*-displacement indicates that the WRB structure is stable. When the top length is reduced to a value of L_{BT} = 2.1 m, the maximum *X*-displacement increases significantly to a value of 0.121 m, which is still far from being able to be qualified as a jump compared to the maximum *X*-displacement of 0.0695 m at L_{BT} = 2.2 m. However, the current yield by shear zones coalesce and form a sliding wedge near the top part of the WRB with a sliding plane passing through the WRB from the downstream slope to the upstream slope. These results indicate that the WRB structure becomes unstable even though the maximum *X*-displacement remains relatively small. The minimum required top length of the WRB is 2.1 m for this case. When the top length of the WRB is further reduced to L_{BT} = 2 m, the maximum *X*-displacement jumps to 2.153 m (the value keeps increasing with more steps), further indicating the occurrence of instability of the WRB structure. In all cases, one sees that only a portion of the material near the top of the WRB fails. One recalls that the instability associated with the sliding of the top part of the WRB is called local instability. The application of the criterion of structure instability based on displacement in such case may lead to an underestimate of the minimum required top length, and subsequently a nonconservative design of WRB.

In this study, the failure of structural instability is evaluated to correspond to the first occurrence among displacement jump and coalescence of current yield zones passing through the WRB structure from the downstream to the upstream slope. The former is generally applied to global instability while the latter to local instability of WRB summarized by numerical simulation results.

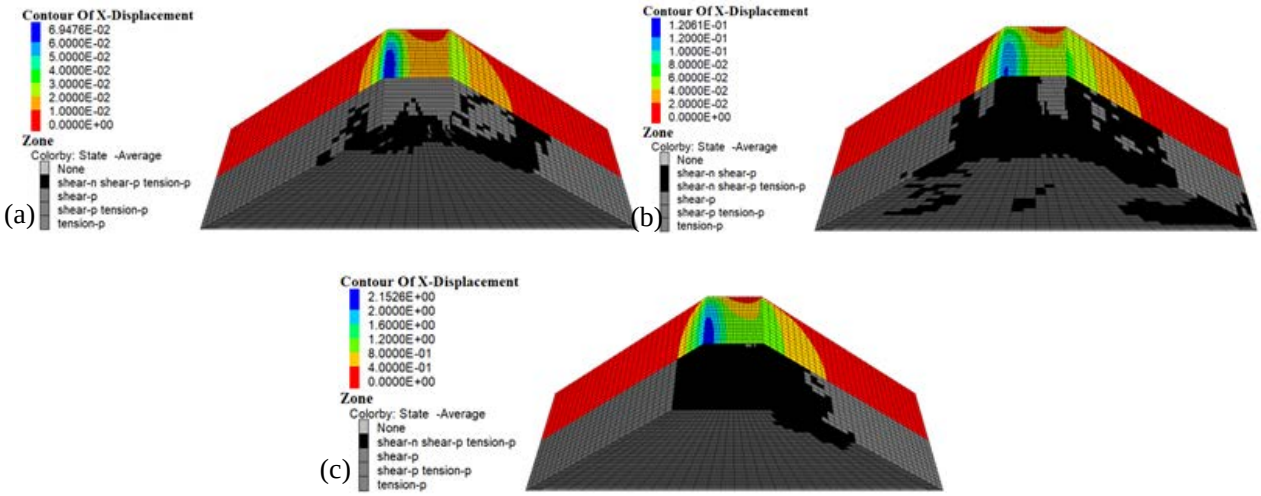

Figure 6.4 Contour of X-displacement (back half) and yield states (front half) of the WRB for δ_{wr} = 35°: (a) L_{BT} = 2.2 m; (b) L_{BT} = 2.1 m; (c) L_{BT} = 2 m (shear-n indicates the occurrence of current yield by shear)

Fig. 6.5 shows the variation of the minimum required top length L_{BT} as a function of interface friction angle δ_{wr}, obtained by numerical modeling with FLAC3D by considering H_d = 5 m, L_d = 5 m, α_1 = 37°, α_2 = 37°, and an iso-geostatic overburden pressure distribution starting with p = 137.2 kPa at the top of the upstream slope face of the WRB, generated by the pour of a fluid-like paste fill plug having H = 12 m and γ_b = 19.6 kN/m^3. The minimum required top lengths L_{BT} predicted by applying the analytical solution of Yang et al. (2017a) with $K = K_a$ and C_M = 1.5 have also been plotted on the figure. The agreement between the numerical results obtained with FLAC3D and those predicted with the solution of Yang et al. (2017a) is poor for all values of δ_{wr}. An improvement to the solution of Yang et al. (2017a) is necessary for both the global and local stability analyses.

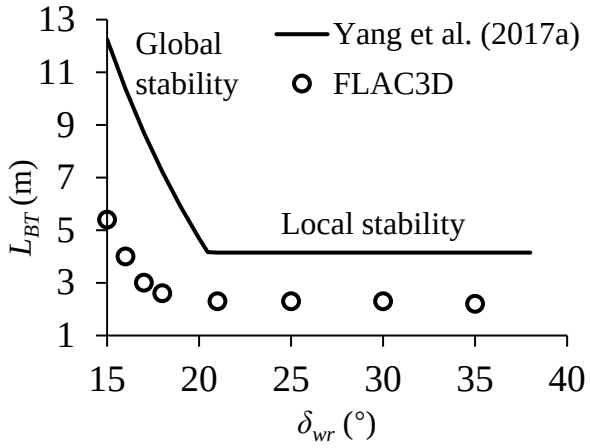

Figure 6.5 Variation of the minimum required top length L_{BT} as a function of the interface friction angle δ_{wr}, obtained by numerical modeling with FLAC3D and calculated with the Yang et al. (2017a) solution [Eq. (6.4) with C_M = 1.5 and $K = K_a$]

6.4 Update of the Yang et al. (2017a) solution

Before making any modification to the solution of Yang et al. (2017a), one needs to understand the origin of the significant differences between the numerical and analytical solutions, shown in Fig. 6.5.

For the global stability analysis ($\delta_{wr} \leq \delta_c$), Eq. (6.4a) of Yang et al. (2017a) solution was developed by considering the shear strength and confining effects of the two sidewalls. The third dimension (L_d) was well considered and the equation is a three-dimensional solution without any calibration. In the numerical modeling, the criterion of structure instability based on displacement has been used in the 2D numerical modeling of Yang et al. (2017a) and the 3D numerical modeling here. When the value of L_d is very large, Eq. (6.4a) becomes close to a 2D solution and the results obtained by the 2D numerical modeling with FLAC2D have been successfully reproduced by 3D numerical modeling with FLAC3D. Good agreements were then obtained between the numerical and analytical solutions, as shown in Yang et al. (2017a). This indicates that the 2D numerical

model of FLAC2D is only a special case of the 3D numerical model of FLAC3D. The significant differences between the 3D numerical modeling and the 3D analytical solution of Yang et al. (2017a) shown in Fig. 6.5 cannot be attributed to the 3D numerical modeling with FLAC3D. One must limit our analysis on the 3D analytical solution [Eq. (6.4a)] of Yang et al. (2017a).

One recalls that the 3D analytical solution of Yang et al. (2017a) for the global stability analysis was developed by considering an earth pressure coefficient (K) equaling to the value of the Rankine's active earth pressure coefficient K_a [see Eq. (6.2)]. It is interesting to note that the value of this parameter does not have any more influence on the required top length of WRB as long as the value of L_d becomes very large compared to the value of H_d (i.e., $L_d >> H_d$). This indicates that even the value of K does not correspond to the reality, one still obtains good agreements between the 3D analytical solution of Yang et al. (2017a) and the 2D and 3D numerical modeling as long as the value of L_d is large enough compared to the value of H_d. When L_d is not much larger than H_d, the value of K can significantly affect the results. If the value of K does not correspond to the reality, the application of Eq. (6.4a) of the Yang et al. (2017) solution can lead to poor estimation of the required top length of WRB. The poor agreements between the minimum required top lengths obtained by the numerical modeling with FLAC3D and those predicted with the solution of Yang et al. (2017a) for the global stability tend to indicate this is the case. To verify this hypothesis, the horizontal normal stresses perpendicular to the sidewalls over an interface between the WRB and a sidewall obtained by the 3D numerical modeling with FLAC3D for the case of Figure 6.3b are examined. The total horizontal force perpendicular to the sidewall can then be obtained through the accumulation of resulting forces on each numerical element. One recalls that K was defined by Yang et al. (2017a) as a ratio between the horizontal stress perpendicular to the sidewalls of the drift and the vertical stress based on the overburden (without any consideration of arching effect). The total horizontal force associated with the horizontal normal stresses perpendicular to one sidewall and the subsequent total shear force was then obtained by Yang et al. (2017a) using a constant value of K and a linearly distributed vertical stress based on the overburden solution.

Comparison between the theoretical and numerical results of the total horizontal force over the sidewall leads to a value of overall K = 1.13; the details are given in Appendix A. Additional calculations for K under different cases show K ranges from 1.06 to 1.26; the details are given in Ph.D. thesis (Zhai 2021).

The updated solution of Yang et al. (2017) for the global stability analysis is then given as follows with K = 1 based on the range estimated by different cases and simplification of calculation:

$$L_{BT} = \frac{\frac{1}{2}(p_t+p_b)\left(\frac{FS}{\tan\delta_{wr}}-\frac{1}{\tan\alpha_1}\right)-\gamma_{wr}H_d\left(\frac{1}{2}+\frac{H_d}{3L_d}\right)\left(\frac{1}{\tan\alpha_1}+\frac{1}{\tan\alpha_2}\right)}{\gamma_{wr}\left(1+\frac{H_d}{L_d}\right)} \tag{6.6}$$

where p_t and p_b are the fluid-like paste backfill pressures at the top and base of the upstream slope of WRB, respectively given as follows:

$$p_t = \gamma_b(H - H_d) \tag{6.7}$$

$$p_b = \gamma_b H \tag{6.8}$$

For the local stability analysis ($\delta_{wr} > \delta_c$), it should first be noted that Eq. (6.4b) of the Yang et al. (2017a) solution does not involve any earth pressure coefficient. Therefore, the poor agreements between the minimum required top lengths obtained by the numerical modeling with FLAC3D and those predicted with the solution of Yang et al. (2017a) for the local stability have nothing to do with the value of K.

In terms of criterion of structure instability, the example of Figure 6.4 shows that the minimum required top length evaluated based on the coalescence of current yield zones passing through the WRB structure is only slightly longer than that obtained by observing the jump of displacement. The use of yield zones to evaluate the instability of WRB structure thus tends to slightly improve the agreements between the numerical and analytical results. The large overestimation of the minimum required top lengths by the analytical solution of Yang et al. (2017a) shown in Figure 6.5 cannot be explained using yield zones to evaluate the failure of WRB.

Despite the significant differences between the 3D numerical modeling and the prediction of Eq. (6.4b) of Yang et al. (2017a) solution shown in Fig. 6.5, good agreements were obtained between the 3D numerical modeling and those obtained by 2D numerical modeling and predicted by the analytical solution of Yang et al. (2017a) as long as the value of L_d is large enough. This indicates once again that the 2D numerical model of FLAC-2D is only one special case of the 3D numerical model of FLAC3D. The significant differences between the 3D numerical modeling and the analytical solution [Eq. (6.4b)] of Yang et al. (2017a) shown in Fig. 6.5 cannot be attributed to the 3D numerical modeling with FLAC3D. Further analysis has to be limited, once again, to the model used by Yang et al. (2017a) to obtain their Eq. (6.4b).

One recalls that Yang et al. (2017a) initially assumed a horizontal sliding plane at a depth of h, as shown in Fig. 6.6 by the trapezoid in light blue color on top of the WRB. Their further theoretical analysis indicated that the most critical case was at $h = 0$, leading to the disappearance of the third dimension L_d in Eq. (6.4b). Based on this model, the sliding only takes place along the top surface of the WRB. This is neither confirmed by numerical modeling, nor by experimental results. Rather, the 2D (see Fig. 8b of Yang et al. 2017a) and 3D (see Fig. 6.4b or 6.4c of this study) numerical modeling and the laboratory WRD instability tests of Nujaim et al. (2020b) showed that the sliding plane is inclined with a certain thickness of h. A new solution needs to be developed by considering an inclined slide plane for the local stability analysis of WRB

Fig. 6.6 schematically shows a vertical cross-section of a WRB along the drift-axis direction for analyzing its local stability. The sliding plane is assumed to start at a depth h below the roof level of the drift and make an angle of β below the horizontal. The sliding block can then be decomposed into a trapezoid on top and a triangle underneath. The trapezoid and the triangle share a common base of length a (m), expressed as follows:

$$a = L_{BT} + h\left(\frac{1}{tan\,\alpha_1} + \frac{1}{tan\,\alpha_2}\right) \tag{6.9}$$

while the triangle has a height of h_1 (m), expressed as follows:

$$h_1 = \frac{a \tan\beta}{1 - \tan\beta / \tan\alpha_2} \tag{6.10}$$

P' (kN) is an acting force exerted by a fluid-like paste backfill on the upstream slope of the sliding block, expressed as follows:

$$P' = \left(p_t + \frac{\gamma_b h}{2}\right)\frac{hL_d}{\sin\alpha_1} \tag{6.11}$$

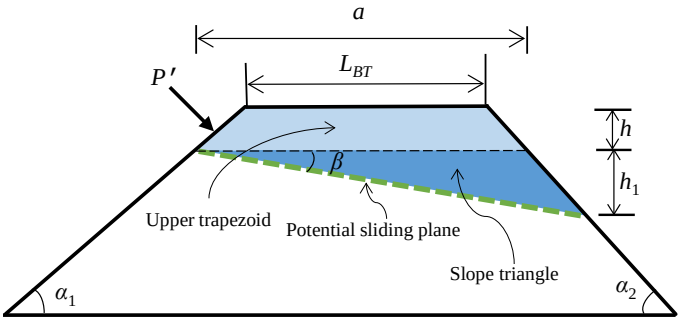

Figure 6.6 Schematic view of a WRB with the inclined plane for local stability analysis

Fig. 6.7 shows a 3D view of the isolated sliding wedge with all the acting forces. In the figure, C_S (kN) is a horizontal force perpendicular to the sidewall along the WRB and sidewall contact of the sliding wedge; C_{S1} (kN), C_{S2} (kN), C_{S3} (kN), and C_{S4} (kN) are the compressive forces by considering different sections along the WRB and sidewall contact of the sliding wedge; S_S (kN) is the shear resistance along the WRB and sidewall contact in a direction parallel to the sliding plane, but against the sliding direction; N (kN) is a supporting force perpendicular to the sliding plane; T (kN) is the shear resistance on the sliding plane against the sliding direction; W (kN) is the weight of the sliding wedge, given by

$$W = \frac{\gamma_{wr} L_d}{2}[(L_{BT} + a)h + ah_1] \tag{6.12}$$

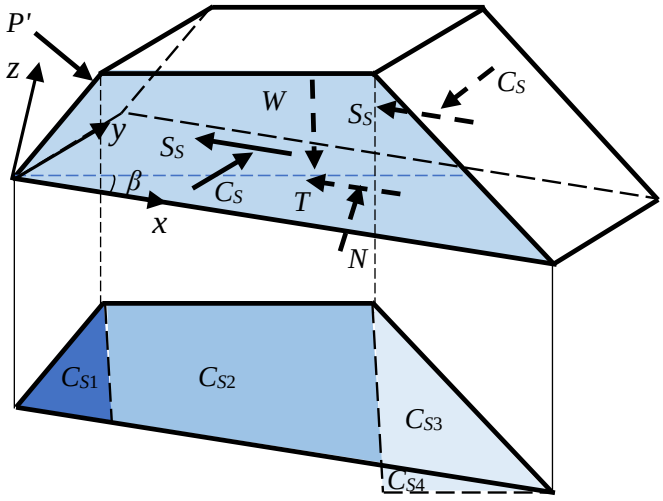

Figure 6.7 A sliding wedge on the top of a WRB with its acting forces and compressive forces of different parts acting along one lateral wall

Considering the equilibrium of the wedge in the direction perpendicular to the sliding plane leads to:

$$N = P' cos(\alpha_1 + \beta) + \frac{\gamma_{wr} L_d \cos\beta}{2}[(L_{BT} + a)h + ah_1] \quad (6.13)$$

Considering the equilibrium of the wedge along the direction of sliding leads to:

$$T + 2S_S = P' sin(\alpha_1 + \beta) + \frac{\gamma_{wr} L_d \sin\beta}{2}[(L_{BT} + a)h + ah_1] \quad (6.14)$$

By considering a stress state based on the overburden solution without any arching, the horizontal stress σ_h (kPa) can be expressed as follows:

$$\sigma_h = K\gamma_{wr} d \quad (6.15)$$

where d (m) is the depth of the calculation position of horizontal stress from the barricade top surface; K value can range from the Rankine's active (K_a) to passive (K_p) earth pressure coefficients:

$$K_p = \frac{1+\sin\phi_{wr}}{1-\sin\phi_{wr}} \geq K \geq \frac{1-\sin\phi_{wr}}{1+\sin\phi_{wr}} = K_a \quad (6.16)$$

By considering the area (upper trapezoid and slope triangle) between the WRB and sidewall contact surface, the horizontal force C_S can be given by:

$$C_S = C_{S1} + C_{S2} + C_{S3} - C_{S4} \tag{6.17}$$

where C_{S1}, C_{S2}, C_{S3}, and C_{S4} can be expressed as follows, respectively:

$$C_{S1} = \int_0^{\frac{h}{tan\alpha_1}} \frac{K\gamma_{wr}(xtan\alpha_1 + xtan\beta)^2}{2} dx = \frac{K\gamma_{wr}h^3(tan\alpha_1 + tan\beta)^2}{6tan^3\alpha_1} \tag{6.18}$$

$$C_{S2} = \int_{\frac{h}{tan\alpha_1}}^{\frac{h}{tan\alpha_1}+L_{BT}} \frac{K\gamma_{wr}(h + xtan\beta)^2}{2} dx$$

$$= \frac{\gamma_{wr}}{6}\left\{3h^2L_{BT} + \frac{3h^2L_{BT}tan\beta(tan\alpha_1 + tan\beta)}{tan^2\alpha_1} + L_{BT}^2tan\beta\left[L_{BT}tan\beta + 3h\left(1 + \frac{tan\beta}{tan\alpha_1}\right)\right]\right\} \tag{6.19}$$

$$C_{S3} = \int_0^{\frac{h+h_1}{tan\alpha_2}} \frac{\gamma_{wr}(xtan\alpha_2)^2}{2} dx = \frac{K\gamma_{wr}(h+h_1)^3}{6tan\alpha_2} \tag{6.20}$$

$$C_{S4} = \int_0^{\frac{h+h_1}{tan\alpha_2}} \frac{K\gamma_{wr}x^2tan\beta(2tan\alpha_2 - tan\beta)}{2} dx = \frac{\gamma_{wr}tan\beta(2tan\alpha_2 - tan\beta)(h+h_1)^3}{6tan^3\alpha_2} \tag{6.21}$$

$$C_S = C_{S1} + C_{S2} + C_{S3} - C_{S4} = \frac{K\gamma_{wr}}{6}\left[\frac{(h' + L_{BT}tan\beta)^3}{tan\alpha_2 - tan\beta} + h'^2\left(\frac{h}{tan\alpha_1} + 3L_{BT}\right) + L_{BT}^2tan\beta(L_{BT}tan\beta + 3h')\right] \tag{6.22}$$

where,

$$h' = h\left(1 + \frac{tan\beta}{tan\alpha_1}\right) \tag{6.23}$$

The equation of C_S is validated by the same result obtained with three different methods (e.g., integrals in the horizontal or vertical direction). The development and validation process is shown in the Ph.D. thesis (Zhai 2021).

The shear resistance in the vertical direction can be given by considering the Mohr-Coulomb criterion:

$$S_{S.\max} = C_S\, tan\,\delta_{wr}$$

$$= \frac{K\gamma_{wr}\,tan\,\delta_{wr}}{6}\left[\frac{(h' + L_{BT}tan\beta)^3}{tan\alpha_2 - tan\beta} + h'^2\left(\frac{h}{tan\alpha_1} + 3L_{BT}\right) + L_{BT}^2tan\beta(L_{BT}tan\beta + 3h')\right] \tag{6.24}$$

The shear resistance along the sliding plane can then be given by

$$T_{max} = N\,tan\,\phi_{wr} = \left\{P'\,cos(\alpha_1 + \beta) + \frac{\gamma_{wr} L_d\,cos\,\beta}{2}\left[(L_{BT} + a)h + ah_1\right]\right\} tan\,\phi_{wr} \tag{6.25}$$

The *FS* of the sliding wedge is then obtained by considering the capacity and demand as follows:

$$FS = \frac{T_{max} + 2S_{S.max}}{T + 2S_S} \tag{6.26}$$

Introducing Eqs. (6.14), (6.24), and (6.25) into Eq. (6.26) leads to an update of the Yang et al. (2017a) solution for the local stability analysis of WRB as follows:

$$FS = \frac{[P\prime\,cos(\alpha_1 + \beta) + b\,cos\,\beta]\,tan\,\phi_{wr} + c\,tan\,\delta_{wr}}{bsin\beta + P\prime\,sin(\alpha_1 + \beta)} \tag{6.27}$$

where,

$$b = \frac{\gamma_{wr} L_d}{2}\left[(L_{BT} + a)h + ah_1\right] \tag{6.28}$$

$$c = \frac{K\gamma_{wr}}{3}\left[\frac{(h' + L_{BT}tan\beta)^3}{tan\alpha_2 - tan\beta} + h'^2\left(\frac{h}{tan\alpha_1} + 3L_{BT}\right) + L_{BT}^2 tan\beta(L_{BT}tan\beta + 3h')\right] \tag{6.29}$$

Eqs. (6.6) and (6.27) constitute the proposed update solution of Yang et al. (2017a) for the design of WRB for retaining fluid-like paste backfill in underground mine stopes.

It should be noted that the proposed solution [Eqs. (6.6) and (6.27)] does not contain any calibration coefficients. The search of the minimum value of FS for the local stability analysis needs to solve the partial differential equations $\partial FS/\partial h = 0$ and $\partial FS/\partial \beta = 0$ to first find the critical values of h and β and after then the critical value of FS. Similarly, the search of the required top length of WRB for the local stability analysis needs to solve the two partial differential equations $\partial L_{BT}/\partial h = 0$ and $\partial L_{BT}/\partial \beta = 0$ to first find the critical values of h and β and after then the critical value of L_{BT}.

Solving $\partial FS/\partial h = 0$ and $\partial FS/\partial \beta = 0$ or $\partial L_{BT}/\partial h = 0$ and $\partial L_{BT}/\partial \beta = 0$ is not easy to obtain simple closed-form expressions. With the Solver of Microsoft Excel®, this is not necessary and the task of looking for the minimum value of FS and the required top length L_{BT} becomes very easy to execute. This is illustrated through an example of calculations with Microsoft Excel®.

One considers a case with a fluid-like paste backfill having a unit weight of γ_b = 20 kN/m^3 and a height of H = 12 m in the stope. The geotechnical properties of the waste rocks used to construct the barricade are characterized as γ_{wr} = 20 kN/m^3, ϕ_{wr} = 38°, and δ_{wr} = 30°. The geometries of the WRB are $H_d = L_d$ = 5 m and $\alpha_1 = \alpha_2$ = 37°. The earth pressure coefficient is considered as K = 1 for global and local stability analyses.

At the starting point of calculation, β = 45°- ϕ_{wr} /2 is taken as the first guess for the value of β. Solving Eq. (6.27) with FS = 1 and different h results in different values of L_{BT}. The maximum value of L_{BT} along with a critical value of h can then be identified. For the example considered here, one obtains a critical top length of L_{BT} = 1.68 m at a critical height of h = 0.425 m. To verify if this is the final and optimal result, the second step of iteration is made by fixing h = 0.425 m. Solving Eq. (6.27) with FS = 1 and different β results in different values of L_{BT}. The maximum value of L_{BT} along with a critical value of β are then identified. For the example here, one obtains a critical top length of L_{BT} = 1.78 m at a critical sliding plane angle of β = 20.5°. These results are different than those of the previous iteration step. New iterations are necessary and should be repeated until the arrival of stable results. These processes are executed in Microsoft Excel® are presented in Appendix B. A copy of the Excel file is attached as Supplementary and accessible to all readers.

Table 6.1 shows a summary of the iterations of calculations. This process of iterations should be performed case by case as long as the geometry or/and material parameters change. For the illustrative example considered here, three steps of iteration are enough to arrive at the final solution with a critical height h = 0.425 m, critical sliding plane inclination angle of β = 20.5°, and the minimum required top length of L_{BT} = 1.78 m. It is interesting to note the critical height h is bigger than zero and the critical sliding angle β is not too far from the value of 45°– ϕ_{wr}/2. These predictions are quite close to what has been shown in the laboratory WRB instability tests of Nujaim et al. (2020b).

Table 6.1 A summary of the iteration steps to obtain the critical value of L_{BT}

Step of iteration	Given β (°)	Critical h (m)	Given h (m)	Criticalβ (°)	L_{BT} (m)
0	26	0.425			1.68
1			0.425	20.5	1.78
2	20.5	0.425			1.78

6.5 Validation of the proposed solution

6.5.1 By 3D numerical modeling

Table 6.2 shows a program of numerical simulations performed with FLAC3D to test the validity of the proposed solution [Eqs. (6.6) and (6.27)]. As the proposed solution does not contain any calibration coefficients, all comparisons shown hereafter are the tests of the predictive ability of the proposed solution.

To obtain stable and reliable numerical results, the sensitivity analysis of mesh must be made case by case for each numerical model to obtain an optimal mesh for each case. The number of iterations through the command “Step” should be increased and large enough as the meshes become finer. A few examples of the sensitivity analyses of mesh are given in Appendix C.

Table 6.2 Program of numerical simulations with FLAC3D for testing the predictive ability of the proposed solution [Eqs. (6.6) and (6.27)] with $\alpha_1 = 37°$, $\gamma_b = 19.6$ kN/m^3, $\gamma_{wr} = 19.6$ kN/m^3, $c_{wr} = 0$ kPa, $\phi_{wr} = 38°$, $E_{wr} = 100$ MPa, $\nu_{wr} = 0.3$, $\gamma_r = 26.5$ kN/m^3, $E_r = 30$ GPa, and $\nu_r = 0.3$

Case	H (m)	H_d (m)	α_2 (°)	ϕ_{wr} (°)	δ_{wr} (°)	L_d (m)
0	9, 12	5	37	38	15 ~ ϕ_{wr}	5
1	9	3, 7	37	38	15 ~ ϕ_{wr}	5
2	9	5	34	38	15 ~ ϕ_{wr}	5
3	9	5	37	40	15 ~ ϕ_{wr}	5
4	9	5	37	38	16, 30	3 ~ 200

Fig. 6.8 shows the variation of the minimum required top length L_{BT} as a function of interface friction angle δ_{wr}, obtained by numerical modeling with FLAC3D and predicted by using the proposed analytical solution [Eqs. (6.6) and (6.27)] for Cases 0 (Fig. 6.8a), 1 (Fig. 6.8b), 2 (Fig. 6.8c), and 3 (Fig. 6.8d) of Table 6.2, respectively.

From Fig. 6.8a, it can be seen that the minimum required top length increases as the fluid-like paste backfill height in the stope increases. This indicates that the pressure in the backfilled stope has a significant influence on the stability of WRB. Good knowledge of the paste fill pressure is thus important to the design of WRB. In addition, the results also indicate that the local instability is the most plausible while global instability may take place when the fluid-like past backfill height is large, and the rock-wall interface friction angle is small. All these are well captured by the proposed solution. The good agreement between the numerical results and those predicted with the proposed solution (without any calibration) indicates that the proposed solution is validated by 3D numerical modeling.

From Fig. 6.8b, one sees again that the local instability is the most plausible while global instability may take place when the barricade has a small height, and the rock-wall interface friction angle is small. When the WRB is tall, the local instability is the most plausible. All these trends are well captured by the proposed analytical solution. The good agreements between the numerical results and those predicted with the proposed solution (without any calibration) show once again the validation of the proposed solution by the 3D numerical modeling with FLAC3D.

When the downstream slope angle is reduced or when using a strong waste rock for the construction of WRB, Figs. 5.8c and 5.8d tend to show that the global instability is less possible. This trend is well captured by the proposed solution. The good agreements between the numerical modeling and analytical prediction indicate once again the validity of the proposed analytical solution.

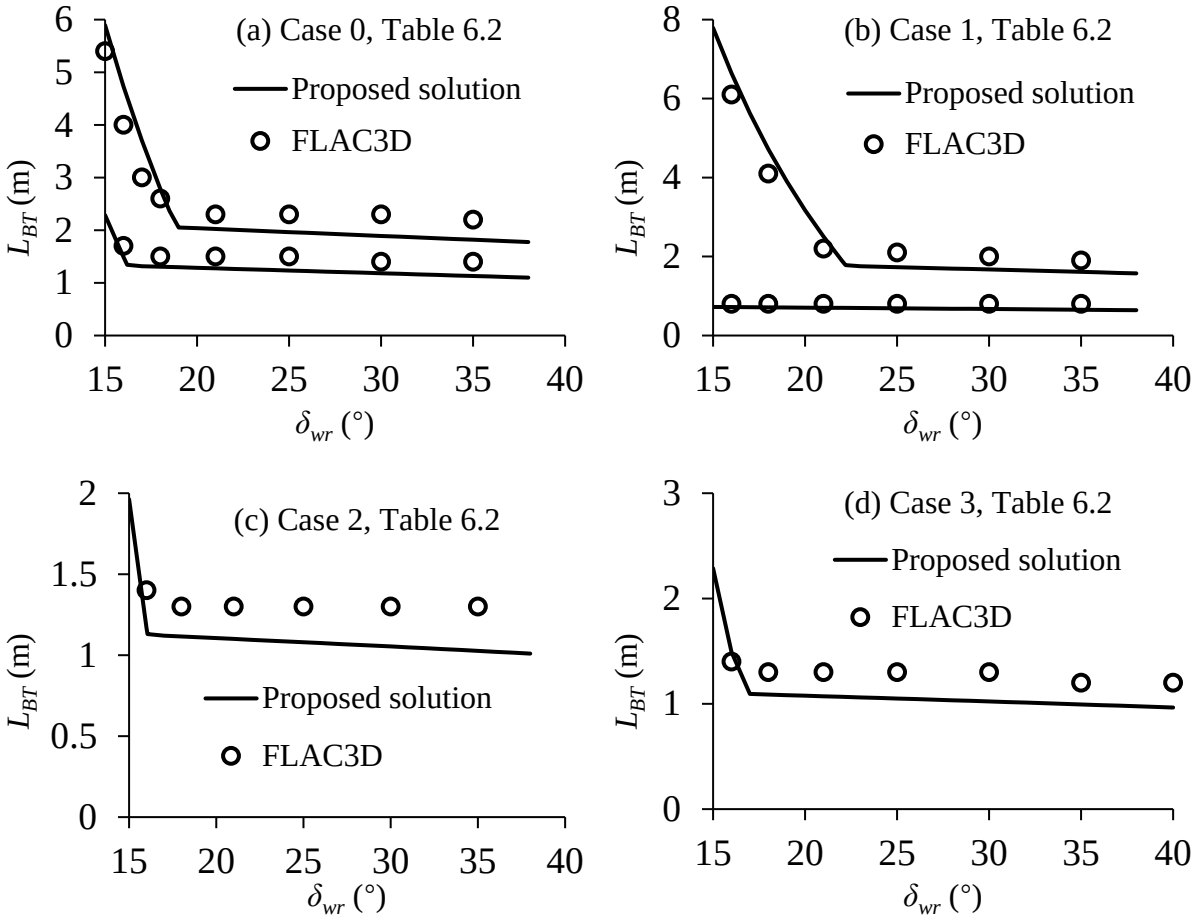

Figure 6.8 Variation of the minimum required top length L_{BT} as a function of interface friction angle δ_{wr}, obtained by numerical simulations with FLAC3D and predicted by using the proposed solution without any calibration for Cases 0 (a), 1 (b), 2 (c), and 3 (d) of Table 6.2.

Fig. 6.9 shows the variation of the minimum required top length L_{BT} as a function of barricade (drift) widths L_d, obtained by numerical modeling with FLAC3D and predicted by using the proposed analytical solution [Eqs. (6.6) and (6.27)] for Cases 4, Table 6.2. An enlarged view is also given on the right side to show the details of the results at small values of L_d.

When the interface friction angle $\delta_{wr} = 30°$, one sees that the stability of the WRB is only controlled by the local instability. The minimum required top length L_{BT} slightly increases when the drift width

L_d increases from 3 m to 200 m. All these trends shown by the 3D numerical modeling are well captured by the proposed solution. Good agreements are obtained between the numerical modeling and the prediction by using the proposed analytical solution [Eq. (6.6)].

When the interface friction angle δ_{wr} = 16°, one sees that global instability takes place as long as the drift width L_d is not smaller than 5 m for the geometry and materials considered here. The increase of the minimum required top length L_{BT} with increasing L_d shown by the 3D numerical modeling is well captured by the proposed solution, qualitatively and quantitatively. However, when L_d is smaller than 5 m, the proposed solution predicts a negative value, indicating that the global instability is impossible; this is further confirmed by the numerical modeling, which indeed shows a local instability of the WRB on the top. A good agreement is obtained between the numerical modeling and the prediction by using the local stability solution [Eq. (6.21) along with Eq. (6.6)], showing once again the proposed solution.

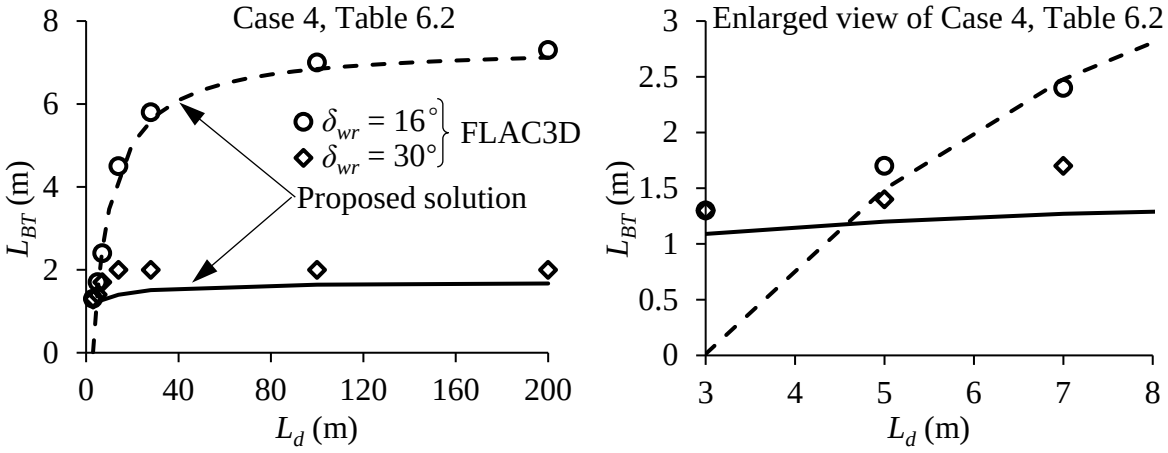

Figure 6.9 Variation of the minimum required top length L_{BT} as a function of drift width L_d, obtained by numerical simulations with FLAC3D and predicted by using the proposed solution without any calibration for Case 4, Table 6.2. Left, full view; right, an enlarged view.

6.5.2 By experimental results

To further test the validity of the proposed analytical solution, a scaled-down laboratory test of WRB conducted by Nujaim et al. (2018, 2020a, 2020b) will be analyzed.

Fig. 6.10 schematically shows the physical model of Nujaim et al. (2018, 2020a, 2020b). The stope and the drift were constructed with plexiglass. The backfill was made of clay having a unit weight of γ_b = 13.5 kN/m^3 (Nujaim et al. 2018, 2020a, 2020b). The WRB are characterized as L_{BT} = 0.072 m, L_{BB} = 0.25 m, H_d = 0.09 m, L_d = 0.09 m, and $\alpha_1 = \alpha_2$ = 45°. The slope angles of the WRB are calculated as $\alpha_1 = \alpha_2$ = 45° based on the geometry of the WRB even though their trapezoidal mold appears to show an angle of 48° to 52° (Nujaim et al. 2018, 2020a, 2020b). The unit weight of the waste rocks used to construct the barricade is estimated to be γ_{wr} = 13.84 kN/m^3 because 1.8 kg of waste rocks were used to construct the WRB having a volume of 0.0013 m^3 (Nujaim et al. 2018, 2020a, 2020b). The friction angle of the waste rocks is assumed to be ϕ'_{wr} = 45° based on the slope angle of the WRB. Regarding the interface friction angle δ_{wr} between the waste rocks and confining walls, one will obtain a value of δ_{wr} = 30° if one applies the typical (and empirical) relationship $\delta_{wr} = 2\phi'_{wr}/3$ (CGS 2006; Pirapakaran 2008; Li et al. 2014).

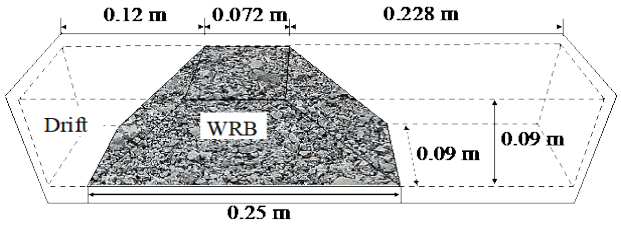

Figure 6.10 A physical model of Nujaim et al. (2018, 2020a, 2020b) to test the stability of a WRB subjected to a paste fill pressure p along the upstream slope.

Fig. 6.11 shows the variation of the minimum required top length L_{BT} as a function of interface friction angle δ_{wr}, predicted by applying the proposed solution by considering H_d = 0.09 m, L_d = 0.09 m, $\alpha_1 = \alpha_2$ = 45°, and an iso-geostatic overburden pressure distribution starting with p_b = 4.63

kPa recorded in Nujaim et al. (2018) and p_t = 3.42 kPa (= p_b - $\gamma_b H_d$) generated by the pour of a paste fill plug having H = 0.343 m and γ_b = 13.5 kN/m^3. The prediction result (L_{BT} = 0.0593 m with a $\delta_{wr} = 2\phi'_{wr}/3 = 30°$) shows a good agreement with an experimental result recorded in Nujaim et al. (2018), in which the top length of the WRB is L_{BT} = 0.072 m.

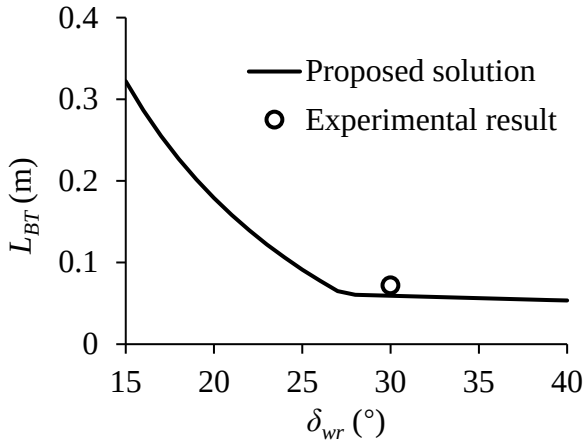

Figure 6.11 Variation of the required minimum top length L_{BT} as a function of interface friction angle δ_{wr}, predicted by applying the proposed solution for the cases of a laboratory; the laboratory test results of Nujaim et al. (2018) are shown in the circle.

6.6 Discussions

In this paper, the validity of the analytical solution of Yang et al. (2017a) has been first tested against 3D numerical results obtained with FLAC3D. An update to the equations for global and local stability analyses was proposed. The proposed analytical solution does not contain any calibration coefficient. The validity and predictability of the proposed analytical solution have been verified by the numerical results obtained with FLAC3D and the experimental result taken from the literature. The proposed solution can thus be used to size WRB for retaining paste backfill in

underground stopes. However, the proposed analytical solution should be used carefully due to several limitations.

The backfill pressure acting on the WRB was considered as an iso-geostatic pressure due to the overburden of paste backfill. This is true when the filling rate is high as shown by field stress measurement (Thompson et al. 2012) and laboratory tests (Li et al. 2013; Jaouhar 2019). It is also reproduced by numerical modeling (El Mkadmi et al. 2014; Jaouhar and Li 2019). However, drainage and consolidation, as well as hydration of cemented backfill, can take place during the filling operation, especially when the filling rate is small or/and the hydraulic conductivity of the backfill is high. In such a case, the consideration of iso-geostatic overburden pressure may lead to over conservative WRB design. Recently, Zheng and Li (2020) have shown that the "short-term" pressure of paste backfill largely depends on the solid content. When the solid content is low, the paste backfill may have a fluid-like behavior and the pressure can be represented by the iso-geostatic overburden. When the solid content is very high, the paste backfill pressure can be small. More work is necessary to correctly quantify the relationship between the pressures and solid content shortly placed in stopes. Nonetheless, the proposed solution can readily be adapted by considering a more realistic pressures distribution over the upstream slope of the WRB.

In this study, water was neglected in the WRB. This assumption is considered reasonable because the hydraulic conductivity of waste rocks is usually several orders higher than that of slurried backfill. Nevertheless, more work is needed to develop a more general solution that can consider the water flow through WRB.

The application of the proposed analytical solution necessities the knowledge of the internal friction angle (ϕ_{wr}) of waste rocks and the interface friction angle between a rock wall and the waste rocks (δ_{wr}). The latter can be taken as equal to the value of the former (i.e., $\delta_{wr} \approx \phi_{wr}$) if the rock walls and floor have a rough surface or to two-third of the former (i.e., $\delta_{wr} \approx 2\phi_{wr}/3$) if the rock and walls and flow have plate surface. Experimental work is necessary to verify if this relationship remains valid when the backfill is compacted to different degrees. In all cases, the measurement of

the friction angle of waste rocks is a key task. It is usually done by direct shear tests. However, the standard of ASTM D3080 (2011) requires that the specimen size over the maximum particle size ratio should be at least 10. Meeting this requirement is not a problem for laboratory standard testing equipment for soils, but very difficult and even impossible for waste rocks or rockfill. Subsequently, several scaling down techniques have been proposed. Among them, the parallel scaling down technique is the most popular and the most used. The ratio of 10 has been largely used in almost all existing direct shear tests. Recently, Deiminiat et al. (2020) made a critical analysis and review of the existing works. They showed that the ratio of 10 suggested by the ASTM standard and used by almost all people is not large enough to eliminate the specimen size effect. More experimental work is necessary to first determine the minimum required ratio between specimen size and maximum particle size. After then a scaling down technique should be identified that can be used to predict the friction angle of field rockfill or waste rocks through extrapolation. This work is ongoing and will be part of future publications.

In this study, the earth pressure coefficient is taken as $K = 1$ based on a series of calculations for the global and local stability analysis because this value is easy to perform calculations for engineers. The plan shown in Table 6.2 has been used to validate the proposed solution [Eqs. (6.6) and (6.27)]. Alternatively, the numerical results for a specific case can be used to obtain calibration coefficient to modify the proposed solution such as Yang et al. (2017a). Two methods can be used to estimate the required geometry of a WRB when used with due regard for its assumptions and conditions. The accuracy of the proposed equation should be kept by conducting all necessary tests and error calculations (e.g., the error between the results obtained with FLAC3D and those calculated by the proposed solution).

As the case of stress estimation in delayed backfill placed in stopes of open mining methods (Li and Aubertin 2009; Chai 2020), the influence of the surrounding rock stiffness is neglected. This is because the building material (waste rocks) of WRB are generally much softer than that of surrounding rocks. The stresses and ensuring subsequent should be minim in the surrounding rock

walls. For the case of shotcrete barricades anchored in the surrounding rock, Ghazi (2011) and Cheng (2012) have shown that the stability depends significantly on Young's modulus of the surrounding rock. More study can be necessary to evaluate the stiffness of the surrounding rock on the stability of WRB.

The effect of dilation angle (e.g., ψ = 0°, 2°, and 10°) on the stability of the WRB was studied for case 0 in Table 6.2 with H = 9 m and δ_{wr} = 35°. The results show that the minimum required top length L_{BT} is obtained with 1.4 m (ψ = 0° and 2°) and 1.5 m (ψ = 10°), which indicates dilation angle has little effect on the WRB stability. The Mohr-Coulomb model (ideal elastoplastic model) was used to build the numerical modeling and analyze the WRB stability. In the ideal elastoplastic model, the shear failure of WRB materials occurs before plastic volumetric deformation, and dilation angle, defined as a parameter of plasticity, controls the amount of plastic volumetric strain for post-failure.

Three failure tests performed by Nujaim et al. (2020b) showed p_b reached up to 120 kPa until the barricade collapsed monitored by a sensor placed in front of the WRB bottom. The geometries of the WRB almost keep unchanged when observing graphs and videos in Nujaim et al. (2020b). The value (p_b = 120 kPa) documented in Nujaim et al. (2020b) shows an obvious difference from the pressure (p_b = 4.63 kPa) recorded in Nujaim et al. (2018). The proposed solution well predicts the L_{BT} of the WRB with 4.63 kPa but fails to predict the one exerted by 120 kPa. To reply to this difference, one considers the details of the construction of the WRB documented by Nujaim et al. (2018, 2020a, 2020b). The pressure (p_b = 4.63 kPa, Nujaim et al. 2018) acting on the WRB is caused by the slurried backfill; an external manual piston was used to apply vertical pressure to increase p_b to 120 kPa for the three failure cases by Nujaim et al. (2020b). A rapidly applied loading (e.g., dynamic loading) condition may result in a sudden increase in pore water pressure of the backfilled stope under the undrained conditions at the early age. A few shims (pieces of plastic) at the base of the access gallery were used to increase the barricade-wall friction and to avoid sliding for the three cases in Nujaim et al. (2020b) instead of the one in Nujaim et al. (2018). The first

video given by Nujaim et al. (2020b) shows the upstream slope angle and downstream slope angle change during the failure process, such as α_1 varies from 45° to 37.22° and α_2 varies from 45° to 49.05° calculated based on the first video screenshot. The decrease of α_1 can result in a decreased horizontal component of the acting force P' and an increase in its vertical component. In addition, tight contact between the plexiglass roof and the WRB top can be observed during the failure process. The roof-WRB shear resistance thus plays a role when contact occurs, which is not considered in the proposed solution. The process of water penetration can be observed in the video, the apparent cohesion from unsaturated suction may increase the strength of the WRB to a certain extent.

The numerical model is used to simulate the global sliding in Nujaim et al. 2018. The test result is shown in the Ph.D. thesis (Zhai 2021). Although the numerical simulation reproduces the test result in Nujaim et al. (2018), the geometrical and mechanical parameters still have some problems that need to be confirmed. For example, two mechanical parameters are assumed to be ϕ'_{wr} = 45° and δ_{wr} = 25°. The internal friction angle should be equal to or bigger than 45° based on the physical meaning (equals upstream and downstream slope angles). The interface friction angle is obtained by FLAC3D by testing the range from 20° to 30°. The global sliding occurs when δ_{wr} varies from 20° to 25°, the local sliding takes place when δ_{wr} changes from 20° to 25°. So, the interface friction determined here is based on the numerical results. More laboratory tests are expected to be conducted to study the internal friction of waste rocks and interface friction between the plexiglass and waste rocks.

Finally, Nujaim et al. (2020b) showed excellent starting work on the WRB instability tests. More laboratory and field tests are necessary to calibrate and validate the proposed analytical solution and numerical models.

6.7 Conclusions

In this study, the existing analytical solutions developed to access the required top length of WRBs have been reviewed and verified by numerical modeling with FLAC3D. The structure instability of WRBs has been, for the first time, evaluated in the numerical modeling, based on the first occurrence among displacement jump or coalescence of current yield zones passing through the WRB structure from the downstream to the upstream slope. A modification has been proposed to the 2017 solution of Yang after considering the 3D feature of WRBs. A new solution for local stability is proposed for local failure with the inclined sliding plane.

The proposed analytical solution was validated by numerical results obtained by numerical simulations with FLAC3D, and partly verified by experimental results taken from the literature. The proposed solution can then be used to size WRBs built to retain paste backfill in underground mine stopes.

Acknowledgments

The authors acknowledge the financial support from the Natural Sciences and Engineering Research Council of Canada (NSERC 402318), Fonds de Recherche du Québec - Nature et Technologies (FRQNT 2015-MI-191676), and the partners of the Research Institute on Mines and Environment (RIME UQAT - Polytechnique; http://rime-irme.ca). Dr. Feitao Zeng and Dr. Pengyu Yang are acknowledged for their helpful discussions with the first author on the model development. Prof. Li is acknowledged for his huge efforts to increase innovation of this paper such as the development of local solution considering the inclined sliding plane and the use of Microsoft Excel® to solve the local equation.

Appendix A. Determination of *K* for the global stability analysis

To verify if the expression of Eq. (6.2) used in the global stability analysis solution [Eq. (6.1)] of Yang et al. (2017a) is valid, the horizontal normal stresses perpendicular to the sidewalls over an interface between the WRB and a sidewall obtained by the 3D numerical modeling with FLAC3D for the case of Figure 6.3b are examined. The pertaining geometries and material parameters are recalled as L_{BT} = 5.2 m, H = 12 m, γ_b = 19.6 kN/m^3, H_d = 5 m, L_d = 5 m, $\alpha_1 = \alpha_2$ = 37°, γ_{wr} = 19.6 kN/m^3, ϕ_{wr} = 38°, and δ_{wr} = 15°.

Table 6.3 presents the horizontal normal stress of each element perpendicular to the sidewall, σ_{YY} (kPa). The area, average horizontal stress, and total horizontal force of each layer of 0.2 m thick are given in Table 6.4. The accumulation of resulting forces on each layer gives a total horizontal force perpendicular to the sidewall as F_h = 2671 kN.

On the other hand, the total horizontal force perpendicular to the sidewall F_h was calculated by Yang et al. (2017a) as [see Eqs. (17) to (19) of Yang et al. 2017a]:

$$F_h = \frac{K\gamma_{wr}{H_d}^2}{2}\left[L_{BT} + \frac{H_d}{3}\left(\frac{1}{tan\,\alpha_1} + \frac{1}{tan\,\alpha_2}\right)\right]$$

$$= \frac{K \times 19.6\ \text{kN/m}^3 \times (5\ \text{m})^2}{2}\left[5.2\ \text{m} + \frac{5\ \text{m}}{3}\left(\frac{1}{tan\,37°} + \frac{1}{tan\,37°}\right)\right]$$

$$= K \times 2358\ \text{kN}$$

Comparison of the theoretical and numerical results of the total horizontal force F_h leads to a value of overall K = 2671 kN/2358 kN = 1.13 for the global stability analysis of WRB.

Table 6.3 The horizontal normal stress of each element perpendicular to the sidewall, σ_{YY} (kPa)

Layer	Element number from upstream to downstream																								
	1	2	3	4	5	6	7	8	9	10	11	12	13	14	15	16	17	18	19	20	21	22	23	24	25
1	49.32	27.77	16.11	11.24	8.36	6.54	5.33	5.12	5.06	4.90	4.49	4.31	3.88	3.59	3.21	2.55	2.35	2.27	2.07	2.07	2.00	2.27	2.54	2.61	2.24
2	62.67	56.40	43.13	31.83	24.05	18.30	14.87	13.04	11.97	11.46	11.58	11.78	11.62	12.10	12.08	11.54	10.96	10.12	9.21	9.16	9.44	10.54	10.54	6.52	3.79
3	55.87	61.77	61.71	49.93	38.08	29.50	23.81	17.92	17.22	17.44	17.25	16.22	15.99	16.30	16.08	15.59	15.29	14.92	14.28	14.20	14.48	16.28	13.68	4.51	2.42
4	57.23	60.85	64.50	61.30	52.86	43.01	34.78	25.20	22.61	20.85	19.40	18.18	17.20	16.46	15.69	15.04	14.43	13.74	13.18	12.86	13.21	14.70	15.17	5.27	2.81
5	59.84	62.21	64.68	62.45	58.79	51.83	43.82	30.92	26.31	23.21	21.04	19.45	17.96	16.71	15.67	14.60	13.73	12.71	12.21	12.18	12.70	14.09	15.73	7.22	3.16
6	61.70	64.44	66.23	63.24	59.54	54.77	41.49	35.03	29.66	25.70	22.92	21.25	19.44	17.61	16.31	15.06	14.03	13.24	12.65	12.38	12.81	14.09	15.47	9.23	3.58
7	62.42	66.84	68.28	65.00	61.20	57.00	44.82	38.73	33.44	29.20	26.13	23.66	21.54	19.70	18.01	16.61	15.30	14.22	13.53	13.50	13.54	14.55	15.37	10.02	3.93
8	64.32	68.70	70.00	67.19	63.60	59.12	48.36	42.40	37.01	32.69	29.31	26.48	24.07	21.93	19.95	18.29	16.99	15.78	14.95	14.76	14.44	14.71	15.09	10.64	4.37
9	66.37	70.32	71.65	69.35	66.01	61.56	51.43	45.60	40.30	35.77	32.01	28.90	26.24	23.94	21.95	20.13	18.57	17.33	16.46	16.25	15.68	14.54	14.39	11.19	4.68
10	67.86	71.47	73.44	71.43	68.31	64.03	54.33	48.71	43.43	38.66	34.69	31.37	28.56	26.04	23.92	22.07	20.39	18.92	18.05	18.09	17.75	14.75	13.38	11.26	4.89
11	68.02	72.55	74.98	73.38	70.41	66.34	56.98	51.56	46.37	41.56	37.39	33.78	30.74	28.14	25.94	24.00	22.18	20.52	19.65	19.88	19.73	15.95	12.26	10.58	5.02
12	68.10	74.14	76.46	75.21	72.49	68.51	59.37	54.37	49.12	44.31	39.91	36.07	32.86	30.24	28.01	25.90	24.07	22.14	21.12	21.40	21.19	17.68	12.10	9.92	4.96
13	69.69	75.29	78.00	76.96	74.51	70.68	66.18	61.68	56.93	51.69	46.80	42.32	38.38	35.05	32.25	29.88	27.65	25.70	23.78	22.57	22.36	18.75	12.89	9.56	4.85
14	71.97	76.16	79.59	78.81	76.56	68.37	63.92	59.15	54.00	49.00	44.43	40.47	37.04	34.01	31.50	29.22	27.18	25.34	23.94	24.06	23.46	19.34	13.92	9.57	4.85
15	70.35	77.98	81.20	80.70	78.40	74.84	70.61	66.23	61.27	56.16	51.13	46.46	42.44	38.90	35.75	33.13	30.75	28.63	26.86	25.23	24.13	19.94	14.56	10.01	4.92
16	70.42	79.88	82.81	82.54	80.34	77.06	73.01	68.45	63.35	58.28	53.20	48.45	44.49	40.87	37.53	34.80	32.33	30.08	28.27	26.65	24.35	20.48	14.83	10.41	5.11
17	71.28	81.55	84.55	84.36	82.40	79.27	75.24	70.53	65.46	60.42	55.30	50.54	46.52	42.81	39.35	36.48	33.94	31.53	29.60	28.16	24.35	20.63	15.02	10.54	5.31
18	72.38	83.51	86.53	86.46	84.60	81.37	77.36	72.55	67.54	62.43	57.30	52.61	48.43	44.63	41.13	38.07	35.41	32.91	30.98	29.73	24.41	20.67	15.24	10.50	5.36
19	74.24	85.49	88.58	88.67	86.69	83.49	79.47	74.70	69.66	64.47	59.38	54.60	50.30	46.40	42.87	39.72	36.92	34.34	32.46	31.30	24.49	20.66	15.35	10.47	5.25
20	76.13	87.65	90.70	90.90	88.81	85.67	81.61	76.86	71.77	66.54	61.39	56.53	52.11	48.12	44.55	41.33	38.43	35.78	33.93	32.78	24.80	20.57	15.40	10.41	5.03
21	78.37	89.83	92.98	93.13	91.09	87.89	83.79	78.98	73.80	68.51	63.28	58.32	53.80	49.74	46.11	42.84	39.85	37.13	35.33	30.93	25.44	20.59	15.55	10.34	4.81
22	79.77	92.01	95.18	95.51	93.54	90.31	86.13	81.20	75.92	70.50	65.16	60.10	55.49	51.37	47.68	44.36	41.32	38.57	36.79	35.40	26.37	20.90	15.85	10.42	4.87
23	80.01	93.96	97.32	97.98	96.07	92.78	88.49	83.44	78.01	72.44	66.99	61.81	57.12	52.93	49.19	45.82	42.74	39.97	38.21	36.65	33.20	21.51	16.43	10.84	5.30
24	80.45	95.91	99.99	100.65	98.77	95.44	91.02	85.85	80.26	74.51	68.87	63.57	58.80	54.56	50.78	47.37	44.24	41.46	39.70	37.98	34.34	22.62	17.45	11.89	6.04
25	76.00	95.96	102.38	103.58	101.77	98.41	93.86	88.51	82.82	76.78	70.84	65.40	60.52	56.21	52.39	48.94	45.77	43.00	41.27	39.40	35.60	24.44	19.11	13.55	6.14

Table 6.4 The area, average horizontal stress and total horizontal force of each layer of 0.2 m thick

Layer	X (m) of corner				Area of the layer (m^2)	Average σ_{YY} (kPa)	Horizontal force (kN)
	top upstream	top downstream	base upstream	base downstream			
1	0	5.2	-0.2654	5.4654	1.09308	7.29	7.97
2	-0.2654	5.4654	-0.5308	5.7308	1.19924	17.55	21.04
3	-0.5308	5.7308	-0.7962	5.9962	1.3054	23.23	30.33
4	-0.7962	5.9962	-1.0616	6.2616	1.41156	26.02	36.73
5	-1.0616	6.2616	-1.327	6.527	1.51772	27.73	42.08
6	-1.327	6.527	-1.5924	6.7924	1.62388	28.87	46.89
7	-1.5924	6.7924	-1.8578	7.0578	1.73004	30.66	53.04
8	-1.8578	7.0578	-2.1232	7.3232	1.8362	32.61	59.87
9	-2.1232	7.3232	-2.3886	7.5886	1.94236	34.42	66.86
10	-2.3886	7.5886	-2.654	7.854	2.04852	36.23	74.22
11	-2.654	7.854	-2.9194	8.1194	2.15468	37.92	81.70
12	-2.9194	8.1194	-3.1848	8.3848	2.26084	39.59	89.50
13	-3.1848	8.3848	-3.4502	8.6502	2.367	42.98	101.72
14	-3.4502	8.6502	-3.7156	8.9156	2.47316	42.63	105.44
15	-3.7156	8.9156	-3.981	9.181	2.57932	46.02	118.71
16	-3.981	9.181	-4.2464	9.4464	2.68548	47.52	127.61
17	-4.2464	9.4464	-4.5118	9.7118	2.79164	49.01	136.81
18	-4.5118	9.7118	-4.7772	9.9772	2.8978	50.48	146.29
19	-4.7772	9.9772	-5.0426	10.2426	3.00396	52.00	156.20
20	-5.0426	10.2426	-5.308	10.508	3.11012	53.51	166.43
21	-5.308	10.508	-5.5734	10.7734	3.21628	54.90	176.57
22	-5.5734	10.7734	-5.8388	11.0388	3.32244	56.59	188.02
23	-5.8388	11.0388	-6.1042	11.3042	3.4286	58.37	200.12
24	-6.1042	11.3042	-6.3696	11.5696	3.53476	60.10	212.44
25	-6.3696	11.5696	-6.635	11.835	3.64092	61.71	224.67

Appendix B. Determination of the critical height h, critical sliding plane angle β, and the minimum (FS = 1) required top length L_{BT} with Microsoft Excel®

The illustrative example is given by considering a fluid-like paste backfill having a unit weight of γ_b = 20 kN/m^3 and a height of H = 12 m in the stope. The waste rocks used to construct the barricade are characterized as γ_{wr} = 20 kN/m^3, ϕ_{wr} = 38°, and δ_{wr} = 30°. The geometries of the WRB are H_d = L_d = 5 m and α_1 = α_2 = 37°. Fig. 6.12 shows a copy-screen of the process with Microsoft Excel®

to obtain the critical height h, critical sliding plane angle β, and the minimum (FS = 1) top length L_{BT}. A copy of the Excel file is also attached as supplementary and accessible to all readers.

Barricade geometry:	
H_d (m) =	5
L_d (m) =	5
a_1 (°) =	37
a_2 (°) =	37
H (m) =	12
Materials properties:	
γ_{wr} (kN/m^3) =	20
γ_b (kN/m^3) =	20
φ (°) =	38
δ (°) =	38
Pressure on barricade:	
p_t (kPa) =	140
Starting guess:	
K =	1
β (°) =	26
Target:	
FS_{target} =	1

Equation 27

$$FS = \frac{[P' cos(\alpha_1 + \beta) + b\cos\beta]\tan\phi_{wr} + c\tan\delta_{wr}}{b\sin\beta + P' sin(\alpha_1 + \beta)}$$

$$P' = \left(p_t + \frac{\gamma_b h}{2}\right)\frac{hL_d}{\sin\alpha_1}$$

$$h_1 = \frac{a\tan\beta}{1 - \tan\beta / \tan\alpha_2}$$

$$a = L_{BT} + h\left(\frac{1}{\tan\alpha_1} + \frac{1}{\tan\alpha_2}\right)$$

$$b = \frac{\gamma_{wr} L_d}{2}[(L_{BT} + a)h + ah_1]$$

$$c = \frac{K\gamma_{wr}}{3}\left[\frac{(h' + L_{BT}\tan\beta)^3}{\tan\alpha_2 - \tan\beta} + h'^2\left(\frac{h}{\tan\alpha_1} + 3L_{BT}\right) + L_{BT}^2\tan\beta(L_{BT}\tan\beta + 3h')\right]$$

$$h' = h\left(1 + \frac{\tan\beta}{\tan\alpha_1}\right)$$

p_t (kPa) = 140 p_t (= $g_b(H - H_d)$)

Results after search:

Critical h (m)	critical L_BT (m)
0.425	1.6814
0.425	0.0000

$S(FS_{Eq.(19)} - FS_{Target})^2$ = 9.16741E-07

β (°)	h (m)	K	L_{BT} (m)	a (m)	h_1 (m)	b (kN)	h' (m)	c (kN)	P' (kN)	$FS_{Eq.(19)}$	$FS_{Eq.(19)} - FS_{Target})^2$
26	0.1	1	1.28834929	1.5538	2.14827	181.1	0.165	19.293	117.1456299	1.000164264	2.69826E-08
26	0.2	1	1.547438173	2.0783	2.87346	334.8	0.329	49.084	235.9529	1.000425959	1.81441E-07
26	0.3	1	1.650158734	2.4464	3.38245	475.2	0.494	83.934	356.4218103	0.99961713	1.4659E-07
26	0.4	1	1.681376789	2.743	3.79257	608.6	0.659	122.98	478.5523606	1.000017883	3.19789E-10
26	0.425	1	1.681438911	2.8094	3.8844	641.1	0.7	133.27	509.3446295	1.000140656	1.97842E-08
26	0.45	1	1.678949306	2.8733	3.9727	673.2	0.741	143.76	540.2407509	1.0002485	6.17523E-08
26	0.5	1	1.667067764	2.9941	4.13975	736.3	0.824	165.25	602.3445512	1.000379822	1.44265E-07
26	0.6	1	1.620466099	3.2129	4.44228	858.6	0.988	210.04	727.7983818	1.000313842	9.8497E-08
26	0.7	1	1.550461143	3.4083	4.71245	976.6	1.153	256.97	854.9138526	0.999952842	2.22391E-09
26	0.8	1	1.463328758	3.5866	4.95894	1091	1.318	305.88	983.6909635	0.999515351	2.34885E-07

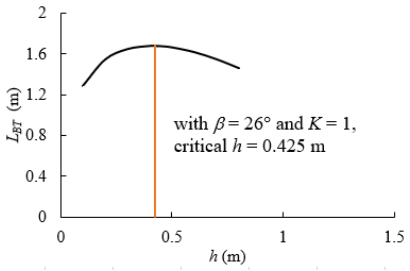

(a) step of iteration 0

Barricade geometry:	
H_d (m) =	5
L_d (m) =	5
a_1 (°) =	37
a_2 (°) =	37
H (m) =	12
Materials properties:	
γ_{wr} (kN/m^3) =	20
γ_b (kN/m^3) =	20
φ (°) =	38
δ (°) =	38
Pressure on barricade:	
p_t (kPa) =	140
Starting guess:	
K_i =	1
Target:	
FS_{target} =	1

Equation 27

$$FS = \frac{[P' cos(\alpha_1 + \beta) + b\cos\beta]\tan\phi_{wr} + c\tan\delta_{wr}}{b\sin\beta + P' sin(\alpha_1 + \beta)}$$

$$P' = \left(p_t + \frac{\gamma_b h}{2}\right)\frac{hL_d}{\sin\alpha_1}$$

$$h_1 = \frac{a\tan\beta}{1 - \tan\beta / \tan\alpha_2}$$

$$a = L_{BT} + h\left(\frac{1}{\tan\alpha_1} + \frac{1}{\tan\alpha_2}\right)$$

$$b = \frac{\gamma_{wr} L_d}{2}[(L_{BT} + a)h + ah_1]$$

$$c = \frac{K\gamma_{wr}}{3}\left[\frac{(h' + L_{BT}\tan\beta)^3}{\tan\alpha_2 - \tan\beta} + h'^2\left(\frac{h}{\tan\alpha_1} + 3L_{BT}\right) + L_{BT}^2\tan\beta(L_{BT}\tan\beta + 3h')\right]$$

$$h' = h\left(1 + \frac{\tan\beta}{\tan\alpha_1}\right)$$

p_t (kPa) = 140 p_t (= $g_b(H - H_d)$)

Results after search:

Critical h (m)	critical L_BT (m)
20.5	1.7764
20.5	0.0000

$S(FS_{Eq.(19)} - FS_{Target})^2$ = 1.16636E-07

β (°)	h (m)	K	L_{BT} (m)	a (m)	h_1 (m)	b (kN)	h' (m)	c (kN)	P' (kN)	$FS_{Eq.(19)}$	$FS_{Eq.(19)} - FS_{Target})^2$
18	0.425	1	1.750692569	2.8787	1.64436	335.1	0.608	55.602	509.3446295	0.999778686	4.89799E-08
19	0.425	1	1.767411523	2.8954	1.83582	364.9	0.619	62.829	509.3446295	1.00016619	2.7619E-08
20	0.425	1	1.77514661	2.9031	2.04384	396.1	0.63	70.578	509.3446295	1.0000553	3.05804E-09
20.25	0.425	1	1.776022379	2.904	2.09892	404.2	0.633	72.618	509.3446295	1.000027967	7.82128E-10
20.5	0.425	1	1.776415353	2.9044	2.15528	412.5	0.636	74.695	509.3446295	0.999983829	2.61492E-10
20.75	0.425	1	1.776363919	2.9044	2.21299	420.8	0.639	76.814	509.3446295	0.999932286	4.58514E-09
21	0.425	1	1.776226049	2.9042	2.27239	429.4	0.641	78.999	509.3446295	0.999968118	1.01646E-09
22	0.425	1	1.771155042	2.8991	2.52529	465.3	0.653	88.176	509.3446295	1.000018384	3.37958E-10
23	0.425	1	1.759094679	2.8871	2.80624	503.8	0.664	98.104	509.3446295	0.999988173	1.39871E-10
24	0.425	1	1.740958691	2.8689	3.12184	545.8	0.676	108.94	509.3446295	1.000172789	2.98559E-08

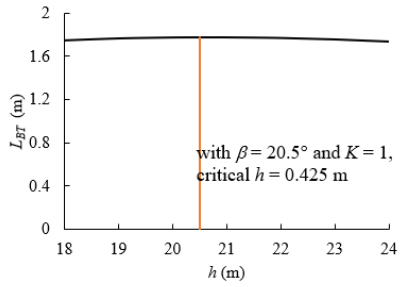

(b) step of iteration 1

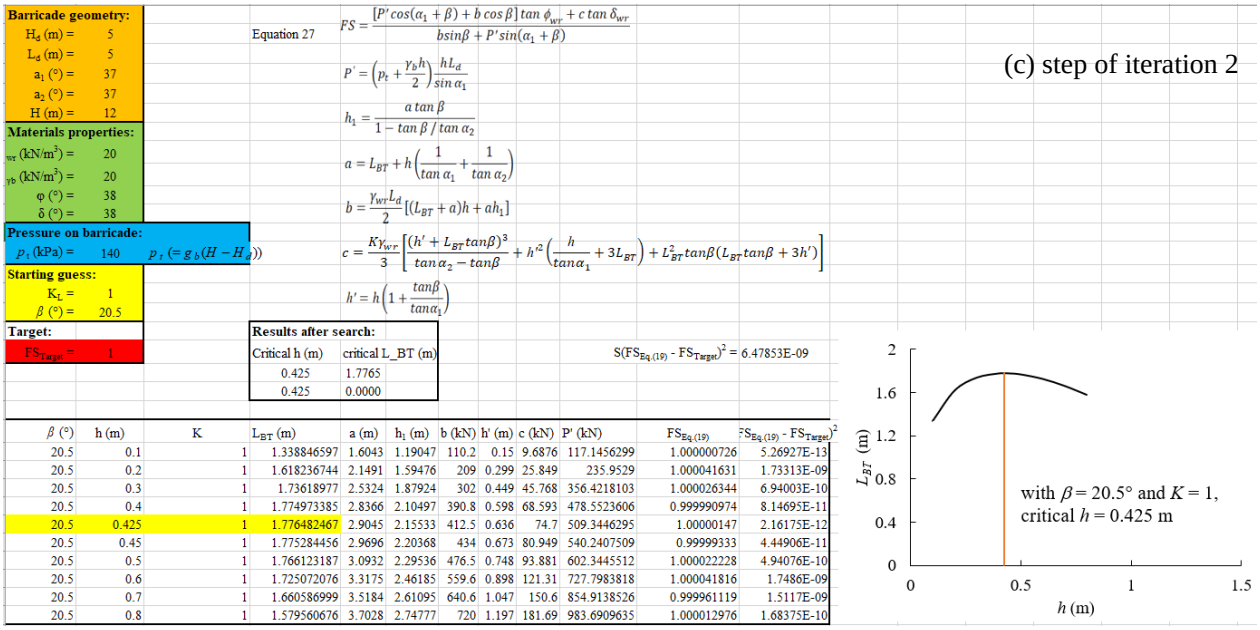

Figure 6.12 A copy-screen of the process with Microsoft Excel® to obtain the critical height h, critical sliding plane angle β, and the minimum (FS = 1) top length L_{BT}: (a) step of iteration 0, (b) step of iteration 1, (c) step of iteration 2

Appendix C. Sample illustration of sensitivity analyses of mesh in numerical modeling

To obtain stable and reliable numerical results, the numerical models must be correctly created. In geotechnical engineering, this can only be guaranteed by using a mesh fine enough and a domain large enough. The former is to make sure that the discretization of the numerical model is close enough to represent the behavior of a continuous material while the latter is for eliminating the effects of the boundary.

In this study, the WRB is constructed after the release of any elastic or plastic displacements associated with the excavation of the drift. There are few displacements associated with the construction of WRB. The boundary effects are considered negligible. No sensitivity analysis of domains is necessary as in the case of stress estimation in delayed backfill placed in stopes of open mining methods (Li and Aubertin 2009; Chai 2020). However, the mesh of each numerical model must be fine enough through sensitivity analysis of mesh for each case.

Normally, the finer the mesh is, the better the numerical results should be. During the numerical modeling, it will be seen that this is not the case, especially when using the command “SOLVER” of FLAC (2d and 3D), which uses a set of by-default parameter values unbalanced forces, steps, and mechanical ratio, etc.) to control the iteration of calculations. Subsequently, when the mesh becomes too fine, the by-default values of controlling parameters may become inappropriate. More steps of iterations may be necessary through the commend “STEP” to make sure that the obtained numerical results are the final and stable ones. More details can be seen in the examples shown hereafter.

Fig. 6.13 illustrates the X-displacement at point R (shown in Fig. 6.2) as a function of mesh size (from Fig. 6.13a to Fig. 6.13e) and as a function of mechanical ratio (Fig. 6.13f) for different cases shown in Table 6.2, showing the displacements become somewhat stable when mesh size decreases to 0.1 m in X-direction (0.25 m in Z-direction and 0.2 m in Y-direction are kept). Fig. 6.13f shows the stable numerical results are obtained when the mechanical ratio reduces to 1×10^{-5} (related step number is 8877).

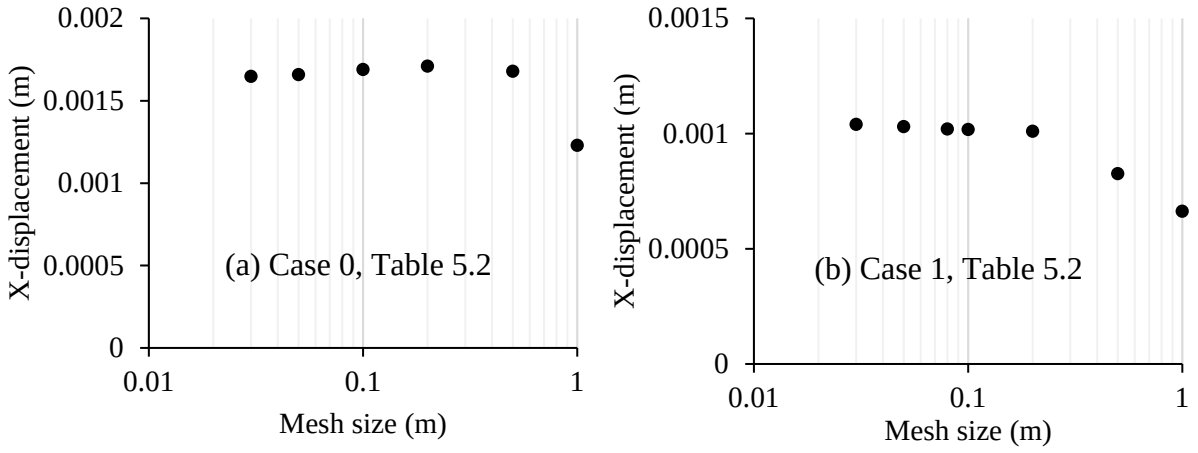

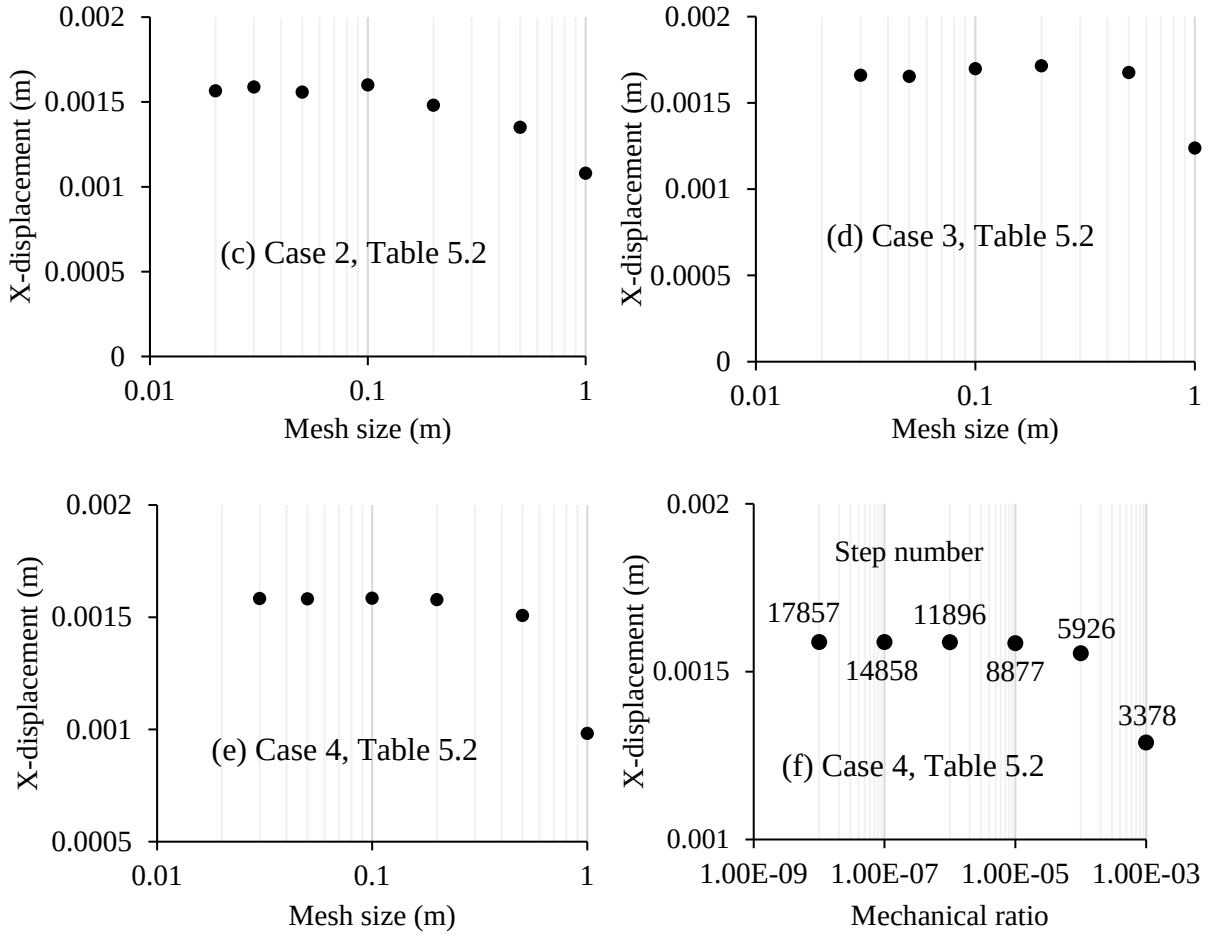

Figure 6.13 Sensitivity analyses of mesh in numerical modeling for Cases 0 with H = 9 m (a), case 1 with H_d = 7 m (b), case 2 (c), case 3 (d), case 4 with L_d = 3 m (e), case 4 with L_d = 3 m (f) of Table 6.2 with c_{wr} = 100 MPa, δ_{wr} = 30°.

The results shown in Fig. 6.13 are one part of the sensitivity analyses. The failure analyses (abrupt displacement jump shown in Fig. 6.3 or coalescence of current yield zones shown in Fig. 6.4) of the WRB with a given L_{BT} as a function of mesh size are also performed to obtain the stable numerical simulation results. More details are shown in the Ph.D. thesis (Zhai 2021).

6.8 References

ASTM D3080. (2011). Direct shear test of soils under consolidated drained conditions. ASTM International, West Conshohocken, PA, USA.

Aubertin, M. (2013). Waste rock disposal to improve the geotechnical and geochemical stability of piles. Proceedings of the world mining congress, CIM, Québec.

Aubertin, M., Bussière, B., and Bernier, L. (2002). Environnement et gestion des rejets miniers (CD-ROM), Presses Internationales Polytechnique, Montréal (in French).

Beer G. (1986). Design of brick bulkheads: numerical modelling. CSIRO Institute of Energy and Earth Resources, Division of Geomechanics, Long Pocket Laboratories, Project Report 1.

Belem, T., Mbonimpa, M., Gélinas, L.P. Alcott, J., and Dallaire, D. (2020). Rational design of Waste Rock (muck) Barricades (WRBs) as paste backfill-retaining structures. In Rock Mechanics for Natural Resources and Infrastructure Development, Volume 6: Proceedings in Earth and Geosciences (p. 2127). CRC Press.

Berndt, C.C., Rankine, K.J., Sivakugan, N. (2007). Materials properties of barricade bricks for mining applications. Geotech. Geol. Eng. 25(4), 449-471.

CGS (Canadian Geotechnical Society). (2006). Canadian foundation engineering manual, BiTech, Vancouver, Canada.

Chai, S.P. (2020). Analytical and numerical studies on the stresses in backfilled stopes and the stability of side-exposed backfill in inclined stopes. MSci. thesis, École Polytechnique de Montréal.

Checkan, G.J. (1985). Design of bulkheads for controlling water in underground mines. US Dept. of the Interior, Bureau of Mines, Vol. 9020.

Cheung, A. (2012). Influence of rock boundary conditions on behaviour of arched and flat cemented paste backfill barricade walls. MSci. thesis, University of Toronto.

Deiminiat, A., Li, L., Zeng, F., Pabst, T., Chiasson, P. and Chapuis, R. (2020). Determination of the shear strength of rockfill from small-scale laboratory shear tests: a critical review. Advances in Civil Engineering.

Djahanguiri, F. and Abel Jr, J.F. (1997). Design and construction of a bulkhead for a simulated underground leaching stope. Mining Engineering, 49(1), 57-64,

El Mkadmi, N., Aubertin, M., and Li, L. (2014). Effect of drainage and sequential filling on the behavior of backfill in mine stopes. Canadian Geotechnical Journal, 51(1), 1–15.

Garcia, J.A., Cassidy, S.M. (1937). Bulkheads for coal mines. American Institute of Mining and Metallurgical Engineers, Technical Publication, No. 789, 1-20.

Garrett, W.S. and Campbell P.L.T. (1958). Tests on an experimental underground bulkhead for high pressures. Journal of the Southern African Institute of Mining and Metallurgy, 59(3), 123-143.

Ghazi, S. (2011). Modeling of an underground mine backfill barricade. MSci. thesis, University of Toronto.

Grabinsky, M. W. (2010). In situ monitoring for ground truthing paste backfill designs. Proc., Paste 2010, Australian Centre for Geomechanics, Crawley, Australia, 85–98.

Grice, A.G. (1998). Stability of hydraulic backfill narricades. In Proceedings of 6th International Symposium on Mining with Backfill: Minefill. Vol. 98, 117-120.

Grice, T. (2001). Recent mine fill developments in Australia. In Proceedings of the 7th international symposium on mining with Backfill: Minefill. Vol. 1, 351-357.

Hambley, D. F. (2011). Backfill mining. SME mining engineering handbook: 1375-1384.

Harteis, S., Dolinar, D. (2006). Water and slurry bulkheads in underground coal mines: design, monitoring, and safety concerns. Mining Engineering, 58(12), 41-47.

Harteis, S.P., Dolinar, D.R., and Taylor, T.M. (2008). Guidelines for permitting, construction, and monitoring of retention bulkheads in underground coal mines. Information Circular 9506, National Institute for Occupational Safety and Health, Pittsburgh, PA.

Hassani, F. P. and Afrouz, A. (2001). Design and construction of bulkheads for underground backfill systems. Society for Mining, Metallurgy, and Exploration, Littleton.

Hughes, P.B. (2008). Performance of paste fill fences at Red Lake mine. MSci.thesis, The University of British Columbia.

Hughes, P.B., Pakalnis, R., Hitch, M., and Corey, G. (2010). Composite paste barricade performance at Goldcorp Inc. Red Lake Mine, Ontario, Canada.International Journal of Mining, Reclamation and Environment ., 24(2), 138–150.

Itasca. (2013). FLAC3D: Fast Lagrangian analysis of continua in 3 dimensions; user’s guide, version 5.01, Itasca Consulting Group, Minneapolis, MN.

Jaouhar, E.M. (2019). Études analytiques, numériques et expérimentales pour évaluer les contraintes et les pressions dans les chantiers remblayés et sur les barricades. Ph.D. thesis, École Polytechnique de Montréal.

Jaouhar, E.M., and Li, L. (2019). Effect of Drainage and Consolidation on the Pore Water Pressures and Total Stresses within Backfilled Stopes and on Barricades. Advances in Civil Engineering.

Kalsi, H. (1994). Underground water bulkhead construction at Pamour No. 1 mine. CIM Bulletin, 87(979), 49-51.

Keita, A.M.T., Jahanbakhshzadeh, A., Li, L. (2021). Numerical analysis of the stability of arched sill mats made of cemented backfill. International Journal of Rock Mechanics and Mining Science, 140, p.104667.

Kuganathan, K. (2002). A method to design efficient mine backfill drainage systems to improve safety and stability of backfill bulkheads and fills. In Proceedings of the 8th AusIMM Underground Operators Conference: Growing our Underground Operations, Townville, QLD, Australia, 29-31.

Li, J., Ferreira, J.V., Lievre, T.L. (2015). Transition from discontinuous to continuous paste filling at Cannington Mine. In Proceedings of the Eleventh International Symposium on Mining with Backfill Australian Centre for Geomechanics, 381-394.

Li, L. and Aubertin, M. (2009). Numerical investigation of the stress state in inclined backfilled stopes. International Journal of Geomechanics, 9(2), 52-62.

Li, L., Alvarez, I.C., and Aubertin, J.D. (2013). Self-weight consolidation of a slurried deposition: tests and interpretation. International Journal of Geotechnical Engineering, 7 (2), 205-213.

Li, L., and Aubertin, M. (2011). Limit equilibrium analysis for the design of backfilled stope barricades made of waste rock. Canadian Geotechnical Journal, 48(11), 1713–1728.

Li, L., Aubertin, J.D., and Dubé, J.S. (2014). Stress distribution in a cohesionless backfill poured in a silo. The Open Civil Engineering Journal, 8(1).

Li, L., Ouellet, S., and Aubertin, M. (2009). A method to evaluate the size of backfilled stope barricades made of waste rock. Proc., 62nd Canadian Geotechnical Conf. and 10th Joint CGS/IAH-

CNC Groundwater Specialty Conf., Canadian Geotechnical Society, Richmond, BC, Canada, 497–503.

Liu, G., Li, L., Yang, X. and Guo, L. (2016). Stability analyses of vertically exposed cemented backfill: A revisit to Mitchell's physical model tests. International Journal of Mining Science and Technology, 26(6), 1135-1144.

Liu, G.S., Li, L., Yang, X.C., Guo, L.J. (2018) Required strength estimation of a cemented backfill with the front wall exposed and back wall pressured. International Journal of Mining and Mineral Engineering 9(1): 1-20.

Mitchell RJ, Olsen RS, Smith JD. (1982). Model studies on cemented tailings used in mine backfill. Canadian Geotechnical Journal, 19(1):14–28.

Mitchell, R.J. (1992). Centrifuge model studies of fill pressures on temporary bulkheads. CIM Bulletin, 85(960), 48-54.

Mitchell, R.J., Smith, J.D., Libby, D.J. (1975). Bulkhead pressures due to cemented hydraulic mine backfills. Canadian Geotechnical Journal, 12, 362-371.

Nortjé, A. S., Meintjies, H.A.C. and Joughin, W.C. (2007). Design of hydraulic backfill bulkheads at south deep gold mine. Minefill 2007, #2580.

Nujaim, M., Auvray, C., and Belem, T. (2018). Geomechanical behaviour of a rock barricade and cemented paste backfill: Laboratory experiments on a reduced-scale model. In Geomechanics and Geodynamics of Rock Masses, Volume 1: Proceedings of the 2018 European Rock Mechanics Symposium (p. 339). CRC Press.

Nujaim, M., Belem, T., and Auvray, C. (2020a). Small-scale model preliminary testing on the interaction between paste backfills and waste rock barricades. In Rock Mechanics for Natural Resources and Infrastructure Development, Volume 6: Proceedings in Earth and Geosciences (p. 1807). CRC Press.

Nujaim, M., Belem, T., Giraud, A. (2020b). Experimental tests on a small-scale model of a mine stope to study the behavior of waste rock barricades during backfilling. Minerals, 10(11), 941.

Pagé, P., Li, L., Yang, P.Y., Simon, R. (2019). Numerical investigation of the stability of a base-exposed sill mat made of cemented backfill. International Journal of Rock Mechanics and Mining Science, 114, 195-207.

Pirapakaran, K. (2008). Load-deformation characteristics of minefills with particular reference to arching and stress developments. Townsville: James Cook University.

Potvin, Y., Thomas, E., and Fourie, A. (2005). Handbook on mine fill, Australian Centre for Geomechanics, Perth, Australia.

Revell, M.B., and Sainsbury, D.P. (2007a). Paste bulkhead failures. 9th International Symposium on Mining with Backfill, Montréal, QC, Canada.

Revell, M.B., and Sainsbury, D.P. (2007b). Advancing paste fill barricade design using numerical modeling. 9th International Symposium on Mining with Backfill, Montréal, QC, Canada.

Salençon, J. (1969). Contraction quasi-statique d'une cavité à symétrie sphérique ou cylindrique dans un milieu élastoplastique. Annales des Ponts et Chaussées, 4, 231-236.

Sawyer, S., Watson, G. (2007). A method to calculate hydrodynamic loads on underground bulkheads. SME Annual Meeting, Feb. 25-28, 2007, Denver, CO. Preprint 07-001, 1-3.

Sivakugan, N. (2008). Geotechnical issues of mining with hydraulic backfills.Electronic Journal of Geotechnical Engineering , Special Volume: Bouquet 08.

Sivakugan, N., Rankine, K. J., and Rankine, R. M. (2006). Permeability of hydraulic fills and barricade bricks.Geotech and Geology Engineering, 24, 661–673.

Smith, J.D., and Mitchell, R.J. (1982). Design and control of large hydraulic backfill pours. CIM Bulletin, 75(838), 102-111.

Thompson, B.D., Grabinsky, M.W., and Bawden, W.F. (2012). In-situ measurements of cemented paste backfill at the Cayeli Mine.Canadian Geotechnical Journal, 49(7), 755–772.

Wang, R.F., Zeng, F.T., Li, L. (2021) Stability analyses of side-exposed backfill considering mine depth and extraction of adjacent stope. International Journal of Rock Mechanics and Mining Science, 142, p.104735.

Wise, S.L., Strache, W. (1914). The design, construction, and cost of two mine bulkheads. Transactions of the American Institutes of Mining Engineers, 1839-1846.

Yang P. Y., Brochu-Baekelmans, M., Li, L., and Aubertin, M. (2014). An improved solution for sizing barricades made of waste rock to retain cemented paste backfill. Proc., 67th Canadian Geotechnical Conf., Canadian Geotechnical Society, Richmond, BC, Canada.

Yang, P., Li, L. and Aubertin, M. (2017b). A new solution to assess the required strength of mine backfill with a vertical exposure. International Journal of Geomechanics, 17(10), 04017084.

Yang, P.Y., Li, L., Aubertin, M. Brochu-Baekelmans, M., and Ouellet, S. (2017a). Stability analyses of waste rock barricades designed to retain paste backfill.International Journal of Geomechanics, 17(3), 04016079.

Yumlu, M., and Guresci, M. (2007). Paste backfill barricade monitoring: A case study from Inmet's Cayeli mine. Proc., 9th Int. Symp. in Min. with Backfill (CD-ROM), CIM, Montreal.

Zhai, Y.L., Li, L., Chapuis, R.P. (2021). Analytical, numerical and experimental study on steady-state seepage through 3D rockfill dikes. Mine Water and the Environment, 1-12.

Zheng, J. and Li, L. (2020). Experimental study of the "short-term" pressures of uncemented paste backfill with different solid contents for barricade design. Journal of Cleaner Production, 275(1), 123068.

CHAPTER 7 GENERAL DISCUSSION

In this thesis, three articles were produced to estimate the total seepage rate under steady-state conditions through a 3D rockfill dike and to design WRB with or without shotcrete sprayed on the upper part of the downstream slope. It is important to keep in mind that these analytical solutions were all developed based on limit equilibrium analysis with several limitations associated with the involved assumptions. The main assumptions and limitations include, for example:

- In Article 1 (Chapter 4), the Dupuit solution was developed by using Navier-Stokes momentum equations as the governing equation and by considering a homogeneous fluid obeying Darcy's law. A single-phase flow was considered. The soil beneath the phreatic surface is assumed to be filled with water and the pores above it are filled with air. There is no consideration of poroelastic coupling, which needs to include yield criterion and plastic potential functions.
- In Article 1 (Chapter 4), the two side walls were assumed to not affect the water flow through the 3D dike. It is well known that water flow is fastest in the middle and static along with the water-wall interfaces. The velocity of river water flow decreases across a transversal section from the center to the banks, with the maximum value at the center and zero at the sidewalls. The seepage rate can be overestimated by the numerical modeling and the proposed analytical solution.
- The water bulk modulus K_f was attributed a value of 3 kPa for the case of a large dike and 90 Pa for the numerical simulation of the laboratory test. Using different values in K_f is to reduce the calculation time for reaching a steady flow condition. When assigning a value as high as 1 MPa to of K_f, the same numerical results for the case of a large dike were obtained with a longer calculation time (about 2 hours, compared to the calculation time of 11 seconds with K_f = 90 Pa). As the bulk modulus of water has a value as high as 2 GPa, it is neither possible nor necessary to use this real value in the numerical calculation.
- The steady seepage laboratory tests were realized by using a stopwatch and a graduated cylinder by averaging 10 measurements. The constant hydraulic heads were maintained by controlling the tap. The accuracy of the tests is not very high.

- The generalized solution of the Dupuit model showed a significant increase of Q/k_h ratio as h_2 increases from zero to a certain value, as shown in Figure 4.5. This abnormal trend is significantly corrected by using two calibration coefficients. Nevertheless, the results presented in Figure 4.6 still show a slight increase in Q/k_h when h_2 increases from 0 to 4 m for the case of h_1 = 20 m. It can be expected that this abnormal trend can become more pronounced when the difference between h_1 and h_2 increases, while this trend based on the analytical solution is not supported by the numerical results.
- In practice, one can commonly observe the migration of fine particles of paste backfill passing through a WRB. The porosity and the hydraulic conductivity of waste rocks used to build barricades can thus be affected. These changes need to be taken into account in the numerical models and analytical solutions.
- In Article 2 (Chapter 5), the values of C_M, C_G, and C_L were obtained by a curve- fitting between the numerical and analytical results. These coefficients do not have any physical meaning. Strictly, the proposed calibrated solution is not a truly analytical solution.
- In Article 2, a horizontal sliding plane was assumed to ease equation development. The numerical results indicate that the sliding plane is inclined. The drawback of the proposed solution by using a horizontal sliding plane has been partly taken into account through the three calibration factors. More work is necessary to improve the analytical solution by considering an inclined sliding plane.
- In the beginning, K_a is used to analyze the stability of WRB. The K value may be different (ranges from 1.06 to 1.26) based on the recent study. It can be seen the K value varies depending on the different cases, such as different backfill heights, barricade heights, interface friction angles.
- This irregular shape of openings may lead to unexpected stress conditions in the barricade (Potvin et al. 2005). Therefore, it raises a problem: How to accurately estimate the stress distribution for barricade design? In Articles 2 and 3 (Chapters 5 and 6), the iso-geostatic overburden pressure is assumed to be the pressure exerted by the backfilled stope acting on the barricades. The backfill pressure acting on the WRB was considered as an iso-geostatic pressure due to the overburden of paste backfill. This is true when the filling rate is high as

shown by field stress measurement (Thompson et al. 2012) and laboratory tests (Li et al. 2013; Jaouhar 2019). It is also reproduced by numerical modeling (El Mkadmi et al. 2014; Jaouhar and Li 2019). However, drainage and consolidation, as well as hydration of cemented backfill, can take place during the filling operation, especially when the filling rate is small or/and the hydraulic conductivity of the backfill is high. In such a case, the consideration of iso-geostatic overburden pressure may lead to over conservative WRB design. Recently, Zheng and Li (2020) have shown that the "short-term" pressure of paste backfill largely depends on the solid content. When the solid content is low, the paste backfill may have a fluid-like behavior and the pressure can be represented by the iso-geostatic overburden. When the solid content is very high, the paste backfill pressure can be small.

- In this thesis, FS = 1 was used to determine the minimum required top length of WRB with or without shotcrete. In practice, a proper value higher than the unit should be used for FS by considering the uncertainties and the possible consequences of barricade failure.
- In this thesis, the value of interface friction angle between the waste rocks and rock walls was assumed to be equal to the value of the internal friction angle of the waste rocks for rough surface of rock walls or to two-third of ϕ_{wr} for smooth and plate surface of rock walls. More work is necessary to study the relationship between the interface friction angle between the waste rocks and rock walls and the internal friction angle of waste rocks.
- The effect of water is neglected in the WRB with or without shotcrete. This assumption is considered reasonable because the hydraulic conductivity of waste rocks is usually several orders of magnitude higher than that of slurried backfill. However, the effect of water on the mechanical properties of the waste rocks should be considered. In addition, the permeability of waste rock could be significantly reduced when shotcrete is applied. More work is necessary to consider the effect of water in the WRB with or without shotcrete.

CHAPTER 8 CONCLUSIONS AND RECOMMENDATIONS

8.1 Conclusions

The project studied the hydromechanical behavior and mechanical problem (deformation analysis and stability analysis) of the WRB with or without shotcrete to retain the backfilled stope at the early age. After a broad literature review about the barricade design, three research objectives are identified and analyzed by analytical, numerical, and experimental methods. The water flow trend and the total seepage rate through a rockfill dike under steady-state conditions were studied. The design of waste rock barricades with and without shotcrete was analyzed. The main conclusions are generalized below.

The research on the total seepage rate of the rockfill dike resting on an impervious base under steady-state conditions is presented in Chapter 4 (Article 1). The study can be concluded below:

- A new solution was proposed that can be used to estimate the total seepage rate under steady-state flow conditions.
- The two coefficients, one for flow path length and another for mean flow cross-section, are calibrated by the numerical results for a specific case. The two coefficients are calibrated by the numerical results for a specific case. The calibrated and proposed solution is validated with additional numerical simulation results.
- The proposed solution was calibrated again with a few numerical results. The predictability of the calibrated solution was tested against additional numerical results and lab test results.
- The equation provides a rapid way of estimating the flow rate when it is used with due regard for its limitations. It is necessary to do all of the necessary experimental tests to ensure the accuracy of this equation for a specific project.
- The power and applicability of the numerical model of FLAC3D were illustrated. FLAC3D can be used to analyze the hydro-geotechnical behavior of waste rocks.

A new analytical solution is developed and presented in Chapter 5 (Article 2) to design the shotcreted WRB for global and local stability, including the thickness with a given material and the strength with a defined geometry. The conclusions of the research are shown below:

- A new solution was proposed to design the shotcreted WRB, including the required shotcrete thickness with a given material, required shotcrete cohesion with a given dimension, and the required top length of WRB with given shotcrete.
- The proposed analytical solution is first calibrated by some numerical results. The predictive capability of the proposed analytical solution was verified with additional numerical simulation results.
- The proposed solution has a good agreement with the numerical simulations for representative stope height (9 m $\leq H \leq$ 18 m), barricade, and shotcrete geometries (3 m $\leq H_d \leq$ 7 m, 3 m $\leq L_d \leq$ 7 m, 1 m $\leq H_s \leq$ 3 m), and properties of waste rock and shotcrete (34° $\leq \phi' \leq$ 40°). The proposed solution can be used to design shotcreted WRB with due consideration given to its limitation.

By considering global and local stability, an updated solution based on Yang et al. (2017) solution was proposed and presented in Chapter 6 (Article 3) to size the waste rock barricades. The research results can be summarized below:

- An update solution was proposed to design the 3D WRB for global and local stability. The earth pressure coefficient is calculated by recalling its definition in Yang et al. (2017), while the solution for local stability is proposed by considering an inclined sliding plane based on limit equilibrium.
- The *K* defined in Yang et al. (2017a) is recalculated against numerical results of FLAC3D. Its value varies from 1.06 to 1.24 based on four cases. The K is then considered as 1 for global and local stability based on the range and simplification of calculation.
- The plane strain condition can be taken into account when the ratio of L_d to H_d equals 40 based on the numerical simulation results. The numerical results present a good agreement with the 2D solution of Yang et al. (2017) when $L_d >> H_d$ (e.g., L_d = 200 m).
- The proposed solution does not contain any calibration coefficients. The predictability of the proposed solution was tested against additional numerical results and lab test results.

8.2 Recommendations

This project employed analytical, numerical, and experimental methods to analyze the hydromechanical behavior and mechanical problem (deformation analysis and stability analysis) of the waste rock barricades. Some issues and limitations are found during the project. The recommendations for further study based on the existing research are described in the following:

- In Article 1 (Chapter 4), further study is expected to consider the poroelastic coupling, including failure criterion and plastic potential functions.
- More research is necessary to figure out the pressures and stresses exerted on the waste rock barricade at an early age.
- More laboratory tests and numerical simulations are expected to be conducted to study the differences in total seepage rate between the center of the barricade and sidewalls.
- More work should be conducted to improve the correlation between the physical parameter and the numerical parameter and study the numerical results with different values of the bulk modulus.
- It is necessary to increase the accuracy of the flow tests under steady-state conditions in the following study in laboratory tests.
- It is suggested to develop a solution without calibration coefficients to figure out the abnormal trend when the between h_1 and h_2 increases.
- More work is necessary to analyze the evolution of the physical and hydraulic properties of WRB with the loss of fine particles in waste rocks during laboratory tests.
- More work is suggested to develop a solution without calibration coefficients for both global and local stability for shotcreted WRB.
- More work is suggested to propose a solution considering the inclined sliding plane for shotcreted WRB.
- More numerical simulations should be performed to find a more representative range of K values. More experimental tests are suggested to be conducted to obtain the earth pressure coefficient.

- In Articles 2 and 3 (Chapters 5 and 6), more work is suggested to study the effect of the solid content of backfills on the pressures acting on the WRB.
- More work is suggested to consider the effect of water on the WRB with or without shotcrete, such as the stability problem of the whole structure and the evolution of the physical and hydraulic properties of the waste rock barricades.
- Experimental tests are suggested to study the relationship between the internal friction angle and the interface friction angle (i.e., interface friction is equal to two-third of the internal friction angle).
- The study in the future is suggested to consider the effect of distance from access brow to the construction location on the barricade design.
- More experimental work both in the laboratory and in the field is necessary to obtain more representative results to consider scale effects.
- More experimental and field tests are suggested to be conducted to validate the proposed solutions to estimate the total seepage rate of the rockfill dike and design the WRB without or without shotcrete.
- More studies are suggested to increase the accuracy of the pressure estimation for barricade design for irregular shapes of openings.
- More studies are suggested to consider joints, mechanical properties, and reinforcement measures into a mathematical model of the barricade and its surrounding rock.
- The earth pressure coefficient in the access drift near the barricade or the barricade is suggested to be studied by experimental tests.

REFERENCES

ACI Committee 318. (1995). Building Code Requirements for Structural Concrete (ACI 318-95) and Commentary (318R-95). American Concrete Institute, Farmington Hills, Mich, 369.

Askew, J., McCarthy, P.L. and Fitzgerald, D.J. (1978). Backfill research for pillar extraction at ZC/NBHC. Proc., Mining with backfill: 12th Can. Rock Mechanics Symp., CIM, Sudbury, 100-110.

Aubertin, M., Li, L., Arnold, S., Belem, T., Bussière, B., Benzaazoua, M. and Simon, R. (2003). Interaction between backfill and rock mass in narrow stopes. Proc., Soil and Rock America, Verlag Glückauf Essen (VGE), Essen, 1, 1157-1164.

Aubertin, M. (2013). Waste rock disposal to improve the geotechnical and geochemical stability of piles. Proc., 23rd World Mining Congress, CIM, Québec.

Azam, S., Wilson, G.W., Fredlund, D.G. and Van Zyl, D. (2009). Geotechnical characterization of mine waste rock. In Proceedings of the 17th International Conference on Soil Mechanics and Geotechnical Engineering, Alexandria, Egypt, 3421-3425.

Barton, N.R. (2008). Shear strength of rockfill, interfaces and rock joints, and their points of contact in rock dump design. In Proceedings of the First International Seminar on the Management of Rock Dumps, Stockpiles and Heap Leach Pads. Australian Centre for Geomechanics, 3-17.

Beer G. (1986). Design of brick bulkheads: numerical modeling. CSIRO Institute of Energy and Earth Resources, Division of Geomechanics, Long Pocket Laboratories, Project Report 1.

Belem T, Mbonimpa M, Gélinas LP, Alcott J, Dallaire D. (2020). Rational design of Waste Rock (muck) Barricades (WRBs) as paste backfill-retaining structures. In Rock Mechanics for Natural Resources and Infrastructure Development, Volume 6: Proceedings in Earth and Geosciences, 2127.

Berndt, C.C., Rankine, K.J. and Sivakugan, N. (2007). Materials properties of barricade bricks for mining applications. Geotechnical and Geological Engineering, 25(4), 449-471.

Bloss, M.L. and Chen, J. (1998). Drainage research at Mount Isa Mines limited 1992-1997. Proc., 6th Int. Symp. on Mining with Backfill, M. Bloss, eds., Brisbane, Australia, 98, 111-116.

Bloss M.L. (1992). Prediction of cemented rock fill stability: design procedures and modelling techniques. Ph.D. Thesis, University of Queensland, Brisbane, Australia.

Britton, S.G., Mutmansky, J.M., Gentry, D.W., Schlitt, W.J., Karmis, M., and Singh, M.M. (1992). SME mining engineering handbook (Vol. 2). Denver: Society for Mining, Metallurgy, and Exploration.

Brown, R., Smith, N., and Carmichael, P. (2019). One year of paste operations at Jabal Sayid, Saudi Arabia. In Proceedings of the 22nd International Conference on Paste, Thickened and Filtered Tailings. Australian Centre for Geomechanics, 387-399.

Bowles J.E. (1996). Foundation Analysis and Design, 5th. Edition, McGraw-Hill, New York.

Casagrande L (1932) Naeherungsmethoden zur Bestimmung von Art und Menge der Sickerung durch geschuettete Dämme (Approximate methods to determine the seepage through spillway dikes). Institute of Technology, Vienna [in German].

Checkan, G.J. (1985). Design of bulkheads for controlling water in underground mines. US Dept. of the Interior, Bureau of Mines, Vol. 9020.

Cowling, R., Grice, A.G., and Isaacs, L.T. (1988). Simulation of hydraulic filling of large underground mining excavations. In Proceedings of 6th International Conference on Numerical Methods in Geomechanics, Innsbruck, Austria, 1869-1876.

Cheung, A. (2012). Influence of Rock Boundary Conditions on Behaviour of Arched and Flat Cemented Paste Backfill Barricade Walls. MSc Thesis, University of Toronto Civil Engineering Department, Toronto, Canada.

Checkan, G.J. (1985) Design of bulkheads for controlling water in underground mines. US Dept. of the Interior, Bureau of Mines, Vol. 9020.

Das BM. (2011) Principles of Foundation Engineering. 7th. Pacific Grove: Brooks/Cole-Thomson Learning.

Djahanguiri, E. and Abel, J.F. (1997). Design and construction of a bulkhead for a simulated underground leaching stope. Mining Engineering, 49(1), 57-64.

Duffield, W.A., Gad, E., and Bamford, W. (2003). Investigation into the structural behaviour of

mine brick barricades. AusIMM Bulletin, 2(2), 44-50.

Dupuit J (1863) Études théoriques et pratiques sur le mouvement des eaux dans les canaux découverts et à travers les terrains perméables. 2nd edit, Dunod, Paris.

Doherty, J.P. (2015). A numerical study into factors affecting stress and pore pressure in free draining mine stopes. Computers and Geotechnics, 63, 331-341.

Doherty, J.P., Hasan, A., Suazo, G.H., and Fourie, A. (2015). Investigation of some controllable factors that impact the stress state in cemented paste backfill. Canadian Geotechnical Journal, 52(12), 1901-1912.

El Mkadmi, N., Aubertin, M. and Li L. (2014). Effect of drainage and sequential filling on the behavior of backfill in mine stopes. Canadian Geotechnical Journal, 51(1), 1–15.

Emad, M.Z., Mitri, H. and Kelly, C. (2015). State-of-the-art review of backfill practices for sublevel stoping system. International Journal of Mining, Reclamation and Environment, 29(6), 544-556.

Fall, M., Adrien, D., Célestin, J.C., Pokharel, M., and Touré, M. (2009). Saturated hydraulic conductivity of cemented paste backfill. Minerals Engineering, 22(15), 1307-1317.

Fahey, M., Helinski, M., and Fourie, A. (2009). Some aspects of the mechanics of arching in backfilled stopes. Canadian Geotechnical Journal, 46 (11), 1322-1336.

Falaknaz, N., Aubertin, M., and Li, L. (2015). Numerical analyses of the stress state in two neighboring stopes excavated and backfilled in sequence. International Journal of Geomechanics, 15(6), 04015005.

Garrett, W.S. and Campbell P.L.T. (1958). Tests on an experimental underground bulkhead for high pressures. Journal of the Southern African Institute of Mining and Metallurgy, 59(3), 123-143.

Grabinsky, M.W. (2010). In situ monitoring for ground truthing paste backfill designs. 13th International Seminar on Paste and Thickened Tailings, Toronto, Canada. ACG. 85-98.

Geo-Slope International Ltd. (2012). Seepage modeling with SEEP/W. Calgary, Alberta, Canada.

Grice, A.G. (1989). Fill research at Mount Isa mines limited. In International Symposium on mining with backfill, 4, 15-22.

Grice, A.G. (1998). Stability of hydraulic backfill barricades. Proc., 6th Int. Symp. on Mining with Backfill, M. Bloss, eds., Brisbane, Australia, 117-120.

Grice, A.G. (2001). Recent mine fill developments in Australia. Proc., 7th Int. Symp. On Mining with Backfill, Seattle, USA, 351-357.

Ghirian, A. and Fall, M. (2014). Coupled thermo-hydro-mechanical–chemical behaviour of cemented paste backfill in column experiments: Part II: Mechanical, chemical and microstructural processes and characteristics. Engineering Geology,170, 11-23

Hamrin, H., Hustrulid, W., and Bullock, R.L. (2001). Underground mining methods and applications. Underground mining methods: Engineering fundamentals and international case studies, 3-14.

Harraz, H.Z. (2016). Topic 4: Mining Methods.

Hassani, F. and Archibald, J. (1998). Mine backfill (CD-ROM), Canadian Institute of Mine, Metallurgy and Petroleum, Montréal.

Hassani, F. P. and Afrouz, A. (2001). Design and construction of bulkheads for underground backfill systems. Society for Mining, Metallurgy, and Exploration, Littleton.

Helinski, M., Fourie, A., and Fahey, M. (2006). Mechanics of early age CPB. Proc., Symp. conducted at the 9th Int. Seminar on Paste and Thickened Tailings, R. Jewell, S. Lawson, and P. Newman, Eds., Australian Centre for Geomechanics, Limerick, Ireland, 313-322.

Helinski, M. and Grice, A. G. (2007). Water management in hydraulic fill operations. Proc., 9th Int. Symp. on Mining with Backfill, Montréal.

Hughes, P.B. (2008). Performance of paste fill fences at Red Lake Mine. Master Thesis, University of British Columbia, Vancouver, Canada.

Hoek, E., Kaiser, P.K., and Bawden, W.F. (1995). Support of Underground Excavations. Hard Rock.

Hoang, L.C. (2011). Punching shear tests on RC slabs with different initial crack patterns. Procedia Engineering, 14, 1183-1189.

Hambley, D.F. (2011). Backfill mining. SME Mining Engineering Handbook (Vol. 1), Darling, P., Eds., SME, 1375-1384.

Itasca. (2002). FLAC - Fast Lagrangian Analysis of Continua, User's Guide. Minneapolis, MN: Itasca.

Itasca. (2013). FLAC3D - Fast Lagrangian analysis of continua in 3 dimensions; user's guide, version 5.01, Itasca Consulting Group, Minneapolis, MN.

Iterson FKTV (1917) Eenige theoretische beschouwingen over kwel, De Ingenieur

Jessome, A.P. (1977). Strength and related properties of woods grown in Canada.

Jones, L.L. and Wood, R.H. (1967). Yield line analysis of slabs. Thames and Hudson, London.

Johansen, K.W. (1972). Yield-line formulae for slabs. Cement and Concrete Association, London.

Jahanbakhshzadeh, A., Aubertin, M., and Li, L. (2017). Three-dimensional stress state in inclined backfilled stopes obtained from numerical simulations and new closed-form solution. Canadian Geotechnical Journal, 55(6), 810-828.

Jaouhar, E.M. and Li, L. (2019). Effect of drainage and consolidation on the pore water pressures and total stresses within backfilled stopes and on barricades. Advances in Civil Engineering.

Jaeger, J.C., Cook, N.G. and Zimmerman, R. (2009). Fundamentals of rock mechanics. John Wiley & Sons.

Kuganathan, K. (2001). Mine backfilling, backfill drainage and barricade construction-a safety first approach. Australia's Mining, 58–64.

Kuganathan, K. (2002). A model to predict bulkhead pressures for safe design of bulkheads. Proc., Filling with Hydraulic Fills Seminar. Section 6, Australian Centre for Geomechanics, Perth.

Kennedy, G. and Goodchild, C. (2004). Practical yield line design. The Concrete Centre.

Le Roux, K., Bawden, W.F., and Grabinsky, M.F. (2005). Field properties of cemented paste backfill at the Golden Giant mine. Mining Technology, 114(2), 65-80.

Li, L., Aubertin, M., Simon, R., Bussière, B., and Belem, T. (2003). Modeling arching effects in narrow backfilled stopes with FLAC. Proc., FLAC and Numerical Modeling in Geomech., Rotterdam, Netherlands, 211-219.

Li, L., Aubertin, M., and Belem, T. (2005). Formulation of a three-dimensional analytical solution

to evaluate stresses in backfilled vertical narrow openings. Canadian Geotechnical Journal, 42(6), 1705-1717.

Li, L., Ouellet, S., and Aubertin, M. (2009). A method to evaluate the size of backfilled stope barricades made of waste rock. Proc., 62nd Canadian Geotechnical Conf. and 10th Joint CGS/IAH-CNC Groundwater Specialty Conf., Canadian Geotechnical Society, Richmond, BC, Canada, 497–503.

Li, L. and Aubertin, M. (2009a). Horizontal pressure on barricades for backfilled stopes. Part I: Fully drained conditions. Canadian Geotechnical Journal, 46(1), 37-46.

Li, L. and Aubertin, M. (2009b). Horizontal pressure on barricades for backfilled stopes. Part II: Submerged conditions. Canadian Geotechnical Journal, 46(1), 47-56.

Li, L. and Aubertin, M. (2009c). Numerical investigation of the stress state in inclined backfilled stopes. International Journal of Geomechanics, 9(2), 52-62.

Li, L., and Aubertin, M. (2011). Limit equilibrium analysis for the design of backfilled stope barricades made of waste rock. Canadian Geotechnical Journal, 48(11), 1713-1728.

Li, L. (2013). A simple solution to assess pore-water pressure in barricades made of waste rock. CIM J., 4(1), 53–60.

Li, J., Ferreira, J.V. and Le Lievre, T. (2014). Transition from discontinuous to continuous paste filling at Cannington Mine. In Proceeding of the llth international Symposium on Mining with Backill, Preth: Australian Centre for Geomechanics, 381-394.

McLemore, V.T., Fakhimi, A., van Zyl, D., Ayakwah, G.F., Anim, K., Boakye, K., Ennin, F., Felli, P., Fredlund, D., Gutierrez, L.A., and Nunoo, S. (2009). Literature review of other rock piles: characterization, weathering, and stability. Questa Rock Pile Weathering Stability Project. New Mexico Bureau of Geology and Mineral Resources. New Mexico Tech, USA.

Mitchell, R.J., Smith, J., and Libby, D. (1975). Bulkhead pressures due to cemented hydraulic mine backfills. Canadian Geotechnical Journal, 12(3), 362-371.

Mitchell, R.J., Olsen, R.S., and Smith, J.D. (1982). Model studies on cemented tailings used in mine backfill. Canadian Geotechnical Journal, 19(1),14–28.

Mitchell, R.J. (1983). Earth structures engineering. Allen and Unwin, Boston, Mass.

Menetrey, P. (2002). Synthesis of punching failure in reinforced concrete. Cement and Concrete Composites, 24(6), 497-507.

Menetrey, P., Walther, R., Zimmermann, T., Willam, K.J., and Regan, P.E. (1997). Simulation of punching failure in reinforced-concrete structures. Journal of Structural Engineering, 123(5), 652-659.

Nujaim M., Auvray C., and Belem T. (2018). Geomechanical behaviour of a rock barricade and cemented paste backfill: Laboratory experiments on a reduced-scale model. In Geomechanics and Geodynamics of Rock Masses, Volume 1: Proceedings of the 2018 European Rock Mechanics Symposium. CRC Press, 339.

Nujaim M., Belem T., and Auvray, C. (2020a). Small-scale model preliminary testing on the interaction between paste backfills and waste rock barricades. In Rock Mechanics for Natural Resources and Infrastructure Development, Volume 6: Proceedings in Earth and Geosciences. CRC Press, 1807.

Nujaim, M., Belem, T., Giraud, A. (2020b). Experimental tests on a small-scale model of a mine stope to study the behavior of waste rock barricades during backfilling. Minerals, 10(11), 941.

Paterson, A.J.C. and Cooke, R. (1993). The design of backfill pipeline distribution systems by use of computer aided techniques, Minefill 93, Johannesburg, SAIMM, 209–213.

Pavlovsky NN (1931) Seepage through earth dikes. Instit. Gidrotekhniki i Melioratsii, Leningrad.

PLAXIS. (2008). Reference manual, 2D – version 9.0, PLAXIS. Delft, Netherlands: Delft University of Technology.

Pirapakaran, K. (2008). Load-deformation characteristics of minefills with particular reference to arching and stress developments. Townsville: James Cook University.

Potvin, Y., Thomas, E., and Fourie, A. (2005). Handbook on mine fill, Australian Centre for Geomechanics, Perth.

Ramos, A.P., Lúcio, V.J., and Regan, P.E. (2011). Punching of flat slabs with in-plane forces. Engineering Structures, 33(3), 894-902.

Ras, D.J.R., Smart, R.M., Harrison, A.T., and Van Blommestein, G. (2007). High strength aerated cement bulkheads for target gold mine, South Africa. Proc., 9th Int. Symp. in Min. with Backfill (CD-ROM), CIM, Montreal.

Revell M.B. and Sainsbury D.P. (2007a). Paste barricade failures. 9th International Symposium on Mining with Backfill, Montréal, QC, Canada.

Revell M.B. and Sainsbury D.P. (2007b). Advancing paste fill barricade design using numerical modeling. 9th International Symposium on Mining with Backfill, Montréal, QC, Canada.

RocScience. (2002). Phase2: 2D finite element program for calculating stresses and estimating support around underground excavations. Toronto, Canada.

Rankine, K.J. (2005). An investigation into the drainage characteristics and behaviour of hydraulically placed mine backfill and permeable minefill barricades. Ph.D. thesis, James Cook University, Townsville City.

Rankine, R.M. and Sivakugan, N. (2007). Geotechnical properties of cemented paste backfill from Cannington Mine, Australia. Geotechnical and Geological Engineering, 25(4), 383-393.

Salençon J. (1969). Contraction quasi-statique d’une cavite a symetrie spherique ou cylindrique dans un milieu elastoplastique. In Annales des ponts et chaussées, 4, 231-236.

Schaffernak F (1917) Über die Standicherheit durchlaessiger geschuetteter Dämme, Allge, Eauzeitung

Sivakugan, N., Rankine, K.J., and Rankine, R.M. (2006). Permeability of hydraulic fills and barricade bricks. Geotechnical and Geological Engineering, 24, 661-673.

Sinopoli, A. (1998). Arch Bridges: History, Analysis, Assessment, Maintenance and Repair. AA Balkema, Rotterdam.

Soderberg, R.L. and Busch, R.A. (1985). Barricades and drains for high sandfill stopes. U.S. Department of the Interior, Bureau of Mines.

Spiegel, L. and Limbrunner, F.G. (2003). Reinforced concrete design, 5th Edition. Prentice Hall.

Stone, D.M.R. (1993). The optimization of mix designs for cemented rockfill. In Minefill, 93, 249-253.

Smith, J.D. and Mitchell, R.J. (1982) Design and control of large hydraulic backfill pours. CIM Bulletin, 75(838), 102-111.

Shahsavari, M. and Grabinsky, M. (2014). Cemented paste backfill consolidation with deposition-dependent boundary conditions. In Proceedings of the 67th Canadian Geotechnical Conference, Regina, SK, Canada, Vol. 28

Tesarik, D.R., Seymour, J.B., and Yanske, T.R. (2009). Long-term stability of a backfilled room-andpillar test section at the Buick Mine, Missouri, USA. International Journal of Rock Mechanics and Mining Sciences, 46(7), 1182-1196.

Timoshenko, S. and Young, D.H. (1972). Elements of Strength of Materials. New York: Van Nostrand.

Timoshenko, S. and MacCullough, G.H. (1949). Elements of strength of materials.

Thompson, B.D., Grabinsky, M.W., and Bawden, W.F. (2012). In-situ measurements of CPB at the Cayeli Mine. Canadian Geotechnical Journal, 49, 755-772.

Veenstra, R.L. (2013). A design procedure for determining the in situ stresses of early age cemented paste backfill. Ph.D. Thesis, University of Toronto, Toronto, Canada.

Widisinghe, S.D. (2014). Stress developments within a backfilled mine stope and the lateral loading on the barricade. Ph.D. Thesis, James Cook University, Queensland, Australia.

Yang, P.Y., Brochu-Baekelmans, M., Li, L., and Aubertin, M. (2014). An improved solution for sizing barricades made of waste rock to retain cemented paste backfill. Proc., 67th Can. Geotech. Conf., Regina, Canada.

Yang, P.Y., Li, L., Aubertin, M., Brochu-Baekelmans, M. and Ouellet, S. (2017). Stability analyses of waste rock barricades designed to retain paste backfill. International Journal of Geomechanics, 17(3), 04016079.

Yang, P.Y., Li, L., and Aubertin, M. (2017a). Stress ratios in entire mine stopes with cohesionless backfill: A numerical study. Minerals, 7(10), 201.

Yang, P.Y., Li, L., and Aubertin, M. (2017b). A new solution to assess the required strength of mine backfill with a vertical exposure. International Journal of Geomechanics. 17(10), 04017084-1–

04017084-13.

Yang, P.Y., Li, L., and Aubertin, M. (2017c). Stress ratios in entire mine stopes with cohesionless backfill: A numerical study. Minerals, 7(10), 201.

Yilmaz, E., Belem, T., and Benzaazoua, M. (2015). Specimen size effect on strength behavior of cemented paste backfills subjected to different placement conditions. Engineering Geology, 185, 52-62.

Yumlu, M. and Guresci, M. (2007). Paste backfill barricade monitoring-A case study from Inmet's Cayeli mine. Proc., 9th Int. Symp. in Min. with Backfill (CD-ROM), CIM, Montreal.

Yu, T.R. and Counter, D.B. (1983). Backfill practice and technology at Kidd Creek Mines. CIM Bulletin, 76(856), 56-65.

Zheng, J., Li, L., Mbonimpa, M., and Pabst, T. (2018). An analytical solution of gibson's model for estimating the pore water pressures in accreting deposition of slurried material under one-dimensional self-weight consolidation. part I: pervious base. Indian Geotechnical Journal, 48(1), 72-8.

Zheng, J., Li, L., and Li, Y. (2019). Total and effective stresses in backfilled stopes during the fill placement on a pervious base for barricade design. Minerals, 9(1), 38.

Zheng, J. and Li, L. (2020). Experimental study of the "short-term" pressures of uncemented paste backfill with different solid contents for barricade design. Journal of Cleaner Production, 275, 123068.

Zheng, J., Li, L., and Li, Y.C. (2020). A solution to estimate the total and effective stresses in backfilled stopes with an impervious base during the filling operation of cohesionless backfill. International Journal for Numerical and Analytical Methods in Geomechanics, 44(11), 1570-1586.

APPENDIX A FIELD TESTS IN YOUNG-DAVIDSON MINE

To realize the use of WRB instead of shotcrete walls in the field, this project tested the pressures exerted by backfilled stopes on the shotcrete wall in Young-Davidson Mine.

The Young-Davidson Mine uses a high-density slurry (e.g., 80% solids concentration) known as paste fill as backfill material composed of full mill tailings, binders (i.e., iron ore slag and Portland cement), and process water. The average bulk unit weight of the CPB γ_b was 20 kN/m^3. The physical parameters for the three stopes are listed in Table A.1.

Table A.1 pH and temperature values of tailings and water

Mixture	Stope level	
	9710-2940	9950-3440
Cement content (%)	5 (plug) 2 (body); 3 (tight)	5 (plug); 2 (body) 2 (cap); 0 (waste cap)
Solids concentration (%)	79.0	82.3
water content (%)	26.6	21.5

Note: sea level is on 10300, 9710 level means 590 m underground;

Tailings created from the crushed mineral rock are thickened to a certain solids concentration and transferred to disk filters in which the tailings are properly dewatered. Water mixed into tailings is drawn from on-site. Table A.2 presents the pH and the temperature values of tailings and water, which was performed by Golder Associates Ltd. The process water in Young-Davidson Mine shows alkalinity.

Table A.2 pH and temperature values of tailings and water

Sample	pH	Temperature (°)
Tailings	9.3	20
Process water	8.3	20

Fig. A.1 presents the particle size distributions (PSDs) determined using mechanical sieving and a Fritsch laser particle size analyzer according to ASTM D4464.

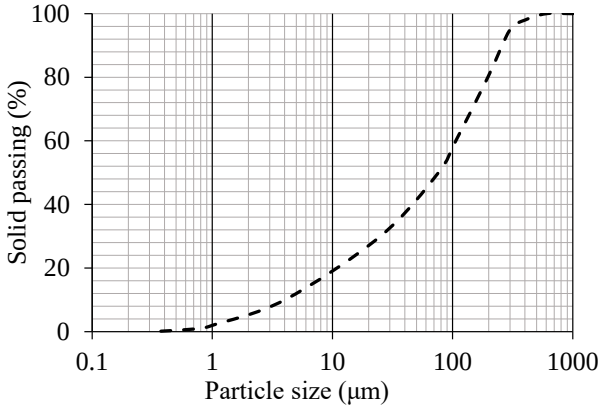

Figure A.1 Particle size distributions (PSDs) of tailings used in Young-Davidson Mine

Depending on the required strength, the paste consists of between 2% and 7.5% binder. For example, a plug with 7.5% binder is used in consideration of the underhand mining method, and the body contains 2% or 3% binder to prevent liquefaction.

A1 Stope geometry and fill plan

The geometry was obtained by Cavity Monitoring System (CMS) in 9710-2940 stope from the front view (Fig. A.2a), right view (Fig. A.2b), the filling plan (Fig. A.2c). In the figure, *H* (m) is the stope height. *L* (m) and *W* (m) are the stope length and width, respectively. Fig. A.2a shows that the stope shows the different lengths at the top and bottom (e.g., 20 m at the top and 38.5 m at the bottom). The relative uniform stope width (W = 20 m) can be observed in Fig. A.2b. The details of the pour parameters are presented in Table A.3. The plug and body of the stope were backfilled from 3rd August 2020 to 7th August 2020. The tight of stope was poured and finished on 15th August 2020.

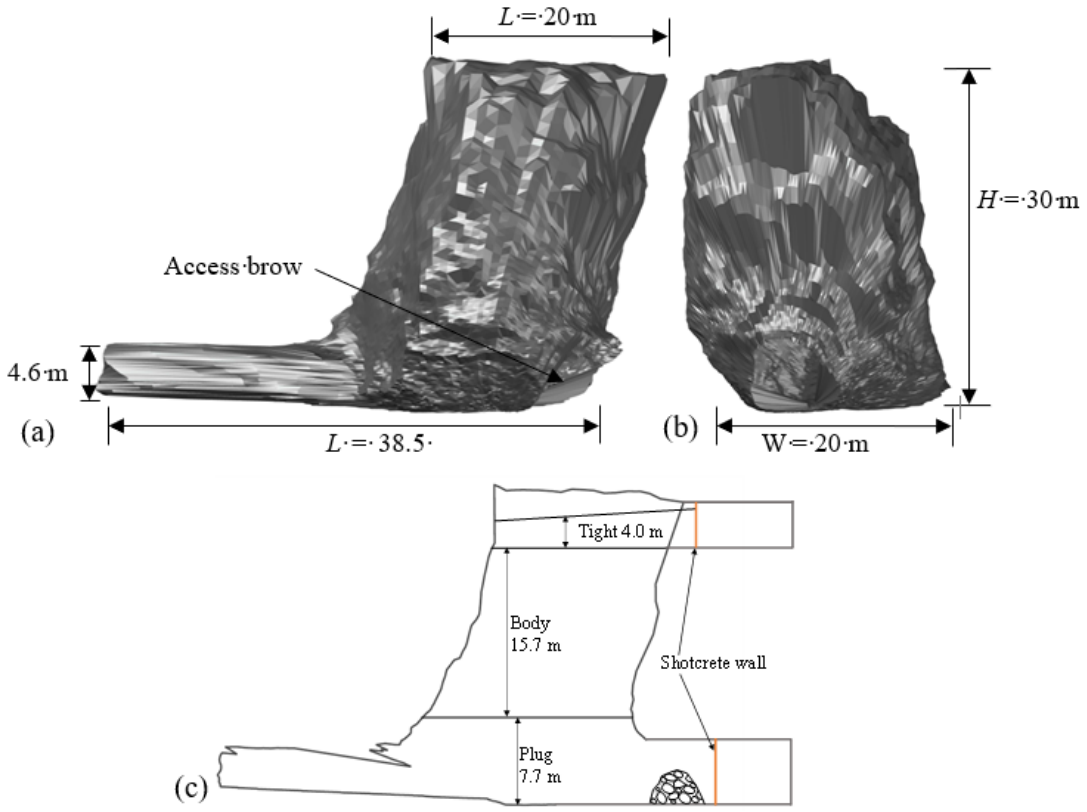

Figure A.2 9710-2940 stope geometry from different perspectives: (a) front view, (b) right view, and (c) fill plan

Table A.3 Backfill parameters in 9710-2940 stope

Portion	Average height (m^3)	Paste volume (m^3)	Planned fill weight (t)	Actual fill weight (t)	Backfill rate (m^3/h)	Rise rate (m/h)
Plug	7.7	2758	5516	6691	250	0.17
Body	15.7	4631	9263	11704	250	0.33
Tight	4.0	979	1957	2423	125	0.17

The geometry images in 9950-3440 stope are presented in Fig. A.3a (front view) and Fig. A.3b (right view), and the filling plan is illustrated in Fig. A.3c. The 9950-3440 stope shows a variable width from the bottom (W = 11.2 m) to the top (W = 11.2 m), and presents a relatively uniform length (L = 19 m). The pouring parameters are detailly presented in Table A.4. The plug and body of the stope were backfilled from 24th August 2020 to 27th August 2020. The second layer of the cap was implemented with waste rock (muck).

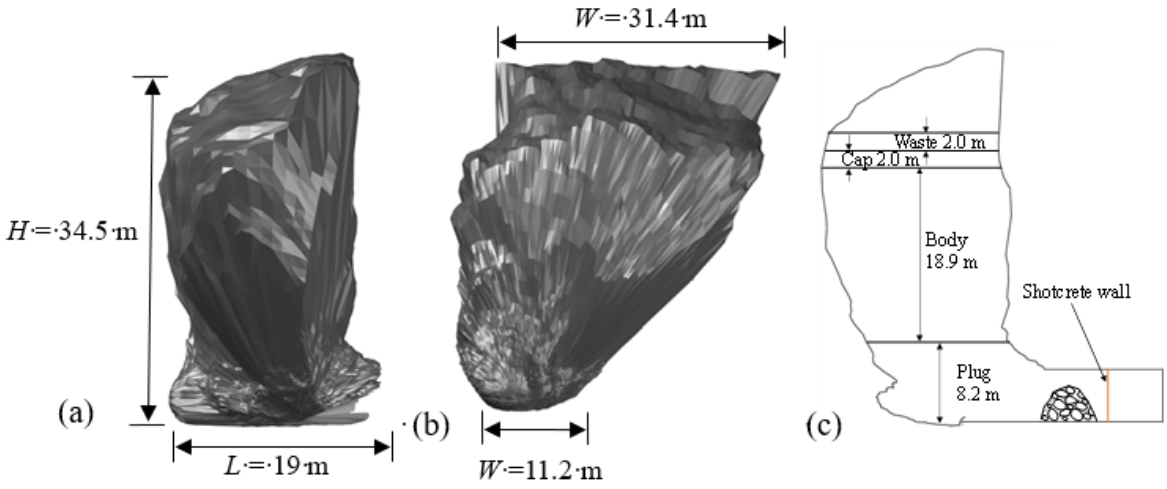

Figure A.3 9550-3440 stope geometry from different perspectives: (a) front view, (b) right view, and (c) fill plan

Table A.4 Backfill parameters in 9950-3440 stope

Portion	Average height (m^3)	Paste volume (m^3)	Planned fill weight (t)	Actual fill weight (t)	Backfill rate (m^3/h)	Rise rate (m/h)
Plug	8.2	2370	4740	7215	250	0.26
Body	18.9	7929	15859	16565	250	0.34
Cap	2.0	998	1997	1438	250	0.5
Waste	2.0	451	903	-	-	-

The geometry scanned by Cavity Monitoring System (CMS) in 9950-3135 stope is shown from the front view (Fig. A.4a) and right view (Fig. A.4b), the filling plan is presented inFig. A.4c. Fig. A.4a shows the different lengths at the top and bottom (e.g., 11 m at the top and 26 m at the bottom). The stope width at the top with 14.7 m can be observed in Fig. A.4b. The backfill parameters are presented in Table A.5.

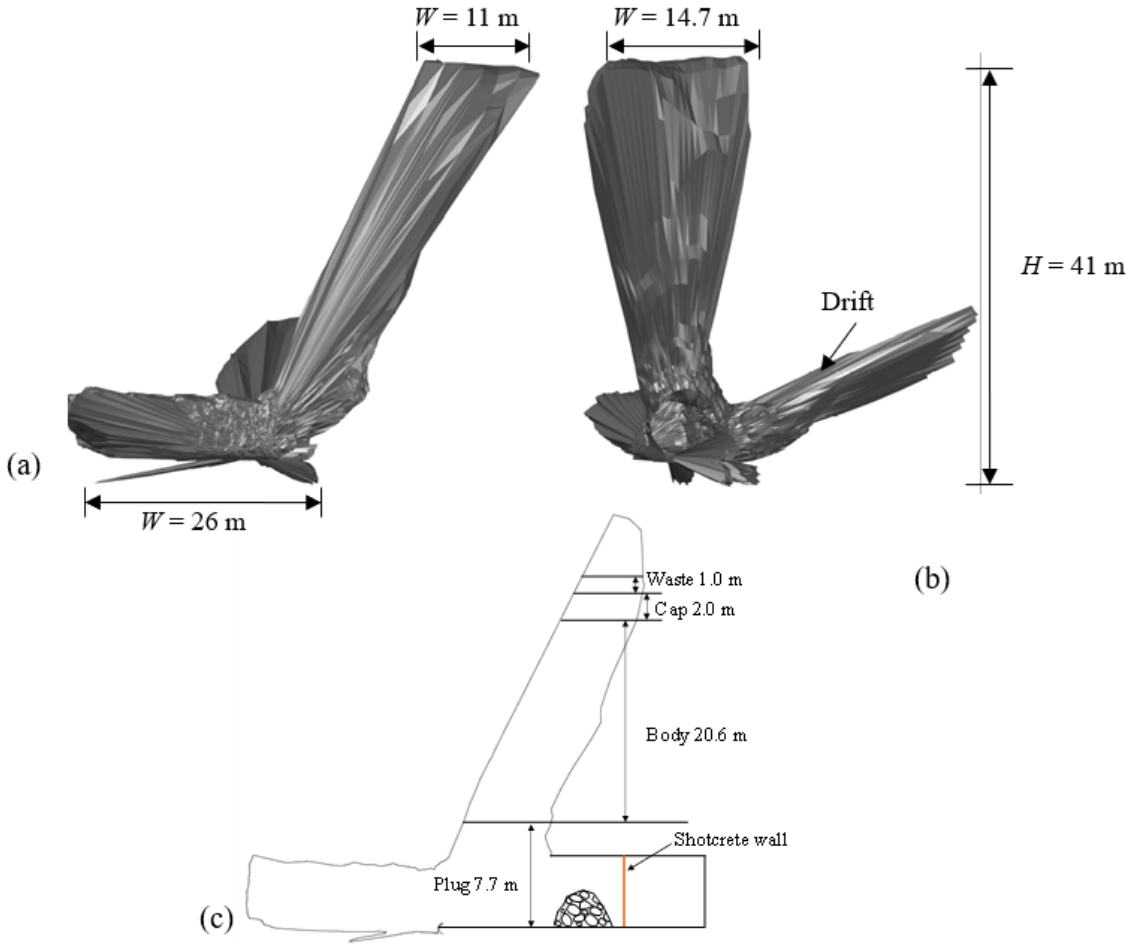

Figure A.4 9950-3135 stope geometry from different perspectives: (a) front view, (b) right view, and (c) fill plan

Table A.5 Backfill parameters in 9950-3135 stope

Portion	Average height (m^3)	Paste volume (m^3)	Planned fill weight (t)	Actual fill weight (t)	Backfill rate (m^3/h)	Rise rate (m/h)
Plug	7.5	5027	10054	-	250	-
Body	20.6	1946	3892	-	250	-
Cap	2.0	289	578	-	250	-
Waste	1.0	140	280	-	125	-

A2 Barricades and instruments setup

The Young-Davidson Mine constructed shotcrete walls with a thickness of about 0.33 m at access

drift of each sublevel intersecting the stope. Fig. A.5a shows the configuration of the shotcrete wall with a designed drainage system (e.g., weeping tile and drainage pipes, shown in Fig. A.5b).

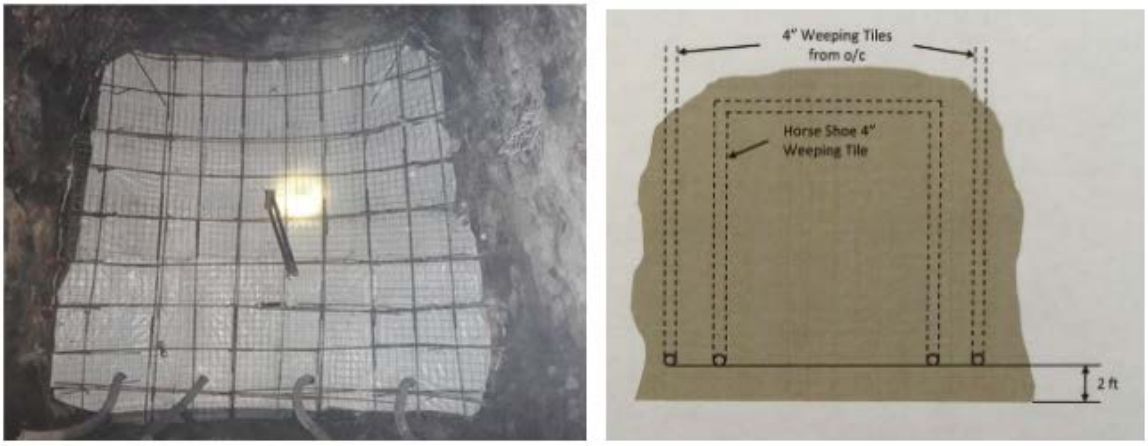

Figure A.5 In situ photo of the steel frame of a shotcrete wall with weeping tiles and reinforcements

Total earth pressures were recorded using a vibrating wire pressure transducer (Geokon model number 4800-1-350 kPa) with a 7 kPa ~ 3 MPa range and the maximum error linear is 0.1 % (total 6 sensors). Total earth pressure cell (TEC) is the sensor connected with a pressure gauge (RST TP-101) with a range up to 2 MPa, which is used to ensure the pressures exerted by the CPB is below P_m = 120 kPa in the Young-Davidson Mine [$P_m = P_d$ / FS, P_m (kPa) is the pressure measured in the field; P_d (kPa) is the pressure designed based on theory, P_d is considered as about 240 kPa for the Young-Davidson Mine (Revell and Sainsbury 2007)].

The EPCs were installed in different elevations of the shotcrete walls to measure the pressure variation versus filling time or fill height. Pore-water pressures (PWP) were monitored using vibrating wire piezometers (Geokon model number 4500S-350 kPa) with the same range with EPC and the maximum error linear is 0.08 %. The sensors (i.e., earth pressure cells and piezometers) were equipped with thermistors to monitor the temperature changes. Similar instruments were successfully used in in-situ tests at the Kanowna Belle Mine by Helinski et al. (2006), Cayeli Mine by Thompson et al. (2012), Raleigh Gold Mine by Doherty et al. (2015). All the sensors (four of each test) were connected to a multichannel data logger to automatically record the data, or a

handheld readout to measure the initial zero reading.

Fig. A.6 schematically shows the pressure installations at different heights and positions. The horizontal pressure is monitored at different elevations (e.g., top, middle, and bottom) for the shotcrete wall. Pressure instruments are mounted on the steel frame by using tie wraps.

Fig. A.6a shows the layout of sensor setups in the 9710-2940 stope, one piezometer is fixed in a bucket with water to keep the saturation. Three earth pressure cells (EPCs) are installed on the steel frame of the shotcrete wall at the same height (i.e., 1.03 m). Fig. A.6b presents two sets of sensors installed on the shotcrete wall at different elevations such as 0.2 m and 2.2 m above the ground in 9950-3440 stope. Fig. A.6c gives the location of a piezometer and an EPC near the access brow in 9550-3135 stope. Two EPCs are installed at the top and the bottom of the shotcrete wall, respectively.

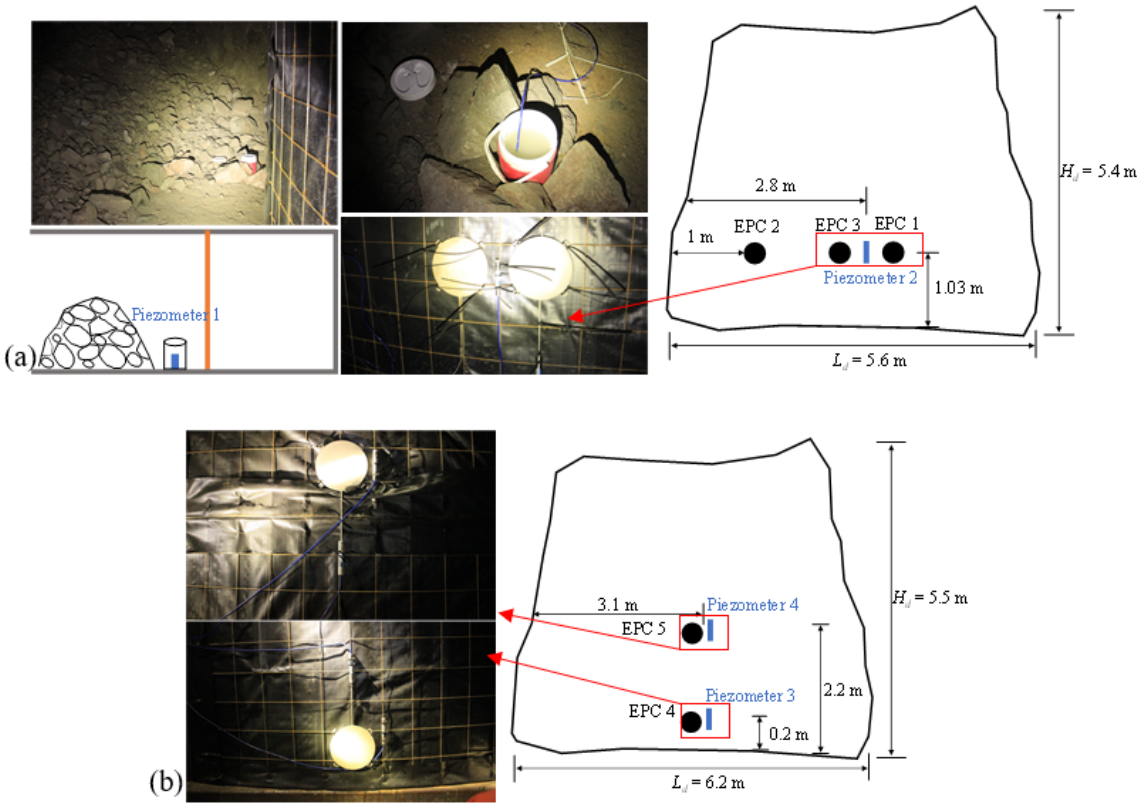

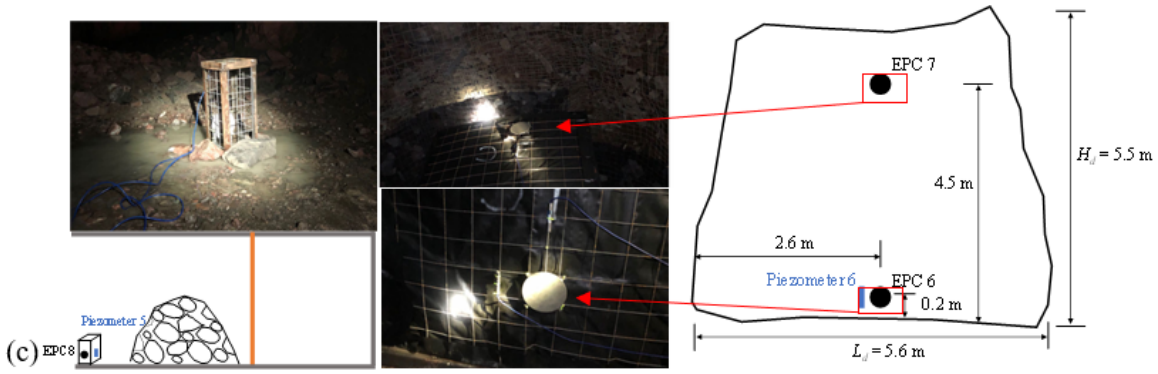

Figure A.6 Schematic view of sensors installation in (a) 9710-2940 stope, (b) 9950-3440 stope, and (c) 9550-3135

A3 Results

A3.1 9710-2940 stope

Fig. A.7 gathers results for total earth pressure obtained from EPC, pore-water pressure obtained with PWP, temperatures monitored from all sensors, overburden, and fill height for the 9710-2940 stope for the different periods on the response during and shortly after the continuous filling. The transition from plug (5% binder) to body (2% binder) occurred after 24 hours. The continuous pour ended at 96 hours and peaked at 50.8 kPa (TEP 1) at 81 hours. The manual reading is recorded by the EPC 3 with a pressure gauge, which was installed at the same height near the EPC 1.

To understand the pressures exerted on the barricade, let us examine in detail the variation trend for the initial 120-hour period, as shown in Fig. A.7a. First, the total stresses have soared to 44.35 kPa (TEP 1) and 30.82 kPa (TEP 2) during 3 hours' fill, respectively. While the pore-water pressures have surged to 33.13 kPa (PWP 1) during 3 hours' fill and 32.67 kPa (PWP 2) during 2 hours' fill, respectively. The quick fill of the space between the muck berm and the shotcrete wall accounts for the sudden increase of the pressures. Then, the total stresses decreased to about half and the pore-water pressures reduced quickly during the next 3 hours. The rapid decrease of pore-water pressure accounts for a significant reduction of the total stresses. It should be noted that the water percolated through the shotcrete wall instead of the weeping tiles based on the in-situ observation. Then, the total stresses (TEP 1) slowly and continuously increased their value up to

50.8 kPa at 81 hours. This confirmed the process of continuous fill (e.g., stope backfill ended at 96 hours). The total stresses (TEP 2) are relatively low in comparison with TEP 1. The CPB seepage along the shotcrete wall observed in the field may be accountable for the difference.

In addition, it was worth questioning the total stresses (TEP 2) are too low (even negative) to be realistic (as shown in Fig. A.7b), which reach up to -33.63 kPa. To understand the negative value of the TEP 2, a pull-out test for the earth pressure cell was performed and the results show a negative value (compression is positive), proving that the tension occurred at a longer period (i.e., 220 hours). The two next figures present the pressure variations and temperature changes versus fill height and filling time, respectively.

Fig. A.7c shows temperatures recorded by four sensors in the access drift. It can be seen that the incremental increase of temperature is about 6 °C (peak value is 30.2 °C) for the 220-hour period, which shows a different magnitude with Thompson et al. (2012) showing an increasing temperature of 26.8 °C (peak value is 55.8 °C) for about 283 hours. The reason is that 100% Portland cement was used by the Cayeli Mine (Thompson et al. 2012), while Young-Davidson Mine employed a specific binder consisting of 90% slag and 10 % Portland cement. The binder (i.e., slag and cement) shows a performance having lower heat of hydration while having about the same weights and density as Portland cement (Stone 1993).

Fig. A.7d illustrates that the pressures vary as a function of filling height at the different stages (e.g, plug, body, and tight). The filling heights were calculated from those above the sensors. The total earth pressures increased quickly at the initial 3-meter height, corresponding to the overburden of CPB. The pore water pressures also showed the same trend at the first 3 meters height. The total stresses obtained from TEP 1 reached up to their maximum value of 50.8 kPa at 21.6 m and keep stable until the fill was finished.

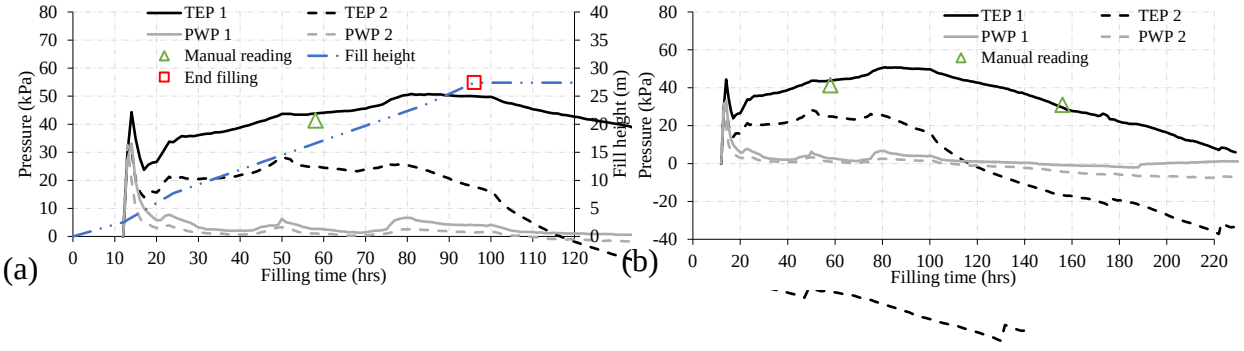

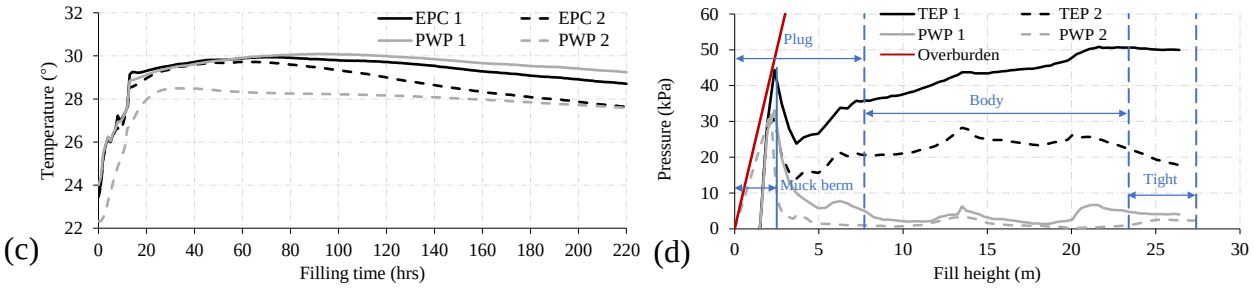

Figure A.7 Total earth pressure (TEP) and pore-water pressure (PWP) in the 9710-2940 stope versus filling time for (a) the 120 hours and (b) 220 hours; (c) temperatures versus the filling time; (d) pressures versus fill height.

A3.2 9950-3440 stope

Fig. A.8 detailly presents total pressure, pore-water pressure, and temperatures collected from sensors in the 9550-3440 stope for a short time (e.g., 110 hours) and a longer period (e.g., 450 hours). The continuous filling terminated at 106 hours and the peak value is 60.1 kPa (TEP 4) at 39 hours.

Fig. A.8a illustrates the variation of pressures as a function of filling time for the initial 110-hour period. After about 14 hours' fill, the CPB overflowed the top of the muck berm and fill the void between two walls (i.e., muck berm and shotcrete wall). Total pressure (TEP 4) and pore-water pressure (PWP 3), located at the bottom of the ground, shot up to 33.7 kPa and 33.8 kPa during 1 hours' fill, respectively. TEP5 increased up to 29.2 kPa during 3 hours while PWP 2 kept about 3 kPa for about 110 hours. Then, total pressure (TEP 4) showed an increase of 60.1 kPa at 30 hours and decreased to 34 kPa at 106 hours, while TEP 5 increased its value up to 31.9 kPa at 53 hours and sustained its value at this level during this period. It should be mentioned that PWP 2 showed a negative value after 59 hours because of the effective drainage system and low water content and low permeability of the paste.

Fig. A.8b shows the variation of pressures versus filling time over a long period. TEP 4 shows an obvious fluctuation from 60.1 kPa at 30 hours to -25 kPa at 247 hours. The negative pressure obtained from TEP 4 occurred at 168 hours (after 62 hours of the end of fill). The tension proved by the pull-out test and the shrinkage due to cement hydration account for the occurrence of

negative values.

Fig. A.8c presents the variation of temperatures monitored by two sets of sensors mounted on the shotcrete wall. An increase in the magnitude of the temperature (e.g., EPC 5) showed 8 °C during 418 hours period, which shows a similar variation trend with the 9710-2940 stope.

Fig. A.8d shows the variation of the pressures versus the filling height divided into different stages. The quick rise in height for all sensors, except for PWP 4, is related to the weight of the overburden at the first 2.5-meter height. The total pressures recorded by TEP 4 showed the maximum value of 60.5 kPa at 6.76 m and decreased 39.3 kPa at final height with 31.5 m, which showed a different trend compared to the 9710-2940 stope. It is assumed that the mounting position of sensors near the weeping tile had a significant influence on the test values.

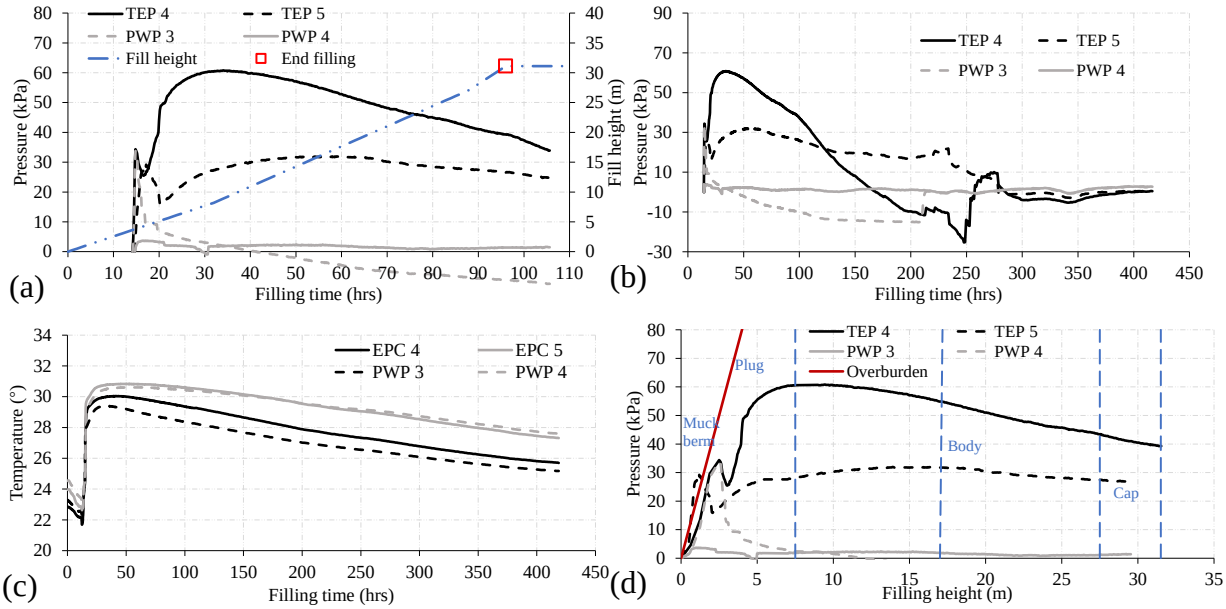

Figure A.8 Total earth pressure (TEP) and pore-water pressure (PWP) in the 9710-2940 stope versus filling time for (a) the 120 hours and (b) 220-hour period; (c) temperatures versus the filling time; (d) pressures versus fill height.

A3.3 9950-3135 stope

Fig. A.9 presents total pressure and pore-water pressure collected from sensors in the 9550-3135

stope located at the access brow of the shotcrete wall.

Fig. A.9a illustrates the variation of pressures as a function of filling time for the initial 70-hour period. Total pressure (TEP 8) and pore-water pressure (PWP 5) located at the access brow keep increasing up to 172.8 kPa and 136.9 kPa, respectively. Fig. A.9b presents the total pressure (TEP 6) and pore-water pressure (PWP 6) located at the bottom of the shotcrete wall keep increasing up to 55.6 kPa and 29.3 kPa, respectively. Total pressure (TEP 7) located at the top of the shotcrete wall keeps increasing up to 14 kPa.

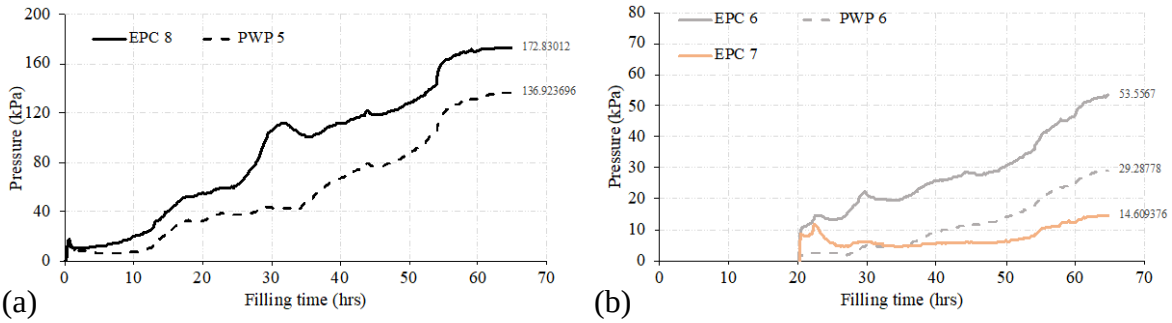

Figure A.9 Total earth pressure (TEP) and pore-water pressure (PWP) in the 9550-3135 stope versus filling time located at (a) the access brow (b) the shotcrete wall

A4 Calibration for the sensors

Fig. A.10 shows the dimension of the earth pressure cells. Total earth pressures were recorded using a vibrating wire pressure transducer (Geokon model number 4800-1-350 kPa) with a 7 kPa ~ 3 MPa range and the maximum error linear is 0.1 %. Horizontal pressure exerted by the CPB is interested in the project of the barricade design. Therefore, the EPCs were installed in different elevations of the shotcrete walls to measure the pressure variation versus filling time or fill height.

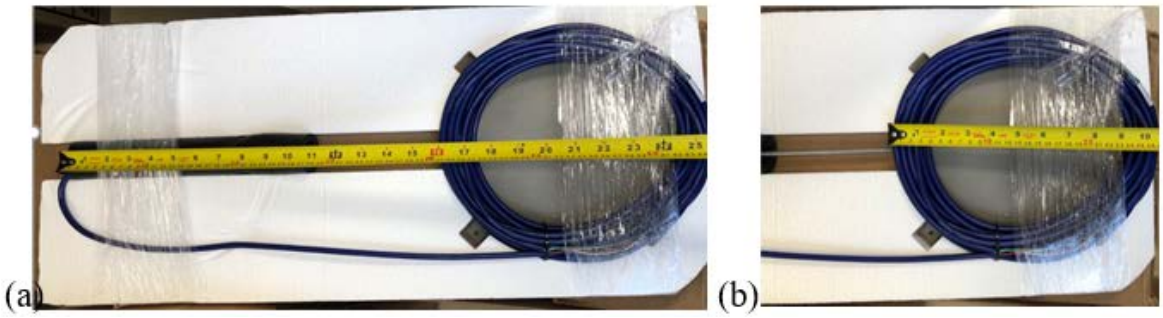

Figure A.10 Dimension of the earth pressure cells with (a) a 0.64 m height, (b) a 0.26 m diameter of the pressure plate

Fig. A.11 shows the dimension of the piezometers. Pore-water pressures (PWP) were monitored using vibrating wire piezometers (Geokon model number 4500S-350 kPa) with the same range with EPC and the maximum error linear is 0.08 %.

Figure A.11 Photo of the piezometer with a 0.14 m height

The sensors (i.e., earth pressure cells and piezometers) were equipped with thermistors to calibrate the results because of the temperature changes. Similar instruments were successfully used in in-situ tests at the Kanowna Belle Mine by Helinski et al. (2006), Cayeli Mine by Thompson et al. (2012), Raleigh Gold Mine by Doherty et al. (2015). All the sensors (four of each test) were connected to a multichannel data logger (shown in Fig. A.12a) to automatically record the data, or

a handheld readout to measure the initial zero reading (shown in Fig. A.12b).

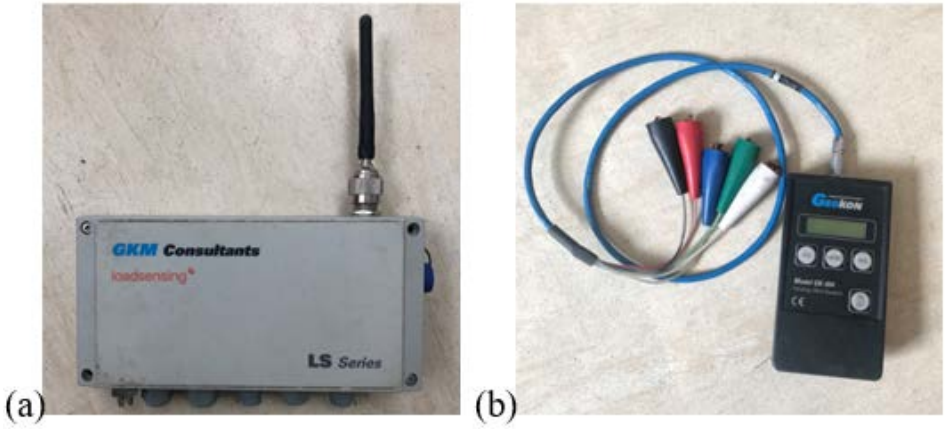

Figure A.12 Photo of the (a) datalogger and (b) handheld readout

The calibration of the sensors is a necessary step to check the validity of these instruments. A laboratory test with a 0.6 m height column was conducted by adding water with uniform height (e.g., 0.12 m) to calibrate the piezometer (serial number is 20019176).

The equation for calculating the pressures measured by the vibrating wire piezometer can be expressed by:

$$P = G\left(R_1 - R_0\right) + K\left(T_1 - T_0\right) - \left(S_1 - S_0\right) \quad \text{(A.1)}$$

where G (kPa/digit) is the linear gauge factor; R_1 is the current gauge reading.

Table A.6 detailly shows the laboratory test results for the piezometer with uniform height (e.g., 0.12 m). By considering the average value of the ratio G_l, the linear gauge factor obtained by the laboratory test can be considered as -0.1477 kPa/digit.

Table A.6 Laboratory test results for the piezometer with uniform height, R_0 is equal to 8963.1 in this test

P_w (kPa)	h_w (m)	R_1	R	G_l	C (°)
0	0	8963.1	0	0	21.2
1.177	0.12	8955	-8.1	-0.1453	21.8
2.354	0.24	8946.5	-16.6	-0.1418	21.6
3.531	0.36	8939	-24.1	-0.1465	21.4
4.708	0.48	8932.8	-30.3	-0.1554	21.2

Note: P_w (kPa) is the water pressure; h_w is the water height; G_l is defined as the ratio of P_w to the corresponding R (i.e., $G_l = P_w / R$) obtained by laboratory test results; R is the difference of R_1 and initial field zero reading R_0 (i.e., $R = R_1 – R_0$).

Based on the vibration wire pressure transducer calibration report provided by Geokon (serial number 2009176), the linear gauge factor G for the piezometer was -0.1477 kPa/digit. Fig. A.13 shows the variation of the water pressure p_w as a function of the R. It can be seen that the value of G_l is very close to the value of G. Both fitting lines have a good agreement with the laboratory test results.

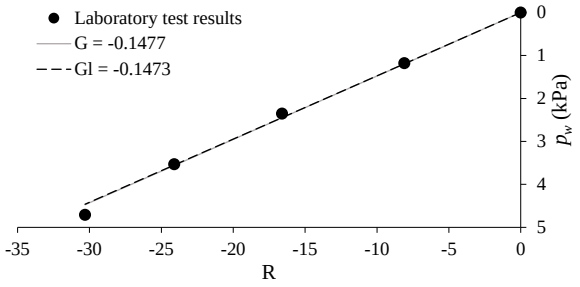

Figure A.13 Variation of the water pressure p_w as a function of the R

Fig. A.14 shows the variation of the water pressure p_w as a function of the R for the other two calibration results.

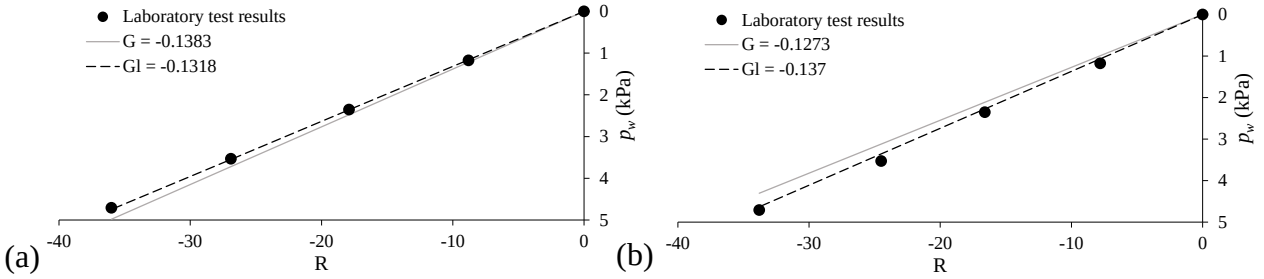

Figure A.14 Variation of the water pressure p_w as a function of the R for (a) serial number 2009178, (b) serial number 2009177

Table A.7 gives the results of pressure calculated from Eq. (A.1) with different linear gauge factors (e.g., G_l and G). Both linear gauge factors show a good agreement with the applied pressures.

Table A.7 Calculation of the pressures with G and G_l

Applied pressure (kPa)	Calculated pressure with G (kPa)	Calculated pressure with G_l (kPa)	R_0	R_1
0	0	0	8963.1	8963.1
70	72.092	71.872	8963.1	8475
140	141.954	141.522	8963.1	8002
210	212.260	211.613	8963.1	7526
280	282.122	281.262	8963.1	7053
350	352.132	351.059	8963.1	6579

There are some details to notice here, including:

- The original calibration range is from 0 to 350 kPa, our calibration is from 0 to 4.7 kPa. It should be noted that the difference is too large.
- Personal error, including inaccurate column scale [2mm about 0.02 kPa error] and artificial reading, should be taken into account.
- It seems that the saturation doesn't have a significant influence on the results. The reading at different periods is should below.
- It seems that the formula provided by Geokon without considering thermal and barometric

factors is enough to estimate the pressure because the variations of the temperature and biometric are relatively low.

APPENDIX B VALIDATION OF FLAC3D

The verification problem of a cylindrical hole in an infinite Mohr-Coulomb or linear elastic material is a basic problem, which can be used to test and to validate the accuracy of the numerical modeling built with FLAC3D (Itasca 2013). The practical engineering problems are commonly analyzed by using numerical modelings. The stable and reliable numerical results are obtained with the proper validating process, such as analyses of meh size, domain size, mechanical ratio, and other factors (e.g., small strain and large strain).

Fig. B.1a presents an overall view of a 3D physical model of the cylindrical hole with boundary condition, Fig. B.1b shows the quarter-symmetry geometry and boundary condition of the physical model. The radius of the hole (i.e., the distance from point O to point M) is 1 m. N is another point located at the boundary. D (m) is the domain for the cylindrical hole. P_0 (MPa) is the stress applied at the boundaries and represents the in-situ stress in the rock mass. The domain for the 3D quarter symmetric physical model is D/2. The origin of coordinates (x, y, z) of the physical model is O (0 m, 0 m, 0 m). Accordingly, the coordinate of M is (1 m, 0 m, 0 m) and N is (D/2 m, 0 m, 0 m).

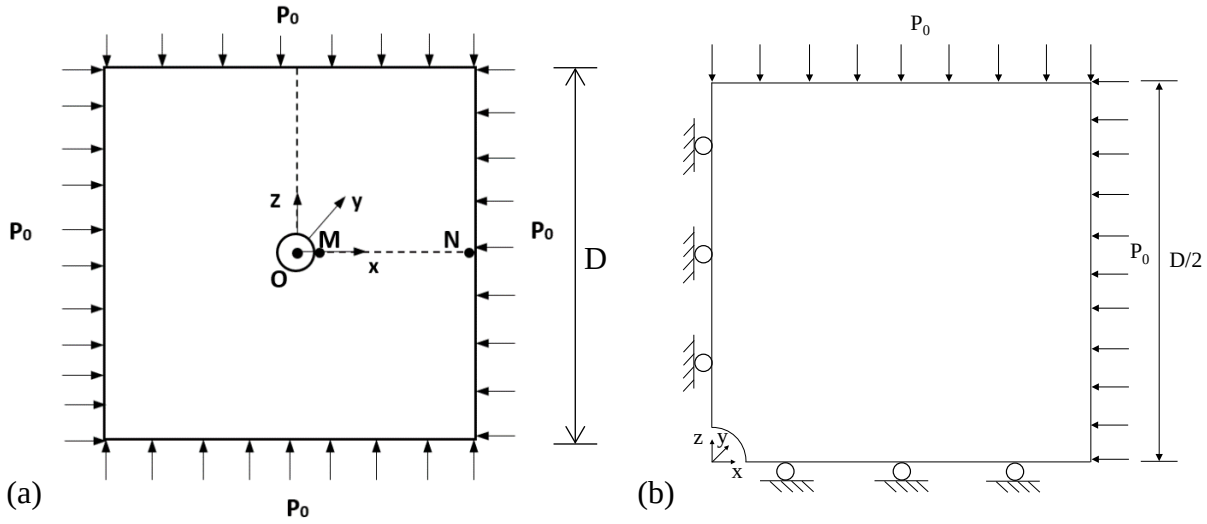

Figure B.1 Physical model of the cylindrical hole with boundary conditions: (a) overall view; (b) quarter symmetry (arrows indicate stress boundary condition; circles attached with solid lines are displacement boundary conditions)

The corresponding numerical model built with FLAC3D is shown in Fig. B.2. A radial mesh

produced with increasing mesh size away from the cylindrical hole is employed, and the radius grid ratio between adjacent grids is 1.1 in the radial direction. The default mechanical ratio (1×10^{-5}) is used to perform the numerical simulation.

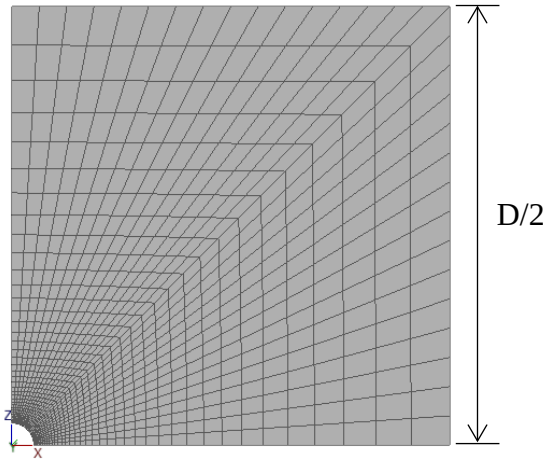

Figure B.2 The numerical model of the cylindrical hole with a quarter-symmetry view

B1 Mohr-Coulomb elasto-plastic model

Table B.1 shows the plan to conduct sensitivity analyses by changing one of the parameters for a specific case with the Mohr-Coulomb model. Young's modulus of rock mass is expressed as E (GPa), and its Poisson's ratio v, internal friction angle ϕ' (°), dilation angle ψ (°), cohesion c (MPa), tensile strength T_0 (GPa), respectively.

Table B.1 Program of numerical simulations in Mohr-Coulomb model for conducting sensitivity analyses; other parameters: P_0 = 30 MPa, v = 0.25, ϕ' = 30°, c = 2.17 MPa

Case	Domain (m)			ψ (°)	T_0 (GPa)	E (GPa)
	x	z	y			
1	10	10	0.2[1]	0	10	7.076
2	Variable		0.2[1]	0	10	7.076
3	10	10	Variable	0	10	7.076
4	10	10	0.2*	0	10	7.076
5	10	10	0.2[1]	30	10	7.076
6	10	10	0.2[1]	0	0	7.076

Notes: [1]: one grid in *y*-direction; *: uniform grid (i.e., the mesh size in the *y*-direction is the same as the one in *x* and *z*-directions).

Mesh size sensitivity analysis

Fig. B.3 shows radial displacements at point M obtained with FLAC3D as a function of the mesh size. The numerical simulation results become somewhat stable when mesh size decreases to 0.05 m.

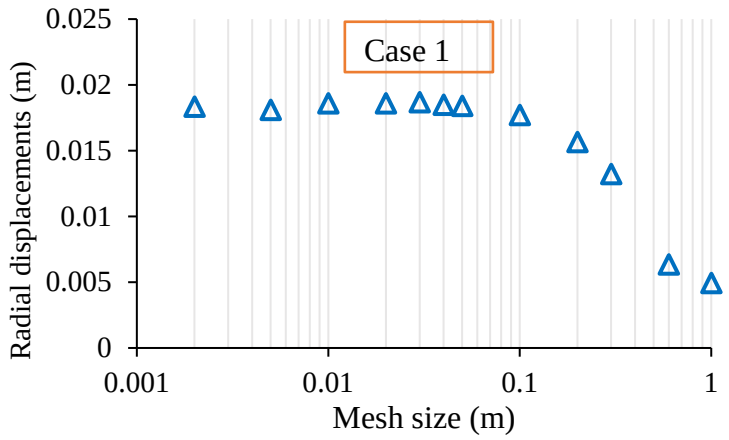

Figure B.3 radial displacements as a function of mesh size at point M

Domain sensitivity analysis in x and z-directions

Fig. B.4a presents radial displacements as a function of mesh size for different domain sizes (e.g., 10 m, 20 m, 30 m), these results are close when mesh size varies from 0.1 m to 0.03 m. Figure B.4b shows the radial displacements as a function of domain size, the results become somewhat stable when domain size increases to 12 m.

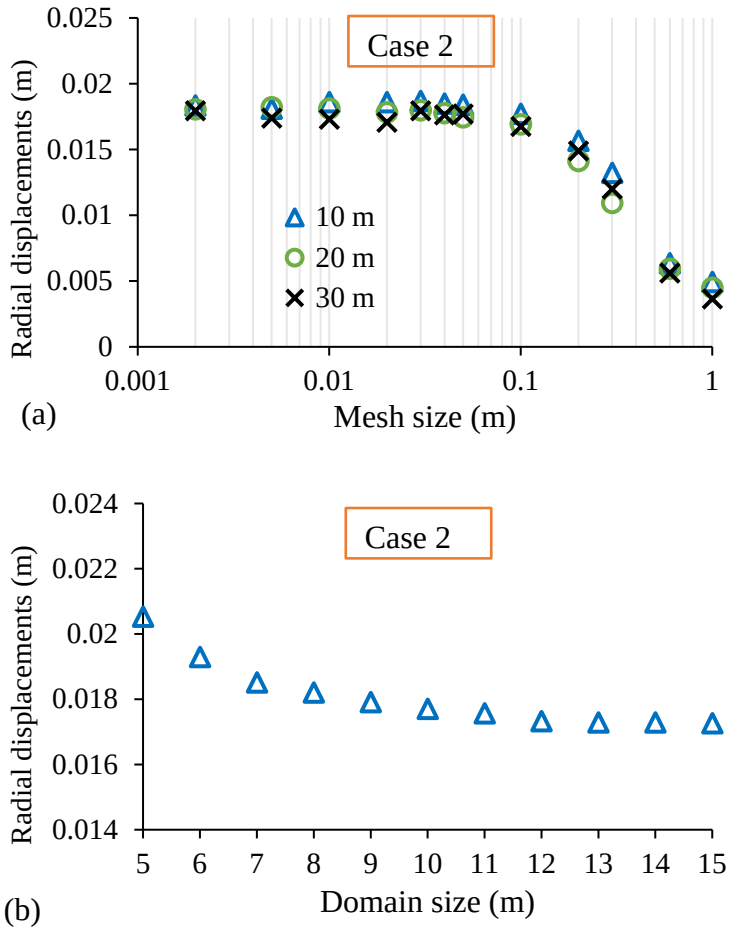

Figure B.4 radial displacements at point M as a function of (a) mesh size for different domain sizes; (b) domain size

Domain sensitivity analysis in the y-direction

Fig. B.5a shows radial displacements as a function of mesh size for different mesh sizes in the *y*-direction. Fig. B.5b gives radial displacements versus mesh size for two types of mesh sizes (i.e., one grid and uniform grid) in the *y*-direction. The results show that the domain size in the *y*-direction and its grid type (one grid or uniform grid) have little influence on the numerical results when mesh size changes from 1m to 0.01m.

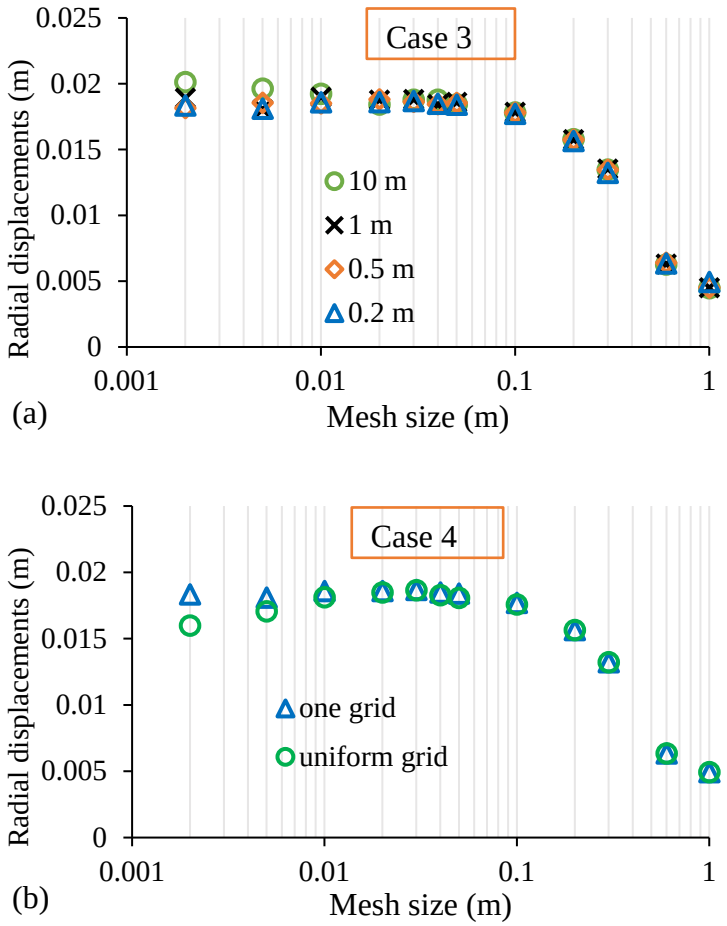

Figure B.5 radial displacements at the point M as a function of mesh size for (a) different mesh sizes in *y*-direction; (b) one grid and uniform grid in the *y*-direction

Associated flow

Fig. B.6 shows the radial displacement at the point M obtained with FLAC3D tends to become somewhat stable when the mesh size changes from 0.05 m to 0.02 m.

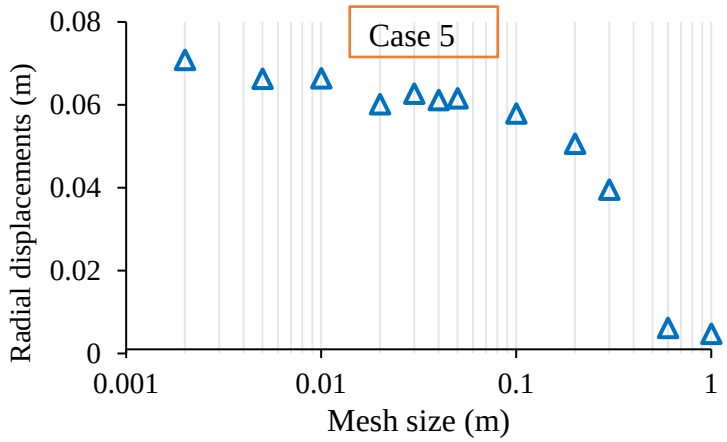

Figure B.6 Radial displacement at the point M obtained with the associated flow for different mesh sizes (Case 5 in Table B.1)

Tensile strength

Fig. B.7 shows the numerical results by using large and small strain, respectively. Fig. B.7a presents the numerical simulation results with a tensile strength of 0 GPa, while Fig. B.7b shows the results with a tensile strength of 10 GPa. The numerical results calculated based on large strain and small strain are very close shown in the figure. It should be mentioned that the 10 GPa (a non-realistic value) is a number to study the effect of tensile strength for the sensitivity analysis.

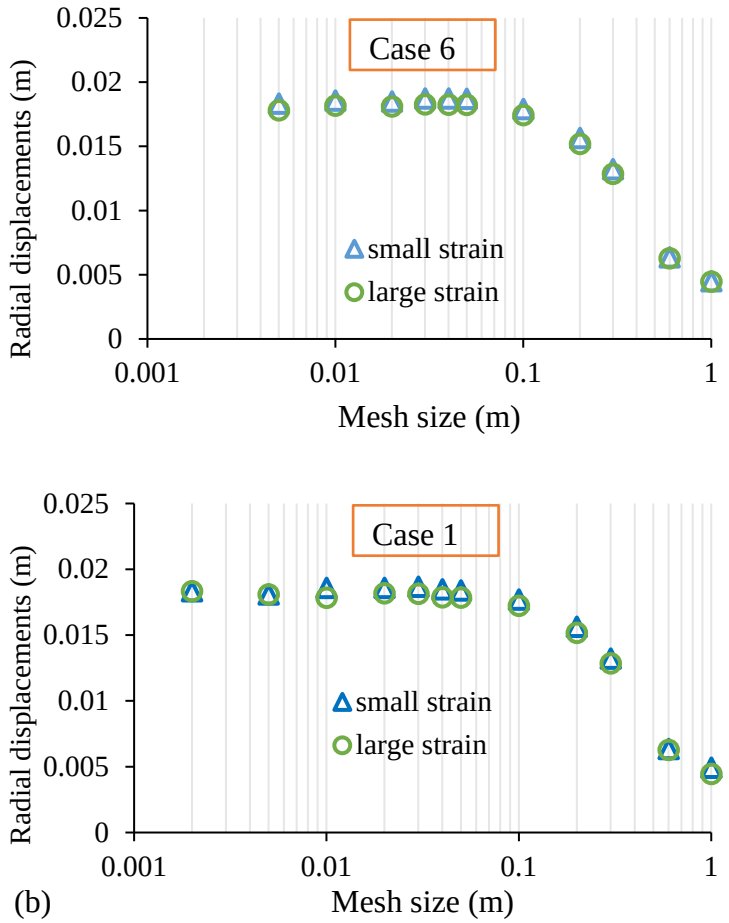

Figure B.7 Radial displacement at the point M as a function of mesh sizes with different tensile strength: (a) 0 GPa; (b) 10 GPa

Validation of numerical modeling with Mohr-Coulomb model

Figure B.8 presents the stresses (e.g., radial and tangential) distribution along MN line as a function of radial distance, obtained with FLAC3D and calculated by the analytical solution proposed by Salençon (1969), with optimal mesh size (0.05 m × 0.05 m) and domain size (12 m). *r* (m) is the distance from the hole axial.

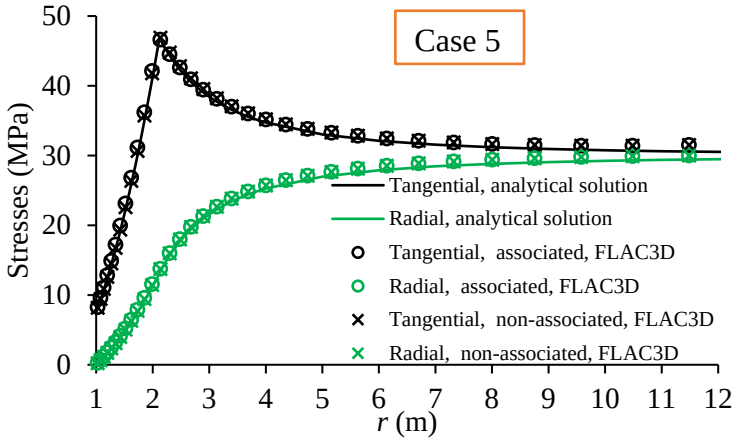

Figure B.8 radial and tangential stresses as a function of radial distance obtained with FLAC3D and analytical solution along MN line (associated flow with $\psi = 30°$; non-associated flow with $\psi = 0°$)

Figure B.9 presents the radial displacements as a function of radial distance along MN, obtained with FLAC3D and calculated by the analytical solution proposed by Salençon (1969), with mesh size (0.05 m × 0.05 m) and domain (12 m).

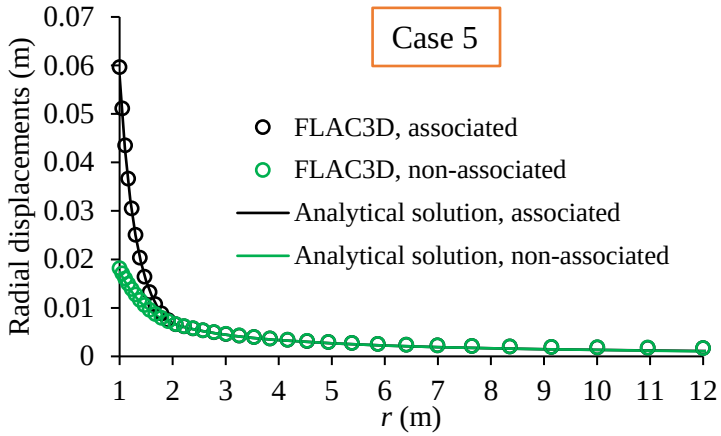

Figure B.9 radial displacement as a function of radial distance obtained with FLAC3D and analytical solution along MN line (associated flow with $\psi = 30°$; non-associated flow with $\psi = 0°$)

The effect of support stresses on shear failure state of the cylindrical hole

Fig. B.10 illustrates the shear failure state (e.g., red shows no failure state, green presents the active

shear failure, and blue depicts shear failure happened in the past) under different support stresses, such as obvious plastic zones with 0 MPa (Fig. B.10a), limited plastic zones with 10 MPa (Fig. B.10b), and no plastic zones with 15 MPa (Fig. B.10c).

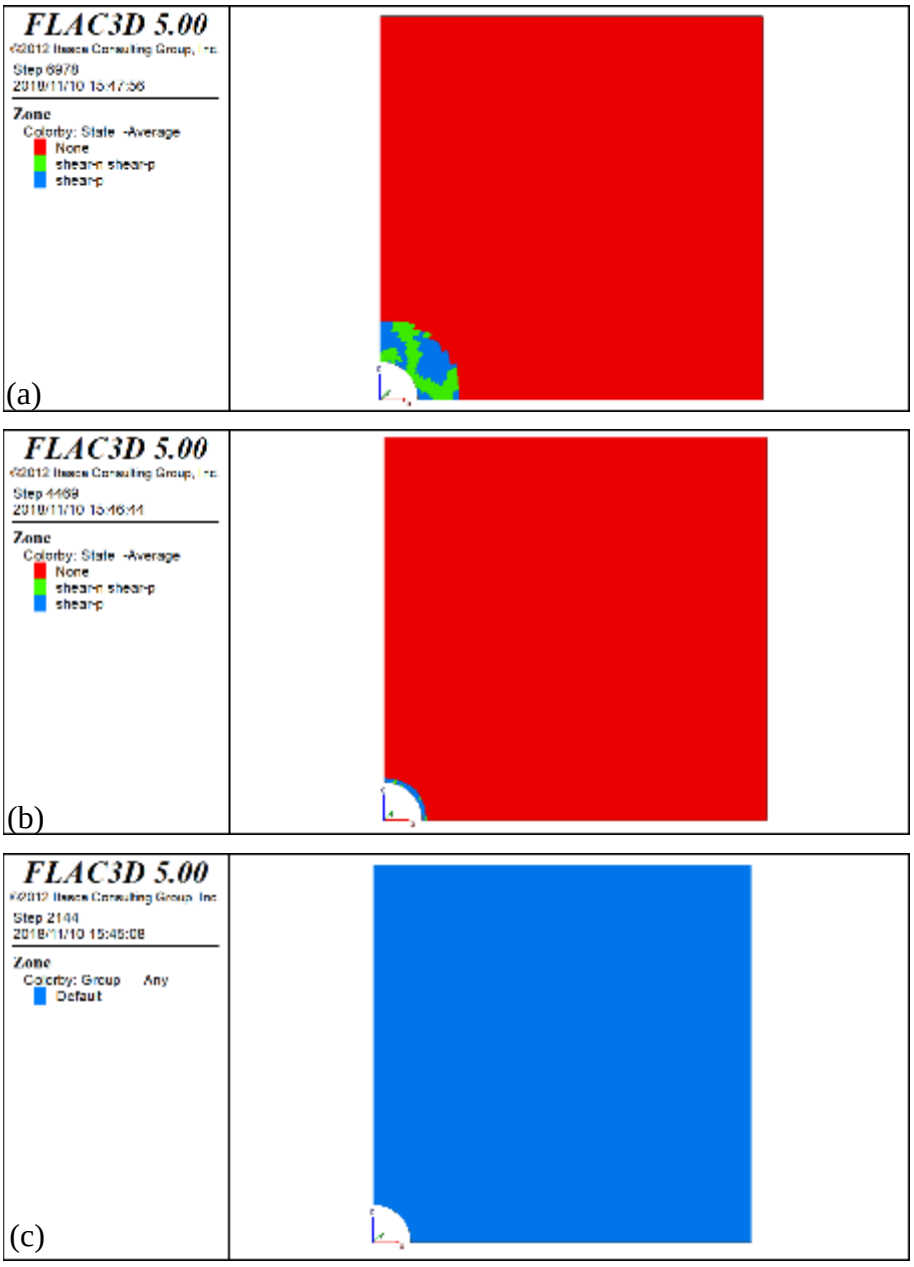

Figure B.10 Shear failure states of the cylindrical hole exerted by different support stresses: (a) 0 MPa; (b) 10 MPa; (c) 15 MPa [shear-n indicates a contiguous line of active plastic zones; shear-p means the yielding elements do not meet the yield criterion after stress redistribution Itasca (2013)]

B2 Linear elastic model

Table B.2 shows the plan performing sensitivity analyses to obtain optimal mesh size and domain size with the linear elastic model. The physical model and numerical model are the same as Figure Fig. B.1 and B.2. In the figure, θ (°) is the angle degree along the MN line in a counterclockwise direction.

Table B.2 Program of numerical simulations in linear elastic model for conducting sensitivity analyses; other parameters: E = 7076 MPa, P_0 = 30 MPa, v = 0.25

Case	Domain (m)			θ (°)
	x	z	y	
7	10	10	0.2[1]	0
8	Variable		0.2[1]	0
9	10	10	Variable	0
10	10	10	0.2*	0
11	10	10	0.2[1]	90

Notes: [1]: there is only one grid in *y*-direction; *: uniform grid (i.e., the mesh size in the *y*-direction is the same as those in *x* and *z*-directions).

Mesh size sensitivity analysis

Fig. B.11 presents the radial displacements become stable when mesh size decreases to 0.1m.

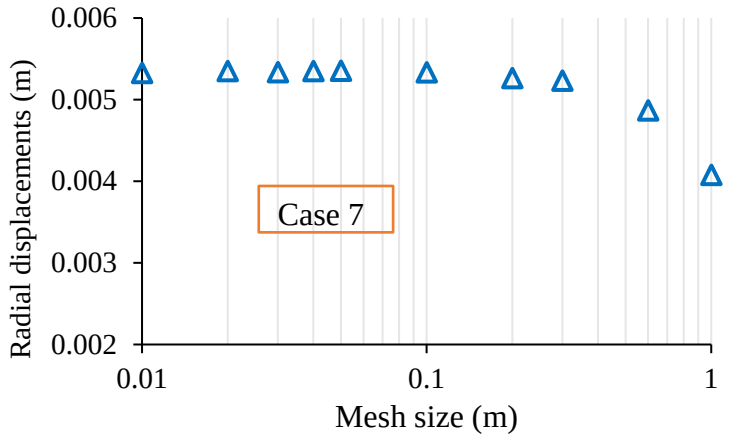

Figure B.11 Radial displacements at point M as a function of mesh size (Case 1 in Table B.1)

Domain senstivity analysis

Fig. B.12 shows that the numerical simulation results become stable when the domain increases to 10 m.

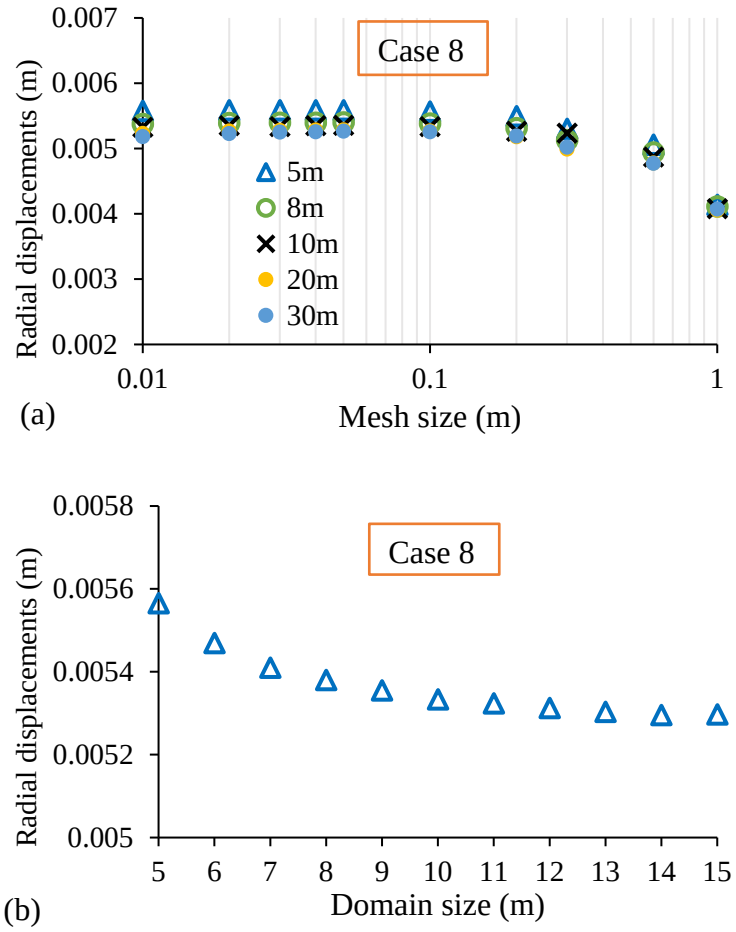

Figure B.12 Radial displacement at the M point as a function of (a) mesh size for different domain sizes and (b) domain size

Analysis in y-dimension

Fig. B.13 illustrates that the length of the third dimension (shown in Fig. B.13a) and its grid type (1 grid or uniform grid, shown in Fig. B.13b) do not affect the numerical results.

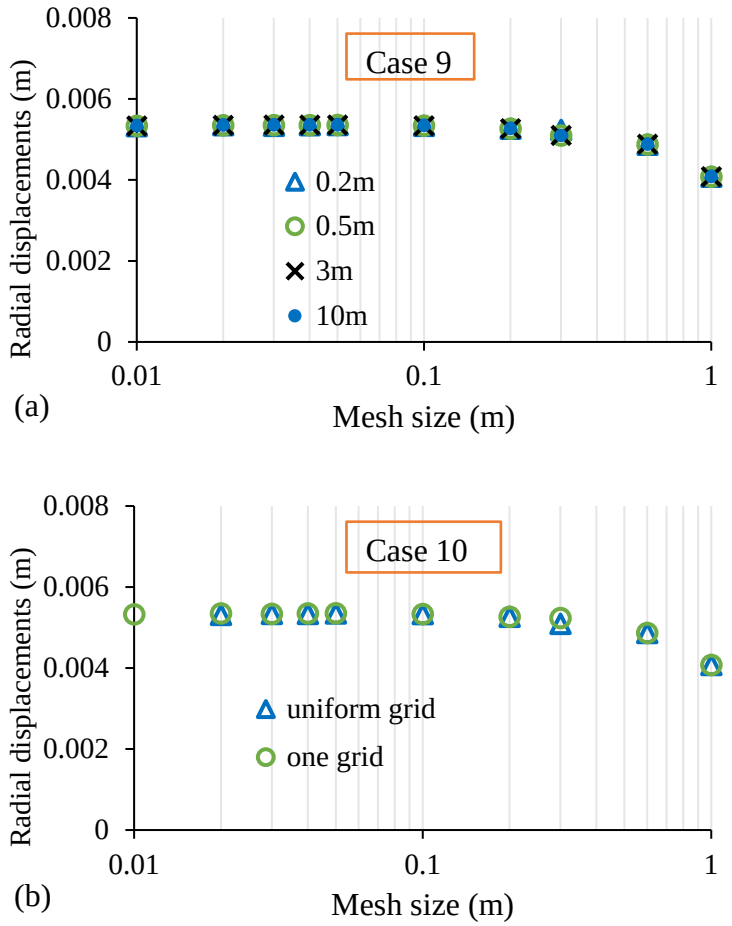

Figure B.13 Radial displacement at point M as a function of mesh size for (a) different mesh sizes in the *y*-direction and (b) one grid and uniform grid in the *y*-direction

Validation of numerical modeling with linear elastic model

Figure B.14 presents the stresses (e.g., radial and tangential) distribution along MN line as a function of radial distance, obtained with FLAC3D and calculated by the analytical solution proposed by Jaeger and Cook (2009), with optimal mesh size (0.1 m × 0.1 m) and domain size (10 m).

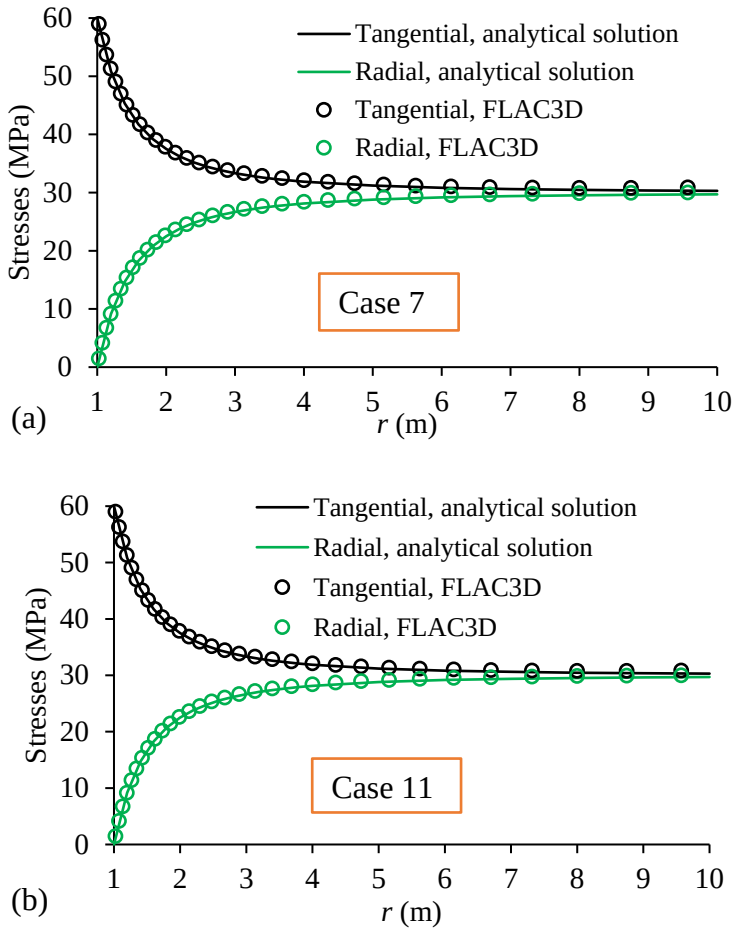

Figure B.14 Stresses as a function of radial distance obtained with FLAC3D and analytical solution for different angle degrees: (a) θ = 0°; (b) θ = 90°

Figure B.15 presents the radial displacement along the MN line as a function of radial distance, obtained with FLAC3D and calculated by the analytical solution proposed by Salençon (1969), with optimal mesh size (0.1 m × 0.1 m) and domain size (10 m).

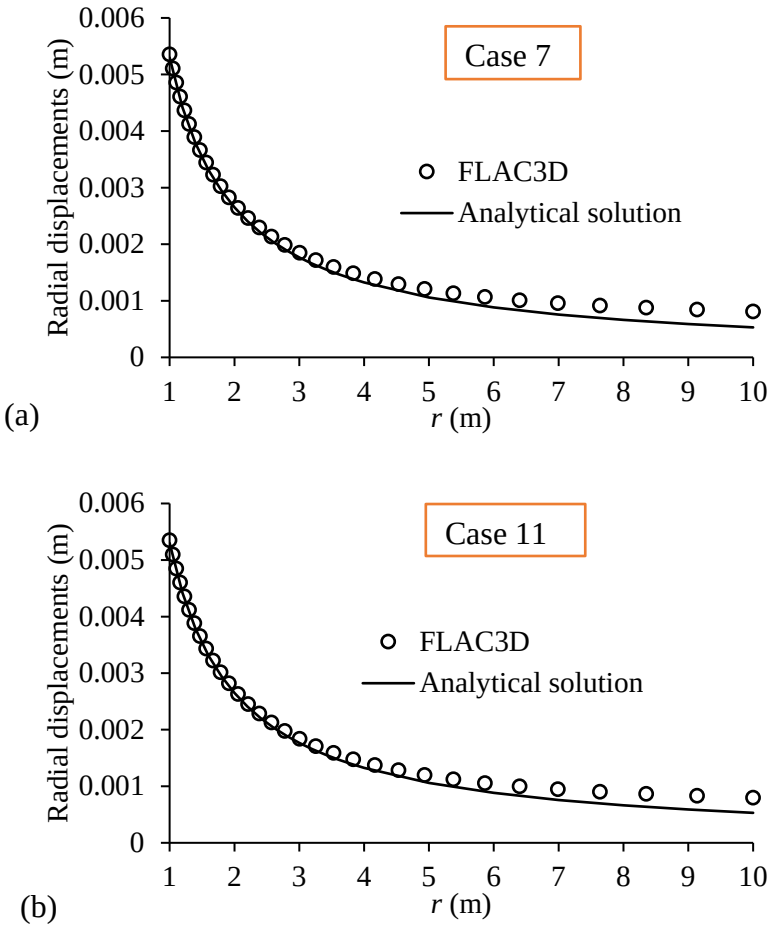

Figure B.15 Stresses as a function of radial distance obtained with FLAC3D and analytical solution under different angle degrees: (a) θ = 0°; (b) θ = 90°

B3 Discussion

The unstable numerical results are noticed in Fig. B.5 when mesh size decreases to 0.005 and 0.002 m. To answer these questions, the details in FLAC3D are recalled. The mechanical ratio 1×10^{-5} (default value) is commonly used by operators. However, it raises a question: can the numerical modeling obtain a stable result?

Fig. B.16 shows the radial displacements at point M as a function of the mechanical ratio. The unchanged value of radial displacement is obtained when the mechanical ratio is 1×10^{-8} (related step number is 16390). A stable trend is observed with a mechanical ratio 1×10^{-6} (step number is

10032) instead of the default value (i.e., 1×10^{-5} and step number is 6978). The sensitivity analysis of mechanical ratio or step number is suggested to perform case by case.

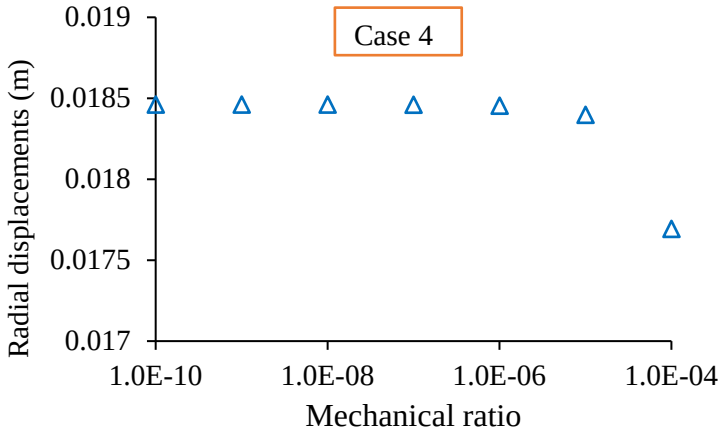

Figure B.16 Radial displacements at point M as a function of mechanical ratio with mesh size 0.05 m

A deviation of numerical simulation results from the analytical solution can be noticed in Fig. B.17 (i.e., enlarged view of Fig. B.9).

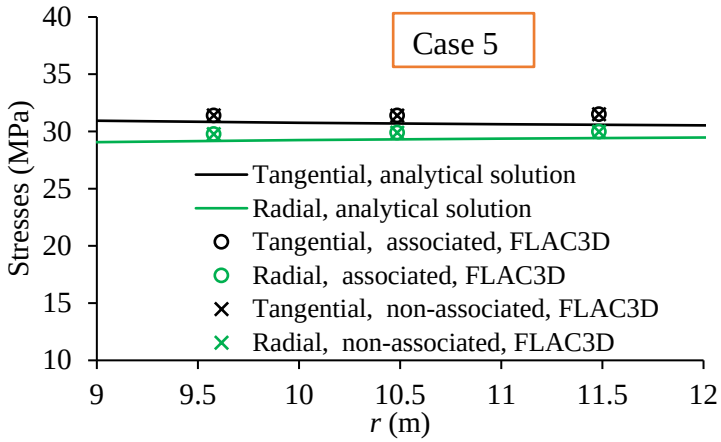

Figure B.17 radial and tangential stresses as a function of radial distance obtained with FLAC3D and analytical solution along MN line

The sensitivity analysis gives the optimal domain size of 12 m, showing the radial displacements

obtained with FLAC3D at point M. Fig. B.17 gives the numerical results near the model boundary of the cylindrical hole. It is necessary to perform a sensitivity analysis at point N.

Fig. B.18 shows the stresses at point N, obtained with FLAC3D and calculated based on boundary condition, as a function of domain size. The stable numerical results are obtained when the domain size increase to 20 m rather than 12 m obtained before.

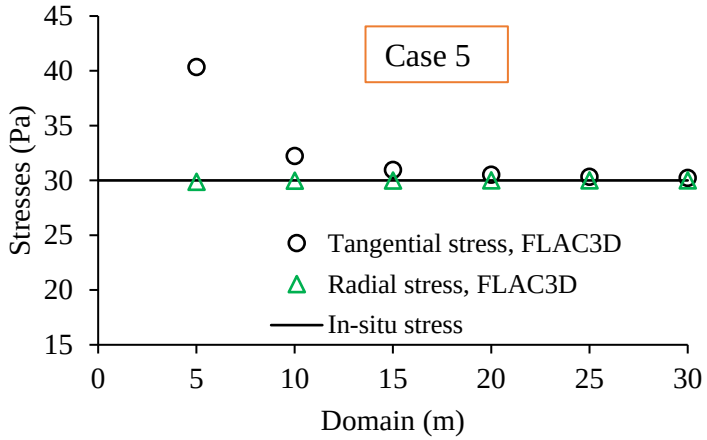

Figure B.18 stresses at point N as a function of domain size

Fig. B.19 shows the stresses as a function of radial distance with mesh size 0.05 m and domain size 20m. An overall view is given in Fig. B.19a, the enlarged view is shown in Fig. B.19b. A good agreement between numerical results and analytical solution is obtained with domain size 20m proposed in Fig. B.18. It should be noted that the required domain is 20 m with the Mohr-Coulomb model and 10 m with the linear elastic model. The plastic zones (shown in Fig. 10a) for the Mohr-Coulomb model can contribute to the difference.

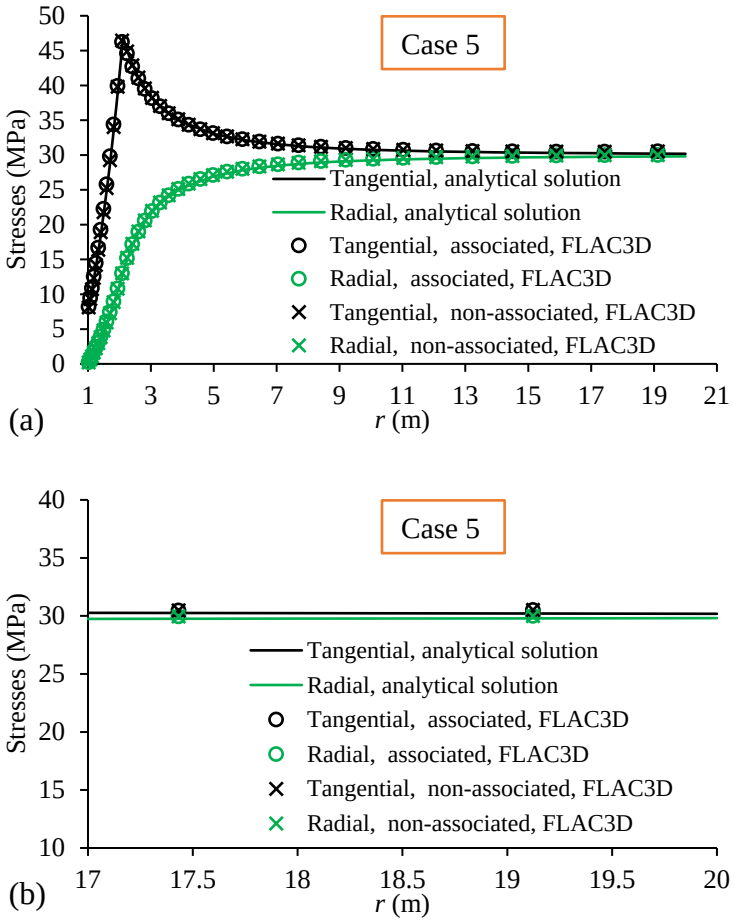

Figure B.19 stresses as a function of radial distance along MN line from (a) overall view and (b) enlarged view

The stresses and displacements as a function of mesh size or domain size at the specific coordinate are usually used to analyze the optimal mesh size and domain size. The numerical simulation of the cylindrical hole with the Mohr-Coulomb model is recalled to perform a further sensitivity analysis. The physical and mechanical parameters of the numerical modeling are characterized as E =7.076 GPa, ν = 0.25, ϕ' = 30°, c = 2.17 MPa, ψ = 0°, T_0 = 10 GPa, and P_0 = 30 MPa. The domain is set as 20 m and a small strain is used. The different mechanical ratios are used case by case to ensure unchanged numerical results.

Fig. B.20 gives radial and tangential stresses (Fig. B.20a), Sxx, Syy, and Szz (Fig. B.20b), and radial displacement (Fig. B.20c) as a function of mesh size for horizontal axis with a logarithmic

scale. The somewhat stable trends of stresses versus mesh size are observed in the figure with the logarithmic scale. An increasing trend of the radial displacements versus mesh size is noticed.

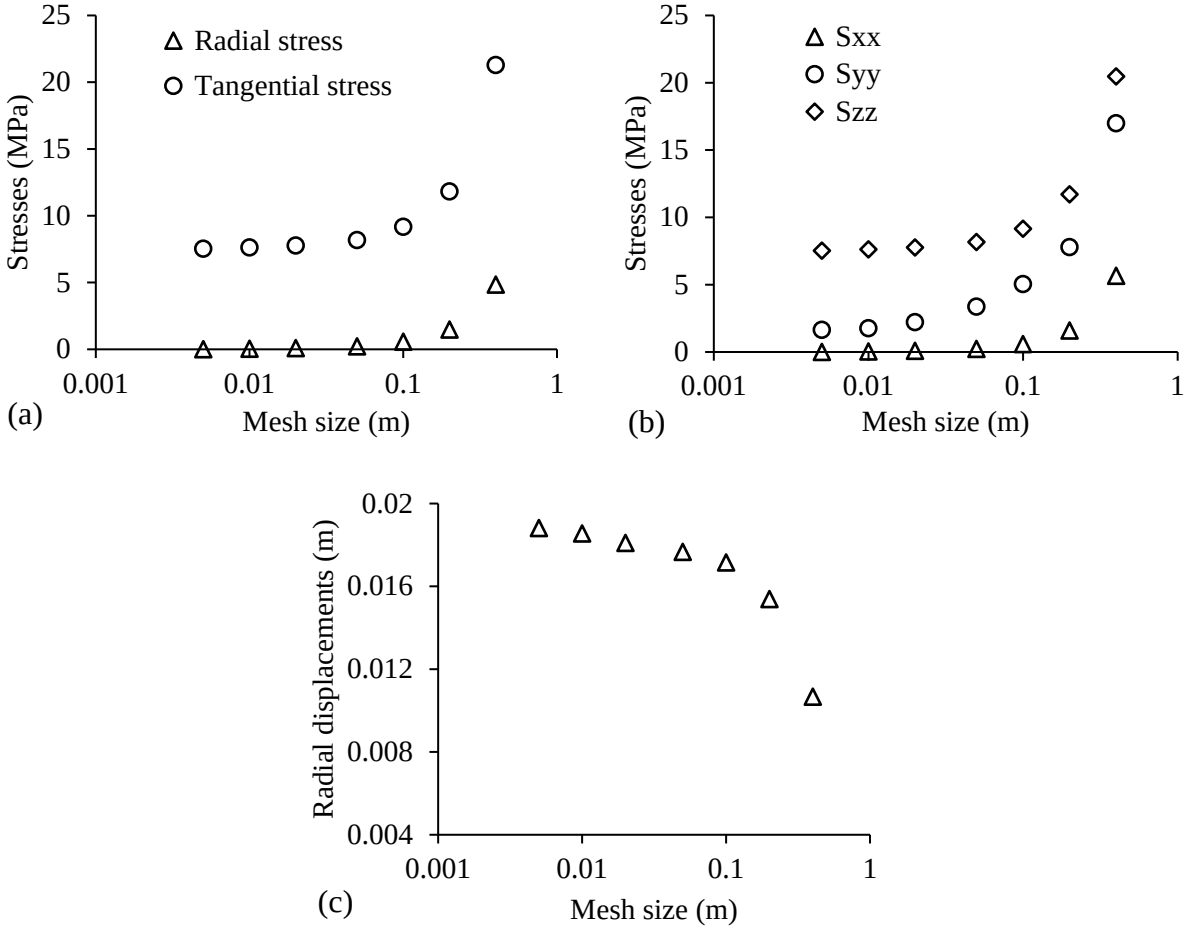

Figure B.20 (a) radial and tangential stresses, (b) stresses (i.e., Sxx, Syy, Szz), and (c) radial displacement as a function of mesh size at point M with a logarithmic scale in the horizontal axis

As a comparison, Fig. B.21 gives radial and tangential stresses (Fig. B.21a), Sxx, Syy, and Szz (Fig. B.21b), and radial displacement (Fig. B.21c) as a function of mesh size for horizontal axis with a regular scale. The obvious unstable trends are observed in the figure. However, it raises a question: is the way (i.e., stresses and displacement as a function of mesh size at a specific coordinate) judging optimal mesh size rational?

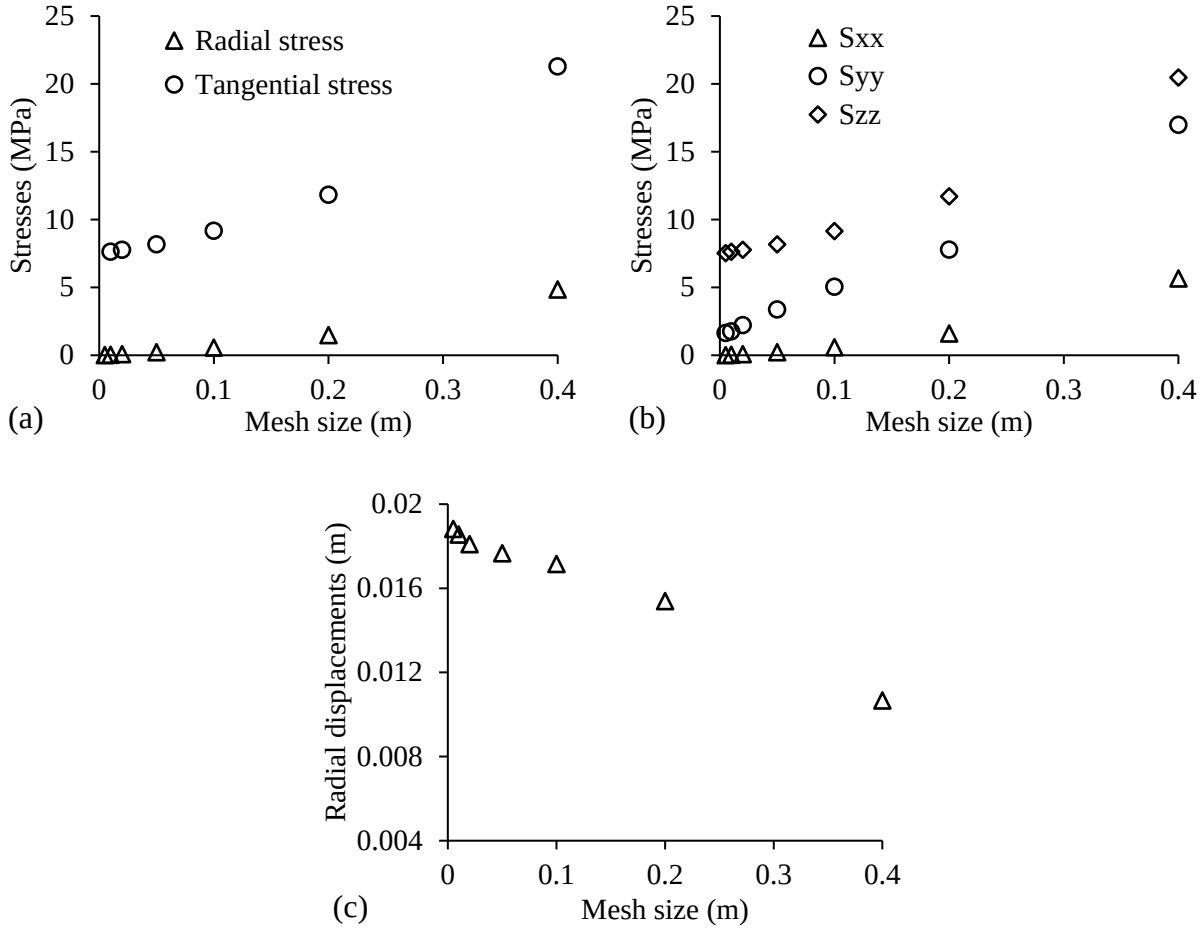

Figure B.21 (a) radial and tangential stresses, (b) stresses (i.e., Sxx, Syy, Szz), and (c) radial displacement as a function of mesh size at point M with a regular scale in the horizontal axis

Alternatively, the analytical solution proposed by Salençon (1969) is used to compare the numerical results obtained by FLAC3D with different mesh sizes (e.g., 0.4 m, 0.2 m, 0.1 m, 0.05 m, 0.02 m, and 0.01 m). Fig. B.22 shows stresses (i.e., tangential and radial stresses) as a function of radial distance along MN line with different mesh sizes at point M, such as 0.4 m (Fig. B.22a), 0.2 m (Fig. B.22b), 0.1 m (Fig. B.22c), 0.05m (Fig. B.22d), 0.02 m (Fig. B.22e), 0.01 m (Fig. B.22f). A poor agreement is observed in Fig. B.22a when radial distance varies from 1 m to 4 m with mesh size 0.4 m. A good agreement can be observed in the rest of the figures. The good agreement between the results calculated by analytical solution and those obtained with FLAC3D with mesh size 0.2 m causes a contradiction between two ways of judging optimal mesh size.

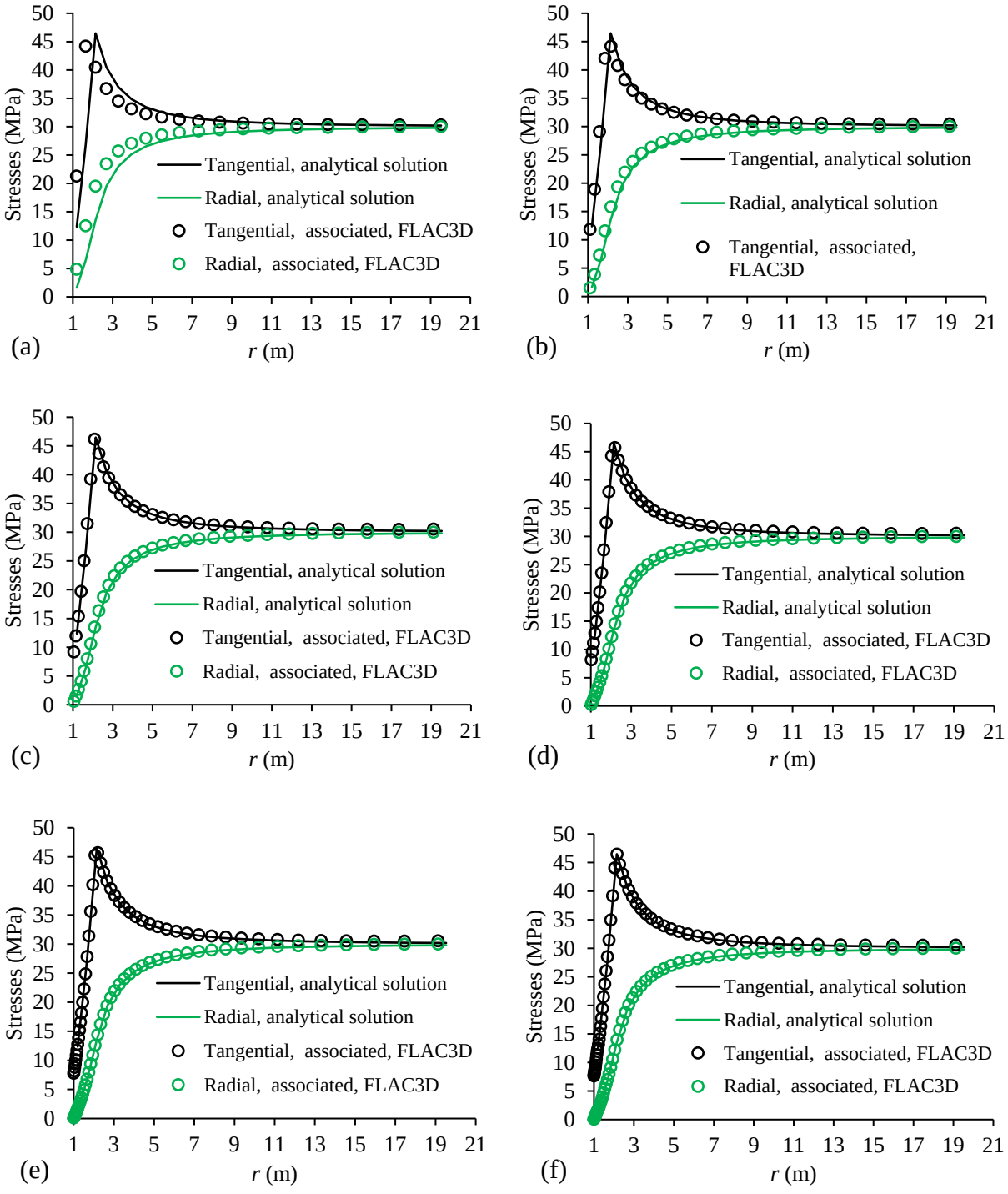

Figure B 22 stresses as a function of radial distance along MN line with different mesh sizes at point M: (a) 0.4 m, (b) 0.2 m, (c) 0.1 m, (d) 0.05m, (e) 0.02 m, (f) 0.01 m

To reply to this problem, the error calculation (Error calculation is defined as err = (tested value - true value) / true value, the true value is analytical results and tested value is numerical results) is used to set a subjective standard to estimate the accuracy instead of the objective way (e.g., observe the trend line from a figure).

Table B.3 shows an illustration to calculate the errors, obtained with FLAC3D and analytical solution, at point M with different mesh sizes. σ_r (MPa) is radial stress, σ_t (MPa) is tangential stress.

Table B.3 error calculation of results calculated by analytical solution and those obtained with FLAC3D at point M with different mesh sizes

Mesh size (m)	r (m)	Analytical results		Numerical results		Error for σ_r (%)	Error for σ_t (%)
		σ_r (MPa)	σ_t (MPa)	σ_r (MPa)	σ_t (MPa)		
0.4	1.196	1.617	12.367	4.849	21.279	66.661	41.882
0.2	1.103	0.817	9.969	1.481	11.819	44.8	15.647
0.1	1.051	0.394	8.699	0.562	9.172	29.835	5.149
0.05	1.026	0.196	8.106	0.221	8.171	10.984	0.789
0.02	1.01	0.074	7.74	0.084	7.767	11.164	0.348
0.01	1.005	0.038	7.631	0.036	7.622	6.721	0.114

A good agreement between analytical results and numerical results is observed in Fig. B.22b. In the Table, the errors are 44.8% for σ_r and 15.647% for σ_t when mesh size is 0.2 m, indicating the objective way may be irrational It is suggested to conduct error analyses case by case.

APPENDIX C INSTABILITY CRITERION RELATED TO FLAC3D

To check the proposed instability criterion (i.e., coalescence of failure zones) related to Chapter 5 and Chapter 6, a uniaxial compressive test simulated by FLAC3D is used to analyze the failure process. The Mohr-Coulomb model (ideal elastoplastic model) is used. The physical and mechanical properties of the column material are characterized as: γ_c = 20 kN/m^3 (unit weight), E_c = 100 MPa (Young's modulus), v_c = 0.3 (Poisson's ratio), ϕ'_{wr} = 40° (internal friction angle), c_c = 1 MPa (cohesion), and T_c = 1 MPa (tensile strength), the initial stress 2 MPa in y-direction was applied in the column.

Fig. C.1a gives the numerical model of the column with sporadic failure zones (e.g., shear and tension failures) when the initial failure zones occur, the corresponding stress-displacement curve is shown in Fig. C.1b.

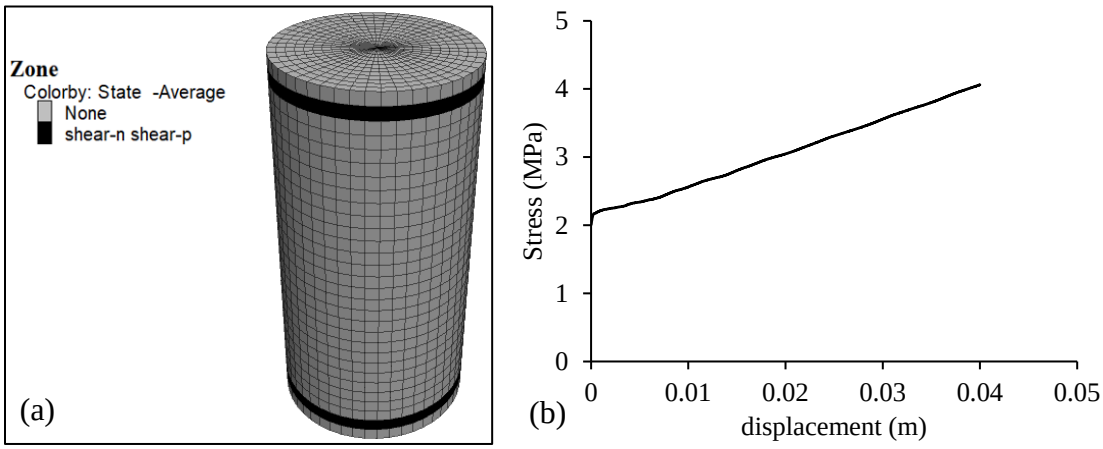

Figure C.1 (a) initial failure zones of the column; (b) stress-displacement curve at the initial stage (grey indicate no failures, black is an active shear failure, and dark grey is shear failure that happened in the past)

Fig. C.2a presents the increasing scattered and active failure zones (i.e., shear-n) of the column with the increased compressive stress, the related stress-displacement curve is shown in Fig. C.2b.

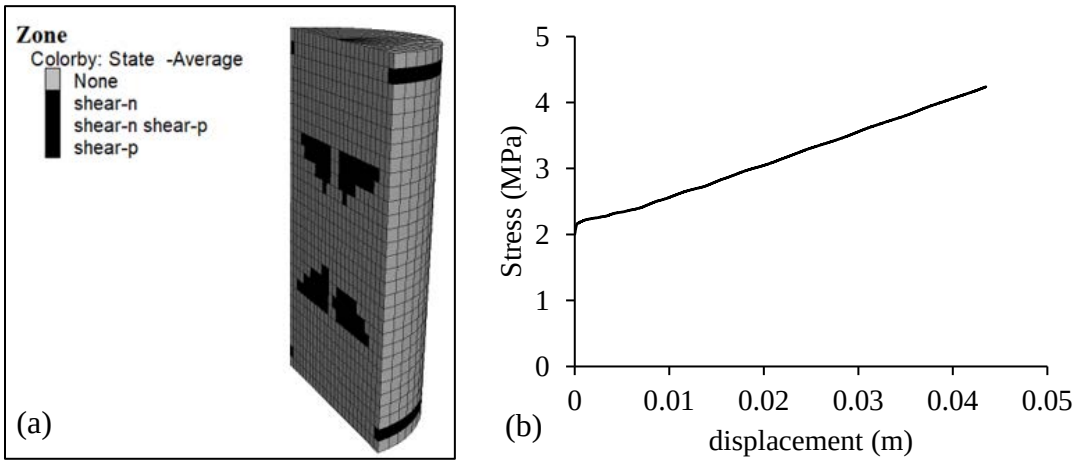

Figure C.2 (a) more active failure zones of the column and (b) displacement-stress curve with the increased stress

Fig. C.3a presents the coalescence of the active failure zones when the compressive stress reaches up to the maximum, the corresponding stress-displacement is shown in Fig. C.3b, and the enlarged view of the stress-displacement is given in Fig. C.3c.

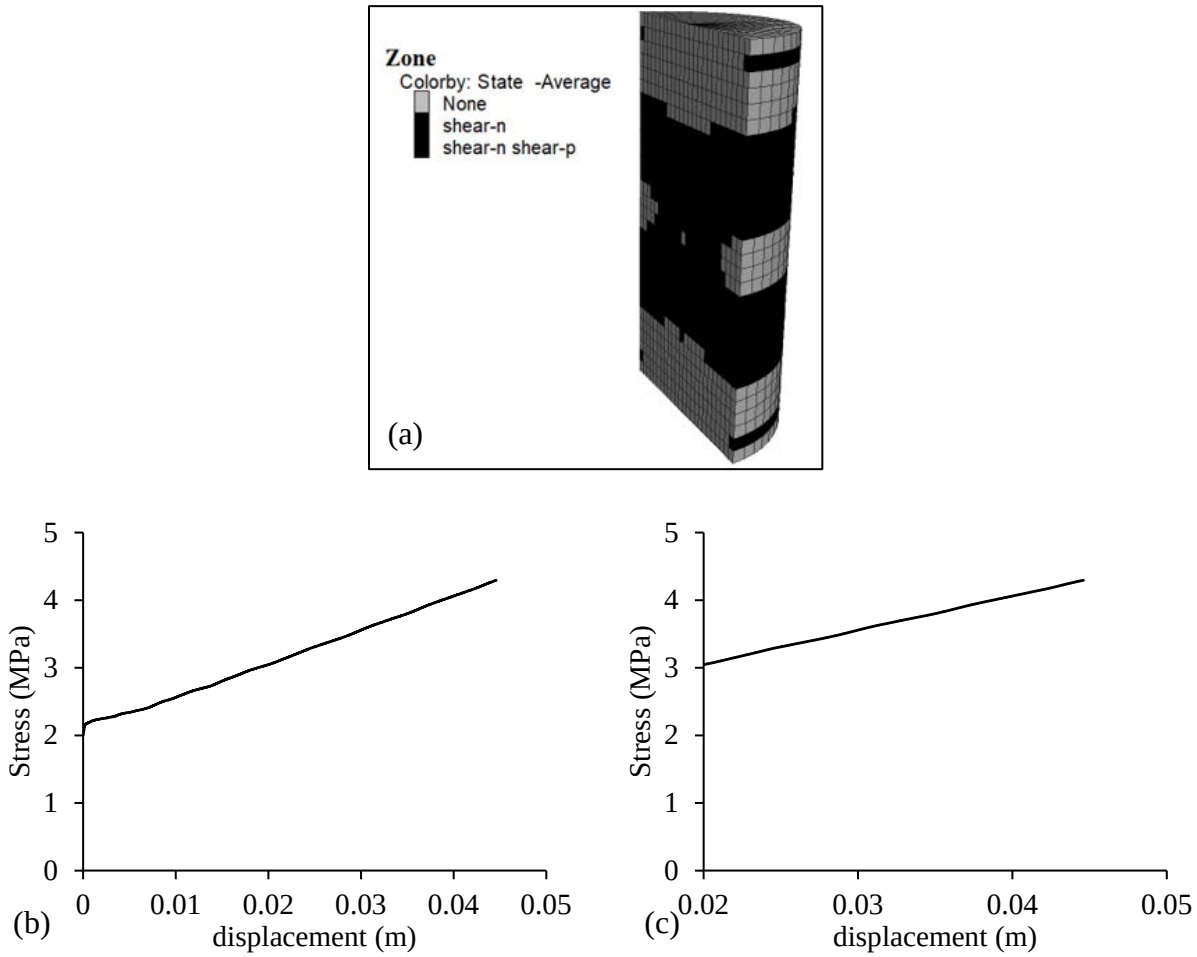

Figure C.3 Through crack occurs: (a) through crack occurs; (b) displacement-stress curve; (c) stress gradually reach the maximum

Fig. C.4 gives the overall stress-displacement curve. The ideal elastoplastic model can be seen from the figure with a cut off because the initial stress 2 MPa in *y*-direction was applied in the column.

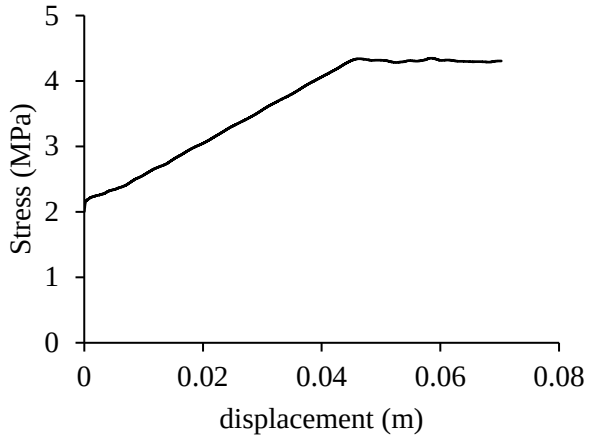

Figure C.4 stress-displacement curve of the uniaxial test simulated by FLAC3D

APPENDIX D SENSITIVITY ANALYSES RELATED TO CHAPTER 4

This section presents the sensitivity analyses related to the numerical results obtained by FLAC3D 6.0 (Itasca 2017) shown in Chapter 4. The sensitivity analyses for mesh size in different directions and mechanical ratio are shown in the following.

D1 Sensitivity analyses for mesh size

Fig. D.1 presents a schematic view of a 3D rockfill trapezoidal dike used for conducting the sensitivity analyses. The homogeneous dike having a limited dimension in the third direction rests on an impervious horizontal base. The boundary conditions are defined as a static pore-pressure distribution up to h_1 level on the upstream face, and up to h_2 on the downstream face, zero pore pressure from h_2 level to top on the downstream face, and to no-flow conditions across the rest of the boundaries.

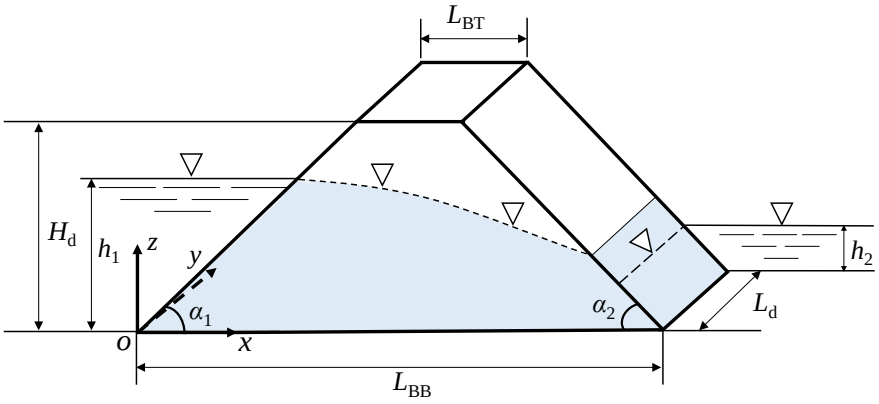

Figure D.1 Physical model of a 3D dike (adapted from Harr 1962).

Table D.1 shows a program of numerical simulations used to perform the sensitivity analyses with different variables. Other parameters are: h_1 = 18.5m, h_2 = 0m, ρ_f = 1000 kg/m^3, g = 10 m/s^2, n = 0.3, k = 6.67 × 10^{-10} m^2(Pa/s), K_f = 3 kPa, and L_z = 1 m.

Table D.1 Program of numerical simulations with FLAC3D for performing the sensitivity analysis

Case	k_h (m/s)	L_d (m)	α_1 (°)	α_2 (°)	L_{BT} (m)	L_{BB} (m)	H_d (m)
0	6.67×10^{-6}	1	21.8	26.6	10	100	20
1	1×10^{-3}	1	21.8	26.6	10	100	20
2	6.67×10^{-6}	5	21.8	26.6	10	100	20
3	6.67×10^{-6}	1	30	26.6	10	100	20
4	6.67×10^{-6}	1	21.8	45	10	100	20

Fig. D.2 shows ratio (i.e., Q/k_h) variation as a function of mesh size, obtained with FLAC3D, for different cases: different k_h (Fig. D.2a and D.2b), dike width (Fig. D.2c), upstream slope angle (Fig. D.2d), and downstream slope angle (Fig. D.2e). On the figure, the numerical results tend to become stable when mesh size decreases to 1 m [i.e., 1.7 m × 1 m × 1 m ($x \times y \times z$) at the bottom of the dike].

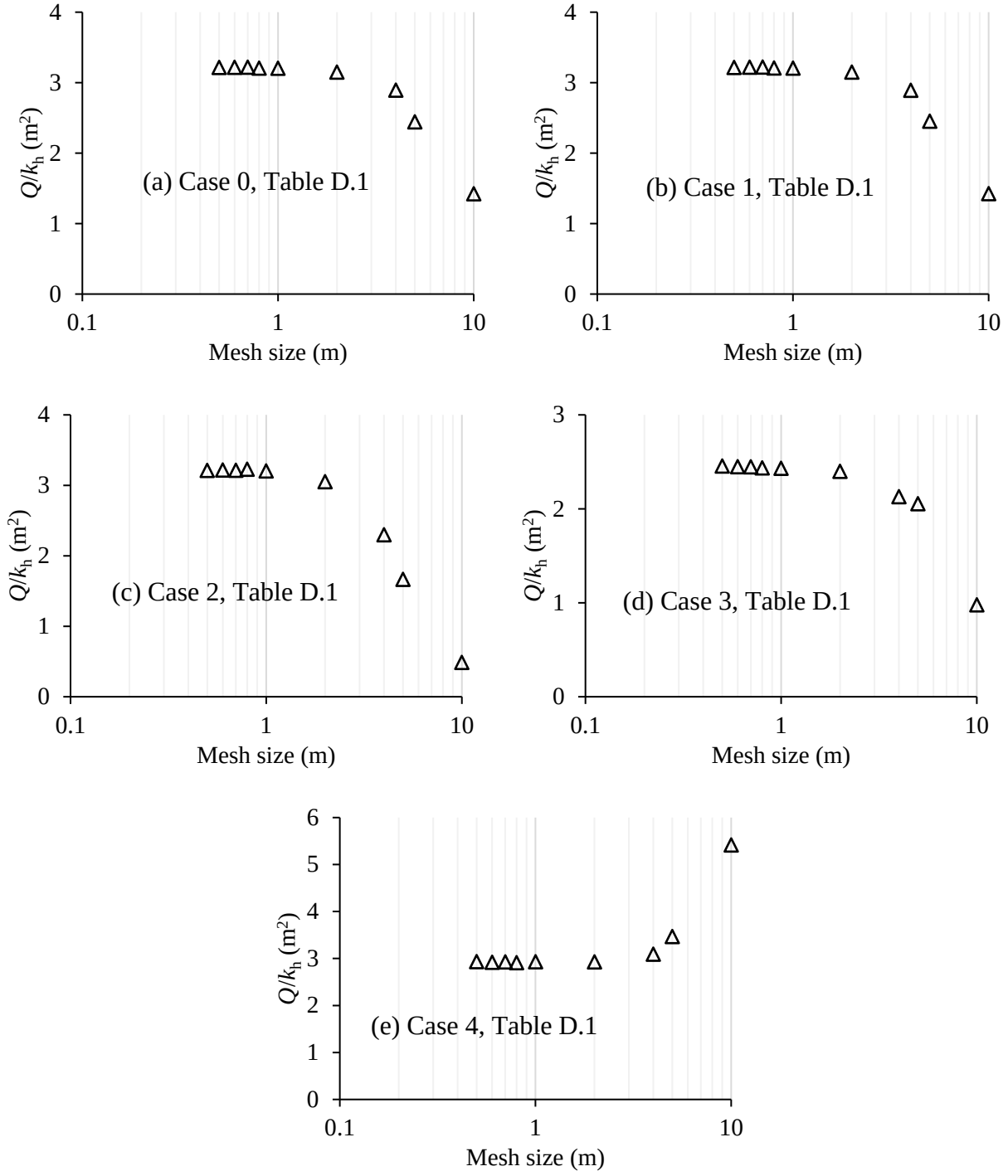

Figure D.2 sensitivity analyses of mesh size in numerical modeling for Cases 0 with k_h = 6.67 × 10^{-6} m/s (a), case 1 with k_h = 1.0 × 10^{-3} m/s (b), case 2 with L_d = 5 m (c), case 3 with α_1 = 30° (d), case 4 with α_2 = 45° (e).

Fig. D.3 presents the ratio Q/k_h as a function of mesh size for the laboratory test. The optimal mesh size is obtained with 0.05 m × 0.05 m × 0.04 m ($x \times y \times z$) at the bottom of the waste rock barricade. All parameters are characterized as: h_1 = 0.25 m, h_2 = 0 m, ρ_f = 1000 kg/m^3, g = 10 m/s^2, n = 0.3, k = 4.39 × 10^{-6} m^2(Pa/s), K_f = 90 Pa, and L_z = 0.03 m, k_h = 4.39 × 10^{-2} m/s, $\alpha_1 = \alpha_2$ = 37°, L_{BT} = 0 m, L_{BB} = 0.8 m, H_d = 0.3 m, L_d = 0.053 m.

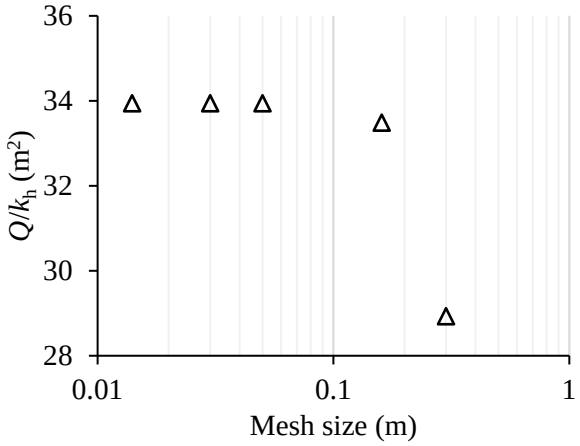

Figure D.3 Variation of the ratio Q/k_h versus mesh size for the laboratory test

Fig. D.4 gives the ratio Q/k_h as a function of mesh size in the y-direction. The numerical modeling is conducted by changing the mesh size only in the y-direction with the mesh size of 1.7 m × 1 m × 0.7 m ($x \times y \times z$) at the bottom of the dike (Case 0 in Table D.1). The results show the mesh size in the y-direction is suggested to keep in a unit thickness (i.e., L_d in the same order as those of H_d). The value of Q/k_h tends to become unstable when L_d decreases smaller than 0.1 (10 times compared with the unit thickness).

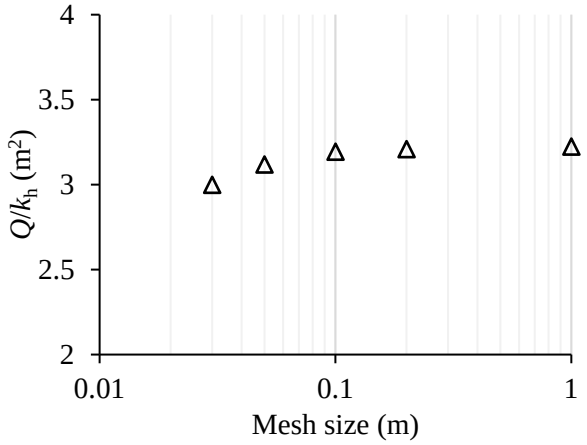

Figure D.4 Variation of the ratio Q/k_h as a function of mesh size in y-direction

D2 Sensitivity analyses for mechanical ratio

Fig. D.5 shows the ratio Q/k_h as a function of mechanical ratio (the default value is 1.0×10^{-5}). The numerical modeling is performed by decreasing the mechanical ratio (e.g., from 1.0×10^{-1} to 1.0×10^{-5}) with the mesh size of 1.7 m × 1 m × 0.7 m ($x \times y \times z$) at the bottom of the dike (Case 0 in Table D.1). In the figure, stable numerical results are obtained when the mechanical ratio decreases to 1.0×10^{-2}.

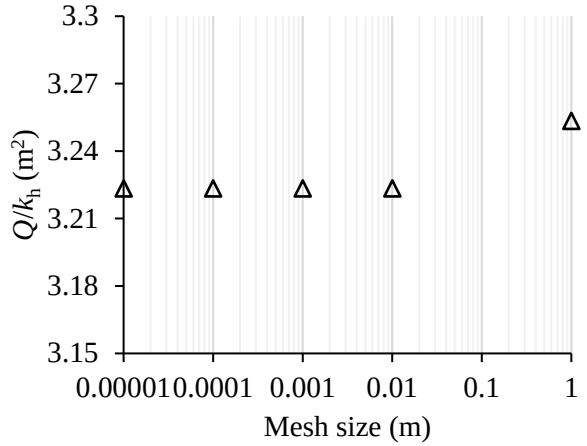

Figure D.5 Variation of the ratio Q/k_h as a function of mechanical ratio

APPENDIX E SENSITIVITY ANALYSES RELATED TO CHAPTER 5

This section gives the sensitivity analyses with FLAC3D 5.01 (Itasca 2013) related to Chapter 6. In the following, the displacement at the top center as a function of mesh size will be analyzed at first. The failure states (abrupt displacement jump and coalescence of failure zones) as a function of mesh size are then summarized to obtain the optimal mesh size.

E1 Displacement at top center versus mesh size

Fig. E.1 presents the numerical model of the waste rock barricade sprayed with shotcrete. A point R was chosen to monitor displacement in *x*-direction as a preliminary analysis. The waste rocks and shotcrete are simulated as the elastoplastic materials with the Mohr-Coulomb failure criterion. The rock mass is modeled as the elastic material. The physical and mechanical parameters of rock mass are characterized as γ_r = 26.5 kN/m^3 (density), E_r = 30 GPa (Young's modulus), and ν_r 0.3 (Poisson's ratio). The physical and mechanical parameters of waste rocks are:γ_{wr} = 19.6 kN/m^3 (unit weight), E_{wr} = 100 MPa (Young's modulus), ν = 0.3 (Poisson's ratio), c' = 0 kPa (cohesion), and ϕ' = 38°, respectively. The shotcrete has a unit weight γ_s = 21.6 kN/m^3, a Young's modulus E_s = 10 GPa, a Poisson's ratio ν_s = 0.3, a friction angle ϕ_s = 38°, and a cohesion c_s = 100 MPa.

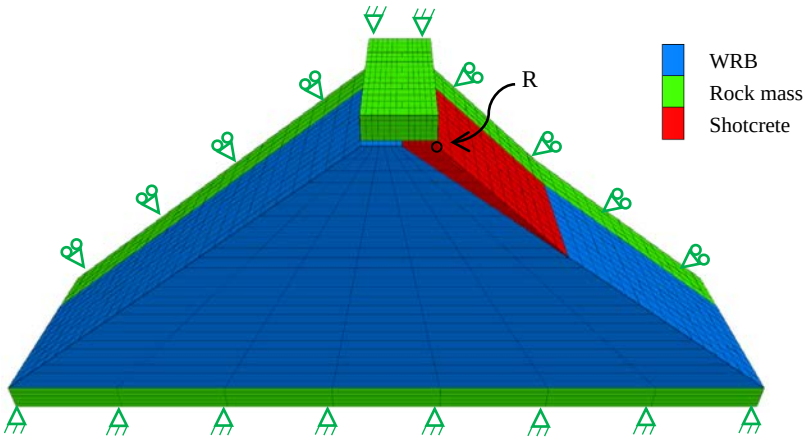

Figure E.1 Numerical model of the waste rock barricade

To obtain the optimal mesh size of the shotcreted WRB at the first stage, a series of sensitivity analyses are made with different cases shown in Table F.1.

Table E.1 program of numerical simulations with FLAC3D to make sensitivity analyses with $\alpha_1 = \alpha_2 = 37°$, $\gamma_b = 19.6$ kN/m^3, $\gamma_{wr} = 19.6$ kN/m^3, $c' = 0$ kPa, $\phi' = 38°$, $E_{wr} = 100$ MPa, $\nu = 0.3$, $\gamma_r = 26.5$ kN/m^3, $E_r = 30$ Gpa, $\delta_{wr} = 30°$, $\nu_r = 0.3$, $\gamma_s = 21.6$ kN/m^3, $E_s = 10$ Gpa, $\nu_s = 0.3$, $\phi_s = 38°$, and $c_s = 100$ Mpa.

Case	H (m)	H_d (m)	ϕ_{wr} (°)	L_d (m)
0	10	5	38	5
1	12	7	38	5
2	12	5	40	5
3	12	5	38	7

Fig. E.2 shows X-displacement at point R as a function of mesh size (from Fig. E.2a to Fig. E.2d) with cases shown in Table F.1, indicating the displacements become stable when mesh size decreases to 0.06 m in X-direction with fixed 0.25 m in Z-direction and 0.2 m in Y-direction.

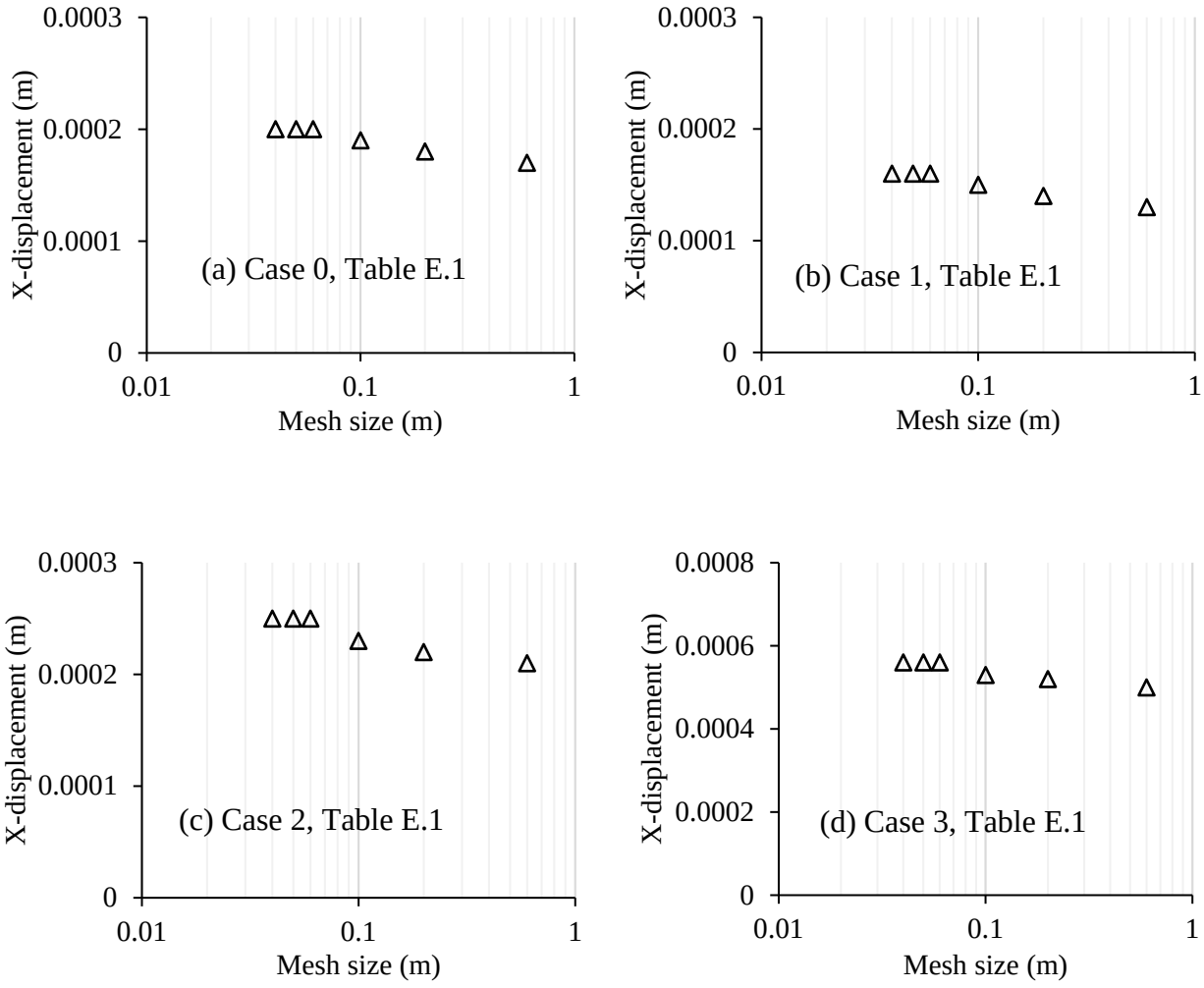

Figure E.2 sensitivity analyses of mesh in numerical modeling for Cases 0 with H = 9 m (a), case 1 with H_d = 7 m (b), case 2 (c), case 3 (d), case 4 with L_d = 3 m (e), case 4 with L_d = 3 m (f) of Table E.1 with c_{wr} = 10 MPa.

E2 Failure states versus mesh size

After the preliminary analyses of the displacements of the point R, the stability of the structure of the shotcreted WRB as a function of the mesh size is analyzed. Case 0 in Table E.1, with H = 14 m c_s = 500 kPa, and L_{BT} = 0.6 m, is used to analyze the failure states as a function of mesh size.

Table E.2 gives the generalized analyses for the shotcreted WRB by varying the mesh size in the *z*-direction.

Table E.2 Summary of the failure states of the shotcreted WRB versus the mesh size in the *z*-direction with fixed meth size in the *x*-direction (0.1 m) and in the *y*-direction (0.25 m)

Mesh size in the *z*-direction	Required top length L_{SL}
1 m	0.1 m, ever-increasing displacement occurs with 0.05 m
0.5 m	0.2 m, occurrence of currently yield by shear with 0.1 m; ever-increasing displacement occurs with 0.05 m
0.25 m	0.2 m, ever-increasing displacement occurs with 0.1 m
0.2 m	0.2 m, ever-increasing displacement occurs with 0.1 m
0.1 m	0.2m, ever-increasing displacement occurs with 0.1 m

Table E.3 shows the generalized analyses for the shotcreted WRB stability by varying the mesh size in the *x*-direction.

Table E.3 Summary of the failure states of the shotcreted WRB versus the mesh size in the *x*-direction with fixed meth size in the *y*-direction (0.25 m) and in the *z*-direction (0.2 m)

Mesh size in *x*-direction	Required top length L_{SL}
0.6 m	The stable status was found even with 0.01 m
0.3 m	0.1 m, ever-increasing displacement occurs with 0.05 m
0.2 m	0.1 m, ever-increasing displacement occurs with 0.05 m
0.1 m	0.2 m, ever-increasing displacement occurs with 0.1 m
0.06 m	0.2m, ever-increasing displacement occurs with 0.1 m
0.03 m	0.2m, ever-increasing displacement occurs with 0.1 m

Table E.4 shows the generalized analyses for the shotcreted WRB stability by varying the mesh size in the *y*-direction.

Table E.4 Summary of the stability of the shotcreted WRB versus the mesh size in the *y*-direction with fixed meth size in the *x*-direction (0.06 m) and in the *z*-direction (0.2 m)

Mesh size in *x*-direction	Required top length L_{SL}
1 m	0.2 m, ever-increasing displacement occurs with 0.1 m
0.5 m	0.2 m, ever-increasing displacement occurs with 0.1 m
0.25 m	0.2 m, ever-increasing displacement occurs with 0.1 m
0.2 m	0.2 m, ever-increasing displacement occurs with 0.1 m
0.1 m	0.2 m, ever-increasing displacement occurs with 0.1 m

APPENDIX F SENSITIVITY ANALYSES AND DETAILS RELATED TO CHAPTER 6

The section gives the sensitivity analyses related to the numerical results obtained by FLAC3D (Itasca 2013) shown in Chapter 5. The displacement of a point at the top center as a function of mesh size is used to perform the preliminary sensitivity analyses. The failure analyses (abrupt displacement jump or coalescence of currently yield zones) of the WRB with a given L_{BT} as a function of mesh size are then performed to obtain stable numerical simulation results.

F1 Displacement at top center versus mesh size

Fig. F.1 shows a physical model (Fig. F.1a) and numerical modeling (Fig. F.1b) of the WRB subjected to the paste backfill pressure p. The waste rocks used to construct the barricade are assumed to be homogeneous, isotropic, and elastoplastic, obeying the Mohr-Coulomb criterion. The physical and mechanical properties are: γ_{wr} = 19.6 kN/m^3 (unit weight), E_{wr} = 100 MPa (Young's modulus), ν_{wr} = 0.3 (Poisson's ratio), ϕ_{wr} = 38° (internal friction angle), and c_{wr} = 0 kPa (cohesion). The rock mass is linearly elastic and characterized as γ_r = 26.5 kN/m^3 (unit weight), E_r = 30 GPa (Young's modulus), and ν_r = 0.3 (Poisson's ratio).

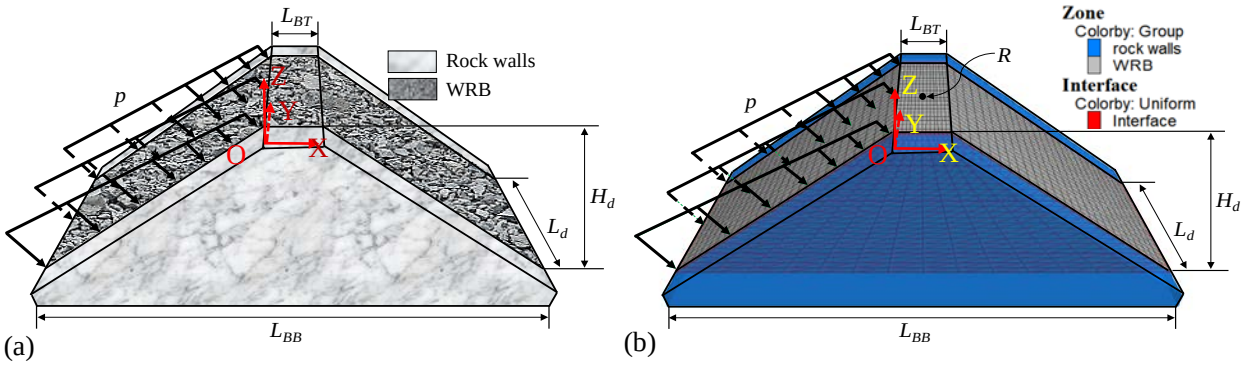

Figure F.1 A physical model of the WRB subjected to a paste backfill pressure p

To determine the optimal mesh size of the WRB at a preliminary step, a series of sensitivity analyses are performed under different cases shown in Table F.1.

Table F.1 program of numerical simulations with FLAC3D for performing sensitivity analyses with $\alpha_1 = 37°$, $\gamma_b = 19.6$ kN/m^3, $\gamma_{wr} = 19.6$ kN/m^3, $c_{wr} = 100$ MPa, $\phi_{wr} = 38°$, $E_{wr} = 100$ MPa, $\nu_{wr} = 0.3$, $\gamma_r = 26.5$ kN/m^3, $E_r = 30$ GPa, $\delta_{wr} = 30°$, and $\nu_r = 0.3$

Case	H (m)	H_d (m)	α_2 (°)	ϕ_{wr} (°)	L_d (m)
0	9	5	37	38	5
1	9	7	37	38	5
2	9	5	34	38	5
3	9	5	37	40	5
4	9	5	37	38	3

Fig. F.2 illustrates the X-displacement at the top center (point R) as a function of mesh size (from Fig. F.2a to Fig. F.2e) and as a function of mechanical ratio (Fig. F.2f) for different cases shown in Table F.1, showing the displacements become somewhat stable when mesh size decreases to 0.1 m in X-direction (0.25 m in Z-direction and 0.2 m in Y-direction are kept). The stable numerical results are observed in Fig. F.2f when the mechanical ratio reduces to 1×10^{-5} (related step number is 8877).

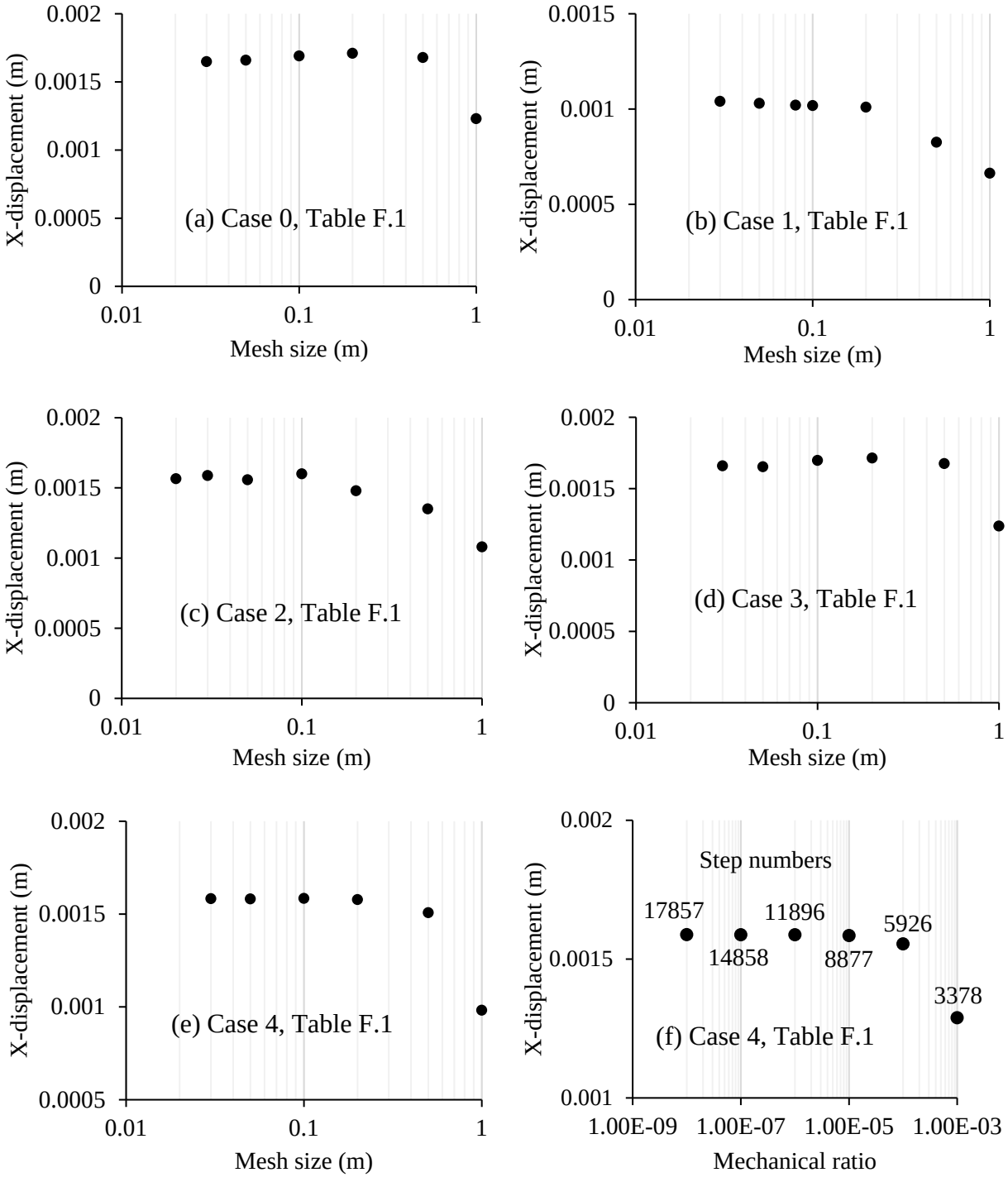

Figure F.2 sensitivity analyses of mesh in numerical modeling for Cases 0 with H = 9 m (a), case 1 with H_d = 7 m (b), case 2 (c), case 3 (d), case 4 with L_d = 3 m (e), case 4 with L_d = 3 m (f) of Table F.1 with c_{wr} = 10 MPa.

F2 Failure analyses versus mesh size

After the preliminary sensitivity analyses, the failure analyses (abrupt displacement jump or coalescence of active failure zones of whole WRB structure) as a function of the mesh size are analyzed. The failure analyses must be conducted case by case to obtain stable numerical simulation results. A sample (Case 0 in Table F.1 with c_{wr} = 0 MPa) showing how to perform the analysis is shown in the following.

Table F.2 summarizes the failure analyses by changing the mesh size in the *z*-direction with the fixed mesh size of 0.1 m in the *x*-direction and 0.25 in the *y*-direction. The minimum required top length L_{BT} is 1.4 m with the optimal mesh size of 0.1 m × 0.25 m × 0.2 m ($x \times y \times z$).

Table F.2 summary of the stability of the WRB as a function of the mesh size in the *z*-direction with fixed meth size in the *x*-direction (0.1 m) and in the *y*-direction (0.25 m)

Mesh size in the *z*-direction	Required top length L_{BT}	Observation of displacement abrupt or coalescence of failure zones with the decrease of L_{BT}
0.5 m	1 m	Displacement abrupt with 0.9 m
0.3 m	1.2 m	Coalescence of failure zones with 1.1 m; Displacement abrupt with 1 m
0.25 m	1.2 m	Coalescence of failure zones with 1.1 m; Displacement abrupt with 1 m
0.2 m	1.4 m	Coalescence of failure zones with 1.3 m and 1.2 m; Displacement abrupt with 1.1 m
0.13 m	1.4 m	Coalescence of failure zones with 1.3 m Displacement abrupt with 1.2 m
0.1 m	1.4 m	Displacement abrupt with 1.3 m

Table F.3 generalizes the failure analyses as a function of mesh size in the *x*-direction. The minimum required top length L_{BT} is 1.4 m with the optimal mesh size of 0.1 m × 0.5 m × 0.2 m ($x \times y \times z$).

Table F.3 summary of the stability of the WRB as a function of the mesh size in the *y*-direction with fixed meth size in the *x*-direction (0.1 m) and in the *z*-direction (0.2 m)

Mesh size in *y*-direction	Required top length L_{BT}	Observation of displacement abrupt or coalescence of failure zones with the decrease of L_{BT}
0.5 m	1.4 m,	Coalescence of failure zones with 1.3 m and 1.2m; Displacement abrupt with 1.1 m
0.25 m	1.4 m,	Displacement abrupt with 1.3 m
0.1 m	1.4 m,	Displacement abrupt with 1.3 m

Table F.4 shows the generalized failure analyses by varying the mesh size in the *x*-direction. The minimum required top length L_{BT} is 1.4 m with the optimal mesh size of 0.1 m × 0.25 m × 0.2 m ($x \times y \times z$).

Table F.4 summary of the stability of the WRB as a function of the mesh size in the *z*-direction with fixed meth size in the *y*-direction (0.25 m) and in the *z*-direction (0.2 m)

Mesh size in *x*-direction	Required top length L_{BT}	Observation of displacement abrupt or coalescence of failure zones with the decrease of L_{BT}
0.55 m	1.1 m,	Displacement abrupt with 1 m
0.25 m	1.1 m,	Displacement abrupt with 1 m
0.2 m	1.2 m,	Coalescence of failure zones with 1.1 m; Displacement abrupt with 1 m
0.1 m	1.4 m,	Coalescence of failure zones with 1.3 m;
0.05 m	1.4 m,	Coalescence of failure zones with 1.3 m;

F3 *K* value calculation

Fig. F.3 illustrates the cross-section used to analyze the horizontal and the vertical stresses along with the interface between the rock walls and the WRB obtained by FLAC3D.

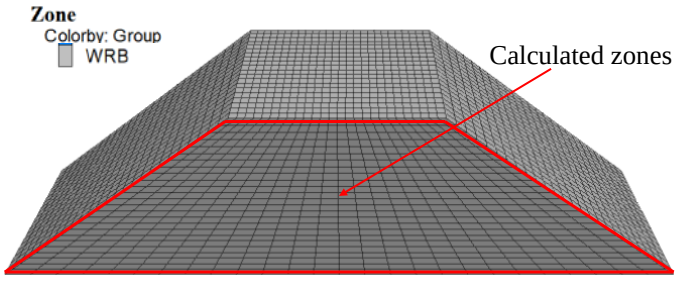

Figure F.3 Highlighted zones used to calculate the value of *K*

Comparison of the numerical results ($C_{LD} + C_{LU} + C_{LD}$) and analytical solution (F_h) leads to the expression below:

$$C_{LD} + C_{LU} + C_{LD} = \frac{K\gamma_{wr}H_d^2}{2}\left[L_{BT} + \frac{H_d}{3}\left(\frac{1}{tan\alpha_1} + \frac{1}{tan\alpha_2}\right)\right] \quad \text{(E1)}$$

K value can be calculated by rearranging:

$$K = \frac{C_{LD}+C_{LU}+C_{LD}}{\frac{\gamma_{wr}H_d^2}{2}\left[L_{BT}+\frac{H_d}{3}\left(\frac{1}{tan\alpha_1}+\frac{1}{tan\alpha_2}\right)\right]} \quad \text{(E2)}$$

Table F.5 gives the plan to calculate the *K* value by considering different cases and to estimate its range.

Table F.5 Program of numerical simulations with FLAC3D to calculate *K* value with α_1 = 37°, γ_b = 19.6 kN/m^3, γ_r = 26.5 kN/m^3, ν_r = 0.3, E_r = 30 GPa, γ_{wr} = 19.6 kN/m^3, c_{wr} = 100 MPa, ϕ_{wr} = 38°, E_{wr} = 100 MPa, ν_{wr} = 0.3, ϕ_{wr} = 38°, and L_d = 5 m.

Case	H (m)	H_d (m)	α_2 (°)	δ_{wr} (°)	L_{BT} (m)
5	12	5	37	15	5.2
6	12	5	37	17	3
7	9	5	37	17	1.7
8	9	5	34	16	1.3

For case 5 in Table F.5, the total horizontal force obtained with FLAC3D perpendicular to the sidewall F_h was calculated as:

$$F_h = \frac{K\gamma_{wr}{H_d}^2}{2}\left[L_{BT} + \frac{H_d}{3}\left(\frac{1}{tan\,\alpha_1} + \frac{1}{tan\,\alpha_2}\right)\right]$$

$$= \frac{K \times 19.6\ \text{kN/m}^3 \times (5\ \text{m})^2}{2}\left[5.2\ \text{m} + \frac{5\ \text{m}}{3}\left(\frac{1}{tan\,37°} + \frac{1}{tan\,37°}\right)\right]$$

$$= K \times 2358\ \text{kN}$$

Comparison of the theoretical and numerical results (shown in Table F.6 and F.7) of the total horizontal force F_h leads to a value of overall *K* = 2671 kN/2358 kN = 1.13 for the global stability analysis of WRB.

Table F.6 the horizontal normal stress (σ_{YY} kPa) of each element perpendicular to the sidewall (Case 5 in Table F.5)

Layer	Element number from upstream to downstream																								
	1	2	3	4	5	6	7	8	9	10	11	12	13	14	15	16	17	18	19	20	21	22	23	24	25
1	49.32	27.77	16.11	11.24	8.36	6.54	5.33	5.12	5.06	4.90	4.49	4.31	3.88	3.59	3.21	2.55	2.35	2.27	2.07	2.07	2.00	2.27	2.54	2.61	2.24
2	62.67	56.40	43.13	31.83	24.05	18.30	14.87	13.04	11.97	11.46	11.58	11.78	11.62	12.10	12.08	11.54	10.96	10.12	9.21	9.16	9.44	10.54	10.54	6.52	3.79
3	55.87	61.77	61.71	49.93	38.08	29.50	23.81	17.92	17.22	17.44	17.25	16.22	15.99	16.30	16.08	15.59	15.29	14.92	14.28	14.20	14.48	16.28	13.68	4.51	2.42
4	57.23	60.85	64.50	61.30	52.86	43.01	34.78	25.20	22.61	20.85	19.40	18.18	17.20	16.46	15.69	15.04	14.43	13.74	13.18	12.86	13.21	14.70	15.17	5.27	2.81
5	59.84	62.21	64.68	62.45	58.79	51.83	43.82	30.92	26.31	23.21	21.04	19.45	17.96	16.71	15.67	14.60	13.73	12.71	12.21	12.18	12.70	14.09	15.73	7.22	3.16
6	61.70	64.44	66.23	63.24	59.54	54.77	41.49	35.03	29.66	25.70	22.92	21.25	19.44	17.61	16.31	15.06	14.03	13.24	12.65	12.38	12.81	14.09	15.47	9.23	3.58
7	62.42	66.84	68.28	65.00	61.20	57.00	44.82	38.73	33.44	29.20	26.13	23.66	21.54	19.70	18.01	16.61	15.30	14.22	13.53	13.50	13.54	14.55	15.37	10.02	3.93
8	64.32	68.70	70.00	67.19	63.60	59.12	48.36	42.40	37.01	32.69	29.31	26.48	24.07	21.93	19.95	18.29	16.99	15.78	14.95	14.76	14.44	14.71	15.09	10.64	4.37
9	66.37	70.32	71.65	69.35	66.01	61.56	51.43	45.60	40.30	35.77	32.01	28.90	26.24	23.94	21.95	20.13	18.57	17.33	16.46	16.25	15.68	14.54	14.39	11.19	4.68
10	67.86	71.47	73.44	71.43	68.31	64.03	54.33	48.71	43.43	38.66	34.69	31.37	28.56	26.04	23.92	22.07	20.39	18.92	18.05	18.09	17.75	14.75	13.38	11.26	4.89
11	68.02	72.55	74.98	73.38	70.41	66.34	56.98	51.56	46.37	41.56	37.39	33.78	30.74	28.14	25.94	24.00	22.18	20.52	19.65	19.88	19.73	15.95	12.26	10.58	5.02
12	68.10	74.14	76.46	75.21	72.49	68.51	59.37	54.37	49.12	44.31	39.91	36.07	32.86	30.24	28.01	25.90	24.07	22.14	21.12	21.40	21.19	17.68	12.10	9.92	4.96
13	69.69	75.29	78.00	76.96	74.51	70.68	66.18	61.68	56.93	51.69	46.80	42.32	38.38	35.05	32.25	29.88	27.65	25.70	23.78	22.57	22.36	18.75	12.89	9.56	4.85
14	71.97	76.16	79.59	78.81	76.56	68.37	63.92	59.15	54.00	49.00	44.43	40.47	37.04	34.01	31.50	29.22	27.18	25.34	23.94	24.06	23.46	19.34	13.92	9.57	4.85
15	70.35	77.98	81.20	80.70	78.40	74.84	70.61	66.23	61.27	56.16	51.13	46.46	42.44	38.90	35.75	33.13	30.75	28.63	26.86	25.23	24.13	19.94	14.56	10.01	4.92
16	70.42	79.88	82.81	82.54	80.34	77.06	73.01	68.45	63.35	58.28	53.20	48.45	44.49	40.87	37.53	34.80	32.33	30.08	28.27	26.65	24.35	20.48	14.83	10.41	5.11
17	71.28	81.55	84.55	84.36	82.40	79.27	75.24	70.53	65.46	60.42	55.30	50.54	46.52	42.81	39.35	36.48	33.94	31.53	29.60	28.16	24.35	20.63	15.02	10.54	5.31
18	72.38	83.51	86.53	86.46	84.60	81.37	77.36	72.55	67.54	62.43	57.30	52.61	48.43	44.63	41.13	38.07	35.41	32.91	30.98	29.73	24.41	20.67	15.24	10.50	5.36
19	74.24	85.49	88.58	88.67	86.69	83.49	79.47	74.70	69.66	64.47	59.38	54.60	50.30	46.40	42.87	39.72	36.92	34.34	32.46	31.30	24.49	20.66	15.35	10.47	5.25
20	76.13	87.65	90.70	90.90	88.81	85.67	81.61	76.86	71.77	66.54	61.39	56.53	52.11	48.12	44.55	41.33	38.43	35.78	33.93	32.78	24.80	20.57	15.40	10.41	5.03
21	78.37	89.83	92.98	93.13	91.09	87.89	83.79	78.98	73.80	68.51	63.28	58.32	53.80	49.74	46.11	42.84	39.85	37.13	35.33	30.93	25.44	20.59	15.55	10.34	4.81
22	79.77	92.01	95.18	95.51	93.54	90.31	86.13	81.20	75.92	70.50	65.16	60.10	55.49	51.37	47.68	44.36	41.32	38.57	36.79	35.40	26.37	20.90	15.85	10.42	4.87
23	80.01	93.96	97.32	97.98	96.07	92.78	88.49	83.44	78.01	72.44	66.99	61.81	57.12	52.93	49.19	45.82	42.74	39.97	38.21	36.65	33.20	21.51	16.43	10.84	5.30
24	80.45	95.91	99.99	100.65	98.77	95.44	91.02	85.85	80.26	74.51	68.87	63.57	58.80	54.56	50.78	47.37	44.24	41.46	39.70	37.98	34.34	22.62	17.45	11.89	6.04
25	76.00	95.96	102.38	103.58	101.77	98.41	93.86	88.51	82.82	76.78	70.84	65.40	60.52	56.21	52.39	48.94	45.77	43.00	41.27	39.40	35.60	24.44	19.11	13.55	6.14

Table F.7 the area, average horizontal stress, and total horizontal force of each layer of 0.2 m thick (Case 5 in Table F.5)

Layer	X (m) of corner				Area of the layer (m^2)	Average σ_{YY} (kPa)	Horizontal force (kN)
	top upstream	top downstream	base upstream	base downstream			
1	0	5.2	-0.2654	5.4654	1.09308	7.29	7.97
2	-0.2654	5.4654	-0.5308	5.7308	1.19924	17.55	21.04
3	-0.5308	5.7308	-0.7962	5.9962	1.3054	23.23	30.33
4	-0.7962	5.9962	-1.0616	6.2616	1.41156	26.02	36.73
5	-1.0616	6.2616	-1.327	6.527	1.51772	27.73	42.08
6	-1.327	6.527	-1.5924	6.7924	1.62388	28.87	46.89
7	-1.5924	6.7924	-1.8578	7.0578	1.73004	30.66	53.04
8	-1.8578	7.0578	-2.1232	7.3232	1.8362	32.61	59.87
9	-2.1232	7.3232	-2.3886	7.5886	1.94236	34.42	66.86
10	-2.3886	7.5886	-2.654	7.854	2.04852	36.23	74.22
11	-2.654	7.854	-2.9194	8.1194	2.15468	37.92	81.70
12	-2.9194	8.1194	-3.1848	8.3848	2.26084	39.59	89.50
13	-3.1848	8.3848	-3.4502	8.6502	2.367	42.98	101.72
14	-3.4502	8.6502	-3.7156	8.9156	2.47316	42.63	105.44
15	-3.7156	8.9156	-3.981	9.181	2.57932	46.02	118.71
16	-3.981	9.181	-4.2464	9.4464	2.68548	47.52	127.61
17	-4.2464	9.4464	-4.5118	9.7118	2.79164	49.01	136.81
18	-4.5118	9.7118	-4.7772	9.9772	2.8978	50.48	146.29
19	-4.7772	9.9772	-5.0426	10.2426	3.00396	52.00	156.20
20	-5.0426	10.2426	-5.308	10.508	3.11012	53.51	166.43
21	-5.308	10.508	-5.5734	10.7734	3.21628	54.90	176.57
22	-5.5734	10.7734	-5.8388	11.0388	3.32244	56.59	188.02
23	-5.8388	11.0388	-6.1042	11.3042	3.4286	58.37	200.12
24	-6.1042	11.3042	-6.3696	11.5696	3.53476	60.10	212.44
25	-6.3696	11.5696	-6.635	11.835	3.64092	61.71	224.67

For case 6 in Table F.5, the total horizontal force obtained with FLAC3D perpendicular to the sidewall F_h can be calculated as:

$$F_h = \frac{K\gamma_{wr}{H_d}^2}{2}\left[L_{BT} + \frac{H_d}{3}\left(\frac{1}{tan\,\alpha_1} + \frac{1}{tan\,\alpha_2}\right)\right]$$

$$= \frac{K \times 19.6\ \text{kN/m}^3 \times (5\ \text{m})^2}{2}\left[3\ \text{m} + \frac{5\ \text{m}}{3}\left(\frac{1}{tan\,37°} + \frac{1}{tan\,37°}\right)\right]$$

$$= K \times 1819\ \text{kN}$$

Comparison of the theoretical and numerical results (shown in Table F.8 and F.9) of the total horizontal force F_h leads to a value of overall K = 2283 kN/1819 kN = 1.26 for the global stability analysis of WRB.

Table F.8 the horizontal normal stress (σ_{YY} kPa) of each element perpendicular to the sidewall (Case 6 in Table F.5)

Layer	Element number from upstream to downstream																		
	1	2	3	4	5	6	7	8	9	10	11	12	13	14	15	16	17	18	19
1	47.11	40.96	34.60	27.49	21.97	17.95	14.93	12.85	11.62	10.61	8.94	7.28	6.14	5.37	4.70	4.15	3.72	3.44	3.27
2	58.80	58.99	54.23	47.76	41.82	36.66	32.20	28.45	24.94	22.06	19.41	16.75	14.52	12.41	10.62	9.06	7.83	7.06	6.53
3	49.68	55.94	60.75	61.90	58.32	52.56	45.44	38.43	32.43	27.49	23.30	20.29	17.60	15.39	13.70	12.49	11.47	10.61	9.95
4	48.88	48.41	53.68	60.50	63.02	62.25	58.83	53.63	47.64	42.13	37.17	32.73	28.90	25.42	22.20	19.21	16.59	14.34	12.71
5	47.29	48.56	51.47	56.76	61.37	64.13	64.18	61.11	55.94	49.66	43.50	37.62	32.52	28.11	24.36	21.23	18.73	16.65	15.00
6	47.56	48.57	52.76	56.33	59.63	63.00	65.76	66.13	63.81	58.74	52.49	46.35	40.51	35.49	31.15	27.40	24.15	21.25	18.77
7	48.28	50.70	54.86	57.67	60.20	62.20	64.35	66.35	67.85	66.56	62.36	56.10	49.12	42.43	36.60	31.77	27.89	24.72	22.20
8	50.53	53.41	58.05	60.68	62.30	62.86	63.47	64.96	67.01	68.52	67.91	64.73	59.33	52.85	46.17	40.18	34.92	30.52	26.93
9	55.09	55.82	61.02	63.47	64.43	64.42	64.26	64.55	65.49	67.01	67.71	67.21	64.44	59.76	54.05	48.10	42.36	37.02	32.41
10	54.87	57.96	63.42	65.80	66.40	66.07	65.62	65.37	65.52	66.14	66.38	66.62	65.42	62.35	57.88	52.52	46.98	41.34	36.06
11	58.64	60.55	65.73	67.76	68.02	67.65	67.25	66.66	66.27	66.02	65.95	65.82	65.12	63.15	59.67	55.03	49.73	44.21	38.64
12	58.61	62.76	67.66	69.26	69.79	69.47	68.93	68.06	67.39	66.83	66.24	65.69	64.95	63.57	60.97	56.97	52.16	46.55	40.61
13	60.66	63.80	69.65	71.13	71.60	71.46	70.73	69.81	68.92	68.08	67.11	66.12	65.28	64.09	62.03	58.61	54.17	48.68	42.38
14	61.81	66.14	71.16	72.89	73.51	73.31	72.61	71.64	70.61	69.50	68.30	67.07	65.92	64.73	62.96	59.97	55.88	50.54	44.16
15	62.08	67.89	73.11	74.60	75.34	75.17	74.54	73.59	72.42	71.17	69.74	68.28	66.91	65.62	63.98	61.25	57.41	52.14	45.73
16	61.89	69.45	75.02	76.37	77.21	77.14	76.60	75.58	74.33	72.91	71.19	69.47	67.90	66.51	64.96	62.47	58.94	53.73	47.27
17	62.17	71.52	76.85	78.32	79.25	79.17	78.61	77.63	76.35	74.89	72.98	70.92	68.94	67.23	65.66	63.50	60.40	55.41	49.04
18	62.59	73.45	78.65	80.50	81.28	81.32	80.70	79.70	78.38	77.06	75.15	72.91	70.51	68.26	66.33	64.26	61.56	56.95	50.97
19	64.15	75.57	80.72	82.74	83.45	83.47	82.86	81.78	80.40	79.18	77.53	75.39	72.73	69.90	67.32	64.89	62.33	58.14	52.68
20	65.36	77.80	82.94	85.12	85.71	85.68	85.03	83.90	82.46	81.13	79.74	77.94	75.43	72.29	69.00	65.87	63.04	59.03	54.11
21	66.70	80.18	85.24	87.32	88.12	87.99	87.27	86.07	84.54	82.91	81.58	80.11	78.03	75.05	71.39	67.55	64.04	59.82	55.24
22	69.32	82.58	87.68	89.79	90.60	90.45	89.63	88.36	86.73	84.88	83.34	81.92	80.25	77.76	74.25	70.04	65.79	61.04	56.52
23	71.55	85.16	90.02	92.25	93.10	92.93	92.06	90.68	88.89	86.85	84.94	83.31	81.74	79.71	76.71	72.70	68.10	62.86	58.18
24	74.16	87.28	92.52	94.84	95.70	95.59	94.70	93.19	91.15	88.75	86.29	84.23	82.32	80.28	77.68	74.37	70.22	65.08	60.40
25	72.57	86.40	94.10	97.46	98.67	98.58	97.65	95.94	93.49	90.36	86.96	84.07	81.41	78.76	75.74	72.54	69.48	66.06	62.58

Layer	Element number from upstream to downstream																	
	20	21	22	23	24	25	26	27	28	29	30	31	32	33	34	35	36	37
1	3.39	3.60	3.77	3.92	4.02	4.09	4.03856	3.97758	3.99283	4.16964	4.43564	4.59711	4.33649	1.66224	1.43855	2.07374	0.517064	0.269186
2	6.19	6.21	6.22	6.23	6.26	6.37	6.62276	6.80896	7.13998	7.66907	7.96477	8.33809	8.37191	3.224	2.74588	3.22162	1.27936	0.382058
3	9.55	9.55	9.76	9.96	10.03	10.14	10.5368	11.0281	11.6703	12.3319	13.1765	13.744	12.5734	4.08142	3.59492	3.67654	1.61284	0.54185
4	11.65	11.10	11.00	11.05	11.11	11.09	11.1583	11.301	11.6178	12.4441	13.8344	15.0859	15.0132	4.92252	4.08773	3.82962	2.32282	0.775475
5	13.63	12.91	12.62	12.57	12.34	12.03	11.6773	11.5919	11.566	11.6262	12.3437	13.934	15.1049	5.96094	4.69885	3.86651	2.39622	0.894722
6	16.92	15.82	15.43	15.19	14.91	14.53	14.088	13.6646	13.2319	12.6429	12.1291	12.4566	13.7794	7.23294	5.06371	4.16734	3.0149	1.09155
7	20.18	19.10	18.80	18.62	18.47	18.19	17.8055	17.2903	16.4002	15.0402	13.3211	12.2457	12.8507	8.1909	5.21014	4.88666	3.45229	1.73841
8	24.45	23.30	23.14	23.08	22.87	22.52	22.0299	21.2254	19.9312	17.8731	15.2047	12.7629	12.4749	8.6685	5.45443	5.48524	3.86783	1.94846
9	29.09	27.65	27.31	27.13	26.95	26.74	26.2795	25.3494	23.5059	20.6976	17.2673	14.0793	12.5359	9.1351	6.41799	5.00063	4.1949	2.03914
10	32.30	30.87	30.56	30.47	30.35	30.17	29.8165	28.9406	27.0937	23.7921	19.6073	15.5139	13.1088	9.88194	6.8107	4.64091	4.1752	2.13544
11	34.66	33.29	32.91	32.72	32.67	32.72	32.5948	31.7597	29.7734	26.4594	22.0456	17.5851	14.3482	10.5592	7.51432	4.93812	3.80612	2.26827
12	36.50	35.10	34.47	34.12	33.97	34.21	34.5156	34.1554	32.2325	28.5225	23.911	19.6222	15.9804	12.0317	8.19046	5.70937	3.61406	2.18101
13	38.10	36.72	36.03	35.34	35.00	35.11	35.5203	35.6894	34.6138	31.0387	25.8247	21.0678	17.9423	13.7154	9.52548	6.73293	3.87381	2.07906
14	39.76	38.30	37.55	36.69	36.09	35.92	36.1302	36.4977	36.1292	33.6349	28.2065	22.47	18.9168	15.3032	11.0971	7.65887	4.33635	1.9312
15	41.38	39.93	39.14	38.17	37.33	36.84	36.6035	36.6048	36.5511	35.2602	31.0466	24.5484	19.3862	16.5622	12.4204	8.31146	5.10943	1.72723
16	42.99	41.55	40.71	39.65	38.57	37.61	36.8193	36.2449	36.0496	35.4791	32.89	26.9295	21.0111	17.3359	13.9802	9.19892	5.79128	1.79154
17	44.89	43.25	42.12	40.81	39.31	37.87	36.6761	35.7474	35.0127	34.4731	33.122	28.9853	22.6524	18.2519	15.1234	10.2916	6.26166	1.92081
18	47.05	45.25	43.89	42.41	40.81	38.92	36.7081	34.8154	33.698	32.9468	32.0515	29.8219	24.4349	19.2733	15.8506	11.4528	6.70232	2.06025
19	49.11	47.31	45.82	44.34	42.88	41.08	38.4161	35.1767	32.3953	30.8893	30.1801	29.1168	25.7218	20.1134	16.1675	12.3902	7.13626	2.21361
20	50.97	49.24	47.68	46.18	44.83	43.31	40.9039	37.117	32.6833	29.4531	27.8719	27.2833	25.5767	20.9431	16.4125	12.5907	7.51792	2.30143
21	52.47	50.87	49.32	47.80	46.43	45.01	42.9938	39.6358	34.7369	29.677	26.4055	24.9781	24.1433	21.3718	16.6091	12.3624	7.71627	2.41333
22	53.89	52.35	50.87	49.41	48.04	46.53	44.5673	41.7002	37.4156	31.8556	26.745	23.7468	22.4206	20.8337	16.9464	12.5045	7.8412	2.64128
23	55.43	53.75	52.26	50.89	49.58	48.00	45.8851	43.1298	39.5013	34.6162	28.908	24.1566	21.5303	20.0466	17.3296	13.1479	8.97542	3.28988
24	57.46	55.47	53.80	52.41	51.16	49.61	47.383	44.5216	41.1505	37.0671	31.9571	26.4954	22.2923	19.9901	17.9806	14.7643	11.2893	4.69338
25	60.01	57.75	55.68	54.02	52.68	51.18	49.0538	46.2443	42.9598	39.2925	35.1011	30.1993	25.2031	21.5062	18.9939	16.6388	13.2356	5.59853

Table F.9 the area, average horizontal stress, and total horizontal force of each layer of 0.2 m thick (Case 6 in Table F.5)

Layer	X (m) of corner				Area of the layer (m^2)	Average σ_{YY} (kPa)	Horizontal force (kN)
	top upstream	top downstream	base upstream	base downstream			
1	0	3	-0.2654	3.2654	0.65308	9.34	6.10
2	-0.2654	3.2654	-0.5308	3.5308	0.75924	16.52	12.55
3	-0.5308	3.5308	-0.7962	3.7962	0.8654	20.95	18.13
4	-0.7962	3.7962	-1.0616	4.0616	0.97156	24.91	24.20
5	-1.0616	4.0616	-1.327	4.327	1.07772	26.48	28.54
6	-1.327	4.327	-1.5924	4.5924	1.18388	29.33	34.72
7	-1.5924	4.5924	-1.8578	4.8578	1.29004	32.27	41.63
8	-1.8578	4.8578	-2.1232	5.1232	1.3962	35.72	49.87
9	-2.1232	5.1232	-2.3886	5.3886	1.50236	38.65	58.06
10	-2.3886	5.3886	-2.654	5.654	1.60852	40.62	65.34
11	-2.654	5.654	-2.9194	5.9194	1.71468	42.28	72.50
12	-2.9194	5.9194	-3.1848	6.1848	1.82084	43.66	79.50
13	-3.1848	6.1848	-3.4502	6.4502	1.927	45.09	86.88
14	-3.4502	6.4502	-3.7156	6.7156	2.03316	46.47	94.48
15	-3.7156	6.7156	-3.981	6.981	2.13932	47.78	102.22
16	-3.981	6.981	-4.2464	7.2464	2.24548	49.01	110.06
17	-4.2464	7.2464	-4.5118	7.5118	2.35164	50.15	117.94
18	-4.5118	7.5118	-4.7772	7.7772	2.4578	51.32	126.12
19	-4.7772	7.7772	-5.0426	8.0426	2.56396	52.59	134.83
20	-5.0426	8.0426	-5.308	8.308	2.67012	53.90	143.93
21	-5.308	8.308	-5.5734	8.5734	2.77628	55.25	153.38
22	-5.5734	8.5734	-5.8388	8.8388	2.88244	56.79	163.69
23	-5.8388	8.8388	-6.1042	9.1042	2.9886	58.44	174.64
24	-6.1042	9.1042	-6.3696	9.3696	3.09476	60.22	186.38
25	-6.3696	9.3696	-6.635	9.635	3.20092	61.57	197.09

For case 7 in Table F.5, the total horizontal force obtained with FLAC3D perpendicular to the sidewall F_h can be estimated as:

$$F_h = \frac{K\gamma_{wr}{H_d}^2}{2}\left[L_{BT} + \frac{H_d}{3}\left(\frac{1}{tan\,\alpha_1} + \frac{1}{tan\,\alpha_2}\right)\right]$$

$$= \frac{K \times 19.6\ \text{kN/m}^3 \times (5\ \text{m})^2}{2}\left[1.7\ \text{m} + \frac{5\ \text{m}}{3}\left(\frac{1}{tan\,37°} + \frac{1}{tan\,37°}\right)\right]$$

$$= K \times 1500\ \text{kN}$$

Comparison of the theoretical and numerical results (shown in Table F.10 and F.11) of the total horizontal force F_h leads to a value of overall K = 1587 kN/1500 kN = 1.06 for the global stability analysis of WRB.

Table F.10 the horizontal normal stress (σ_{YY} kPa) of each element perpendicular to the sidewall (Case 7 in Table F.5)

Layer	Element number from upstream to downstream																				
	1	2	3	4	5	6	7	8	9	10	11	12	13	14	15	16	17	18	19	20	21
1	30.29	27.01	22.43	16.28	11.08	7.70	5.04	3.64	2.83	2.38	2.13	1.95	1.81	1.76	1.75	1.86	2.08	2.46	2.49	1.40	0.75
2	34.36	29.80	25.78	23.42	20.90	18.93	15.48	11.98	9.42	7.69	6.68	6.20	6.15	6.09	5.97	6.08	6.58	6.08	5.62	3.10	1.27
3	24.59	30.27	30.59	27.88	24.93	21.84	18.68	15.59	12.98	11.14	10.08	9.53	9.19	8.95	8.77	8.87	9.06	8.77	6.47	4.44	1.43
4	24.44	28.79	34.46	34.40	30.24	25.25	21.55	18.86	16.40	14.23	12.52	11.69	11.24	10.80	10.69	10.33	10.22	9.58	7.00	4.57	1.50
5	31.79	36.85	42.69	46.04	43.42	36.94	29.88	24.20	20.44	17.75	15.84	15.12	14.63	13.91	13.06	12.41	11.23	9.78	7.69	4.81	1.65
6	37.24	41.07	45.62	49.74	51.92	48.59	41.27	33.54	27.67	23.41	19.77	17.74	17.15	16.82	15.78	14.68	12.97	10.77	8.15	5.04	1.78
7	36.34	38.02	41.71	45.65	49.75	52.43	49.85	42.85	34.76	28.85	24.10	21.43	19.99	18.82	18.01	16.90	14.89	11.99	8.81	5.49	1.95
8	36.08	36.53	39.71	42.55	45.59	49.35	51.16	48.36	41.65	34.80	28.87	24.95	22.83	21.07	19.41	17.89	16.21	13.42	9.40	6.14	2.19
9	37.37	37.25	40.34	42.32	44.05	46.73	49.27	49.39	45.53	39.74	33.32	28.74	26.11	23.77	20.70	18.26	16.33	14.44	10.57	6.60	2.46
10	39.50	39.27	42.32	43.61	44.32	45.76	47.42	48.03	46.27	42.25	36.74	32.12	29.54	26.90	23.43	19.51	16.46	14.34	11.50	7.03	2.62
11	41.13	42.05	44.40	45.03	45.29	45.96	46.77	47.14	46.10	42.95	38.37	34.45	32.29	30.03	26.30	21.65	17.29	14.12	11.87	7.74	2.61
12	42.41	44.30	46.38	46.73	46.58	46.79	47.03	47.06	46.07	43.20	38.98	35.57	33.79	32.10	29.10	24.21	18.80	14.49	11.79	8.32	2.81
13	43.26	46.77	48.29	48.44	48.23	48.04	47.86	47.55	46.38	43.48	39.44	36.18	34.51	33.26	30.82	26.33	20.62	15.52	11.87	8.68	3.17
14	44.95	49.03	50.28	50.33	49.97	49.49	48.99	48.50	47.14	43.99	39.87	36.74	35.04	33.93	31.83	27.73	22.18	16.83	12.30	8.67	3.48
15	46.75	50.75	52.34	52.31	51.80	51.16	50.46	49.83	48.31	45.07	40.46	37.38	35.56	34.44	32.75	28.92	23.31	18.09	13.06	8.84	3.66
16	48.10	52.75	54.28	54.33	53.77	53.07	52.06	51.12	49.63	46.65	41.68	38.11	36.14	34.74	33.35	30.23	24.39	18.81	13.88	9.24	3.64
17	49.19	54.69	56.36	56.39	55.89	54.92	53.68	52.37	50.87	48.34	43.69	39.52	36.78	34.77	33.33	31.03	25.76	19.30	14.56	9.64	3.68
18	50.34	56.96	58.48	58.61	57.96	56.72	55.35	53.71	52.06	49.80	45.87	41.70	38.17	35.06	32.87	31.01	27.03	20.17	14.85	10.06	3.70
19	51.26	59.15	60.61	60.80	59.95	58.62	57.06	55.20	53.28	51.02	47.65	43.98	40.28	36.27	32.70	30.30	27.54	21.48	15.06	10.27	3.69
20	53.34	61.28	62.83	62.98	61.93	60.54	58.80	56.74	54.65	52.22	49.06	45.90	42.59	38.27	33.46	29.75	27.15	22.53	15.61	10.34	3.66
21	55.28	63.66	65.08	65.13	63.96	62.41	60.51	58.29	55.97	53.36	50.20	47.27	44.44	40.41	35.01	29.92	26.69	22.86	16.52	10.55	3.73
22	57.56	66.12	67.42	67.38	66.06	64.33	62.23	59.84	57.24	54.45	51.30	48.31	45.74	42.25	37.03	31.07	26.64	23.12	17.49	11.13	4.20
23	58.49	68.08	69.84	69.68	68.07	65.96	63.62	61.07	58.28	55.26	51.98	49.00	46.39	43.36	38.80	32.80	27.24	23.46	18.55	12.34	5.33
24	61.22	70.69	72.57	72.23	69.87	66.91	64.12	61.45	58.57	55.44	52.11	49.02	46.27	43.49	39.82	34.74	28.71	24.29	19.91	14.12	6.78
25	58.90	72.44	75.43	75.27	71.45	66.19	61.90	59.03	56.30	53.29	50.07	47.40	44.90	42.05	39.27	36.16	31.15	25.91	21.52	15.87	6.95

Table F.11 the area, average horizontal stress, and total horizontal force of each layer of 0.2 m thick (Case 7 in Table F.5)

Layer	X (m) of corner				Area of the layer (m^2)	Average σ_{YY} (kPa)	Horizontal force (kN)
	top upstream	top downstream	base upstream	base downstream			
1	0	1.7	-0.2654	1.9654	0.39308	7.10	2.79
2	-0.2654	1.9654	-0.5308	2.2308	0.49924	12.27	6.12
3	-0.5308	2.2308	-0.7962	2.4962	0.6054	14.48	8.77
4	-0.7962	2.4962	-1.0616	2.7616	0.71156	16.61	11.82
5	-1.0616	2.7616	-1.327	3.027	0.81772	21.43	17.53
6	-1.327	3.027	-1.5924	3.2924	0.92388	25.75	23.79
7	-1.5924	3.2924	-1.8578	3.5578	1.03004	27.74	28.58
8	-1.8578	3.5578	-2.1232	3.8232	1.1362	28.96	32.90
9	-2.1232	3.8232	-2.3886	4.0886	1.24236	30.16	37.47
10	-2.3886	4.0886	-2.654	4.354	1.34852	31.38	42.31
11	-2.654	4.354	-2.9194	4.6194	1.45468	32.55	47.35
12	-2.9194	4.6194	-3.1848	4.8848	1.56084	33.64	52.51
13	-3.1848	4.8848	-3.4502	5.1502	1.667	34.70	57.85
14	-3.4502	5.1502	-3.7156	5.4156	1.77316	35.77	63.43
15	-3.7156	5.4156	-3.981	5.681	1.87932	36.92	69.38
16	-3.981	5.681	-4.2464	5.9464	1.98548	38.09	75.63
17	-4.2464	5.9464	-4.5118	6.2118	2.09164	39.27	82.15
18	-4.5118	6.2118	-4.7772	6.4772	2.1978	40.50	89.01
19	-4.7772	6.4772	-5.0426	6.7426	2.30396	41.72	96.13
20	-5.0426	6.7426	-5.308	7.008	2.41012	43.03	103.71
21	-5.308	7.008	-5.5734	7.2734	2.51628	44.35	111.59
22	-5.5734	7.2734	-5.8388	7.5388	2.62244	45.76	119.99
23	-5.8388	7.5388	-6.1042	7.8042	2.7286	47.03	128.32
24	-6.1042	7.8042	-6.3696	8.0696	2.83476	48.21	136.65
25	-6.3696	8.0696	-6.635	8.335	2.94092	48.16	141.65

For case 8 in Table F.5, the total horizontal force obtained with FLAC3D perpendicular to the sidewall F_h can be estimated as:

$$F_h = \frac{K\gamma_{wr}{H_d}^2}{2}\left[L_{BT} + \frac{H_d}{3}\left(\frac{1}{tan\,\alpha_1} + \frac{1}{tan\,\alpha_2}\right)\right]$$

$$= \frac{K \times 19.6\ \text{kN/m}^3 \times (5\ \text{m})^2}{2}\left[1.3\ \text{m} + \frac{5\ \text{m}}{3}\left(\frac{1}{tan\,37°} + \frac{1}{tan\,37°}\right)\right]$$

$$= K \times 1466\ \text{kN}$$

Comparison of the theoretical and numerical results (shown in Table F.12 and F.13) of the total horizontal force F_h leads to a value of overall K = 1575 kN/1466 kN = 1.07 for the global stability analysis of WRB.

Table F.12 the horizontal normal stress (σ_{YY} kPa) of each element perpendicular to the sidewall (Case 8 in Table F.5)

Layer	Element number from upstream to downstream															
	1	2	3	4	5	6	7	8	9	10	11	12	13	14	15	16
1	25.04	22.53	18.60	13.30	9.55	6.28	4.21	3.13	2.68	2.47	2.39	2.67	3.09	2.99	2.22	0.76
2	32.00	29.84	26.00	21.80	17.98	14.80	11.91	9.54	7.70	6.82	6.72	6.87	6.71	5.69	4.24	1.63
3	30.68	36.11	37.45	33.87	27.65	21.78	16.90	13.13	10.64	9.74	10.39	10.68	9.29	6.58	4.94	1.81
4	30.61	33.75	41.47	44.68	41.13	33.36	25.56	20.10	16.29	14.36	14.02	13.74	11.65	7.73	4.58	1.97
5	31.30	33.75	38.72	42.54	43.67	40.79	34.24	27.07	21.16	18.23	17.40	17.16	14.84	10.46	5.31	2.20
6	32.64	34.70	38.41	40.01	41.11	40.63	36.27	30.09	24.05	20.76	19.61	19.07	16.94	13.27	6.17	3.08
7	35.23	36.23	38.93	39.90	39.89	38.91	35.67	30.84	25.22	21.92	20.65	19.76	18.10	14.79	8.14	3.65
8	36.58	38.03	40.26	40.90	40.87	39.52	35.78	30.39	25.15	22.61	21.25	20.64	18.77	15.82	9.92	3.57
9	38.66	39.84	41.90	42.19	42.37	42.00	38.35	31.21	24.63	21.99	21.08	20.69	19.55	16.43	10.79	3.56
10	42.07	41.82	43.76	43.62	43.56	43.87	42.09	35.00	26.60	21.75	20.06	19.87	19.50	17.04	12.12	3.51
11	45.09	43.31	45.79	45.27	44.81	44.80	44.44	39.26	31.02	24.73	20.13	18.67	18.59	17.05	12.81	3.55
12	46.57	44.84	47.74	47.01	46.22	45.52	45.38	41.69	34.86	29.09	23.09	18.04	16.97	16.39	13.04	3.48
13	47.59	46.62	49.55	48.71	47.50	46.45	45.88	42.65	37.28	32.66	27.25	20.12	15.59	14.95	13.25	4.06
14	49.50	48.62	51.31	50.27	48.92	47.71	46.34	43.03	38.53	35.02	30.45	23.76	16.00	13.20	12.28	4.98
15	50.51	50.54	53.14	51.92	50.60	49.16	47.12	43.38	39.26	36.36	32.82	26.73	18.60	12.62	10.49	5.12
16	51.83	52.62	54.96	53.82	52.46	50.63	48.16	44.05	39.92	37.13	34.30	28.98	21.30	13.76	9.57	4.50
17	52.81	54.96	56.81	55.85	54.22	52.01	49.42	45.21	40.75	37.68	34.90	30.53	23.34	15.53	9.98	4.29
18	53.50	57.50	58.62	57.93	55.99	53.45	50.81	46.69	41.79	38.18	35.07	31.43	24.96	16.94	10.87	4.61
19	54.67	59.95	60.60	60.04	57.79	55.04	52.29	48.33	43.18	38.97	35.29	31.68	26.19	18.19	11.66	4.92
20	56.64	62.31	62.72	62.07	59.64	56.65	53.67	49.83	44.85	40.15	35.83	31.77	26.94	19.35	12.31	5.22
21	58.82	64.63	64.90	64.05	61.42	58.24	55.02	51.07	46.37	41.59	36.65	31.89	27.27	20.42	12.94	5.73
22	60.17	67.04	67.14	66.02	63.16	59.80	56.22	52.13	47.68	43.03	37.80	32.45	27.53	21.39	13.83	6.59
23	60.76	69.59	69.44	67.82	64.58	61.03	57.14	52.82	48.43	44.11	38.98	33.29	27.94	22.30	15.09	7.49
24	61.95	72.53	72.17	69.23	65.12	61.33	57.33	52.85	48.40	44.44	39.88	34.44	28.91	23.43	16.67	8.02
25	61.36	74.91	75.53	69.58	63.22	58.72	55.05	50.87	46.98	43.19	39.69	35.52	30.50	24.93	18.07	7.90

Table F.13 the area, average horizontal stress, and total horizontal force of each layer of 0.2 m thick (Case 8 in Table F.5)

Layer	X (m) of corner				Area of the layer (m^2)	Average σ_{YY} (kPa)	Horizontal force (kN)
	top upstream	top downstream	base upstream	base downstream			
1	0	1.3	-0.2654	1.59652	0.316192	7.62	2.41
2	-0.2654	1.59652	-0.5308	1.89304	0.428576	13.14	5.63
3	-0.5308	1.89304	-0.7962	2.18956	0.54096	17.60	9.52
4	-0.7962	2.18956	-1.0616	2.48608	0.653344	22.19	14.50
5	-1.0616	2.48608	-1.327	2.7826	0.765728	24.93	19.09
6	-1.327	2.7826	-1.5924	3.07912	0.878112	26.05	22.87
7	-1.5924	3.07912	-1.8578	3.37564	0.990496	26.74	26.48
8	-1.8578	3.37564	-2.1232	3.67216	1.10288	27.50	30.33
9	-2.1232	3.67216	-2.3886	3.96868	1.215264	28.45	34.58
10	-2.3886	3.96868	-2.654	4.2652	1.327648	29.76	39.52
11	-2.654	4.2652	-2.9194	4.56172	1.440032	31.21	44.94
12	-2.9194	4.56172	-3.1848	4.85824	1.552416	32.50	50.45
13	-3.1848	4.85824	-3.4502	5.15476	1.6648	33.76	56.20
14	-3.4502	5.15476	-3.7156	5.45128	1.777184	34.99	62.19
15	-3.7156	5.45128	-3.981	5.7478	1.889568	36.15	68.30
16	-3.981	5.7478	-4.2464	6.04432	2.001952	37.37	74.82
17	-4.2464	6.04432	-4.5118	6.34084	2.114336	38.64	81.71
18	-4.5118	6.34084	-4.7772	6.63736	2.22672	39.90	88.84
19	-4.7772	6.63736	-5.0426	6.93388	2.339104	41.17	96.31
20	-5.0426	6.93388	-5.308	7.2304	2.451488	42.50	104.18
21	-5.308	7.2304	-5.5734	7.52692	2.563872	43.81	112.33
22	-5.5734	7.52692	-5.8388	7.82344	2.676256	45.12	120.76
23	-5.8388	7.82344	-6.1042	8.11996	2.78864	46.30	129.12
24	-6.1042	8.11996	-6.3696	8.41648	2.901024	47.29	137.20
25	-6.3696	8.41648	-6.635	8.713	3.013408	47.25	142.38

F4 Development of the solution for local stability

F4.1 Method 1

Fig. F.4 shows an illustration of vertical integration of the inclined sliding plane for local stability. C_{S1} (kN), C_{S2} (kN), C_{S3} (kN), and C_{S4} (kN) are the compressive forces by considering different sections along the WRB and sidewall contact.

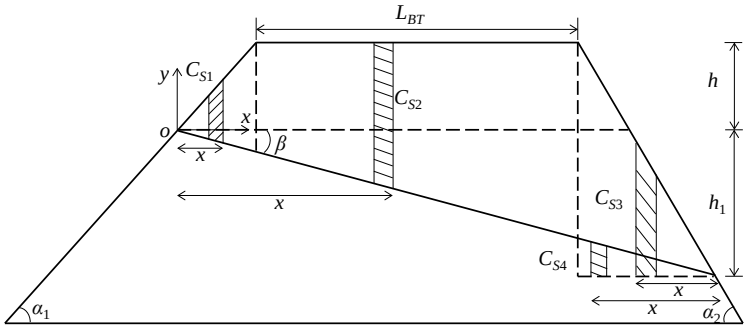

Figure F.4 Schematic diagram of integration in the *y*-direction of the inclined sliding plane for local stability with method 1

$$C_S = C_{S1} + C_{S2} + C_{S3} - C_{S4}$$

C_S (kN) is a horizontal force of the inclined sliding plane perpendicular to the sidewall along the WRB and sidewal.,.,m hcxl contact.

$$C_{S1} = \int_0^{h/\tan\alpha_1} \frac{K\gamma_{wr}\left(x\tan\alpha_1 + x\tan\beta\right)^2}{2} dx = \frac{K\gamma_{wr}\left(\tan\alpha_1 + \tan\beta\right)^2}{2} \frac{x^3}{3}\Big|_0^{h/\tan\alpha_1}$$
$$= \frac{K\gamma_{wr}\left(\tan\alpha_1 + \tan\beta\right)^2 h^3}{6\tan^3\alpha_1}$$

$$C_{S2} = \int_{h/\tan\alpha_1}^{h/\tan\alpha_1 + L_{BT}} \frac{K\gamma_{wr}\left(h + x\tan\beta\right)^2}{2} dx = \frac{K\gamma_{wr}h^2}{2} x\Big|_{h/\tan\alpha_1}^{h/\tan\alpha_1 + L_{BT}} + K\gamma_{wr}h\tan\beta\frac{x^2}{2}\Big|_{h/\tan\alpha_1}^{h/\tan\alpha_1 + L_{BT}} + \frac{K\gamma_{wr}\tan^2\beta}{2}\frac{x^3}{3}\Big|_{h/\tan\alpha_1}^{h/\tan\alpha_1 + L_{BT}}$$
$$= \frac{K\gamma_{wr}h^2 L_{BT}}{2} + \frac{K\gamma_{wr}hL_{BT}\tan\beta\left(2h + L_{BT}\tan\alpha_1\right)}{2\tan\alpha_1} + \frac{K\gamma_{wr}L_{BT}\tan^2\beta\left(3h^2 + 3hL_{BT}\tan\alpha_1 + L_{BT}^2\tan^2\alpha_1\right)}{6\tan^2\alpha_1}$$

$$C_{S3} = \int_0^{(h+h_1)/\tan\alpha_2} \frac{K\gamma_{wr}\left(x\tan\alpha_2\right)^2}{2} dx = \frac{K\gamma_{wr}\tan^2\alpha_2}{2}\frac{x^3}{3}\Big|_0^{(h+h_1)/\tan\alpha_2}$$
$$= \frac{K\gamma_{wr}\left(h+h_1\right)^3}{6\tan\alpha_2}$$

$$C_{S4}=\int_0^{(h+h_1)/\tan\alpha_2}\frac{K\gamma_{wr}x^2\left(2\tan\alpha_2\tan\beta-\tan^2\beta\right)}{2}dx=\frac{K\gamma_{wr}\left(2\tan\alpha_2\tan\beta-\tan^2\beta\right)}{2}\frac{x^3}{3}\Big|_0^{(h+h_1)/\tan\alpha_2}$$
$$=\frac{K\gamma_{wr}\left(2\tan\alpha_2\tan\beta-\tan^2\beta\right)\left(h+h_1\right)^3}{6\tan^3\alpha_2}$$

$$C_S=C_{S1}+C_{S2}+C_{S3}-C_{S4}$$
$$=\frac{K\gamma_{wr}}{6}\left[\begin{array}{l}\dfrac{h^3\left(\tan\alpha_1+\tan\beta\right)^2}{\tan^3\alpha_1}+3h^2L_{BT}+\dfrac{3hL_{BT}\tan\beta\left(2h+L_{BT}\tan\alpha_1\right)}{\tan\alpha_1}\\+\dfrac{L_{BT}\tan^2\beta\left(3h^2+3hL_{BT}\tan\alpha_1+L_{BT}^2\tan^2\alpha_1\right)}{\tan^2\alpha_1}+\dfrac{\left(h+h_1\right)^3\left(\tan\alpha_2-\tan\beta\right)^2}{\tan^3\alpha_2}\end{array}\right]$$

F4.2 Method 2

Fig. F.5 shows an illustration of vertical integration of the inclined sliding plane for local stability. C_{S1} (kN), C_{S2} (kN), and C_{S3} (kN) are the compressive forces by considering different sections along the WRB and sidewall contact; C_{LU} (kN) and C_{LD} (kN) are the compressive forces of the upstream and downstream triangular sections, respectively; C_{LC} (kN) is the compressive force of the central rectangular section.

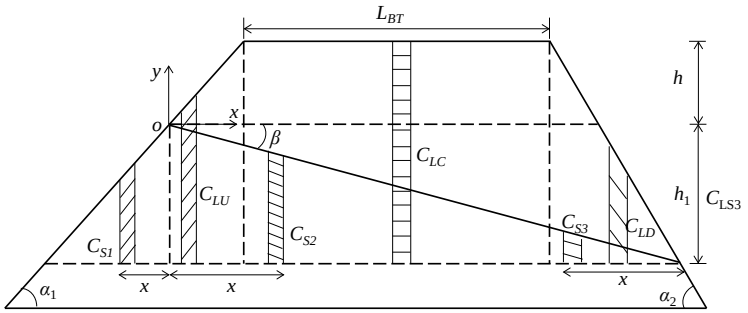

Figure F.5 Schematic diagram of integration in the *y*-direction of the inclined sliding plane for local stability with method 2

$$C_S=C_{LU}+C_{LC}+C_{LD}-C_{S1}-C_{S2}-C_{S3}$$

$$C_{LU}=\int_0^{(h+h_1)/\tan\alpha_1}\frac{K\gamma_{wr}\left(x\tan\alpha_1\right)^2}{2}dx=\frac{K\gamma_{wr}\left(\tan\alpha_1\right)^2}{2}\frac{x^3}{3}\Big|_0^{(h+h_1)/\tan\alpha_1}=\frac{K\gamma_{wr}\left(h+h_1\right)^3}{6\tan\alpha_1}$$

$$C_{LC}=\int_0^{L_{BT}}\frac{K\gamma_{wr}\left(h+h_1\right)^2}{2}dx=\frac{K\gamma_{wr}\left(h+h_1\right)^2}{2}x\Big|_0^{L_{BT}}=\frac{K\gamma_{wr}L_{BT}\left(h+h_1\right)^2}{2}$$

$$C_{LD}=\int_0^{(h+h_1)/\tan\alpha_2}\frac{K\gamma_{wr}\left(x\tan\alpha_2\right)^2}{2}dx=\frac{K\gamma_{wr}\left(\tan\alpha_2\right)^2}{2}\frac{x^3}{3}\Big|_0^{(h+h_1)/\tan\alpha_2}=\frac{K\gamma_{wr}\left(h+h_1\right)^3}{6\tan\alpha_2}$$

$$C_{S1}=\int_0^{h_1/\tan\alpha_1}\frac{K\gamma_{wr}\left(x\tan\alpha_1\right)^2}{2}dx=\frac{K\gamma_{wr}\left(\tan\alpha_1\right)^2}{2}\frac{x^3}{3}\Big|_0^{h_1/\tan\alpha_1}=\frac{K\gamma_{wr}h_1^3}{6\tan\alpha_1}$$

$$C_{S2}=\int_0^{h/\tan\alpha_1}\frac{K\gamma_{wr}\left(h_1^2+2h_1x\tan\alpha_1-2x^2\tan\alpha_1\tan\beta-x^2\tan^2\beta\right)^2}{2}dx+\int_{h/\tan\alpha_1}^{h/\tan\alpha_1+L_{BT}}\frac{K\gamma_{wr}}{2}\left(h_1^2+2hh_1-x^2\tan^2\beta-2xh\tan\beta\right)dx$$

$$=\frac{K\gamma_{wr}h_1^2}{2}x\Big|_0^{h/\tan\alpha_1}+K\gamma_{wr}h_1\tan\alpha_1\frac{x^2}{2}\Big|_0^{h/\tan\alpha_1}-K\gamma_{wr}\tan\alpha_1\tan\beta\frac{x^3}{3}\Big|_0^{h/\tan\alpha_1}-K\gamma_{wr}\tan^2\beta\frac{x^3}{6}\Big|_0^{h/\tan\alpha_1}$$

$$+\frac{K\gamma_{wr}h_1^2}{2}x\Big|_{h/\tan\alpha_1}^{h/\tan\alpha_1+L_{BT}}+K\gamma_{wr}hh_1x\Big|_{h/\tan\alpha_1}^{h/\tan\alpha_1+L_{BT}}-K\gamma_{wr}\tan^2\beta\frac{x^3}{6}\Big|_{h/\tan\alpha_1}^{h/\tan\alpha_1+L_{BT}}-K\gamma_{wr}h\tan\beta\frac{x^2}{2}\Big|_{h/\tan\alpha_1}^{h/\tan\alpha_1+L_{BT}}$$

$$=\frac{K\gamma_{wr}h_1^2h}{2\tan\alpha_1}+\frac{K\gamma_{wr}h_1h^2}{2\tan\alpha_1}-\frac{K\gamma_{wr}h^3\tan\beta}{3\tan^2\alpha_1}-\frac{K\gamma_{wr}h^3\tan^2\beta}{6\tan^3\alpha_1}+\frac{K\gamma_{wr}h_1^2L_{BT}}{2}+K\gamma_{wr}hh_1L_{BT}$$

$$-\frac{K\gamma_{wr}\tan^2\beta L_{BT}\left(3h^2+3hL_{BT}\tan\alpha_1+{L_{BT}}^2\tan^2\alpha_1\right)}{6\tan^2\alpha_1}-\frac{K\gamma_{wr}h\tan\beta L_{BT}\left(2h+L_{BT}\tan\alpha_1\right)}{2\tan\alpha_1}$$

$$C_{S3}=\int_0^{(h+h_1)/\tan\alpha_2}\frac{K\gamma_{wr}x^2\left(2\tan\alpha_2\tan\beta-\tan^2\beta\right)}{2}dx=\frac{K\gamma_{wr}\left(2\tan\alpha_2\tan\beta-\tan^2\beta\right)}{2}\frac{x^3}{3}\Big|_0^{(h+h_1)/\tan\alpha_2}$$

$$=\frac{K\gamma_{wr}\left(2\tan\alpha_2\tan\beta-\tan^2\beta\right)\left(h+h_1\right)^3}{6\tan^3\alpha_2}$$

$$C_S=C_{LU}+C_{LC}+C_{LD}-C_{S1}-C_{S2}-C_{S3}$$

$$=\frac{K\gamma_{wr}}{6}\left[\begin{array}{l}\dfrac{\left(h+h_1\right)^3}{\tan\alpha_1}+3L_{BT}\left(h+h_1\right)^2+\dfrac{\left(h+h_1\right)^3}{\tan\alpha_2}-\dfrac{h_1^3}{\tan\alpha_1}-\dfrac{3h_1^2h}{\tan\alpha_1}-\dfrac{3h_1h^2}{\tan\alpha_1}+\dfrac{2h^3\tan\beta}{\tan^2\alpha_1}\\+\dfrac{h^3\tan^2\beta}{\tan^3\alpha_1}-3h_1^2L_{BT}-6hh_1L_{BT}+\dfrac{L_{BT}\tan^2\beta\left(3h^2+3hL_{BT}\tan\alpha_1+{L_{BT}}^2\tan^2\alpha_1\right)}{\tan^2\alpha_1}\\+\dfrac{3h\tan\beta L_{BT}\left(2h+L_{BT}\tan\alpha_1\right)}{\tan\alpha_1}-\dfrac{\left(2\tan\alpha_2\tan\beta-\tan^2\beta\right)\left(h+h_1\right)^3}{\tan^3\alpha_2}\end{array}\right]$$

$$=\frac{K\gamma_{wr}}{6}\left[\begin{array}{l}\dfrac{h^3\left(\tan\alpha_1+\tan\beta\right)^2}{\tan^3\alpha_1}+3h^2L_{BT}+\dfrac{3hL_{BT}\tan\beta\left(2h+L_{BT}\tan\alpha_1\right)}{\tan\alpha_1}\\+\dfrac{L_{BT}\tan^2\beta\left(3h^2+3hL_{BT}\tan\alpha_1+L_{BT}^2\tan^2\alpha_1\right)}{\tan^2\alpha_1}+\dfrac{\left(h+h_1\right)^3\left(\tan\alpha_2-\tan\beta\right)^2}{\tan^3\alpha_2}\end{array}\right]$$

F4.3 Method 3

Fig. F.6 shows an illustration of horizontal integration of the inclined sliding plane for local stability.

C_{S1} (kN), C_{S2} (kN), C_{S3} (kN), and C_{S4} (kN) are the compressive forces by considering different sections along the WRB and sidewall contact; C_{LU} (kN) and C_{LD} (kN) are the compressive forces of the upstream and downstream triangular sections, respectively; C_{LC} (kN) is the compressive force of the central rectangular section.

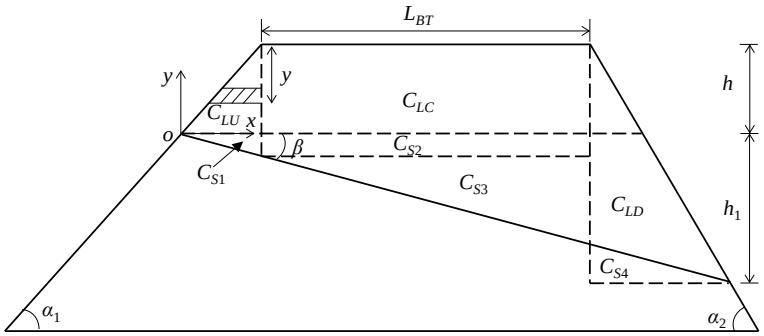

Figure F.6 Schematic diagram of integration in the *x*-direction of the inclined sliding plane with method 3

$$C_S = C_{LU} + C_{LC} + C_{LD} + C_{S1} + C_{S2} + C_{S3} - C_{S4}$$

$$C_{LU} = \int_0^h \frac{K\gamma_{wr} y^2}{2\tan\alpha_1} dy = \frac{K\gamma_{wr}}{2\tan\alpha_1} \frac{y^3}{3}\Big|_0^h = \frac{K\gamma_{wr} h^3}{6\tan\alpha_1}$$

$$C_{LC} = \int_0^h K\gamma_{wr} L_{BT} y dy = K\gamma_{wr} L_{BT} \frac{y^2}{2}\Big|_0^h = \frac{K\gamma_{wr} L_{BT} h^2}{2}$$

$$C_{LD} = \int_0^{h+h_1} \frac{K\gamma_{wr} y^2}{2\tan\alpha_2} dy = \frac{K\gamma_{wr}}{2\tan\alpha_2} \frac{y^3}{3}\Big|_0^{h+h_1} = \frac{K\gamma_{wr}\left(h+h_1\right)^3}{6\tan\alpha_2}$$

$$C_{S1} = \int_0^{h\tan\beta/\tan\alpha_1} \frac{K\gamma_{wr}}{2}\left[\frac{2yh}{\tan\alpha_1} - y^2\left(\frac{\tan\alpha_1}{\tan^2\beta} + \frac{2}{\tan\beta}\right) + \frac{h^2}{\tan\alpha_1}\right] dy$$

$$= \frac{K\gamma_{wr} h}{\tan\alpha_1} y^2\Big|_0^{h\tan\beta/\tan\alpha_1} - \frac{K\gamma_{wr}}{2}\left(\frac{\tan\alpha_1}{\tan^2\beta} + \frac{2}{\tan\beta}\right)\frac{y^3}{3}\Big|_0^{h\tan\beta/\tan\alpha_1} + \frac{K\gamma_{wr} h^2}{2\tan\alpha_1} y\Big|_0^{h\tan\beta/\tan\alpha_1}$$

$$= \frac{K\gamma_{wr}}{2}\left(\frac{h^3\tan^2\beta}{\tan^3\alpha_1} - \frac{h^3\tan\beta}{3\tan^2\alpha_1} - \frac{2h^3\tan^2\beta}{3\tan^3\alpha_1} + \frac{h^3\tan\beta}{\tan^2\alpha_1}\right)$$

$$= \frac{K\gamma_{wr} h^3\tan\beta\left(\tan\beta + 2\tan\alpha_1\right)}{6\tan^3\alpha_1}$$

$$C_{S2}=\int_0^{h\tan\beta/\tan\alpha_1} K\gamma_{wr}\left(h+y\right)L_{BT}dy$$

$$=K\gamma_{wr}hL_{BT}y\Big|_0^{h\tan\beta/\tan\alpha_1}+K\gamma_{wr}L_{BT}\frac{y^2}{2}\Big|_0^{h\tan\beta/\tan\alpha_1}=\frac{K\gamma_{wr}h^2L_{BT}\tan\beta}{\tan\alpha_1}\left(1+\frac{\tan\beta}{2\tan\alpha_1}\right)$$

$$C_{S3}=\int_0^{L_{BT}\tan\beta} K\gamma_{wr}\left(h+y+\frac{h\tan\beta}{\tan\alpha_1}\right)\left(L_{BT}-\frac{y}{\tan\beta}\right)dy$$

$$=K\gamma_{wr}hL_{BT}y\Big|_0^{L_{BT}\tan\beta}-\frac{K\gamma_{wr}h}{\tan\beta}\frac{y^2}{2}\Big|_0^{L_{BT}\tan\beta}+K\gamma_{wr}L_{BT}\frac{y^2}{2}\Big|_0^{L_{BT}\tan\beta}-\frac{K\gamma_{wr}}{\tan\beta}\frac{y^3}{3}\Big|_0^{L_{BT}\tan\beta}$$

$$+\frac{K\gamma_{wr}hL_{BT}\tan\beta}{\tan\alpha_1}y\Big|_0^{L_{BT}\tan\beta}-\frac{K\gamma_{wr}h}{\tan\alpha_1}\frac{y^2}{2}\Big|_0^{L_{BT}\tan\beta}$$

$$=K\gamma_{wr}\left(L_{BT}^2h\tan\beta-\frac{L_{BT}^2h\tan\beta}{2}+\frac{L_{BT}^3\tan^2\beta}{2}-\frac{L_{BT}^3\tan^2\beta}{3}+\frac{hL_{BT}^2\tan^2\beta}{\tan\alpha_1}-\frac{hL_{BT}^2\tan^2\beta}{2\tan\alpha_1}\right)$$

$$=\frac{K\gamma_{wr}L_{BT}^2\tan\beta}{2}\left(h+\frac{L_{BT}\tan\beta}{3}+\frac{h\tan\beta}{\tan\alpha_1}\right)$$

$$C_{S4}=\int_0^{(h+h_2)\tan\beta/\tan\alpha_2}\frac{K\gamma_{wr}}{2}\left(h_1+h_2-2y+\frac{y\tan\alpha_2}{\tan\beta}\right)\left(\frac{h_1+h_2}{\tan\alpha_2}-\frac{y}{\tan\beta}\right)dy$$

$$=\frac{K\gamma_{wr}\left(h_1+h_2\right)^2}{2\tan\alpha_2}y\Big|_0^{(h+h_2)\tan\beta/\tan\alpha_2}-\frac{K\gamma_{wr}\left(h_1+h_2\right)}{2\tan\alpha_2}y^2\Big|_0^{(h+h_2)\tan\beta/\tan\alpha_2}+\frac{K\gamma_{wr}\left(2\tan\beta-\tan\alpha_1\right)}{2\tan^2\beta}\frac{y^3}{3}\Big|_0^{(h+h_2)\tan\beta/\tan\alpha_2}$$

$$=\frac{K\gamma_{wr}}{2}\left[\frac{\left(h_1+h_2\right)^3\tan\beta}{\tan^2\alpha_2}-\frac{\left(h_1+h_2\right)^3\tan^2\beta}{\tan^3\alpha_2}+\frac{\left(h_1+h_2\right)^3\left(2\tan^2\beta-\tan\alpha_1\tan\beta\right)}{3\tan^3\alpha_2}\right]$$

$$=\frac{K\gamma_{wr}\left(h_1+h_2\right)^3\left(2\tan\alpha_2\tan\beta-\tan^2\beta\right)}{6\tan^3\alpha_2}$$

$$C_S=C_{LU}+C_{LC}+C_{LD}+C_{S1}+C_{S2}+C_{S3}-C_{S4}$$

$$=\frac{K\gamma_{wr}h^3}{6\tan\alpha_1}+\frac{K\gamma_{wr}L_{BT}h^2}{2}+\frac{K\gamma_{wr}\left(h+h_1\right)^3}{6\tan\alpha_2}+\frac{K\gamma_{wr}h^3\tan\beta\left(\tan\beta+2\tan\alpha_1\right)}{6\tan^3\alpha_1}+\frac{K\gamma_{wr}h^2L_{BT}\tan\beta}{\tan\alpha_1}\left(1+\frac{\tan\beta}{2\tan\alpha_1}\right)$$

$$+\frac{K\gamma_{wr}L_{BT}^2\tan\beta}{2}\left(h+\frac{L_{BT}\tan\beta}{3}+\frac{h\tan\beta}{\tan\alpha_1}\right)-\frac{K\gamma_{wr}\left(h_1+h_2\right)^3\left(2\tan\alpha_2\tan\beta-\tan^2\beta\right)}{6\tan^3\alpha_2}$$

$$=\frac{K\gamma_{wr}}{6}\left[\begin{array}{l}\dfrac{h^3\left(\tan\alpha_1+\tan\beta\right)^2}{\tan^3\alpha_1}+3h^2L_{BT}+\dfrac{\left(h+h_1\right)^3\left(\tan\alpha_2-\tan\beta\right)^2}{\tan^3\alpha_2}+\dfrac{6h^2L_{BT}\tan\beta}{\tan\alpha_1}\left(1+\dfrac{\tan\beta}{2\tan\alpha_1}\right)\\ +3L_{BT}^2\tan\beta\left(h+\dfrac{L_{BT}\tan\beta}{3}+\dfrac{h\tan\beta}{\tan\alpha_1}\right)\end{array}\right]$$

F4.4 Validation between method 1, method 2, and method 3

For method 1 and method 2, the C_S can be expressed as:

$$C_S = \frac{K\gamma_{wr}}{6}\left[\begin{array}{l}\dfrac{h^3\left(\tan\alpha_1+\tan\beta\right)^2}{\tan^3\alpha_1}+3h^2L_{BT}+\dfrac{3hL_{BT}\tan\beta\left(2h+L_{BT}\tan\alpha_1\right)}{\tan\alpha_1}\\ +\dfrac{L_{BT}\tan^2\beta\left(3h^2+3hL_{BT}\tan\alpha_1+{L_{BT}}^2\tan^2\alpha_1\right)}{6\tan^2\alpha_1}+\dfrac{\left(h+h_1\right)^3\left(\tan\alpha_2-\tan\beta\right)^2}{\tan^3\alpha_2}\end{array}\right]$$

$$= \frac{K\gamma_{wr}}{6}\left[\begin{array}{l}\dfrac{h^3\left(\tan\alpha_1+\tan\beta\right)^2}{\tan^3\alpha_1}+3h^2L_{BT}+\dfrac{\left(h+h_1\right)^3\left(\tan\alpha_2-\tan\beta\right)^2}{\tan^3\alpha_2}\\ +\dfrac{6h^2L_{BT}\tan\beta}{\tan\alpha_1}+3hL_{BT}^2\tan\beta+\dfrac{3h^2L_{BT}\tan^2\beta}{\tan^2\alpha_1}+\dfrac{3hL_{BT}^2\tan^2\beta}{\tan^2\alpha_1}+L_{BT}^3\tan^2\beta\end{array}\right]$$

For method 3, the C_S can be expressed as:

$$C_S = \frac{K\gamma_{wr}}{6}\left[\begin{array}{l}\dfrac{h^3\left(\tan\alpha_1+\tan\beta\right)^2}{\tan^3\alpha_1}+3h^2L_{BT}+\dfrac{\left(h+h_1\right)^3\left(\tan\alpha_2-\tan\beta\right)^2}{\tan^3\alpha_2}+\dfrac{6h^2L_{BT}\tan\beta}{\tan\alpha_1}\left(1+\dfrac{\tan\beta}{2\tan\alpha_1}\right)\\ +3L_{BT}^2\tan\beta\left(h+\dfrac{L_{BT}\tan\beta}{3}+\dfrac{h\tan\beta}{\tan\alpha_1}\right)\end{array}\right]$$

$$= \frac{K\gamma_{wr}}{6}\left[\begin{array}{l}\dfrac{h^3\left(\tan\alpha_1+\tan\beta\right)^2}{\tan^3\alpha_1}+3h^2L_{BT}+\dfrac{\left(h+h_1\right)^3\left(\tan\alpha_2-\tan\beta\right)^2}{\tan^3\alpha_2}\\ +\dfrac{6h^2L_{BT}\tan\beta}{\tan\alpha_1}+\dfrac{3h^2L_{BT}\tan^2\beta}{\tan^2\alpha_1}+3hL_{BT}^2\tan\beta+L_{BT}^3\tan^2\beta+\dfrac{3hL_{BT}^2\tan^2\beta}{\tan^2\alpha_1}\end{array}\right]$$

The same result is obtained with three methods.

By simplifying the equation, C_S can be expressed as:

$$C_S = \frac{K\gamma_{wr}}{6}\left[\frac{h'+L_{BT}\tan\beta}{\tan\alpha_2-\tan\beta}+h'^2\left(\frac{h}{\tan\alpha_1}+3L_{BT}\right)+L_{BT}^2\tan\beta\left(L_{BT}\tan\beta+3h'\right)\right]$$

where

$$h' = h\left(1+\frac{\tan\beta}{\tan\alpha_1}\right)$$

F5 Numerical simulation of the experimental test of Belem et al. (2018)

To further test the elastoplastic model of FLAC3D, a scaled-down laboratory test of WRB conducted by Nujaim et al. (2018, 2020) will be reproduced by numerical modeling with FLAC3D. The experimental results of the physical model tests were given in Nujaim et al. (2018) while the details of the tested WRB geometries can be found in Nujaim et al. (2020).

Fig. F.7a schematically shows the physical model of Nujaim et al. (2018, 2020). The stope and the drift were constructed with plexiglass of 3 mm in thickness estimated based on a photo of the physical model given in Nujaim et al. (2018, 2020). The plexiglass is assumed to have a unit weight of γ_p = 11.8 kN/m^3, Young's modulus of E_p = 3 GPa, and Poisson's ratio of μ_p = 0.3 (Lu et al. 1997; Ishiyama and Higo 2002). The backfill was made of clay having a unit weight of γ_b = 13.5 kN/m^3 (Nujaim et al. 2018, 2020). The WRB was built with a trapezoidal mold. The WRB are characterized as L_{BT} = 0.072 m, L_{BB} = 0.25 m, H_d = 0.09 m, L_d = 0.09 m, and α_1 = α_2 = 45°. The slope angles of the WRB are calculated as α_1= α_2 = 45° based on the geometry in Nujaim et al. (2018, 2020). The unit weight of the waste rocks used to construct the barricade is estimated to be γ_{wr} = 13.84 kN/m^3 because 1.8 kg of waste rocks were used to construct the WRB having a volume of 0.0013 m^3 (Nujaim et al. 2018, 2020). The friction angle of the waste rocks is assumed to be ϕ'_{wr} = 45° based on the slope angle of the WRB while the Poisson's ratio is assumed to be μ_{wr} = 0.3. Regarding the interface friction angle δ_{wr} between the waste rocks and confining walls, one would obtain a value of δ_{wr} = 30° if one applies the typical (and empirical) relationship $\delta_{wr} = 2\phi'_{wr}/3$ (to add the references). This value seems to be overly high for the smooth and stiff plexiglass walls. In this study, the interface friction angle δ_{wr} between the waste rocks and plexiglass walls is assumed to be in the range of 20° to 30°. The WRB instability test was conducted by increasing the pressure p on the upstream slope face of the WRB until a value of 4.63 kPa (recorded by Nujaim et al. 2018) at the bottom of the WRB, at which the sliding of the WRB took place.

Fig. F.7b shows a numerical model of the WRB constructed in the plexiglass drift, built with FLAC3D. The plexiglass drift is fixed in all directions at the base and in the x-direction on the left end. The right end and the outside faces of the two side walls and roof remain free. A void space of 0.01 mm is left between the WRB top and the plexiglass drift roof to reproduce the void space observed in the physical model of Nujaim et al. (2018, 2020). Interface elements are introduced

between the WRB and two lateral plexiglass walls as well as between the WRB and the plexiglass floor. The optimal meshes near the top of the barricade are estimated to be 0.5 mm × 0.6 mm × 0.6 mm after mesh size sensitivity analysis. A sensitivity analysis of the plexiglass thickness indicates that it does not affect the numerical results when its values change from xx mm to yy mm.

The large strain option of FLAC3D was chosen to simulate the sliding process of the WRB. The simulation was made by increasing the backfill pressure *p* on the upstream slope face of WRB until the instability occurrence of the WRB.

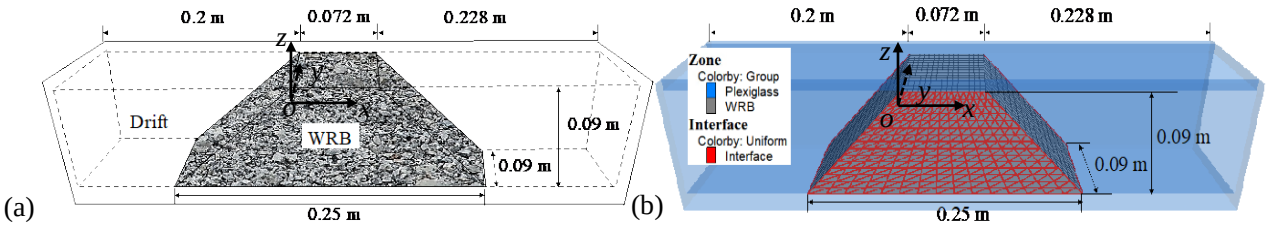

Figure F.7 (a) A physical model of WRB subjected to a paste fill pressure *p* along the upstream slope (adapted from Nujaim et al. 2018, 2020); (b) a numerical model of the WRB built with FLAC3D.

Fig. F.8a shows a photo of the test result of Nujaim et al. (2018, 2020) when the WRB slipped a certain distance of about 0.072 m, as a stiff block when the applied pressure at the WRB bottom was increased to a value of 4.63 kPa. The corresponding pressure at the top of the WRB is estimated to be 3.46 kPa by considering the unit weight and the height of the clay backfill.

Fig. F.8b presents the iso-contour of displacement as well as the initial and final positions of the WRB after the application of a backfill pressure of 3.46 kPa at the top and 4.63 kPa at the base of WRB, obtained by considering an interface friction angle δ_{wr} = 25° in the numerical model of FLAC3D. One sees that the sliding of the WRB block observed in the physical model test is successfully reproduced by the numerical modeling with FLAC3D.

It should be noted that the sliding of 0.038 m is only an illustration. As the system becomes unstable, the large strain takes place and the numerical model becomes non converged. Larger sliding can be obtained by increasing the number of step iteration. On the other hand, when the WRB slipped and

moved away from the stope, the height of the clay backfill in the stope should decrease, resulting in a decrease in the backfill pressure on the upstream slope face of the WRB. The WRB stopped further sliding when the backfill pressure was reduced to a certain value. In the numerical model, the reduction of backfill pressure with the sliding of the WRB was not taken into account. This explains well the ceaseless increase of the sliding of the WRB with more step iterations in the numerical modeling with FLAC3D. This indicates that the quantitative comparison between the sliding observed in the physical model test and that obtained by numerical modeling with FLAC3D is unnecessary. Rather, it would be more interesting to see if the numerical modeling can reproduce the triggering state of sliding of the WRB associated with the pressure increase in the stope.

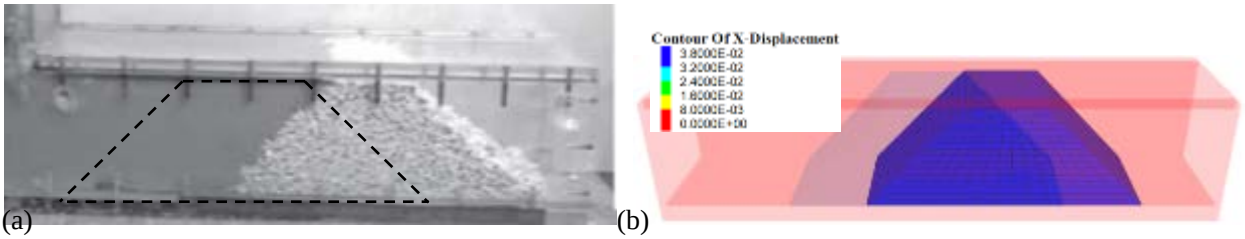

Figure F.8 (a) A laboratory test results subjected to a paste fill pressure p along the upstream slope face and showing sliding, the original place is shown by dotted lines (adapted from Nujaim et al. 2018, 2020); (b) displacement contour of the numerical result with FLAC3D, the original location is shown by transparent blue color (simulation made with δ_{wr} = 25°).

Although the numerical simulation reproduces the test result in Nujaim et al. (2018), the geometrical and mechanical parameters still have some problems that need to be confirmed. For example, the internal friction angle and interface friction angle are of great importance in this study. Two parameters are assumed to be ϕ'_{wr} = 45° and δ_{wr} = 25°. The internal friction angle should be equal to or bigger than 45° based on the physical meaning (equals upstream and downstream slope angles). The interface friction angle is obtained by FLAC3D by testing the range from 20° to 30°. The global sliding occurs when δ_{wr} varies from 20° to 25°, the local sliding takes place when δ_{wr} changes from 20° to 25°. So, the interface friction determined here is based on the numerical results. More laboratory tests are expected to be conducted to study the internal friction and interface friction.